



HAL
open science

Tip-Enhanced Raman Spectroscopy (TERS) under electrochemical conditions: towards the in situ characterization of functional nanomaterials

Aja Ana Pavlič

► **To cite this version:**

Aja Ana Pavlič. Tip-Enhanced Raman Spectroscopy (TERS) under electrochemical conditions: towards the in situ characterization of functional nanomaterials. Theoretical and/or physical chemistry. Sorbonne Université, 2022. English. NNT : 2022SORUS264 . tel-03869392

HAL Id: tel-03869392

<https://theses.hal.science/tel-03869392>

Submitted on 24 Nov 2022

HAL is a multi-disciplinary open access archive for the deposit and dissemination of scientific research documents, whether they are published or not. The documents may come from teaching and research institutions in France or abroad, or from public or private research centers.

L'archive ouverte pluridisciplinaire **HAL**, est destinée au dépôt et à la diffusion de documents scientifiques de niveau recherche, publiés ou non, émanant des établissements d'enseignement et de recherche français ou étrangers, des laboratoires publics ou privés.

Sorbonne Université

Ecole doctorale 388
Chimie Physique et Chimie Analytique

Laboratoire Interfaces et Systèmes Electrochimiques (LISE), UMR CNRS 8235

Tip-Enhanced Raman Spectroscopy (TERS) under electrochemical conditions

*Towards the in situ characterization of functional
nanomaterials*

Par Aja Ana Pavlič

Thèse de doctorat de chimie physique

Dirigée par Ivan T Lucas

Co-encadrée par Emmanuel Maisonhaute

Pour une soutenance publique prévue le 25 mai 2022

Devant un jury composé de :

M. Bonhommeau Sébastien	MCF HDR, Université de Bordeaux	Rapporteur
M. Zigah Dodzi	Prof., Université de Poitiers	Rapporteur
M ^{me} Mangeney Claire	Prof., Université Paris Descartes	Examinatrice
M ^{me} Deniset-Besseau Ariane	MCF, Université Paris-Saclay	Examinatrice
M. Maisonhaute Emmanuel	Prof., Sorbonne Université	Co-encadrant
M. Lucas Ivan T	MCF HDR, Sorbonne Université	Directeur de thèse

Contents

General introduction	9
Chapter 1 - State of the art	13
Introduction	13
1.1. How to retrieve chemical information at the nanoscale?	13
1.1.1. The rise of spectroscopy	13
1.1.2. Towards spatially resolved measurements	14
1.2. The atomic force microscope	16
1.2.1. Technical description of an AFM	16
1.2.2. Interaction forces at the nanoscale	18
1.2.3. Different operating modes	19
1.2.4. Coupling AFM with IR spectroscopy	21
1.3. Raman spectroscopy and Surface Enhanced Raman Spectroscopy	23
1.3.1. Raman spectroscopy	23
1.3.2. Confocal Raman microscopy	25
1.3.3. Raman process efficiency	27
1.3.4. Localized Surface Plasmon Resonance at a nanoparticle	28
1.3.5. Surface-Enhanced Raman Spectroscopy (SERS)	29
1.3.6. Implementation <i>in situ</i>	30
1.4. Tip Enhanced Raman Spectroscopy	31
1.4.1. Different TERS configurations	32
1.4.2. TERS sensitivity and spatial resolution	32
1.4.3. TERS implementation in liquids and under electrochemical conditions	35
1.4.4. TERS in LISE - Description of the set-up	38
1.4.5. A typical TERS implementation sequence	40
Conclusions / Challenges for AFM-EC-TERS	42
Chapter 2 - Development of TERS active AFM probes	44
Introduction	44
2.1. Brief review of TERS probe manufacturing processes	46
2.1.1. Physical deposition of plasmonic material on silicon tips	46
2.1.2. (Electro) chemical deposition	51
2.1.3. Electrochemical etching	54
2.1.4. AFM probes from bulk metal to AFM-TERS probes	61
2.2. Fabrication/optimization of TERS active AFM probes in this work	64
2.2.1. From bulk metal wire to AFM probe	64
2.2.2. Cantilever immobilization on Si chips	65
2.2.3. "Shaping" of tapered gold tip by electrochemical etching	66
2.2.4. Optimization of the etching electrochemical cell	68
2.3. Characteristics of handmade AFM probes	69
2.3.1. Tip profile and radius of curvature	70
2.3.2. Cantilever features	73
2.2.3 Fabrication of bulk silver Ag AFM probes	80

Conclusion	82
Chapter 3 - Performances of home-made TERS probes	85
Introduction	85
3.1. AFM-TERS configurations	86
3.2. AFM imaging performances in the air and in liquid	89
3.2.1. Tip properties and convolution effects	89
3.2.2. Imaging of nano-objects in the air in semi-contact mode	91
3.3. TERS activity of bulk metal AFM probes in the air	100
3.3.1. Sample preparation	101
3.3.2. Point TERS spectra using side illumination	101
3.3.3. Point TERS spectra using bottom illumination	105
3.3.4. Comparison of EF between etched silver and gold probe	111
3.4. TERS mapping performances of bulk metal AFM probes	113
3.5. First TERS implementation in liquid (point spectra) using bulk metal AFM- probes	118
Conclusion	121
Chapter 4 - Characterization of electroactive systems by EC-AFM-TERS	124
Introduction	124
4.1. Electrochemical reduction of 4-NBM	126
4.1.1. Description of 4-NBM	126
4.1.2. Electrochemical signature of 4-NMB on model electrodes	129
4.2. Experimental design for EC-TERS on transparent samples	133
4.2.1. Electrochemical cell for EC-TERS using bottom illumination	133
4.2.2. Optimization of electrochemical conditions for TERS analyses	134
4.3. Study of 4-NMB electrochemical reduction by EC-TERS	139
4.3.1. <i>Ex situ</i> TERS characterization	139
4.3.2. Real-time tracking of composition changes by <i>in situ</i> TERS	143
4.4. EC-TERS implementation on opaque samples	152
4.4.1. Liquid cell design for side illumination	152
4.4.2. Laser focusing and hot-spot mapping in liquid	154
4.4.3. EC-TERS study using side illumination – Preliminary results	155
Conclusions	160
General conclusion	163
References	174

General introduction

The large interest and development of nanomaterials in areas as diverse as heterogeneous catalysis, energy conversion, molecular electronics and storage, bio-sensing or therapeutics, can be explained by the virtually limitless functionalities offered by this class of material. The understanding and optimization of functional nanomaterials requires the development of characterization techniques with sufficient sensitivity which can operate at the nanoscale and under the **operating conditions of these materials** (*in situ, operando*), i.e. active site identification, operating mechanism (chemical modification), detection of reaction intermediates...

Characterization of nanomaterials is usually achieved by microscopy and spectroscopy techniques which operation conditions can however strongly compromise *in situ* applications, e.g. Ultrahigh Vacuum (UHV), possible beam damages, signal screening by the solvent or by the atmosphere. Among benchtop spectroscopies, the emergence of vibrational Raman spectroscopy for *in situ* characterizations this last two decades, especially when coupled to optical microscopy (Raman microscopy: **μ Raman**), is spectacular. The wealth of information contained in vibrational signatures, the clear vibrational signatures, the non-invasive sampling process and the possibility to work in aqueous solutions (visible excitation and weak scattering signal of water) explain this burst of interest among the material science community. The introduction of Surface Enhanced Raman Spectroscopy (**SERS**) in the early 70's, which circumvented the poor sensitivity of Raman spectroscopy and brought the detection threshold of Raman spectroscopy down to the molecular level constitutes a major breakthrough. Ultimately, the association of scanning probe microscopy techniques (**SPM**) with signal enhancement processes laid the foundation to the introduction of Tip-Enhanced Raman Spectroscopy (**TERS or nanoRaman**).

TERS is an emerging technique with an exceptional sensitivity, which can resolve vibrational signature of single nanoobjects, i.e. nanoparticles down to single molecule. Introduced in the late 90s, this technique almost remained at the conceptual stage of its development for many years, being a privilege of only a handful of research groups worldwide. The first demonstration of TERS implementation in water in 2009 (and under electrochemical conditions **EC-TERS** a few years later) and the concomitant apparition of the commercial instruments with advertised TERS capability triggered a surge of interest, especially in the

material chemistry and life science communities. The exceptional sensitivity of TERS and the wealth of information, contained in its vibrational signatures, was demonstrated in 2013 through imaging under vacuum of the vibration modes, of a single porphyrin molecule on an Ag(111) surface. In 2014, it was demonstrated through the composition imaging in the ambient of a single carbon nanotube with a 1.7 nm resolution.¹

If TERS ready instruments, which provide a robust optical coupling, have emerged on the microscopy market, the main impediment to the fast emergence of TERS has been and still remains the difficult conception of probes with controlled properties. Defined taper angle and radius of curvature, chemical stability (silver oxidation) and wear resistance are crucial parameters, which determine the occurrence and the stability at the probe apex of an effective plasmon resonance at a given excitation laser wavelength, prerequisite to high and reproducible signal enhancements. The difficult optical coupling in liquids between the Raman probe (monochromatic laser) and the TERS-active scanning probe, due to the optical path distortion at the multiple interfaces, constitutes a major challenge to the development of *in situ/operando* TERS, where each imaging mode (Tunneling microscopy: **STM**, Atomic Force Microscopy: **AFM**, Shear-force microscopy **SfM**) introduces various levels of technical complexity. Despite significant achievements of a few groups worldwide, the application in liquid environment remains challenging, without existing commercial solution so far.

As early as 2015, LISE took part in the race to develop TERS by acquiring a robust optical coupling system and by developing efficient TERS probes by electrochemical dissolution of gold and silver wires. LISE has since joined the few leaders in the field by producing the first TERS composition mapping of a molecular layer in a liquid medium (organic solvent) in 2016, and by demonstrating TERS mapping measurements under electrochemical conditions with 8 nm lateral resolution in 2018, using partially insulated STM-TERS probes. The *in situ* **STM-TERS** mode has been developed so far, however still limits the TERS study field to conductive, low height objects/samples, strongly immobilized on surfaces.

The main objective of this work has been to broaden the range of systems possibly studyable, e.g. nanoobjects (nanoparticles, 2D materials on insulating substrates) and poorly conducting layers (passive layers, semiconductor materials), by expanding TERS developments in the AFM mode, in liquids and under polarization (**EC-AFM-TERS**).

This work, which focuses around the development of robust TERS active AFM probes and of electrochemical Tip-Enhanced Raman spectroscopy, is divided into 4 independent chapters, organized as follows.

Chapter 1 presents the general background of the techniques used in this work. The general principles of Raman spectroscopy will be detailed, along with the SPM techniques, with a focus on AFM microscopy. Progress in TERS implementation in liquids and under electrochemical conditions will be exposed chronologically. The different set-up developed in LISE laboratory and the bottleneck to the development of AFM-based EC-TERS in this work will then be exposed.

Chapter 2 will focus on the manufacturing of TERS-active AFM probe. The chapter will first present a brief review of TERS probe fabrication processes established throughout the years, highlighting the major optimization steps. Further, the manufacturing process of the probes for this study will be presented. The procedure optimization leading to the production of TERS-active AFM probes made from bulk metal (gold and eventually of silver) will be detailed. Finally, the characteristics (e.g. the tip radius of curvature) and the mechanical properties, *i.e.* resonance frequency, spring constant and cantilever features of the bulk metal AFM probes, will be exposed.

Chapter 3 will cover the performance evaluation of the home-made TERS probes, and their ability to resolve nanostructures; topography (AFM) and composition (TERS). The initial technical developments in the work, allowing the evaluation of the TERS performance of the handmade probe in liquid, will then be exposed.

Chapter 4 is dedicated to the characterization of electroactive systems by EC-AFM-TERS. Associated instrumental developments, *i.e.* optimization of spectro-electrochemical cells, will be presented. The ability to track the electrochemical reduction of a molecular compound carrying a redox entity (nitro) by TERS, will be evaluated on transparent and non-transparent electrodes.

In conclusion, we will summarize the most important results achieved through this work and present the envisaged perspectives.

Chapter 1 - State of the art

Introduction

1.1. How to retrieve chemical information at the nanoscale?

1.1.1. The rise of spectroscopy

Even prior any idea of atomic description of the matter, Archimedes realized one of the first chemical analysis by measuring the density of a crown and determining that silver had been added to gold. This example underlines that determining the composition of mixtures, considering from organic to inorganic compounds, has always been an important topic that has stimulated development of innovative techniques over history. Our present society being based on technological developments, complex materials are being synthesized in almost any aspect of daily life. In electrocatalysis for example, one needs to tailor electrodes that trigger reactions as close as possible to the thermodynamic limits, in order to optimize energetic yield while preventing catalyst poisoning.² Usually, mechanisms are explained by considering subtle changes at the nanometric scale, that need to be observed in *operando* conditions.

In this context, electromagnetic radiation from light energy has always been used to follow chemical evolutions or degradations. The panel of spectroscopic approaches is now so extended that being exhaustive is impossible. UV-visible spectroscopy is indeed an easy way to follow reaction kinetics in a bulk solution. The rise of pump-probe absorption and fluorescence approaches in the femtosecond (even sometimes attosecond) domain now allows to determine chemical reaction paths, as recognized by the Nobel prize attributed to Ahmed Zewail in 1999.³ From the visible domain, spectroscopy has been also extended towards lower and larger wavelengths. From the initial radiographies, the success of X-Ray diffraction resorts from deduction of atom positions in a crystal from the Bragg's law: atomic planes act like a grating and have typical lengths close to the incident wavelength. Nowadays, synchrotron sources provide access to 3D structures of thin films or complex proteins, even with temporal dynamic resolution in some cases.⁴ *Operando* X-ray photoelectron spectroscopy in addition gives access to oxidation states of a catalyst as a function of electrode potential.⁵ At the other range of the spectrum, IR (and to a minor extent terahertz) spectroscopies are probing molecular vibrations.⁶ Their use for deciphering product composition played a major role in elaborating novel synthetic methods in organic or

organometallic chemistry, even if nowadays these tend to be supplanted by NMR spectroscopies.

Last but not least, non-linear or scattering spectroscopies are also key in some domains. Second harmonic or sum/difference frequency generation (SFG/DFG) are still very complex methods to implement, but Raman approaches become increasingly important since cheap and "plug and play" systems, however with good sensitivity, are now available on the market.⁷ Raman spectroscopy, like IR, is sensitive to molecular vibrations.⁸ Nevertheless, a visible source is usually used. Since this PhD work relies on Raman spectroscopy, more details will be provided below.

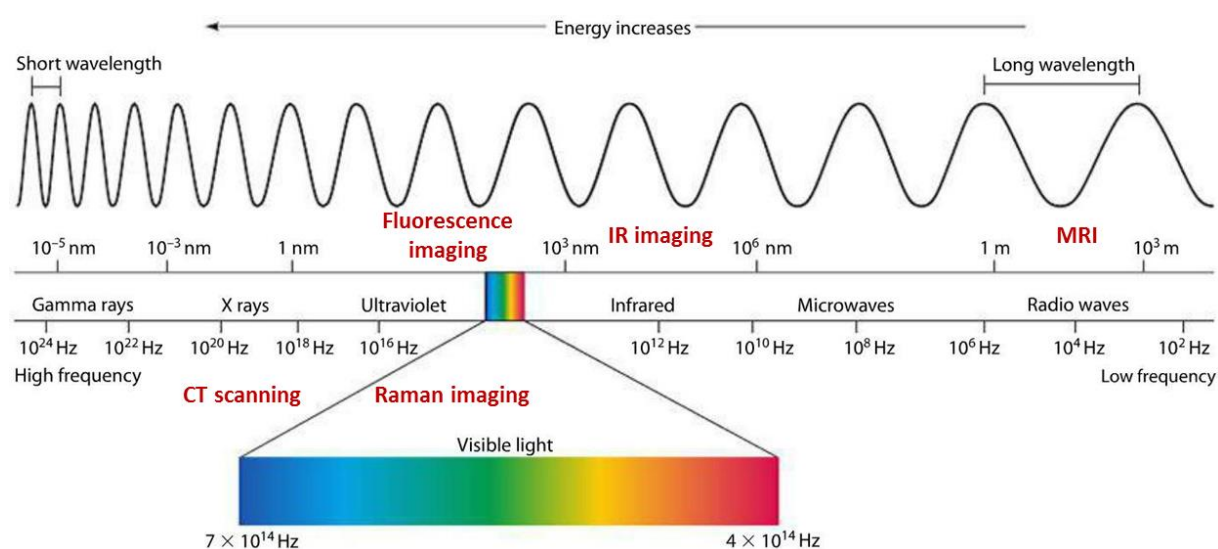


Figure 1.1. Typical wavelengths of various imaging modalities within the electromagnetic spectrum. Adapted from [9].

1.1.2. Towards spatially resolved measurements

All the above mentioned approaches focus on adapting the excitation wavelength to the physicochemical parameters that are probed, but are by default bulk and not local methods (see below for their combination). However, as mentioned above, looking at the nanoscopic composition is also a key problem in modern science. The optical microscope, invented by Antonie van Leeuwenhoek in the 17th century, is particularly adapted to objects with dimensions greater than micron, like living organisms.¹⁰ Abbe and Rayleigh demonstrated that the lateral resolution of a microscope depends on the wavelength and numerical aperture of the objective according to:

$$d = \frac{\lambda}{2n \sin \theta} = \frac{\lambda}{2NA} \quad (1.1)$$

Hence, with a 400 nm light and an objective with NA = 1.4, one gets 143 nm in the best conditions, which is not sufficient for scrutinizing complex materials such as nanoparticles.

To face this issue, super-resolution approaches were developed and found exceptional applications in biophysics, providing 3D images of cell components distributions. Quite different strategies and variations were implemented, from fluorescence correlation spectroscopy up to photobleaching recovery.¹¹ Many of them take profit from the intense signal arising from fluorescent tags, which further gives the access to temporal resolution. The Nobel prize was attributed in 2014, on surpassing the limitations of the light microscope by developing super-resolved fluorescence microscopy.¹²

Another strategy for overcoming optical diffraction limit, and therefore increase spatial resolution, is to use lower wavelengths, as proposed by electron microscopies.¹³ Indeed, Heisenberg uncertainty principle states that:

$$\Delta x \Delta p \geq \frac{h}{4\pi} \quad (1.2)$$

where Δp is the uncertainty on the momentum and Δx is the one on the position.

In an electron microscope, electrons are accelerated under high voltages so that exceptional spatial (pm) and energy resolutions (meV) are attained. All concepts pertaining to visible optics (lengths aberration corrections, interferences, etc) can be transposed with the electrons. Even if electron microscopies (in transmission or field emission) are currently used in many laboratories, their implementation *in situ* is particularly heavy. Another limitation stands from the high energy beams utilization that triggers decomposition of the solvent or studied material arising from radiolytic reactions. These effects may be hard to control and even strongly interfere with the mechanism that is scrutinized.¹⁴

In this general context, the birth of scanning probe microscopies (SPMs) initiated a scientific revolution in 1982 when Binnig and Rohrer invented the scanning tunneling microscope (STM). They were attributed the Nobel prize in 1986, only 4 years after the first proof of concept.¹⁵ Here, spatial resolution does not rely onto optical concepts. Rather, a tip with a low curvature radius is approached close enough to a surface until a tunnel current is detected. Keeping this tunnel current constant, thanks to a feedback loop, is typically used to access

topography with atomic or molecular resolution, even in liquids.¹⁶ At low temperature and in vacuum, scanning tunneling spectroscopy is sensitive to the molecular structure and composition (local density of electronic states by inelastic tunneling spectroscopy IETS), but these conditions are very far from *operando* ones. Nevertheless, the major inconvenient of STM is that since a tunnel current should be detected, the material to be studied should be electrically conductive (or at least semi-conductive).

To circumvent this problem, the same team gave birth to the atomic force microscope (AFM) in 1985. Here, any substrate can be scrutinized, so that now AFM has supplanted STM. Indeed, 7484 references were found for a search in Web of Science with "Scanning tunneling microscopy" in the title, whereas 14989 were obtained for "Atomic force microscopy". Many different ways of using AFM are now available. The operating principles of AFM will be provided below.

However, scanning probe microscopies (SPMs), *i.e.* STM and AFM still lack true chemical analysis at the nanoscale. This gap is being filled by the two complementary methodologies of AFM-IR and TERS that are depicted in the following.

1.2. The atomic force microscope

Even if the original AFM involved an STM above a cantilever, this technique was popularized following the implementation of the cantilever movement tracking by a 4-quadrant photodiode. We recall below the main characteristics related to common AFM measurements.

1.2.1. Technical description of an AFM

An AFM interfaces the nanoworld with the human scale. The key components of an AFM are:

➤ **A nanoprobe for raster scanning**

The AFM tip mounted on a thin cantilever ($\sim 100 \mu\text{m}$ long) and attached to a millimeter size silicon chip to ease its handling.

The cantilever is characterized by its spring constant k . If one considers $k = 5 \text{ N}\cdot\text{m}^{-1}$ (a common value), a displacement of 1 nm involves a force of only 5 nN. While it may seem small, the

pertinent physical quantity is the applied pressure to the surface, which is performed by the tip.

At the extremity of the cantilever, the tip interacts with the surface. The most important characteristic of the tip is its radius of curvature R . Current silicon tips have R on the order of 2-10 nm. However, smaller (but much more expensive and fragile) tips are also available. In fact, as will be further described in Chapter 3, the obtained image always results from the convolution of the studied object and the tip shape. Hence, more reliable images are obtained with smaller tips.

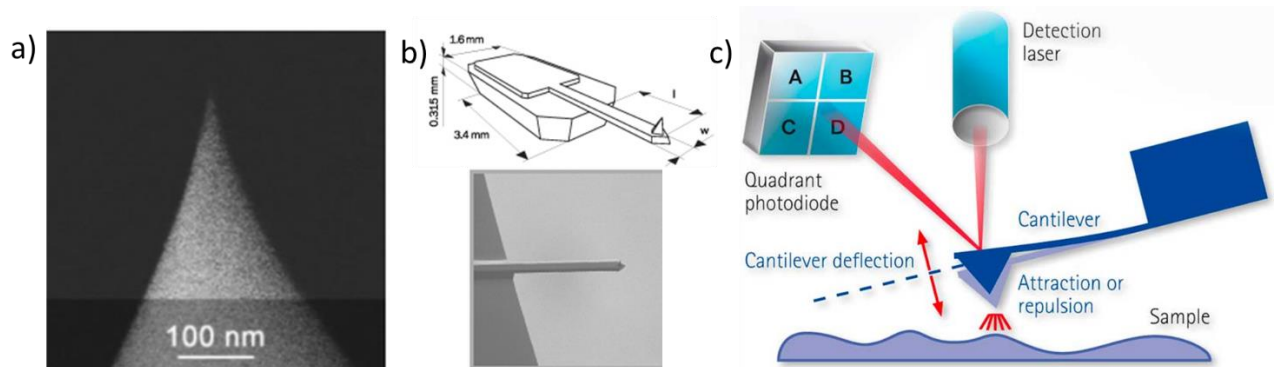


Figure 1.2. **a)** SEM image of tip apex of commercial MikroMasch probe (model: HQ:NSC14/AL BS), **b)** its cantilever schematic drawing (b top) and SEM image of the cantilever (b bottom); **c)** scheme showing the sample, tip, cantilever and laser deflection measurement system used in most modern AFMs.¹⁷

The upper surface of the cantilever is usually coated with a metallic layer (if the tip itself is not metallic), since it should reflect the laser as explained below.

➤ A laser and a 4 quadrant photodiode

As sub-nanometer movements of the tip need to be followed, those need to be translated in larger displacements. This is performed thanks to illumination of the cantilever by a laser (registration laser) as described in **Figure 1.2c**. A small change in the deflection angle of the cantilever (arising from the substrate topography) translates into a micrometric or millimetric distances after a few centimeters trajectory. The laser spot may be easily followed thanks to a 4-quadrant photodiode detector. In fact, this device is thus sensitive to a vertical movement of the cantilever (deflection), but also to lateral ones that may be induced by friction on the surface, for example. A calibration procedure allows the tensions on the photodiode to be converted into movements of the cantilever (in nm).

➤ A piezo stage for nanodisplacements

Imaging with subnanometric resolution necessitates a very precise positioning system. Conventional stepper motors do not possess the necessary precision and are only used for global approach. Instead, in piezoelectric systems high voltages are translated in small displacements, which is ideal for nanopositioning. The electronics and mechanical integration of piezoelectric systems for nanoscience are now routinely performed. Since the movement does not vary perfectly linearly with the voltage, capacitive sensors are often added to ensure a good linearity. The signal of the photodiode is then used to adjust the z piezo position thanks to a feedback loop.

➤ **A feedback loop**

As the force on the tip increases, the deflection signal shifts from the value far from the surface. If the force is ought to be too large, the tip may be damaged or even broken. In order to avoid this, an electronic feedback loop aims at maintaining the applied force constant. More precisely, a set-point corresponds to the desired applied force. At a constant frequency, the deviation (“error”) to this set-point is measured. The tension of the piezo stage is then corrected so as to compensate the error. The reactivity of the systems can be tuned thanks to the so-called integral gain. At a fixed position, integration over a long time averages electrical and mechanical noise. However, while imaging or approaching the tip towards the surface, the system should be reactive enough to adjust the force (proportional gain). Those two opposite considerations induce that for each imaging conditions, an optimal gain needs to be found to obtain the best possible image.

1.2.2. Interaction forces at the nanoscale

Many different forces may play a role in AFM measurements. We recall below a few of them.

Van der Waals (VDW) forces - VDW arise when polarizable systems are separated by a distance d interact together, giving rise to an attraction decreasing proportionally to d^{-6} . However, integration of VDW forces for a sphere over a plane as relevant for AFM leads to:

$$F_{VDW}(d) = -A_H R / 6d^2 \quad (1.3)$$

With A_H the Hamaker constant, R the sphere radius of curvature and d the distance between the surfaces.

For very short distances, Pauli principle states that two fermions with same characteristics cannot be at the same position, so that there is necessarily a repulsion. It depends in $1/d^{12}$ in the VDW model.

Capillary forces - In the air, condensation of physisorbed water on the substrate, or on the probe, leads to formation of a water layer that creates a meniscus. The attractive force, associated to rupture of this meniscus, is usually very high and may prevent any precise measurement.

Electrostatic forces - If the surface and the tip are charged, electrostatic repulsion or attraction occur. Kelvin probe AFM takes benefit from these interaction to extract the local work function from the surface.

Double-layer forces - These forces may be viewed as electrostatic ones when the experiment is carried out in liquids. Here, the electrode charge is compensated by ions from the electrolyte, creating the so-called double layer. If the tip is charged as may occur with silicon tips in water (this is strongly pH dependent), a force may arise. As the double layer structure is potential-dependent, the forces may vary during an electrochemical experiment.

Chemical forces - Specific chemical interactions may occur between a modified tip and the scrutinized surface. They are usually studied when the tip/surface distance is varied in the mode called force spectroscopy. Imaging by force spectroscopy has been used for example to recognize specific proteins on a cell surface. In the work presented here only bare tips will be used, thus minimizing specific interactions.

1.2.3. Different operating modes

There are many different approaches to image a surface. The most common are described below.

➤ **Contact mode**

This mode is the original one developed. Here, the tip interaction with the surface is maintained constant thanks to the z feedback loop, while surface is scanned in the XY plane. The main advantage of this mode is its simplicity, but several drawbacks are nevertheless commonly faced. In fact, if a hard surface is modified by a soft layer such as molecular ones or biological systems, the tip may scratch the surface and damage the sample upon scanning. In some cases the tip may be even eroded. This drawback may however be turned into an

advantage to evaluate the thickness of a hard surface modified with a soft system: a first small area is first imaged so as to remove the coating, and afterwards a larger image is acquired in oscillating mode that leaves the sample intact.

➤ **Oscillating mode “tapping”**

This mode has now become the most popular. Here, a small piezoelectric actuator, integrated to the tip holder, is used to modulate the z position of the cantilever with a sinusoidal excitation. Prior the experiment, the resonance frequency of the cantilever oscillation is found by sweeping the “piezo frequency”. It relies typically between 50 and 300 kHz for standard commercial tips. Then, a constant frequency, close to the resonance one, is chosen. In the case of amplitude modulation, the signal fed to the feedback loop is the vertical oscillation amplitude (deflection), whereas frequency modulation change is monitored in resonant frequency. Near the surface, the oscillation amplitude of the cantilever becomes lower. The great advantage of tapping mode is that the contact with the surface is only intermittent, preserving its integrity. One drawback, however, is that the precise force applied between the tip apex and the sample is unknown. This is the reason why some AFM constructors developed hybrid modes.

➤ **Hybrid modes**

First introduced by Bruker under the name PeakForce[®], hybrid modes present complex tip movements. Even if each manufacturer has its own implementation, the same general idea is to benefit from the oscillating mode to move to different sample location in xy at a rather large distance from the sample, and perform at each sample point location (pixel) an approach curve up to a force set-point that is precisely defined. This gentle imaging mode has become very popular to analyze biological samples and cells since the applied force may be reduced up to a few piconewtons.

Another advantage of these modes is to allow electrical conductivity to be estimated, since a true contact is established upon the approach.

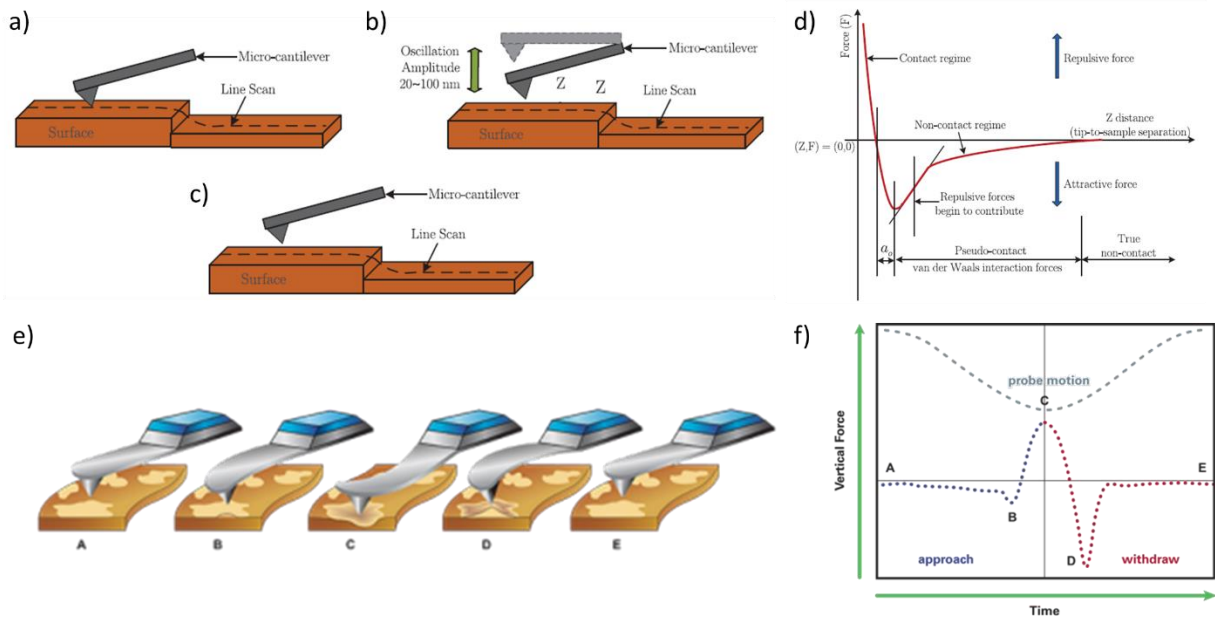


Figure 1.3. Operating modes of the AFM - **a)** contact mode; **b)** tapping mode; **c)** non-contact mode; **d)** force versus distance curve for different operating modes of an AFM¹⁸; **(e-f)** hybrid mode (PeakForce Tapping – Bruker).

Apart from force, many other measurements such as electrical or magnetic ones can be performed simultaneously with those based on force. Infrared or Raman spectroscopies may also be coupled with AFM as described below.

1.2.4. Coupling AFM with IR spectroscopy

Obtaining spectroscopic information below the diffraction limit necessitates a change in paradigm. For vibrational spectroscopy, several approaches were proposed. In this section we focus on those pertaining to IR spectroscopy.

Scattering IR SNOM (s-SNOM) - Platinum/iridium coated AFM probes are scanned in tapping mode over the sample, while illuminated by a focused infrared laser beam. The resulting backscattered radiation, modulated by the tapping frequency (f_{tap}), interferes at an infrared sensitive detector with a reference beam, whose phase is modulated continuously by reflection from an oscillating mirror (f_M). The pseudo-heterodyne detection setup utilizes demodulation of the overall IR signal at frequency side-bands $n f_{tap} \pm m f_M$ (for integers m and n) to supply the background-free amplitude (S_n) and phase (φ_n) of the IR near-field signal at harmonics n of the probe tapping frequency. The near-exponential dependence of the near-field interaction versus the tip-sample separation distance implies that signal harmonics at $n \geq 2$ are directly attributable to nearfield polarization of the tip in the case of harmonic tapping

motion. Contrasts in intensity and phase at these near-field signal harmonics therefore correspond with variations in the local chemical composition of the sample.

Fast raster-scan imaging of sample surfaces (single frequency / integration time of < 10 ms per image pixel allowed) is possible using tunable fixed-frequency quantum cascade lasers (QCL). AFM topography and the mechanical phase of the probe oscillation were recorded simultaneously with all near-field IR images. Single-point nearfield spectra can be acquired using a tunable broadband mid-infrared laser. This coherent mid-infrared light is generated through the nonlinear difference-frequency combination of beams from two near-infrared fiber lasers. An asymmetric Michelson interferometer using translating mirror enables the collection of demodulated nearfield amplitude (S_n) and phase (φ_n) spectra. Lucas *et al.*¹⁹ showed the possibility of studying phase distribution in Li_xFePO_4 microcrystals by *ex situ* nanoscale IR imaging. The latter showed high sensitivity by detecting not only spectral signatures of LiFePO_4 and FePO_4 , but also their metastable intermediates, such as $\text{Li}_{0.34}\text{FePO}_4$ and $\text{Li}_{0.66}\text{FePO}_4$, exhibiting excellent chemical contrast, as seen on the **Figure 1.4** below. Note that the full interpretation of the IR s-SNOM near-field spectra requires modeling as they can differ drastically from far-field FTIR spectra, this limitation has hampered the development of the techniques in the material science community.

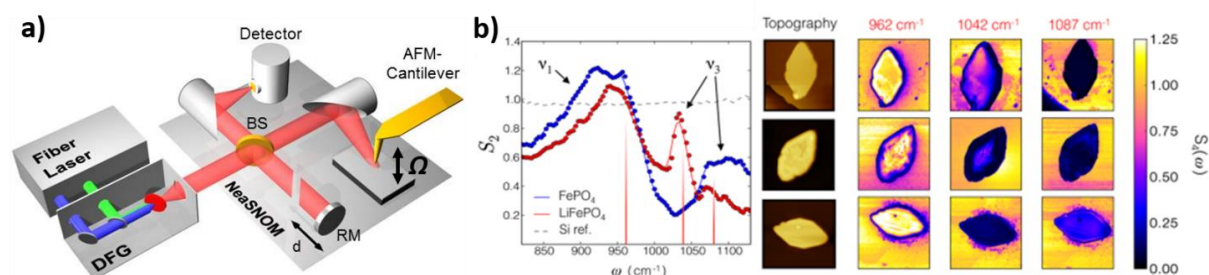


Figure 1.4. IR s-SNOM: **a)** pseudo-heterodyne detection setup using demodulation of the overall IR scattered signal at the platinum tip apex to supply the background-free amplitude (S_n) and phase (φ_n) of the IR near-field signal at harmonics n of the probe tapping frequency (*Neaspec*, Germany); **b)** left: nano-FTIR S_2 spectra (2nd harmonic amplitude of the backscattered field) of pure-phase LiFePO_4 and FePO_4 microcrystals (symmetric v_1 and antisymmetric v_3 vibrational modes). Right: AFM topography and corresponding infrared near-field amplitude S_4 (4th harmonic) images acquired at (top to bottom) 1087, 1042, and 962 cm^{-1} for LiFePO_4 , $\text{Li}_{0.5}\text{FePO}_4$, and FePO_4 crystals. Extracted from Lucas *et al.*¹⁹

AFM-IR - The second one, proposed by Alexandre Dazzi in 2005²⁰ and now available commercially, benefits from a photothermal effect. Indeed, if a system absorbs IR light corresponding to vibration of a molecular analyte that should be detected, then heating occurs locally. As a consequence, dilatation occurs, which translates into a vertical

displacement of the tip. Pulsed IR laser are then used in this technique. Initially, the ringtone of the tip, induced by the laser pulse was measured, and the spectrum was reconstructed afterwards. The rising of QCL lasers now allows the pulse frequency to be adjusted in order to optimize signal acquisition, perform faster imaging and detect smaller objects.

AFM-IR finds applications in wide range of domains, from polymers to art to biology.²¹ As example, **Figure 1.5b-d** presents an image showing phage virus that have contaminated a bacteria.

However, AFM-IR is not yet adapted to measurements in liquid conditions since most of the signal would vanish, due to IR solvent absorption. In order to circumvent IR absorption by the solvent, Raman approaches are very promising. Those are described in the next section.

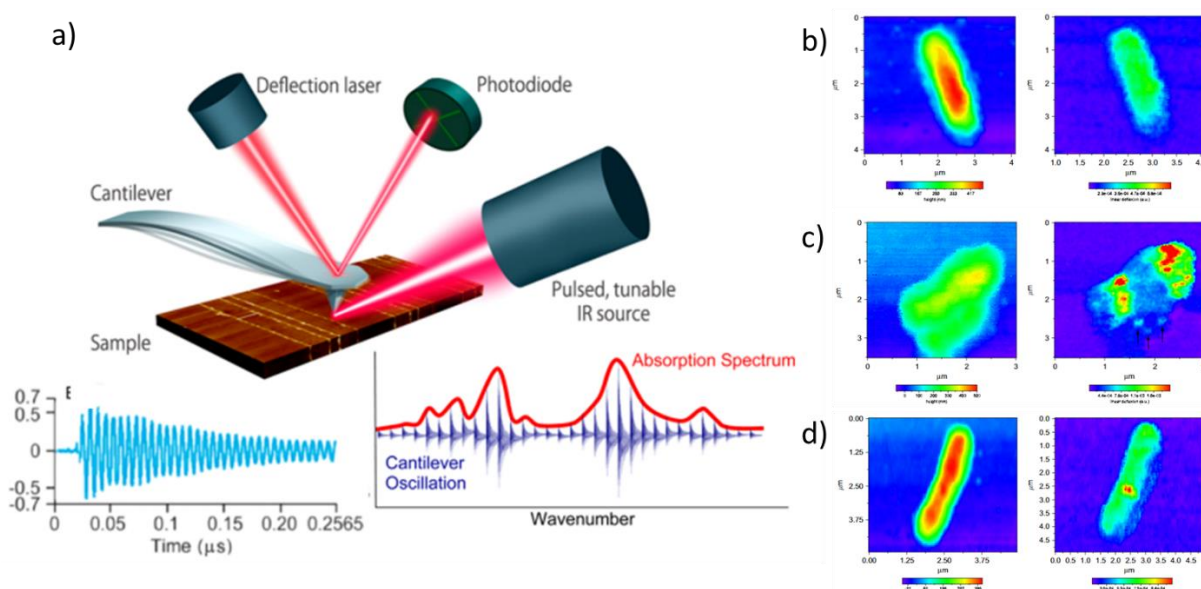


Figure 1.5. AFM-IR - a) principle of the photo-induced AFM-IR spectroscopy. The IR incident radiation from the laser is absorbed by the material, which expands and triggers an oscillation of the AFM cantilever²²; **right:** AFM-IR chemical mapping showing three infection stages of bacteria with virus; **b)** uninfected bacteria or in the first step of infection; **c)** the most advanced state of infection; **d)** a state of partial infection.²¹

1.3. Raman spectroscopy and Surface Enhanced Raman Spectroscopy

1.3.1. Raman spectroscopy

Light-matter interactions are at the core of an extremely large range of physicochemical methods. With photons in the Ultra-Violet (UV) or in the Infra-Red (IR) range, two processes can occur: photons can be absorbed, if their energy matches an electronic or a vibrational transition, or they can be scattered.²³ These electronic and/or vibrational transitions are summarized in the simplified Perrin-Jablonski diagram, displayed in **Figure 1.6**. In the IR range,

transitions occur between two vibrational levels. In the UV-Visible range, one electron is promoted in to an excited state. It may return back to the ground state either non-radiatively, or by emitting a photon by fluorescence or phosphorescence. Possibly, chemical reactions may interfere, thus the molecule in the excited state may react either through a monomolecular or bimolecular path.

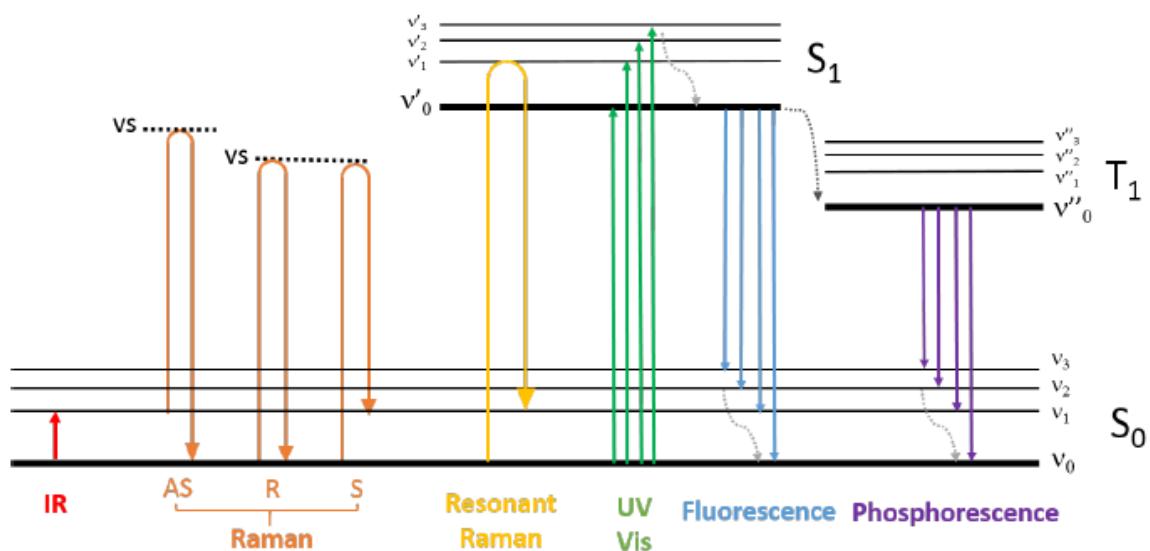


Figure 1.6. Simplified Jablonski diagram for most of the vibrational or electronic transitions in the IR to UV light range. IR: Infra-red; AS: Anti-Stokes, R: Rayleigh, S: Stokes; UV: ultra-violet, Vis: visible; S_1 : singlet state, T_1 : triplet state, v_i : vibrational state; vs : virtual state; light grey dashed arrow: vibrational relaxation, dark grey dashed arrow: intersystem crossing.

But even if the photon energy does not match any vibrational or electronic transition, it may be scattered. The majority of the photons are scattered elastically, therefore with the same energy as the incident photon. This is also called Rayleigh scattering. However, some photons are scattered inelastically, with an energy higher (anti-Stokes) or lower (Stokes) than the incident photon. The energy difference corresponds to molecular vibrations and allows Raman spectrum to be acquired. As anti-Stokes Raman scattering requires the molecule to be usually in the first excited vibrational state, it is less likely to occur. Also, anti-Stokes Raman scattering is much weaker than the Stokes one.

From the molecular point of view, Raman scattering depends on the polarizability of the molecule. In addition, selection rules are also important criteria to take into account, so that Raman spectra are usually very different from IR ones. Because of the development of easy to use and sometimes cheap systems, Raman spectroscopy is now becoming increasingly popular among the community of analytical chemistry.

1.3.2. Confocal Raman microscopy

Raman spectroscopy can be coupled to optical microscopy and piezo-stages offering high resolution compositional mapping capabilities (the so called microRaman spectroscopy).

In plan-resolution - The lateral (in the XY sample plane) resolution, i.e. the ability to distinguish two surface objects as separate entities, is diffraction limited (Abbe, 1873) and can be defined according to the Abbe, Rayleigh (1896) or Sparrow criterions as roughly half of the wavelength of illumination:

$$Abbe\ resolution_{x,y} = \frac{\lambda_{exc}}{2NA} \sim \frac{\lambda_{exc}}{2} \quad (1.4)$$

with NA the numerical aperture of the objective defined as $n \cdot \sin(\vartheta)$ with n the refraction index and ϑ the half-angle of collection. This lateral resolution in Raman microscopy, is much lower than with IR microscopy, i.e. (sub) micrometric (1 μm at 785 nm, 0.336 μm at 248 nm excitation with a 0.90 NA /100x objective). Note that for Raman spectroscopy, the spatial resolution is nearly constant along the spectrum as a typical Raman spectrum (4000 cm^{-1}), is contained within 30 to 200 nm, depending on the excitation wavelength. Since lateral resolution is equivalent to the half of the laser excitation wavelength, this means that excitation lasers in a shorter wavelength range provide better resolution. On the other hand, objectives with the larger numerical aperture improve the spatial resolution. One of the main difficulties is finding the best compromise of using the laser of short excitation wavelength and still avoid fluorescence effect, which would perturb the observation of the final Raman signal.

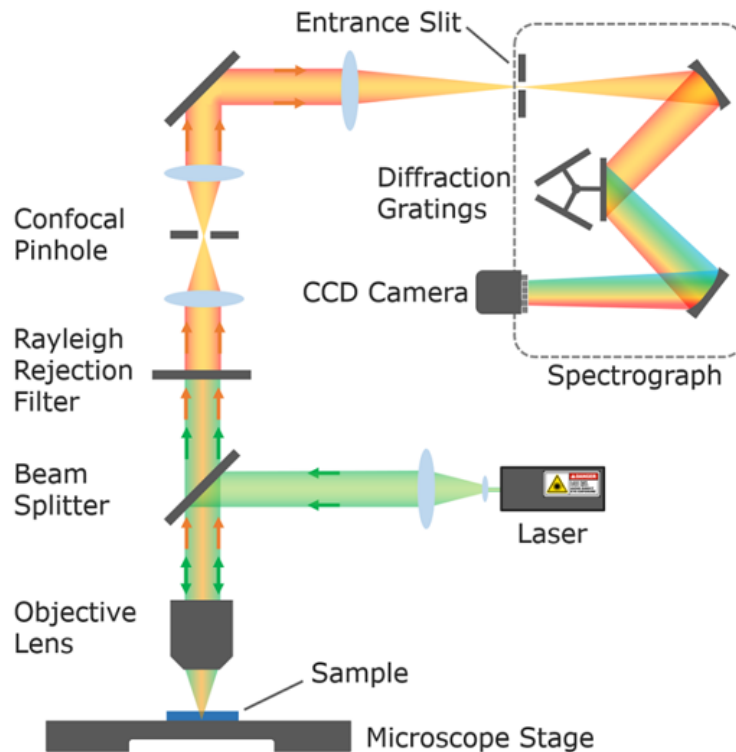


Figure 1.7. Design of a (dispersive) Raman confocal microscope: The microscope is equipped with one or several monochromatic laser sources (Raman probe) with cleaning filters to narrow their spectral emission (bandpass filters and intensity attenuation filters not represented here), a rejection filter to suppress the dominant *Rayleigh* scattering (green beam), a confocal pinhole to selectively collect photons originating only from the sample focal plane (orange beam), a diffraction grating to spread the Raman photons of different energy (optical transition of the various molecular entities in the sample) on the detector (*CCD* camera). Image: [Edinburgh Instruments](#).

Depth resolution - By placing a pinhole aperture at the entrance of the spectrometer (see **Figure 1.7**), it is possible to block the photons which do not originate from the focal plane on the sample (before and after); the so-called confocal Raman microscopy. By selecting objectives with low field depth (high NA objectives with large collection angle) and minimizing the pinhole size, the penetration depth of the analysis (depth resolution along the *Z* axis of the sample) can be reduced and the lateral resolution increased. Also the contribution of signal originating from the medium between the sample and the objective (atmosphere or liquid) can be minimized. Note that in such confocal configuration, the sensitivity of the analysis (Raman intensity) critically depends on the accuracy of the Raman probe focalization on the sample (and of the optical alignment). Proper focalization of the Raman probe can be difficult to achieve on rough and inhomogeneous samples, compromising the quality of compositional mapping. The depth resolution (*Z* axis) defined by Abbe is significantly lower than the lateral resolution, in the order of 1 to 2 μm depending on the wavelength of illumination:

$$Abbe\ resolution_z = \frac{2\lambda_{exc}}{NA^2} \quad (1.5)$$

The discrimination of different structures in a sample strongly relies on the confocal instrument design and pinhole diameter. When the latter is fully adjustable, the possible depth resolution can be of 1-2 μm in Raman. This can allow precise analyzing of individual sample layers. Hence, besides the excitation wavelength and microscope objective, the final depth resolution depends also on the sample structure.

1.3.3. Raman process efficiency

When a molecule scatters an external incident light source, the total intensity of the radiation is proportional to the square of the induced dipole moment:

$$I = \frac{16\pi^4}{3c^3} \nu^4 \cdot \mu_{i,0}^2 \quad (1.6)$$

where c is the speed of light and $\mu_{i,0}$ is the amplitude of the induced dipole moment. Due to the dependence on the fourth power of the frequency, the scattered intensity is much stronger for radiations of short wavelength, i.e. high frequency.

The intensities of the scattered lines depend also on the intrinsic properties of the studied system, more specifically on the scattering cross-section σ , which is defined as the ratio between the total scattered power (in W) and the irradiance of the incoming radiation (in W/m^2) and has therefore the dimensions of an area. For a single Stokes transition i , the number N_s of light quanta inelastically scattered per atom, per length of material dz per solid angle element $d\Omega$, can be defined as:

$$dN_s = N_a N_o \left(\frac{\partial \sigma_i}{\partial \Omega} \right)_i d\Omega dz \quad (1.7)$$

where N_a is the number of molecule per unit volume in the lower energy state, N_o is the number of incident light quanta and the ratio $\left(\frac{\partial \sigma_i}{\partial \Omega} \right)_i$ is the differential cross-section, described by a complex formula.

With respect to other optical spectroscopies (e.g. fluorescence), the Raman effect appears to have the lowest cross section. Taking the example of a benzene molecule, the Raman scattering cross-section of the ring respiration mode at 992 cm^{-1} , with excitation at 514.5 nm ,

is $4.0 \cdot 10^{-28} \text{ cm}^2$. For comparison, its fluorescence cross-section is of the order of 10^{-17} cm^2 . In summary, not only the Raman transitions are difficult to observe, but also they can be easily and completely screened by other light-emitting effects (as fluorescence).

Since Raman scattering cross-sections are usually rather weak, one should find amplification methods when low quantities of analyte should be detected. Using resonant Raman molecules may be an alternative, but this cannot be applied to any situation. This problem is emphasized for fluorescent systems since in some cases fluorescence emission may completely dominate the recorded signal. For that purpose, Surface-Enhanced Raman Spectroscopy (SERS) has now become a key domain. It is described in the next sections.

1.3.4. Localized Surface Plasmon Resonance at a nanoparticle

In 1908, Mie formulated a famous theory that is commonly used to explain the color of nanoparticle solutions. If visible light with wavelength 400-800 nm is shined onto a spherical metallic object that is much smaller than the wavelength (typically less than 50 nm), the electric field can be considered homogeneous inside the nanoparticle. The applied electric field polarizes the metal constituting the sphere by displacing the free electrons cloud, as shown in **Figure 1.8**. As a result, a polarization electric field results inside the NP.

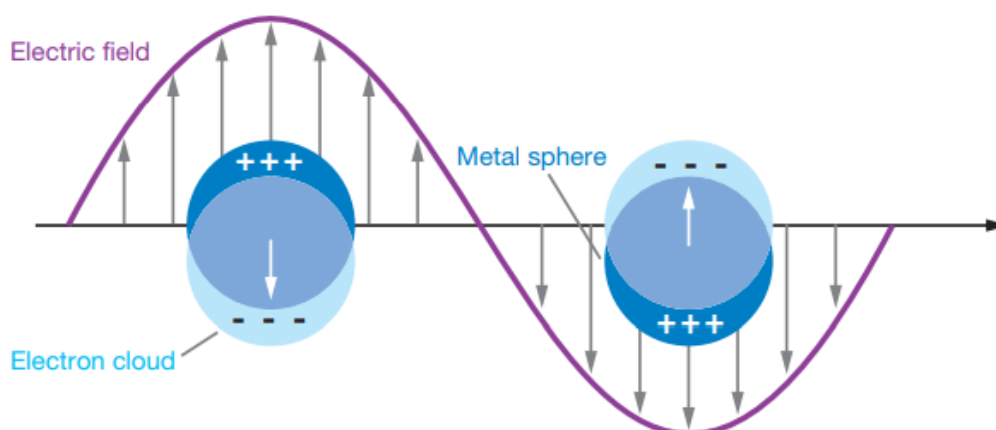


Figure 1.8. Scheme of a localized surface plasmon (LSP) in a metal nanoparticle.²⁴

By solving Poisson equation for the electrostatic potential, and by taking into account the finite dimensions of the NP and the nature of the external medium, Mie showed that the cross section for absorption may be expressed as²⁵:

$$\kappa_{Abs} = 12\pi R^3 \frac{\omega}{c} \epsilon e^{\frac{3}{2}} \frac{\Im m(\epsilon_m)}{(\Re e(\epsilon_m) + 2\epsilon_e)^2 + \Im m(\epsilon_m)^2} \quad (1.8)$$

Where R is the radius of the sphere, ϵ_m the dielectric constant of the metal, ϵ_e the dielectric constant of the environment and ω the pulsation. Dielectric properties strongly depend on the wavelength. Hence, when the denominator is minimum, an absorption occurs at the so-called localized surface plasmon resonance (LSPR) peak. For silver and gold, the maximum is usually in the visible range, so that nanoparticles solutions are colored. The position and intensity of LSPR peak depends on the size and shape of the nanoparticle, but also on their possible aggregation and dielectric surrounding medium. In comparison, aluminum presents a plasmon absorption in the UV range.

Another essential parameter that can affect both LSPR and field enhancement is the coupling between several nanostructures: a simple example is the LSPR of a gold NP dimer. As the gap between two NPs decreases from 20 nm to 1 nm, the LSPR is red-shifted by ca. 145 nm and the field is highly enhanced in the gap.²⁶ This specific region of space, where the field enhancement is maximum, is called a hot spot. This term will be used in the following for SERS and TERS experiments. One can now understand why these properties of nano-sized metallic materials can be of tremendous interest for Raman spectroscopy: the intensity of the scattered signal can be considerably increased in presence of metallic nano-objects, opening the way to enhanced spectroscopy for the characterization of low cross section materials, molecules or nano-objects.

1.3.5. Surface-Enhanced Raman Spectroscopy (SERS)

SERS makes profit of the strong electric field enhancement, provided by a nanostructured substrate with plasmonic properties.

Discovery - This enhancement of Raman signal was first experienced by Fleischman in 1974 in his studies on the changes of Raman scattering of a pyridine monolayer, adsorbed on a silver electrode as a function of the applied electrochemical potential.²⁷ The enhancement mechanism of the signal was then discovered by Van Duyne and Creighton, simultaneously in 1977, in works where the role of the silver substrate was pointed out.^{28,29} Initially SERS was performed on electrochemically roughened substrates, which displays a random distribution of hot spots on the surface. Since the 90's, potentialities of SERS have been increasingly exploited and single-molecule detection could be achieved in 1997.^{30,31} Top-down or bottom-up nanofabrication processes now allow the design of reproducible and tunable SERS substrates (lithography, 3D NP assembly).³²

Electromagnetic enhancement vs chemical enhancement - SERS effect mainly depends on the electromagnetic enhancement, determined by the LSPR on the metal surface. Along with the metal type and substrate surface structure, also the molecular structure at the surface proximity plays an important role. This so-called chemical effect originates from the presence of specific interactions between the adsorbed molecule and the substrate (adsorption, complex formation). Although it is widely discussed, this effect could be related to the charge transfer resulting from the interaction between the molecule under study and the metal substrate (charge transfer between the LUMO energy level of the molecule and the Fermi level of the metal or the HOMO level of the molecule and the free levels of the metal, which should be as close as possible). The chemical effect, therefore, requires a strong coupling between the molecules and the substrate, such as a direct absorption of the molecule on the surface.

Beyond the modifications, induced by the change of geometry of the molecule associated with a simple physisorption, the existence of a charge transfer is likely to modify the selection rules, or however the Raman activity of the various modes of vibrations of the molecule. Under certain conditions, this interaction could make the Raman excitation resonant and thus explain the exacerbated intensity of the Raman signal. The chemical effect, which is difficult to characterize, nevertheless seems to contribute less significantly than the electromagnetic effect to the amplification of the Raman signal. The prediction of chemical enhancement has been calculated between the 10^2 - 10^3 , while SERS enhancement can increase up to 10^8 - 10^9 .

The total SERS enhancement is presented as:

$$EF_{SERS} = \frac{I_{SERS}/N_{SERS}}{I_{NRS}/N_{NRS}} \quad (1.9)$$

where I_{SERS} and I_{NRS} represent intensity of SERS effect and normal Raman scattering, while N_{SERS} and N_{NRS} correspond to the number of the molecules regarding molecules adsorbed on the substrate (metal) surface and those in the sample bulk, respectively.³³

1.3.6. Implementation *in situ*

Conventional Raman uses visible lasers. Hence, carrying out Raman measurements in liquid media can be performed rather easily, as long as the medium remains transparent.

However, the implementation might be rather tedious, when scattering by the solvent (or the supporting electrolyte in electrochemical experiments) may interfere and dominate the signal arising from the analyte. Signal may however be recovered when SERS is implemented.

Besides, a great advantage of working in water is that the Raman cross section of this solvent is very weak. MicroRaman and SERS experiments are thus routinely implemented in water³⁴, as well under electrochemical conditions. Another advantage to implement Raman versus IR spectroelectrochemical experiments is that electrodes of reduced sizes can be used in thin layer cells, which are purposely tailored. This allows ones to reach conditions closer to classical electrochemical experiments for which the working electrode size should be much lower than the counter electrode one.

1.4. Tip Enhanced Raman Spectroscopy

In 2000, four groups simultaneously proposed to combine the Raman enhancement, provided by a metallic nanostructure with a scanning probe method, inventing Tip Enhanced Raman Spectroscopy (TERS). TERS can be seen as nanometric single SERS hot spot, positioned at the apex of a SPM probe, enabling the chemical imaging of a sample. The strength of this approach is that the scrutinized sample is not altered and its Raman response can be extracted at each point of the sample by a strong and localized electric field by scanning the metal tip over the sample. **Figure 1.9** compares TERS to SERS and confocal Raman spectroscopy.

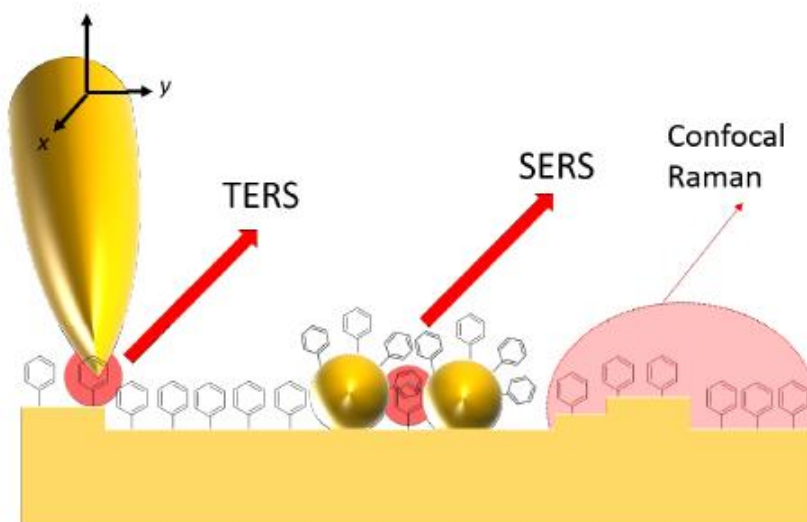


Figure 1.9. Schematic of TERS, SERS and confocal Raman spectroscopy.³⁵

Below, we describe the main aspects to take into consideration when realizing TERS experiments.

1.4.1. Different TERS configurations

There are three main geometries that are implemented in TERS experiment as depicted in **Figure 1.10**. For each one, laser illumination and signal collection are achieved through the same objective. In side and top illumination, a linearly polarized beam is focused onto the tip apex *via* a long-working distance objective. A significant fraction of the electric field is parallel to the tip shaft in this configuration, allowing an important field enhancement. The advantage of the transmission set-up is that high NA oil-immersion objectives may be used. They however require a substrate that is at least semi-transparent. Also, since in principle the electric field is now orthogonal to the tip shaft, amplification should not occur. To circumvent the problem, a circularly polarized beam, provided by a liquid crystal device, can be used.³⁶ However, it has been observed that even without this beam conditioning, obtaining TERS is sometimes possible.³⁷ This stresses the major role, played by the local geometry and atomic tip configuration at the apex, which can only barely be determined.

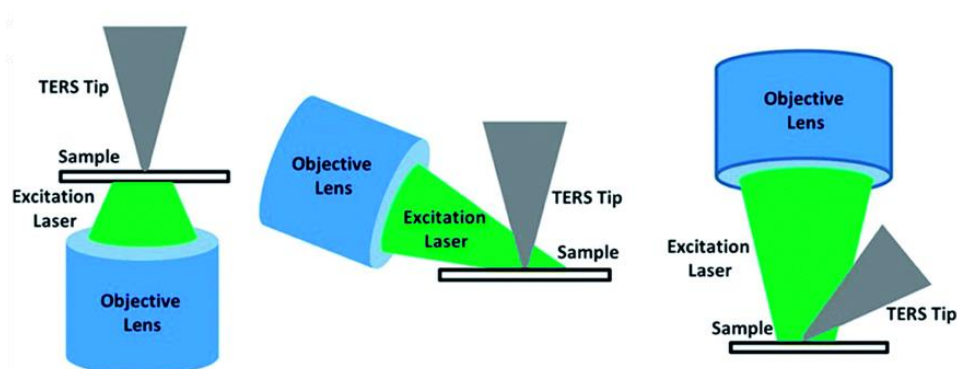


Figure 1.10. TERS illumination configurations – Schematic illustrations of laser/probe optical coupling: **a)** bottom-illumination (inverted SPM microscope, transparent sample); **b)** side-illumination and **c)** top-illumination (upright SPM microscope).³⁸

Other configurations using either two objectives or a parabolic mirror are less common.^{39,40}

1.4.2. TERS sensitivity and spatial resolution

The TERS enhancement factor is defined as the ratio between the signal intensity obtained in TERS, compared to the one obtained in standard confocal Raman measurements, taking into account the number of molecules that are probed for each technique:

$$EF = \frac{I_{NF}}{I_{FF}} \times \frac{N_{FF}}{N_{NF}} \quad (1.10)$$

where I_{NF} is the near-field intensity of a vibrational mode provided by TERS and I_{FF} the intensity of the same mode in the far-field spectrum (microRaman). N_{NF} and N_{FF} are the number of molecules probed in near-field and far-field, respectively. Practically, the evaluation of the EF requires to be able to distinguish between the pure TER signature and the far-field signal and to assess the number of molecules probed in each case.

The discrimination between the far-field and the near-field signal is easy as a TER spectrum is the sum of I_{NF} and I_{FF} . The pure far-field signal is obtained usually by collecting a spectrum after pulling the tip away from the sample. When the objective and the tip are fixed and when a side or top illumination mode is used (which is our case in this work), the FF contribution is obtained after retracting the sample by a few nanometers (usually 10 to 50).

In TERS, the substrate also plays a key role in the EF. Indeed, in gap-mode TERS, a noble metal substrate is used to carry the analyte, in other words, the sandwich metal/analyte/metal is a plasmonic junction. This configuration is similar to the one met, when two NPs are displayed close one to each other. A hybrid plasmonic mode is created in those conditions, and the LSPR is modified.⁴¹ It is then observed that TERS signal is larger and strongly depends on the distance.⁴²

The electric field enhancement may be calculated numerically. A first purely electromagnetic approach resorts to the dipole/dipole approximation (DDA). For example, Lagugne-Labarthe *et al.* could calculate the field confinement at different distances between a gold surface and a gold tip as displayed in **Figure 1.11**.⁴³ Nevertheless, this approach does not justify spectra obtained in SERS or TERS at very short distances. Indeed, intensity of the signal became much larger, and new peaks appeared, suggesting that selection rules were overpassed. Recently, the group of J. Aizpurua theoretically introduced the concept of picocavity: a single atom, positioned at the tip apex, produces an extreme confinement of the field. Here, quantum calculations are necessary to explain the spectrum.⁴⁴ These also justify the extreme spatial resolution that can be attained in TERS, as described in the next paragraph.

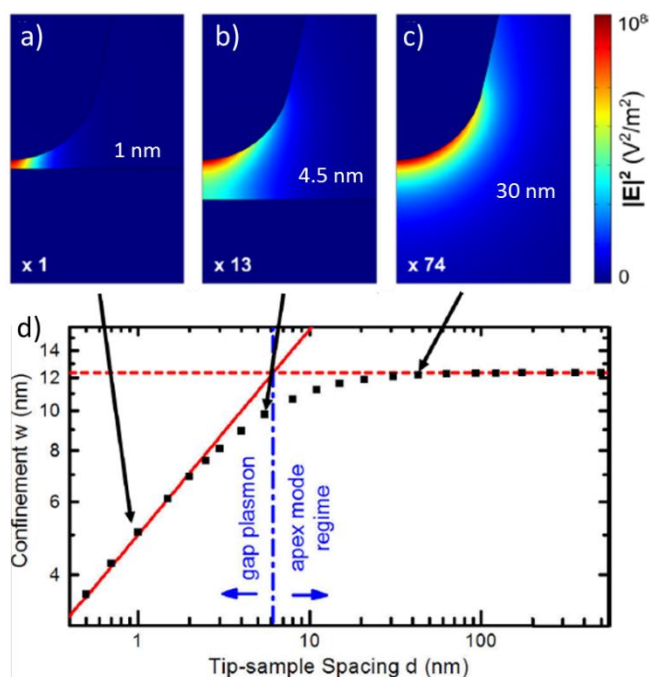


Figure 1.11. Field distribution on a gold TERS tip (R around 10 nm) above gold substrate with three gap distances (Finite element method FEM calculations) of: 1 nm (a), 4.5 nm (b), 30 nm (c). Numbers in the bottom left corner of each image correspond to multiplying factors, adapted to the color scale (on the right); **d)** electric field confinement from 2 nm to several hundred of nm gap distance. Adapted Becker *et al.* (2016).⁴³

Submolecular Raman imaging was first shown by Zhang *et al.* in 2013.⁴⁵ In 2019, the same group, and independently the one of Apkarian *et al.*, reached a spatial resolution within angstrom-scale.⁴⁶ This means that each bond can be addressed individually at a single molecule level, which represents an ultimate resolution. Nevertheless, these experiments are performed at low temperature and in ultra-high vacuum in dedicated specific set-ups, which are thus very far from conditions that are under focus in the present work (room temperature and in liquids).

In the air, a lateral resolution of 1.7 nm was reached by Kawata *et al.* on single-wall carbon nanotubes. It is noticeable that here the radius of curvature of the tip was 30 to 80 nm, thus much larger than the studied object. This raises the question of the origin of spatial resolution in TERS. While a picocavity is supposed to be involved for submolecular resolution, the confinement was calculated to be proportional to $(R_{tip}d)^{1/2}$ in standard gap mode configuration.⁴³ This model, which considers only classical electromagnetic theory, can easily account for resolution below 10 nm and down to 1 nm for a tip radius around 5 nm. Biological objects, such as DNA or peptide assemblies, can also be scrutinized by TERS as shown by the group of Bonhommeau.^{47,48}

The TERS tip radius, EF factor and cantilever stiffness thus play a major role in the quality of TERS images. Many different approaches, either starting from commercial silicon tips or home-made ones were elaborated to create TERS-active AFM probes. They will be described in Chapter 2.

1.4.3. TERS implementation in liquids and under electrochemical conditions

There are major challenges to implement TERS in liquids. The first one is that the laser illumination (focusing of the laser beam onto the tip apex) and signal collection through the liquid are not straightforward. In fact, at the liquid/air interface, light refraction deviates the beam, preventing a proper focusing on the tip. Several experimental tricks were implemented to circumvent that issue. In 2009, Zenobi *et al.*⁴⁹ used a transparent gold sample and a bottom illumination (inverted configuration) to record the signal of a thiol monolayer self-assembled on gold. This work was followed by Funjinami *et al.* in 2013 and Van Duyne *et al.* in 2015⁵⁰.

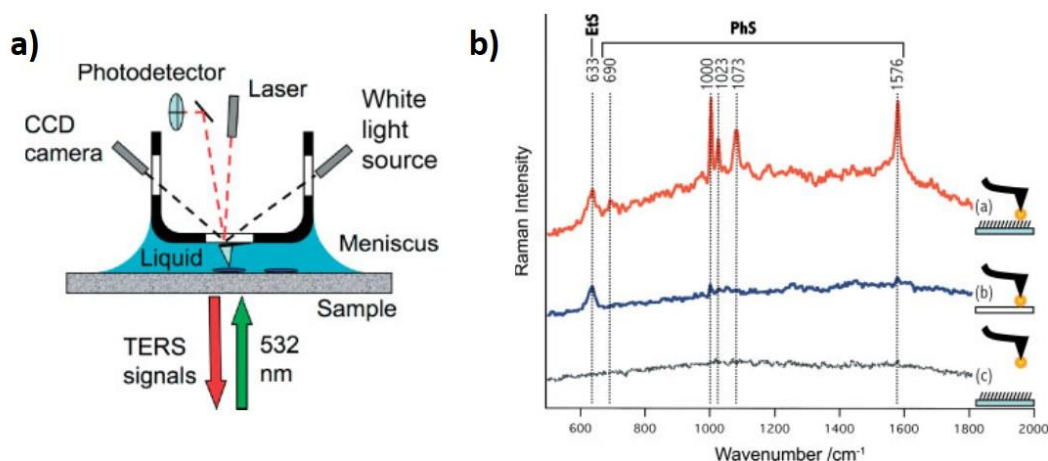


Figure 1.12. First liquid TERS experiment (2009) – **a)** depiction of the TERS setup in aqueous environment developed by Zenobi (AFM system, bottom illumination); **b)** from top to bottom: TERS spectrum recorded on a PhS functionalized gold surface using an EtS-coated silver AFM tip (a), on a clean gold surface (b), with the probe retracted (c) (far-field spectrum corresponding to measurement (a)). (λ_{exc} : 532 nm, 10 s). Adapted from [49].

The upright configuration for non-transparent samples, using top or side illumination represents the most challenging implementation of TERS in liquid, due to the difficulty of optical coupling at air/liquid interface. In the same year (2015), Ren *et al.*⁵¹ first performed electrochemical STM TERS in side illumination by designing a specific cell equipped with a flat optical window. The same strategy was applied by Domke *et al.* in 2016. Introduction of an immersion objective improved the signal collection in 2019, by Huang/Bin Ren *et al.*. This approach improved sensitivity and effectively excluded optical distortion. However, upon scanning the sample/cell, displacement induces a defocusing/misalignment of the laser.

Hence, either low magnification objectives should be used, or only small area should be imaged.⁴² Most of the EC-TERS set ups are based on the electrochemical coupling with STM. However, the STM technique requires conductive samples and surface features (roughness, surface object) of small dimensions. Coupling AFM with EC-TERS can overcome these drawbacks and allows application to a variety of samples with no requirement for the tip insulation.

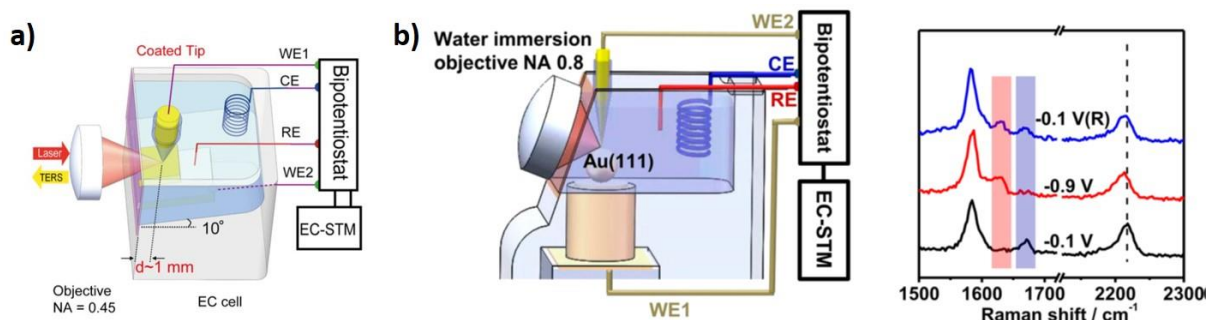


Figure 1.13. EC-STM-TERS with side illumination (2015-2016): a) B. Ren's setup using a 4-electrode cell and a bipotentiostat (the insulated STM probe acts as the second working electrode) - The bottom of the sample holder/electrochemical cell is tilted of 10° towards the glass wall of the cell. A long-distance objective can therefore be placed horizontally and illuminate the tip with a 90° angle. Adapted from [51]; **b) K. Domke's setup** - The glass window is tilted towards a water dipping objective separated of the optical window by a thin layer of water. TERS spectra acquired on a polarized gold surface derivatized with anthraquinone-based SAMs. Adapted from [42].

Van Duyne *et al.* introduced EC-AFM-TERS in inverted configuration with a gold coated AFM probe in 2015, following electrochemical transformation of Nile Blue (NB) model dye deposited on a well defined Au (111) nanoplate on a polycrystalline ITO substrate. In 2019, this group for the first time spatially resolved local heterogeneity in redox behavior on an electrode surface and at nanoscale.⁵²

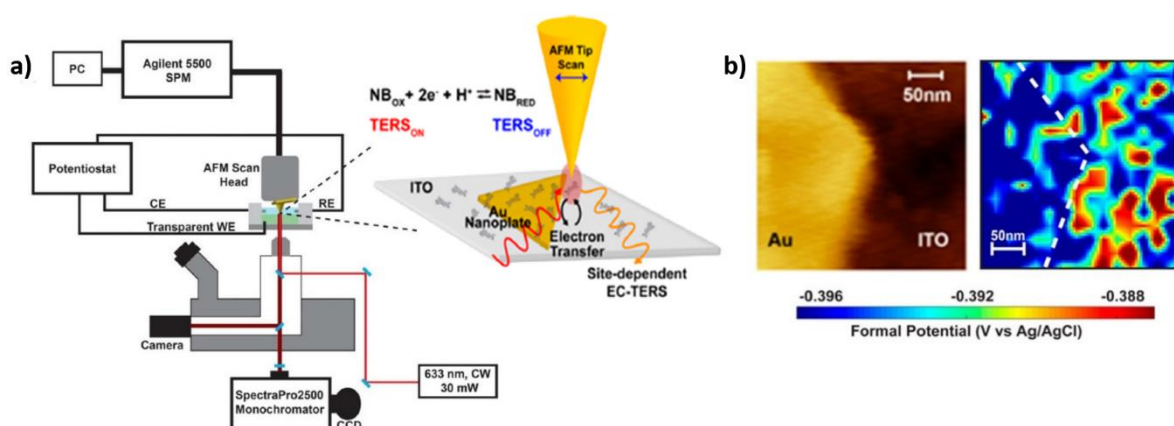


Figure 1.14. EC-AFM-TERS (2015) with bottom-illumination: a) depiction of the inverted microscope. Adapted from [50]; **b)** potential map (right) acquired on the edge of a gold nanoplate deposited on an ITO substrate,

both functionalized with a sub-monolayer of NB. Areas of different color evidence the heterogeneities of the NB reduction process on the two substrates. Adapted from [52].

Recent development of Ren *et al.*⁵³ (2020) further broadened AFM-EC-TERS measurements by using top-illumination with immersion water objective of a high numerical aperture. The efficiency of implemented system was confirmed by electrochemical redox study on polyaniline.

Initiated in LISE laboratory in 2015, STM-TERS imaging in liquids has been demonstrated for the first time in 2016. Here, an air objective in top configuration was used, and only a thin layer of liquid was dispatched on the sample. To minimize evaporation, the chosen solvent was hexadecane. This configuration is however only hardly suitable to study electrochemical systems requiring to handle at least three electrodes. Therefore, water immersion objectives were introduced in 2017.⁵⁴ The great advantage is that focusing of the laser on the tip is rather straightforward. A first step consisted in inventing the tip-SERS methodology for which molecules are grafted on a TERS tip. This represents easier implementation since no substrate is required. Then, in 2019,⁵⁵ with a similar configuration, electrochemical TERS imaging was realized with a spatial resolution of approximately 8 nm (see **Figure 1.15a**). Here, the tip is bent to ca 45° to allow the laser focus. However, the use of STM-TERS is restricted to only conductive, low height objects/samples that are strongly immobilized on surfaces.

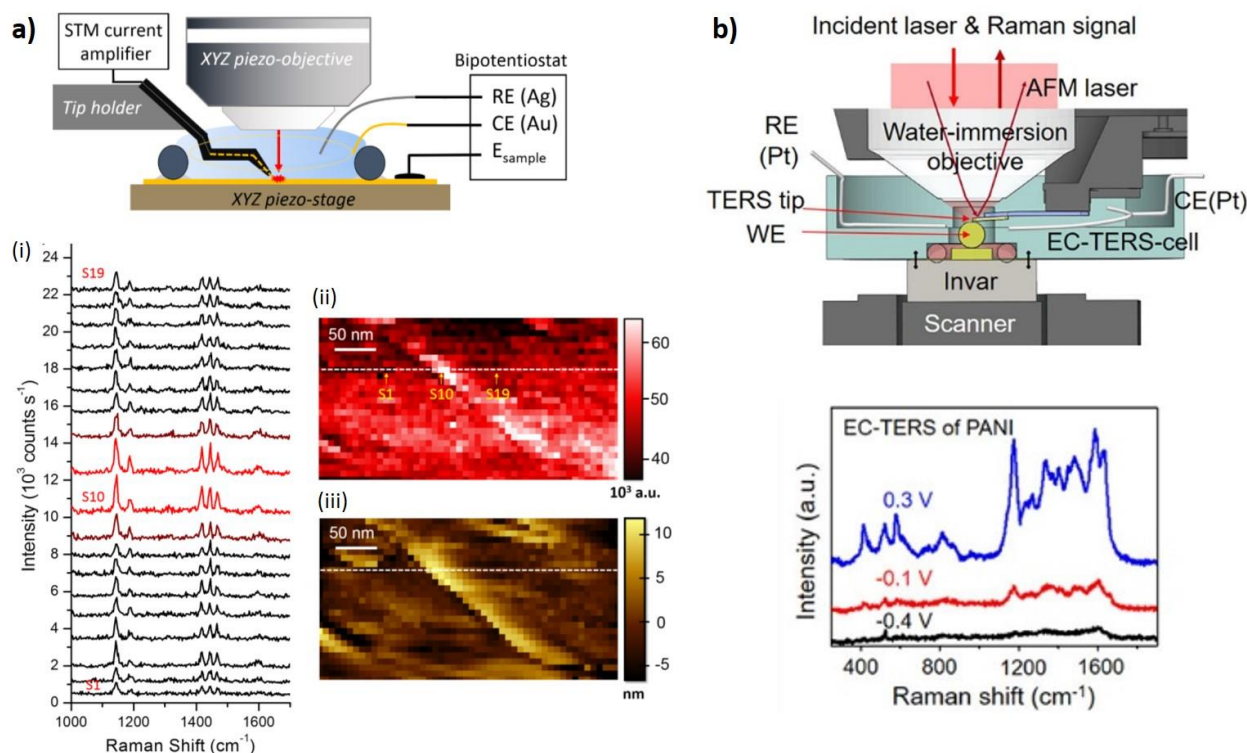


Figure 1.15. EC-TERS with top-illumination configuration: a) EC-STM-TERS - Top, depiction of the setup developed at LISE using a water-dipping objective, a partially insulated STM bent at 45° and a bipotentiostat. Bottom, TERS mapping at fixed polarization (0 V) of a gold substrate functionalized with an azobenzene-derived alkanethiol immersed in 50 mmol.L⁻¹ Na₂SO₄ spectra extracted from the TERS map across a surface feature (setp). Adapted from [55]; b) EC-AFM-TERS - Top, setup (NT-MDT microscope) using a water-dipping objective guiding both lasers (AFM registration laser illuminating the cantilever and the Raman laser focused on the tip apex). Bottom, potential-dependent TERS spectra of 2.2 nm PANI layer on Au film in 0.1 mol.L⁻¹ HCl solution. Adapted from [53]. Note that in both configurations, a sample scanner is used, so that the tip-laser alignment is not lost upon mapping.

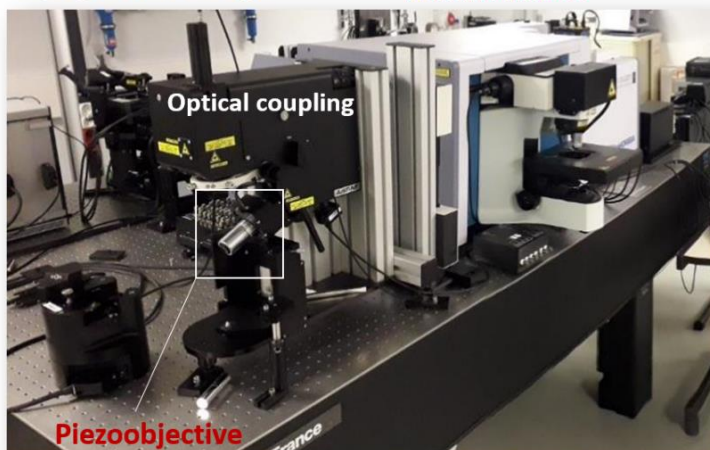
1.4.4. TERS in LISE - Description of the set-up

The TERS-ready system acquired in 2015 in LISE, coupling a Raman spectrometer and two SPM microscopes, was acquired from Horiba/ AIST.

The Raman system is a *LabRam HR Evolution* Raman microscope with 5 illumination wavelength (473, 532, 594, 633 and 785 nm). A first EM-amplified Andor Newton camera allows us to record fast imaging still with a good sensitivity using the so-called swift mode. It is completed with a second camera, more sensitive in the near-infrared region, typically combined with 785 nm excitation. The laser may be directed to the Raman microscope translating stage or toward two SPM systems (upright and inverted microscope).

Upright microscope

Raman HR800



Inverted microscope

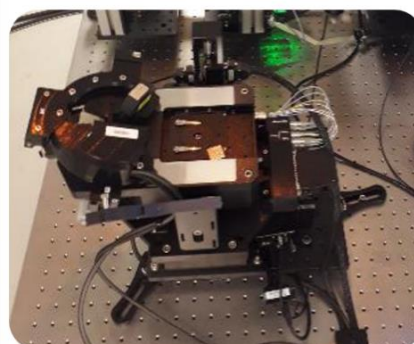


Figure 1.16. NanoRaman platform in LISE. a) *OmegaScope 1000* optical platform carrying a piezo-controlled objective and coupling the upright SPM microscope *SmartSPM* (on the left) to a *LabRAM HR Evolution* Raman spectrometer (on the right); **b)** an inverted SPM microscope (*Combiscope*) positioned behind the *OmegaScope*, which can be also optically coupled to the Raman spectrometer.

A first scanning probe microscope (*SmartSPM*) is placed onto an optical coupling system (*Omegascope*). The laser may be directed either above the sample or to the side. For samples studied in the air, the side access is the most common one as the apex of the tip can be easily visualized without shadowing effects of the probe holder (STM) or the cantilever (AFM). The AFM registration laser has a wavelength of 1300 nm to avoid any possible interference with the TERS measurements recorded at 633 nm. An automatic alignment procedure allows us to adjust the position of the AFM registration laser on the cantilever and to search for the excitation frequency, leading to the max cantilever amplitude in non-contact mode (oscillating/tapping mode). A second system (*Combiscope*) allows illumination of the tip apex from below through the sample. It thus requires that the sample is at least partially transparent to allow illumination and collection of the scattered light.

Measurements in liquids - Note that these two optical coupling system were not primarily conceived for implementations in liquids. Therefore, even if for both systems, liquid cells (see **Figure 1.18**) and liquid AFM tip holders (see **Figure 1.17**) were provided for topography measurements or micro Raman measurements in liquids, those were not adapted to implement STM/AFM-TERS measurements.

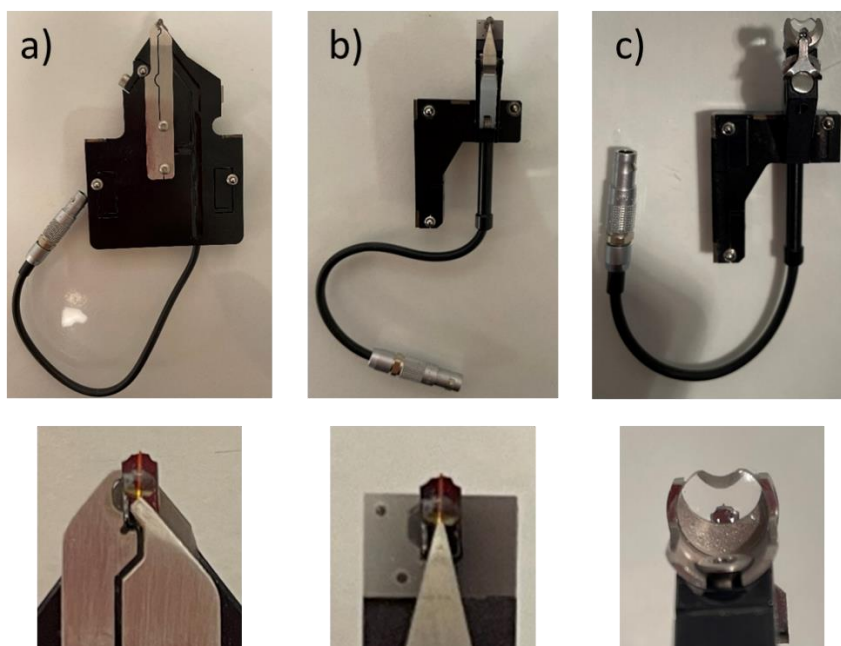


Figure 1.17. Different AFM-probe holders designed by AIST-NT with the installed probes (with zoomed images below), adaptable for measurements with upright configuration in the air (a), inverted configuration in the air (b) and for measurements in liquid with both configurations (c).

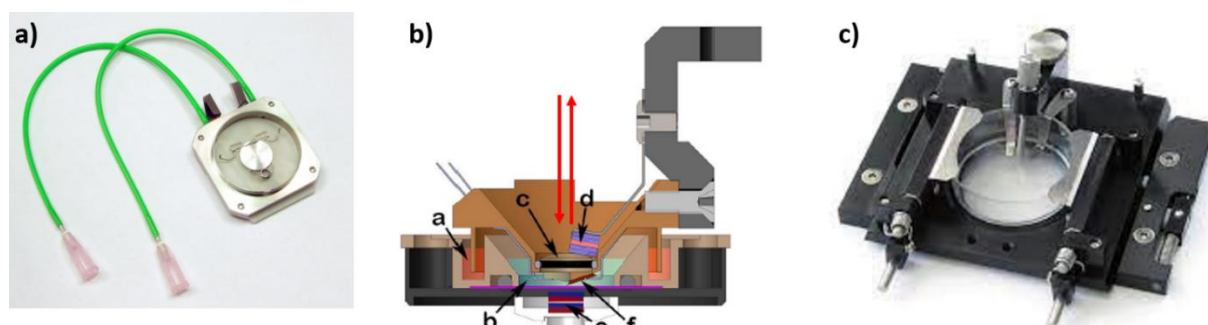


Figure 1.18. Different cells designed by AIST-NT for liquid AFM measurements: **a)** AFM liquid cell for the upright microscope (*SmartSPM*, AIST), the bottom of the cell is a polymeric membrane enabling free movement of the sample/piezo stage within the cell attach to the microscope; **b)** AFM electrochemical cell for the upright microscope, the tip holder closes the cell and carries with a top window (c) enabling the focus of the AFM registration laser on the cantilever and possibly of a Raman probe for microRaman measurements; **c)** Liquid cell (petri dish) for the inverted microscope (*Combiscope*, AIST).

1.4.5. A typical TERS implementation sequence

For precise implementation of the *in situ* AFM-TERS measurements (i.e. in liquid environment), there are several necessary steps to be followed, preferably in the air, to ensure the quality of the tip and/or the sample for sufficient AFM and TERS experiments.

➤ Tip-sample approach and landing

The AFM tip holder with firmly fixed tip and the cell-sample-holder are mounted on the *Combiscope* microscope (or *SmartSPM*) with the connected tip holder to the AIST-NT

conductive unit. When the tip is applied to the tip holder and connected to the AIST-NT conductive unit, first step is to search for the reflective cantilever in the Laser Adjustment window using the find tip procedure (**Figure 1.19a**). The next necessary step is to find the resonance frequency of the cantilever and set the amplitude of vibration at this frequency (**Figure 1.19b**). After choosing the right frequency the *Combiscope measuring* head, carrying the tip holder is positioned vertically above the *Combiscope* base with adjusted sample-holder. In the next step, the tip can be finally approached to the sample with the automatic distance control. During the movement, the electronic system measures following signals: the amplitude, phase, normal deflection of the probe and the intensity of the reflected laser beam. When the tip reaches the surface the motor stops and the scanner moves the sample approximately 1 micron away from the tip. After sample approach, the tip is landed on the sample surface, displaying so-called “landing curve” with the magnitude (z) dependence (**Figure 1.19c**).

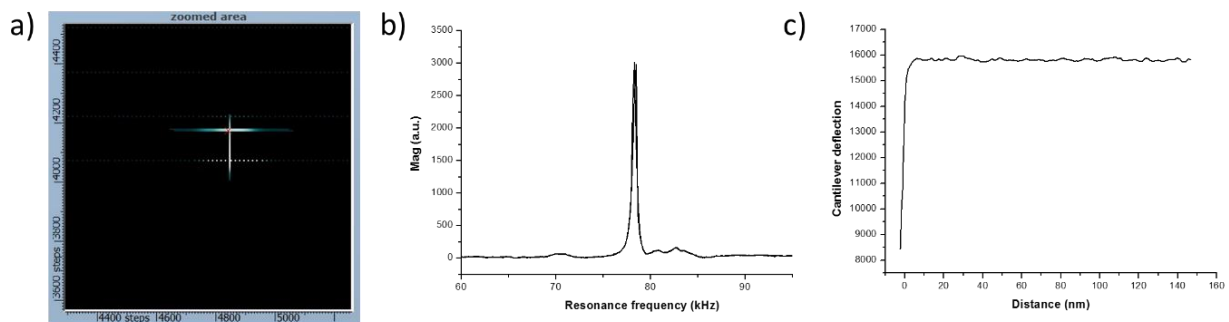


Figure 1.19. **a)** Search of the reflective cantilever with the photodiode laser; **b)** search for the resonance frequency of the cantilever amplitude oscillation by screening of piezo frequency (AC-voltage applied to the piezo actuator integrated into the probe holder); **c)** “landing” curve (variation of the cantilever oscillation amplitude as a function of the sample-tip apex distance).

➤ Rough optical alignment

The second implementation step consists in the rough alignment of the tip apex and the laser using under optical control (manual alignment of the *SmarSPM* microscope position X, Y, Z on the *Omegascope* optical coupling platform and motorized alignment of the whole AFM head on the *Combiscope*). After the tip is approached on the sample, the laser position is readjusted on the tip apex using objective piezo-scanner controls (XY and XZ).

➤ Hot-spot screening

Once the tip is “landed” on the sample surface, a precise search of the hotspot position, i.e. the point of the tip apex which provides the maximal signal enhancement, can be

conducted through “objective” mapping. Hyperspectral objective maps XY and XZ of the tip apex are acquired to determine the hotspot position accurately, as shown in **Figure 1.20c**. TERS signal (Raman signature of thiolated azobenzene) is measured at the *hotspot* position (bright (white) intensity) while no signal is acquired slightly away from the *hotspot* (far-field/microRaman signal).

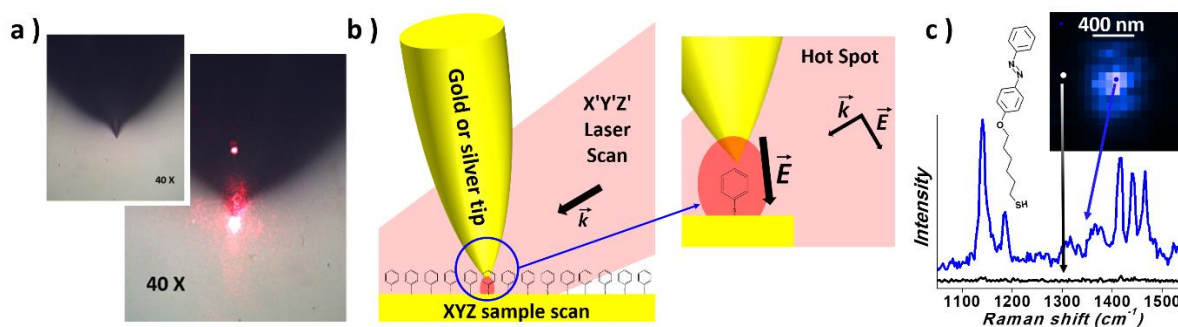


Figure 1.20. TERS implementation: **a)** rough alignment of the laser on the apex of the tip by micrometer displacements of the SPM microscope on the optical coupling platform carrying the objective (here a 40x water-dipping objective as used by T. Touzalin); **b)** the tip is brought in close proximity to the substrate to be analyzed and the position of the “hot-spot” can be identified through raster displacement of the objective piezo-scanner in the XY and XZ plans and simultaneous collection of the scattered signal. The illumination of the tip-sample junction creates a the drastic enhancement of the local electromagnetic field and therefore of the scattered Raman signal (near-field signal); **c)** the Raman signature of a molecular layer (here a thiolated azobenzene derivative on gold) can be obtained at the exact hot spot location (near-field/TERS signature), no Raman signal is collected away from the hotspot (far-field/microRaman signal).

Conclusions / Challenges for AFM-EC-TERS

As by 2022, there has been only several published works about TERS implementation in liquid and under electrochemical conditions (EC-TERS), and even a fewer coupling AFM-EC-TERS. Inverted configuration using bottom illumination and transparent samples has been shown as the easiest configuration to be implemented and therefore has been used the most. If liquid or EC-TERS point spectra are usually presented in published works, TERS composition maps under similar conditions are seldom encountered (work of R. Van Duyne), because of technical bottleneck around optical coupling. The development of TERS-efficient AFM probes, which can sustain liquid medium, still remain the main challenge in the development of the TERS technique in *in situ* conditions, object of the following chapter.

Chapter 2 - Development of TERS active AFM probes

Introduction

This chapter will cover the development of hand-made TERS active metallic AFM-probes. Since TERS implementation requires sharp metal nano-tip to guarantee a high sensitivity (high enhancement of the Raman scattering) and a nanoscale chemical mapping (high lateral and axial resolution), probe manufacturing has always been the bottleneck to the fast and large development of the technique. This is especially true for measurements in liquids, where enhancement performances have been reported to degrade by damping of the TERS intensity when changing of the surrounding dielectric medium (air to liquid) and by possible tip wear.

The classical strategy, followed for probe fabrication and detailed in the first part of this chapter, has been coating of a commercial silicon/silicon nitride AFM probes with thin films of plasmonic materials. These materials enable precise tuning of the tip composition and design, and therefore of the resulting plasmonic properties, but at the expenses of the robustness. Gold coated AFM probes for instance, provide strong enhancement in the red spectral region⁵⁶, Ag-coated probes exhibit the highest enhancement in the blue-green spectral region, but are prone to oxidation. Aluminum, which exhibits enhancement in the UV and deep UV spectral regions, can be another possible plasmon material for coating AFM probes, but it is not commonly used.⁵⁶ Additional layers are usually required such as adhesion layers (e.g. Cr, Ti)⁵⁷⁻⁶⁴ to limit fast mechanical peeling-off, and protective layer (e.g. alumina, silica) to protect from the oxidation.

An alternative to these fragile coated-probes is to design bulk metal AFM probes, as already proposed for local electrical properties measurements either in the ambient (e.g. bulk platinum probes for conductive AFM: CAFM) or in liquids and under polarisation (e.g. gold probe partially insulated for Scanning Electrochemical Microscopy using AFM feedback: SECM-AFM). This technical solution, allowing the production of robust AFM probes, was the one followed in this work to enable the development of TERS measurements under electrochemical conditions. Later in this chapter, we will therefore introduce an optimized manufacturing process of TERS-active AFM probes, inspired from the protocol proposed by Macpherson in 2000 and further developed by Demaille's group. A few refinements of these protocols and of procedures developed in our group earlier for the production of TERS-active

STM probes will be described. The properties of the manufactured gold probes will then be extracted, i.e. tip geometry (tapper angle and radius of curvature ROC), cantilever features, resonance frequency, quality factor and spring constant.

Although the fabrication of silver probes has been also covered in this work, this chapter will mainly expose the results from the optimized procedure for gold hand-made AFM-TERS probes, achieved in this work.

2.1. Brief review of TERS probe manufacturing processes

Different classes of TERS-active probes are reported in the literature: probes with tips covered with an uniform metallic layer⁶⁵, tips coated with rough metal nanoparticles⁶⁶, tip apex functionalized with single metal nanoobjects⁶⁷, tip design engineered by precise “milling” techniques⁶⁸ and tips made of bulk metal⁶⁹. The different techniques used to produce such TERS-active probes will be presented in the following.

2.1.1. Physical deposition of plasmonic material on silicon tips

Physical vapour deposition (PVD) techniques consist in “vaporizing” materials from a solid source at very high vacuum, generating physical coating onto a substrate either by the condensation or accumulation of atoms or clusters. Most common PVD techniques are thermal deposition, electron beam evaporation and sputtering. The latter is using magnetron sputter process in the vacuum chamber, delivering more significant roughness and overall broader morphological quality of deposited material.⁷⁰ Thermal evaporation produces tips with aggregated metal grains⁷¹, while sputtering and electron beam evaporation create deposition of smoother films.

Tunability of enhancement properties with physical vapor deposition (PVD)

Sub or top dielectric layers - It has been shown that refractive index (n) strongly affects the surface plasmon resonance of metal-coated AFM tip. In the early stage of TERS development, Fisher’s group used tips made from glass instead of silicon as a base material. Also Lewis *et al.*⁷² used glass tips, changing the enhancement factors (EF), by lowering the refractive index and gaining better plasmon resonance in shorter wavelength region. Gao *et al.*⁷³ for instance, found that adhesion layer of materials with low refractive index, such as SiO_2 ($n = 1.5$), SiO_x ($n = 1.5$ - 2.05) and AlF_3 ($n = 1.4$), are beneficial to TERS signal enhancement of AFM tips coated with silver films. While silver island clusters deposited by sputtering method show SPR in the range of 600 nm ⁷⁴, the use of adhesive layers of high refractive index shifts the SPR to the 500 nm range.

Effect of corrugation – Signal enhancement properties of the probe are strongly affected by the nature of the plasmonic material, but also by its structure and morphology. The lowest enhancements have been reported from smooth metal coated tips in the visible region, while the highest enhancement are obtained for roughened or corrugated metal coated

surfaces.^{71,75,76} The metal nanostructures or the grains on the surface of a tip work as resonant dipole antennas, which efficiently couple the optical radiation between far-field and near-field. The latter depends on the grains size, which are comparable to the surface plasmon polaritons (SPPs) wavelength.⁷⁷ Note that a smooth and sharp tip can still have reasonable amount of enhancement due to the lightning rod effect, which however is independent from the wavelength of the irradiation. Differences in the EF between discretely arranged grains on the tip, rough corrugated and smooth tips are seen on the **Figure 2.1** below.

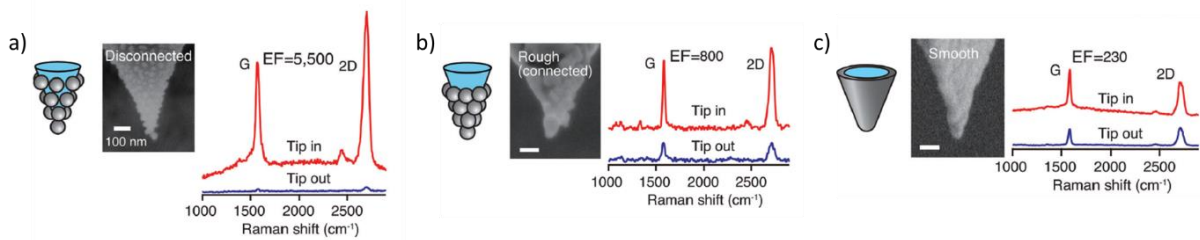


Figure 2.1. Enhancement factor from silver probes with different shapes. a) Discretely arranged grains on a tip; **b)** rough corrugated granular tip; **c)** smooth tip.⁷⁸

Shaping of Ag and Au tips by FIB - Since the size and the shape of the tip greatly affect the signal enhancement, different techniques have been implemented for shaping Ag and Au tips.

Focused ion beam (FIB) can be used for precise shaping of coated metal probe (**Figure 2.2**). This technique yields high reproducibility fabrication, well defined and adjustable resonance frequency and increased EF ($> 10^3$).⁷⁹

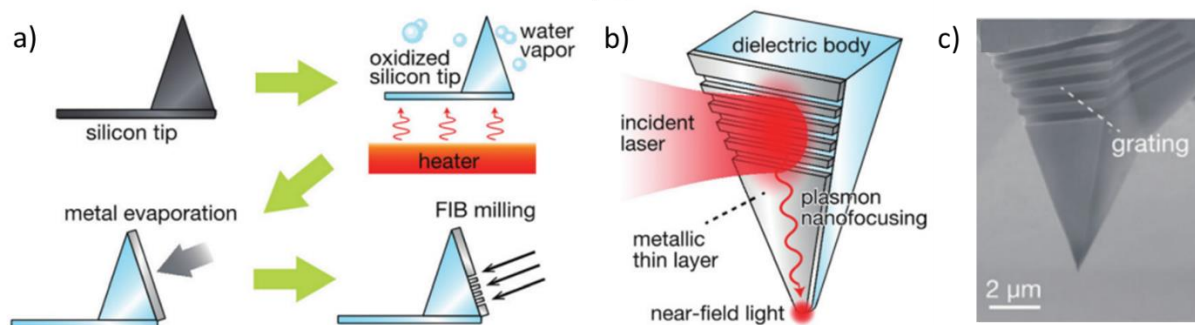


Figure 2.2. Shaping process by FIB-SEM: a) schematic of the tip structure for plasmon nanofocusing, which is composed of a dielectric pyramidal structure and a metallic thin layer on one surface of the pyramidal structure; **b)** metal deposition and milling by Ar ion by focussed ion beam; **c)** SEM micrograph of the produced plasmonic waveguide. Adapted from [68].

In gold tip fabrication, nanocones have been obtained by combination of metallization, FIB induced deposition of an etch mask and Ar ion milling.⁷⁹ Coaxial Optical Antenna shaped by FIB has been also reported to provide great enhancement enabling TERS imaging of nano-objects deposited on dielectric substrates.⁸⁰ In 2005, Farahani *et al.*⁸¹ designed a bow tie-

shaped antenna at the AFM tip apex, resulting in tips with strong Raman signal enhancement, but low quality AFM imaging. Schuck *et al.*⁸² fabricated similar probes with good AFM imaging properties. Plasmon nanofocusing using light-plasmon couplers have been also proposed. This allows the excited plasmons to travel toward the tip apex creating an intense confined field at the tip apex. Di Fabrizio *et al.*^{83,84} placed a photonic crystal cavity and a plasmonic waveguide on an AFM cantilever (**Figure 2.3d**). Light-plasmon coupler in the form of a grating shaped in the upper area of the tip (10 μm far from the sample) have been also proposed by Verma *et al.*⁶⁸. Despite the potential, FIB technique is time consuming and not yet applicable for large tip quantity production.

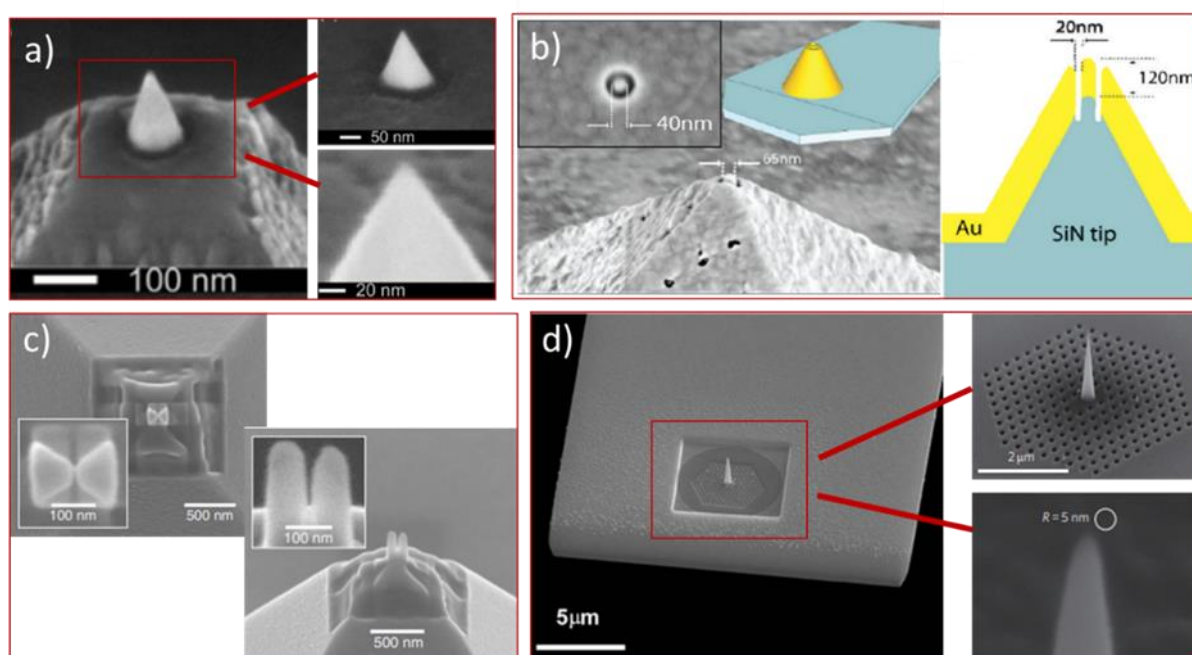


Figure 2.3. Exotic design of Ag and Au AFM probes for TERS application: a) cone, adapted from [79]; **b)** optical coaxial antenna adapted from [80]; **c)** optical antenna with feed gap, adapted from [81]; **d)** conical photonic-crystal associated with a plasmonic waveguide, adapted from [83-84].

Protection against wear out and oxidation (air and liquid) - Another important challenge is to prepare TERS-active probes, which can stand measurements in liquid media. As already mentioned, silver coated tips are significantly exposed to fast oxidation, when exposed to the air or to aqueous environment. Moreover, they also show a tendency to mechanically wear out in liquid.

In order to improve the mechanical resistance and the attachment ability of deposited metal, different research groups have proposed deposition of an additional adhesive layer onto the AFM probe before tip coating with plasmonic materials. In 2007, Yeo *et al.*⁸⁵

presented different adhesion layers made of either SiO₂, SiO_x or AlF₃ before Ag deposition. Ag-coated AFM tips prepared with SiO_x adhesion layers showed increased enhancement factor (> 10³) with no indicative difference in morphology of silver layer after exposition in the water, while AlF₃/Ag-coated tips resulted in detachment of silver nanoparticles after water exposure (see **Figure 2.4** below).⁴⁹

In 2009, Taguchi *et al.*⁸⁶ introduced thermal oxidation (~1000 °C) of silicon AFM probe before silver coating to generate SiO₂ layer between the silicon probe and the Ag layer. In 2018, Kumar *et al.*⁸⁷ refined the procedure by deposition of Cr (3.5 nm) and Cr (3.5 nm)-Au (10 nm) adhesion layers on 300 nm thermally grown SiO₂ before Ag layer (100 nm). Pre-oxidation of silicon cantilever has been also introduced for fabricating Au coated tips. Au-coated AFM probes were produced in 5 steps: pre-heating at 1000 °C for 10 h, deposition of a 50-60 nm thick Au-layer, annealing at 900 °C for 10 h, deposition of another 50 nm Au layer and post-heating at 300 °C for 2h. This procedure has shown drastically improved attachment of Au nanostructures and silicon, verified with scotch tape adhesion test, mechanical test with AFM and increased TERS enhancement. The strong adhesion can originate from diffusion of Au into the SiO₂ layer upon thermal treatment. Deposition of two gold layers with the combination of intermediate heating promoted the grains growth at the extremity of tip apex and gave beneficial properties for nano-mechanical and nano-optical measurements.⁶⁴

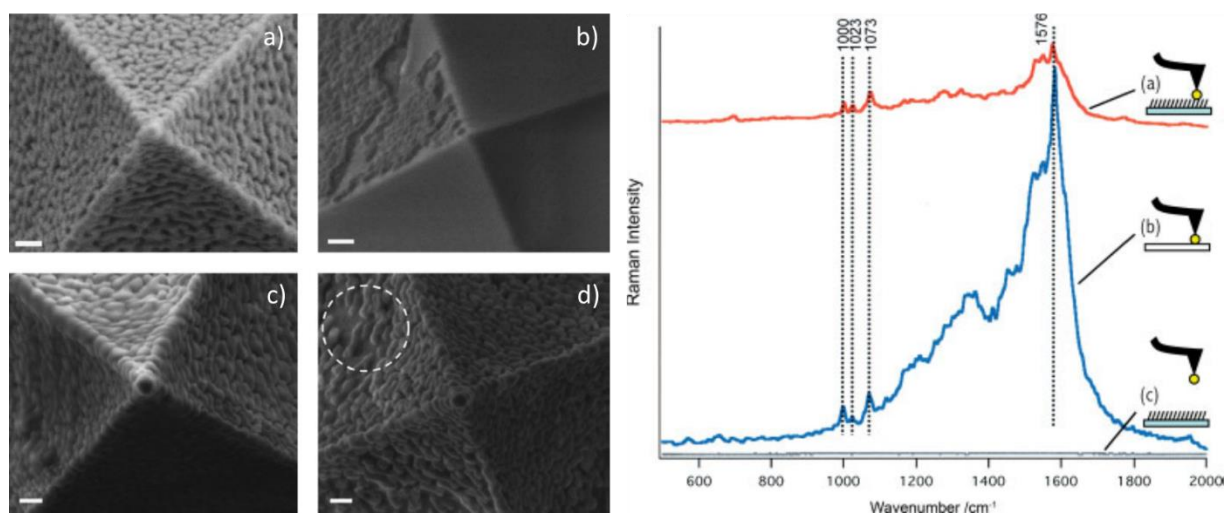


Figure 2.4. Stability of TERS active Ag-coated silicon probe in liquid – (Left): SEM images of Ag-coated probes with adhesion layer of AlF₃ or SiO_x; AlF₃/Ag-coated tip before (a) and after (b) soaking in water for 1 h, and SiO_x/Ag-coated tip before (c) and after (d) soaking in water for 1 h. (Right) TERS measurements of PhS SAM on gold surface in water with acquisition time 10 s; (a) TERS obtained with SiO_x/Ag-coated tip in contact with the sample, (b) TERS after measurements in water, performed on a clean Au substrate; (c) far-field spectrum on gold.⁴⁹

Zenobi *et al.*⁸⁸ proposed the addition of silica layers on Ag and Au tips (STM-TERS probes) as protection against wear, oxidation and also contamination (with thiophenol for instance). The procedure involves tip functionalization with 3-mercaptopropyltriethoxysilane (MPS) followed by silica shell growth on the nanotip in contact with an activated sodium silicate solution. They show the possibility of producing controlled thickness of protective silica coating layer for gold and silver tips (**Figure 2.5** below). The final tips can also be applicable for AFM-TERS measurements.⁸⁸

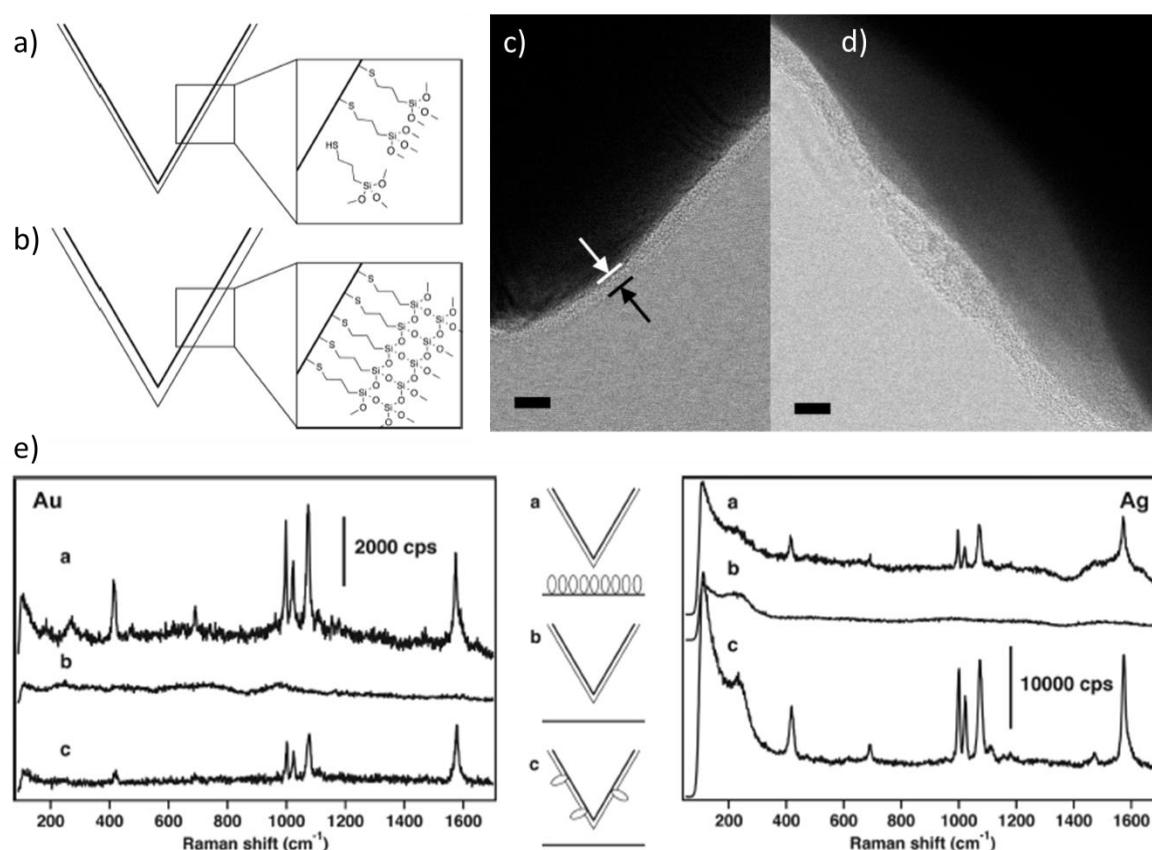


Figure 2.5. Tip protection with silica shell – a) scheme of tip functionalization with MPS, b) followed by the thin silica shell growth in contact with activated silica solution, c) & d) HR-TEM images of Au and Ag tip respectively both protected by the silica layer (2h of growth time) showing thin amorphous silica layer (<3 nm) on Au tip and less uniform silica layer on Ag tip ; e) STM-TERS measurements using Au@SiO₂ (left) and Ag@SiO₂ (right) tips: (a) on an Au substrate functionalized with PhS SAM, (b) & (c) on a bare Au substrate after immersion of the tip in a thiophenol solution. The observation of the PhS spectrum attests of the presence of pinhole in the silica when the shell growth procedure is not optimized.⁸⁸

Tip recovery - One of the most common tip contamination during TERS performance is contamination with carbon. Gold tips have been well recovered by dipping in concentrated sulfuric acid.⁸⁹ Moreover, Ag and Au-tips, have been successfully cleaned after carbon contamination by washing in solvents, Ar plasma cleaning, etc. Nonetheless, those procedures still do not prevent tips from further contamination during experiments.⁷⁴

Partial conclusion - One of the advantages of probe coating with PVD are easy and controlled tuning of the plasmon absorbance by adjusting the coating properties such as thickness, grain size and composition.⁵⁶ Many other procedures have been proposed, such as shaping tips with FIB or tip fabrication including probe pre- and post-heating with annealing steps in between. Those methods provide controlled thickness of coated layers with enhanced TERS signal.

On the other hand, disadvantages as weaker EF compared to electrochemically etched gold or silver tips^{90,91}, low reproducibility^{91,92}, short-lifetime^{92,93} due to the poor mechanical stability and weak mechanical resistance of deposited material are reported. Therefore, additional deposition of adhesive layer of silica onto gold and silver probes, was obtained as a successful method for achieving high TERS enhancement and prolonged lifetime of coated tips.

2.1.2. (Electro) chemical deposition

Other alternatives for TERS active probe coating, based on a deposition of a metal layer (Au or Ag) onto a silicon AFM probe, are chemical and electrochemical deposition.

Electrochemical deposition - Different approaches have been used for obtaining uniform coating, such as direct-current (DC), direct-potential and pulsed electrodeposition. The latter technique was introduced by Bin Ren *et al.*⁹⁴ in 2015, who investigated the influence of the deposition potential (pulse sequence) and time on the final tip radius and morphology of deposited Au layer. That protocol allows good deposition control, high reproducibility and the highest TERS signal from fabricated probes with radius between 60-70 nm (tested in gap mode). The surface morphology of the coated gold layer can be controlled by the deposition potential (high surface roughness is obtained at high overpotential) and the tip radius can be controlled by the deposition time.

Single particle TERS - Preparation of “single particle” TERS probe is a powerful alternative to physical deposition techniques. Deposition techniques of a single nanoparticles on the tip apex have also been obtained from electrochemically grown gold nanoparticle^{94,95} or chemically grown silver nanoparticle, using electroless deposition, silver mirror deposition or photo induced reaction^{96–98}. Enhancement of signal up to 20 times compared to regular TERS tips were reported.^{79,99,100} Vakarelski and Higashitani *et al.*¹⁰¹ alternatively proposed attachment/immobilization of Au NPs on the AFM tip apex by covalent bonding (**Figure 2.6**

below). Another technique has been introduced by Walke *et al.*¹⁰², showing fast and cost-effective fabrication, proceed from silver nanowires attachment by applying a square voltage between the cantilever and a conductive plate in a silver wire solution. The tips exhibited 10 times higher TERS enhancement compared to the electrochemically etched tips and showing more than 90% reproducibility for TERS.

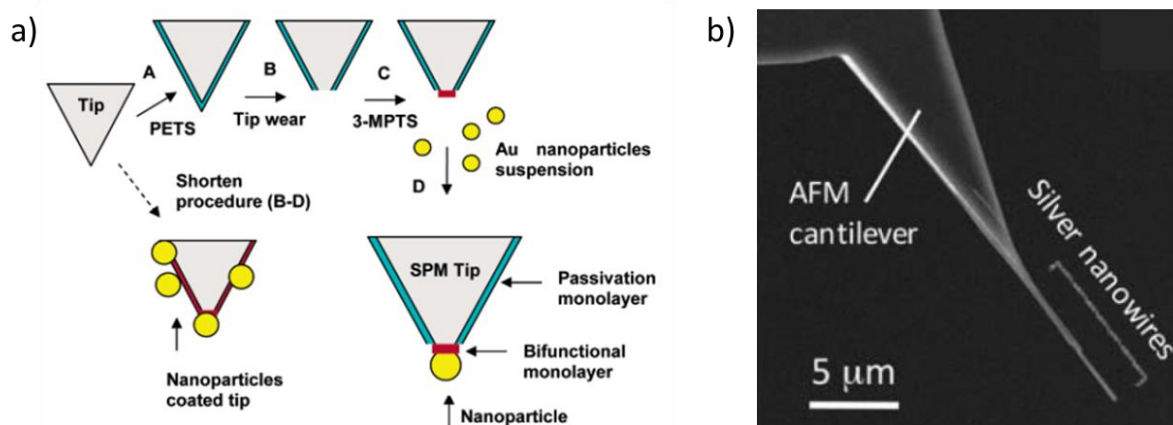
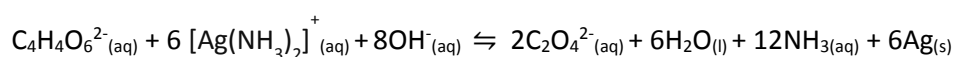
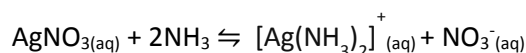


Figure 2.6. “Single particle” TERS probe: a) schematic procedure of a wet surface-assembly technique for single NP attachment to an AFM tip apex.¹⁰¹; b) SEM image of an AFM tip after functionalisation by a silver nanowire using polarization in a silver nanowire solution.¹⁰²

Electroless deposition - Electroless deposition of Ag probes is proceeded from $[\text{Ag}(\text{NH}_3)_2]^+$ ion adsorption and following reduction on the commercial Si AFM probe. Two main procedures of that deposition method are surface hydrophilization and sensitizing.^{103,104} When the probe is immersed in the mixture of silver nitrate stock solution including ammonia, as complexing agent and tartrate, as reducing agent, probe is instantly coated from the autocatalytic electroless deposition.



Different deposition time results in various morphologies of the probe coating and thickness. Longer deposition time, such as 15 min, forms silver aggregates which decrease TERS signal, while shorter deposition time of 5 min provides smooth silver coating. Despite the fact that this deposition process can generate uniform coating on “difficult” substrate shapes¹⁰⁵ and can produce tips with ROC between 30 and 50 nm, the method still shows low reproducibility.

Precise metal coating thickness can be also obtained *via* wet-chemistry procedure (**Figure 2.7**), combining self-assembly and surface chemistry as proposed by Gao *et al.* (2018)¹⁰⁶. The silicon probe is first silanized using thiol-terminal silane (MPTS) and immersed in the HAuCl₄ aqueous solution containing reducing agents (MPTS and NaBH₄).

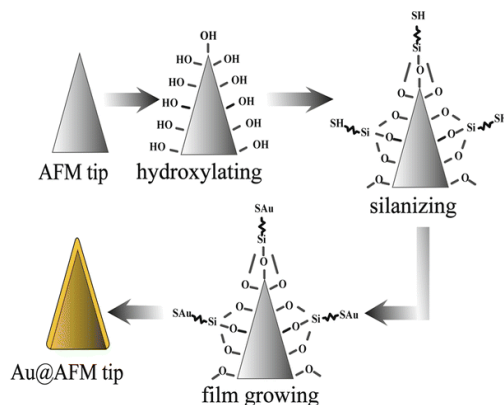


Figure 2.7. Wet-chemistry procedure – Precise gold coating obtained by successive hydroxylation of the silicon tip by ozone cleaning, silanization in contact with a mercaptopropyltrimethoxysilane (MPTS) methanol solution and metal deposition by gold salt reduction (HAuCl₄) using MPTS and NaBH₄.

Galvanic displacement reaction - Silver coated Si probes prepared by the sputtering technique provide smooth and uniform coating with cone-shaped apex and smallest radius of 40 nm with 1 min sputtering time. Compared to previously mentioned electroless deposition, this technique provides lower intensity Raman signal.¹⁰⁷ Ramanauskaite *et al.*¹⁰⁸ introduced another alternative, *i.e.* galvanic displacement reaction, which is a rapid method for metallic deposition of silver onto commercial Si AFM probe. The most challenging step during fabrication process is controlling the galvanic replacement reaction rate to provide smooth and uniform silver coating, which is achieved *via* the control of reagent concentration, temperature and the reaction time. Nevertheless, described technique provided fabricated tips with ROC of 20 nm and less.

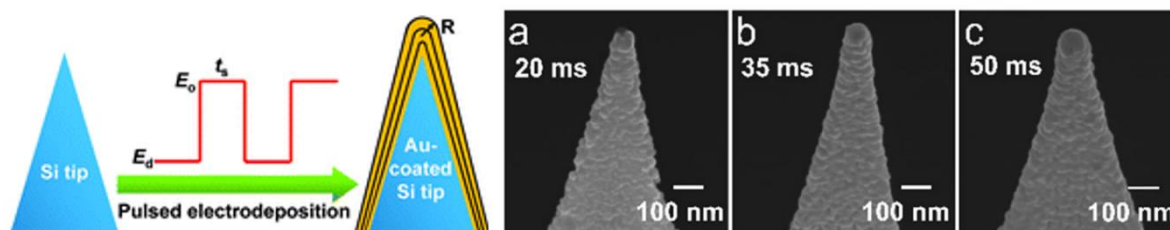


Figure 2.8. Pulsed electrodeposition procedure of AFM-TERS probes fabrication. Silicon tips are first etched in a HF buffer solution to remove the native oxide layer and immersed in the electrodeposition bath (KAu(CN)₂ potassium citrate, citric acid, sodium phosphate and small amount of additives). Au-coated tips prepared using a sequence alternating deposition (-1.85 V) and recovery potentials (-0.2 V). SEM micrograph of tips after various step time (a) 20 ms, (b) 35 ms, (c) 50 ms. Adapted from [94].

Partial conclusion - The benefits of coating by (electro)chemical deposition are controlled morphology, acquired through adjustment of the solution concentration, applied potential, reaction time, and thin deposition thickness between few angstroms to several mm. Compared to vacuum deposition processes, this method is simpler, environmentally friendlier and more cost-effective⁶⁵ with tip time preparation within only few minutes. On the other hand, fabricated probes undergo chemical degradation and nanoparticle-coated tips exhibit mechanical loss of surface material under large applied forces during measurements.

2.1.3. Electrochemical etching

Electrochemical etching is yet another alternative for manufacturing TERS active probes. Among other fabrication processes, this is the most broadly used method, due to its endurance, low-cost production and high yield performance, along with optimized conditions. This method is based on EC etching of thin metallic wire, which most commonly uses platinum (or W, Mo, Pt/Id) for STM application. This method was further adapted by TERS research teams using plasmonic materials (Ag, Au).

General principle - Electrochemical etching is based on the anodic dissolution of a metal wire in an etching electrolyte. The composition of the etching bath and applied polarization (DC or AC polarization, galvanostatic or potentiostatic) is optimized for every material. A metallic wire, with its diametric size ranging between 100 and 250 μm , is partially immersed in an electrolyte solution called etchant, and positioned in the center of a ring electrode, in a two-electrode configuration, to promote homogeneous dissolution of the wire (**Figure 2.9a**). The etching processes proceed till the immersed part of the wire falls into the solution (**Figure 2.9c**). During etching, the wire diameter progressively decreases at the electrolyte surface along with the lowered position of the meniscus (**Figure 2.9b**), causing tapered profile and sharp apex of etched wire with the approximately 30 nm radius size. The mechanical stability and precise control of polarization sequence are crucial to prevent wire over-etching after its lower part falls down, which leads to a blunt tip profile.

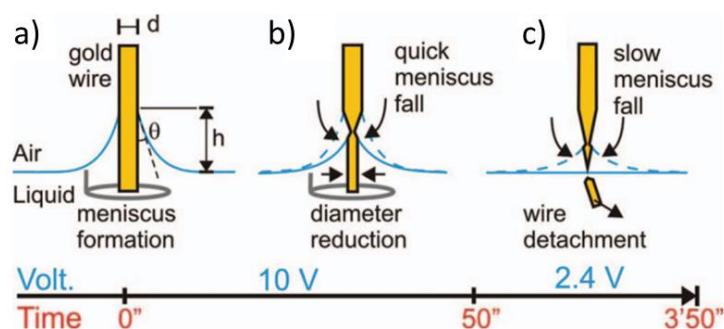


Figure 2.9. Generation of tapered-tip profile by electroetching: a) meniscus formation at the air-liquid interface upon wire immersion in solution; b) the meniscus lowers rapidly during the etching at the 10 V_{DC} as consequence of the diameter reduction of the wire in bulk; c) the slow drop of the meniscus during the etching at 2.4 V_{DC}. The process ends with the detachment of immersed wire leaving a sharp gold tip.¹⁰⁹

As the immersion depth of the gold wire is not well controlled from one experiment to another one, as the meniscus position can fluctuate or abruptly drop, leading to various tip profiles, and as the etching termination can be erratic, S. Choi *et al.* (2021) introduced an automated electrochemical etching system for reproducible fabrication of TERS probes with 85 % of yield, whereas D.H. Kim *et al.*¹¹⁰ reported final yield up to 95 % (**Figure 2.10**). The system gathers information on the electrical parameters, such as current and voltage as a function of time and then controls both the waveform generator and the stepper controller. When the etching current drops to zero because the Au tip is separated from the etchant the waveform generator immediately shuts down.

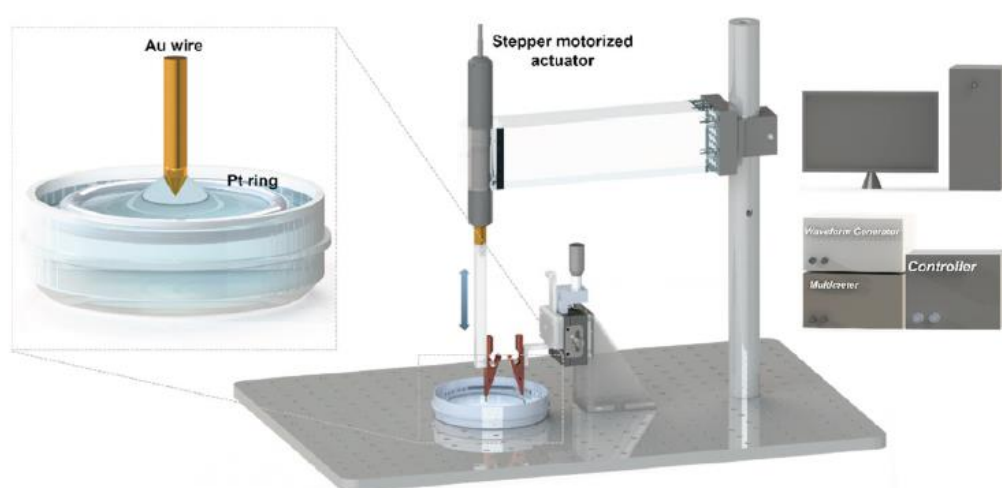


Figure 2.10. Homemade electrochemical etching system developed by Kim *et al.*¹¹⁰ The enlarged illustration represents the electrochemical etching process with bias applied. The stepper motorized actuator, stepper controller, waveform generator and multimeter are connected to a computer to automate the electrochemical etching process.

2.1.3a – Electrochemical etching of gold

Gold can be etched with CN^- or Cl^- containing solutions. Given the severe toxicity of KCN solutions, they cannot be used as an etching bath, despite producing smooth tip surface. Therefore, only nontoxic chloride-based etchant bath and associated electrochemical procedure will be described hereafter. Gold is usually etched within an electrochemical bath composed of HCl and ethanol and low etching voltage (e.g. 3.0 V). The reactions during Au etching process were explained by Bin Ren *et al.* (2004)^{111,112} as:



which can be decomposed into the two half-reactions:



Dissolution is the first step of etching process, where the gold-chloride complexes are formed (e.g. AuCl_4^-). A downward flow of AuCl_4^- appears along the wire, slowing down the etching of the wire lower part. The accumulation of gold-chloride complexes at the electrode induces depletion of Cl^- ions and formation of gold oxides which temporarily passivates the gold and stop the etching processes.¹¹³ Dissolution can resume temporarily when chlorine complexes diffuse away (relaxation) giving rise to current spikes (oscillations)^{96,111,114}. Note that at high potential, spikes of dissolution overlay with the oxidation of the solvent (gas evolution: see **Figure 2.12**). Sudden meniscus jumps upon polarization during the etching process can result in stepped structure of the gold tip surface.

Gas evolution (“bubbling effect”) - Bubbling effect comes from formation of Cl_2 and O_2 at the gold anode and H_2 at the ring-shaped cathode. This causes undesirable bubbling, mechanical instability which has a negative influence on probe surface, accounting for rough surface profile and not precise cut-off. Generated gas can also cause sudden jumps of the meniscus during EC etching as mentioned above. Another issue is associated to over-etching, when the tip apex and the solution surface remain in contact through the micro-meniscus after the lower part of the wire detaches.⁹² Presence of ethanol in the etching solution reduces bubbling effect during etching process and provides smooth tip surface.

Varieties of etching bath solutions and polarization - The most common etching bath solution is based on hydrochloric acid solution. For instance Ren *et al.*¹¹¹ studied etching using

HCl/ethanol solution (1:1) and DC voltage ranging between 2.2 and 2.4 V. Obtained tips showed smooth surface, cone shape and radius of curvature below 30 nm. The method was reproducible with a 50 % success rate of tips suitable for TERS measurements.

However hydrochloric acid, is volatile and has a corrosive nature from its fuming, degrading the metallic part of the etching station, including contacts. To resolve this issue, alternative chloride salts are used, such as CaCl₂ and NaCl.

Melmed *et al.*¹¹⁵ and Ito *et al.*¹¹⁶ used etching bath with CaCl₂ salt (10-50 % saturation) and DC polarization 30 V, for fabrication of STM probe, and 3 M NaCl and KCl solution at DC polarization 10 V, resulting in tips with the large apex size for TERS study.

Yang *et al.*¹¹⁷ showed highly reproducible etching with KCl (2.79 mol.L⁻¹) aqueous solution and a salt bridge between saturated KCl and agar, using three-electrode etching system (CE: Au ring, RE: Ag/AgCl; DC potential to WE 1.1-1.5 V) for precise control of the etching potential as will be detailed below.

Polarization - Final tip shape is determined by the reaction rate, which is controlled by the applied potential and not by the shape of the meniscus.¹¹⁷ In general, DC electrochemical etching is more simple and common method for fabricating Au tips, giving more reproducible apex radius of curvature and smooth apex profile, as compared to the other etching techniques.¹¹⁸ AC polarization or rectangular voltage pulses was introduced to limit blocking of the electrochemical process as observed upon DC polarization. AC polarization enables the control of etching parameters (high and low limit voltage, time, cycles)¹¹⁹ and exhibits a possible way of limiting overetching.¹¹⁴

DC polarization at low voltages (1.5 V, 1.7 V, 1.9 V) in the HCl/ethanol (1:1) electrolyte provide faster EC etching. Optimal etching, producing smooth and sharp tips, was acquired between 1.8-2.2 V.¹¹⁴ AC polarization, with square wave voltage at amplitudes 1.5 and 1.9 V and impulse duration of 220 ms, provides smooth tip profile with tip ROC of 18 nm.

2.1.3b – Refinements of the etching platform and sequence

Beaker cell – As mentioned above, hydrogen gas evolution at the cathode can disturb the etching process. Kharintsev *et al.*¹¹⁴ proposed the use of additional “beaker” in the solution to separate the cathode and the anode (gold wire), therefore limiting the “bubbling effect” (**Figure 2.11a**). Modified EC cell with etching potentials at 1.5, 1.7 and 1.9 V, provided more uniformed supply of Cl⁻ into the “necking” region, where the corrosion of the gold is faster.

Improved etching process of gold wire provided increased reproducibility of TERS probes manufacturing and produces smooth tip surface and radius of curvature with approximate size of 27 nm. Note that the introduction of the beaker separation may increase the electrolyte resistance between the two electrodes, affect the actual potential of the etched wire.¹¹⁴

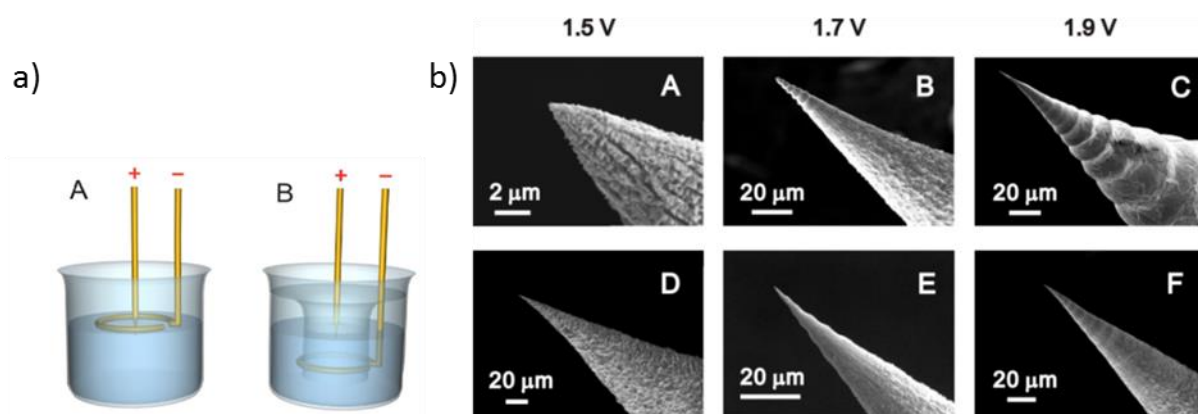


Figure 2.11. Modified etching cell ("Beaker" cell) - a) the schematic of the standard (A) and modified (B) electrochemical cells; b) SEM images of tips electrochemically etched in both standard (A-C) and modified (D-F) EC cells at different voltages.¹¹⁴

Three-electrode system - Initial etching methods used a two-electrode system. The newly use of three-electrode systems, introducing a reference electrode (RE), has been only recently proposed. The EC etching with only two electrodes proceeded upon anodic dissolution versus several different counter electrodes (platinum, gold, copper), with no control over applied potential at the etched metal tip. Further implementation of three-electrode configuration and potentiostat ensured better stability of applied EC potential at the gold wire and provided higher reproducibility in the manufacturing process.¹¹⁷

Although production of TERS-active probe using a three-electrode system was first published in 2018 by Yang *et al.*¹¹⁷, our group started using it as early as 2014. As illustrated in **Figure 2.12a**, a shift in potential of the gold electrochemical response and the strong oscillation regime is observed in a two-electrode configuration, as compared to a three-electrode setup. When using a DC polarization (2.2 V) without reference electrode, the potential of the gold wire keeps oscillating and shifting toward higher values, as illustrated on **Figure 2.12b**.

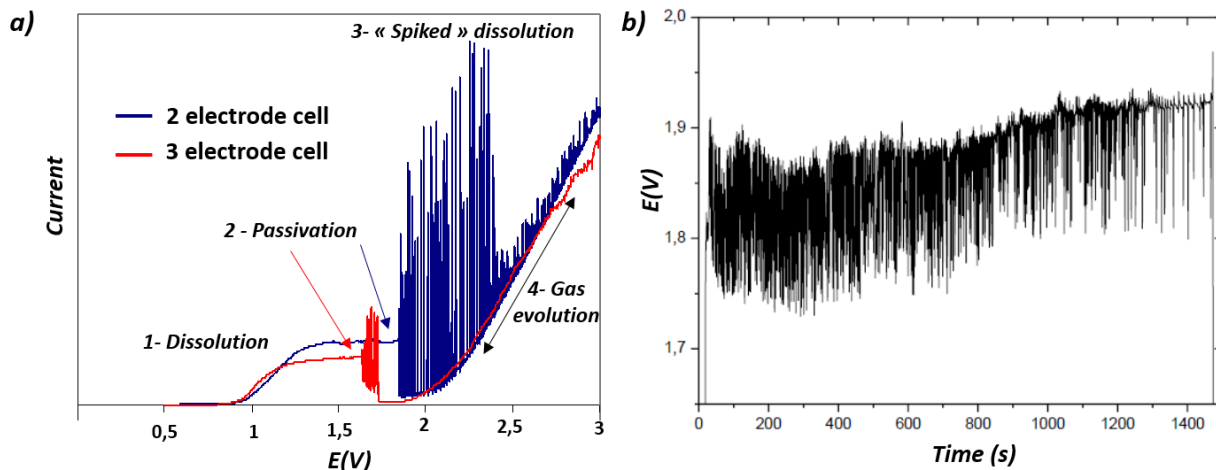


Figure 2.12. Importance of the potential control during electrochemical etching - a) electrochemical response of a 200 μm -diameter gold wire in HCl/EtOH (V:V, 50:50) in a 2 electrode cell (CE : platinum ring) and in a 3 electrode cell (Ag/AgCl pseudo reference electrode, CE : platinum ring), linear potential sweep: 0-3V; **b)** evolution during a DC polarization at 2.2V in a two electrode configuration (CE: Pt) of the gold wire potential measured with vs an Ag/AgCl electrode using a high impedance voltmeter. Adapted from Alice Dauphin bachelor report (LISE laboratory, 2014).¹²⁰

Cut-off – Circuit cut-off was introduced for better control in the final step of EC etching. A current detection device cuts off the circuit (disconnects the CE for instance), when the etching current drops below a threshold value. This step is crucial, when the lower part of the wire, being just below the meniscus surface, is cut off and falls down. Therefore, using the cut off device, the upper part (the final etched tip) of the wire is protected from possible further tip etching. A similar device was developed in LISE (see section 2.2.1).

Pulling system - A pulling system was proposed by Kharintsev *et al.*¹¹⁴ in 2011, to provide upward movement of the gold wire during the etching process. By using the precise drawing rate of the wire (at $5 \mu\text{m}\cdot\text{s}^{-1}$ and $20 \mu\text{m}\cdot\text{s}^{-1}$) at DC voltage of 1.9 V control, tip profile can be obtained. To control the tip meniscus properties, isooctane, which forms an organic layer at the solution-air interface, was added to the etching bath. This constitutes an original and straightforward way to limit over-etching leading to rough and blunt tip profile. Designed tips have a smooth and cone profile with the opening angle of 5° and a possibility of fabricating filament-like gold tips (see **Figure 2.13**).¹¹⁴

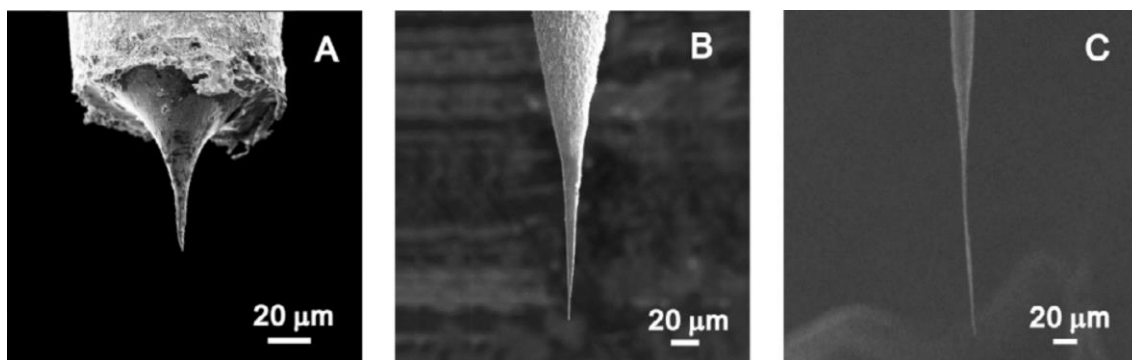


Figure 2.13. SEM images of EC etched tips by DC voltage with organic buffer layer (iso-octane layer formed on the etching batch surface) at 1.8 V (A) and pulling system out of the solution at a rate $5 \mu\text{m s}^{-1}$ (B) and $20 \mu\text{m s}^{-1}$ (C).¹¹⁴

2.1.3c – Electrochemical etching of silver

Silver electrochemical etching mechanism - EC etching set ups designed for fabrication of silver probes are similar to the one proposed for gold wire etching, i.e. an Ag wire anode and a Pt ring wire cathode connected to a potentiostat-galvanostat. A variety of silver etching bath solutions has been proposed, such as citric acid¹²¹, ammonia solutions¹¹⁸, nitric acid¹²², concentrated sulfuric acid¹²³ (**Figure 2.14a** below), perchloric acid¹²⁴ with additives (methanol, ethanol) and neutral aqueous electrolyte of ammonium nitrate (NH_4NO_3).

In 2011, Zhang *et al.*¹²⁵ showed etching in perchloric acid and methanol with the 1:4 ratio and DC voltage at 1.0 V, which yields sharp straight cone shape. In the same year, Lloyd *et al.*¹²² introduced etching bath solution composed of 2 M nitric acid and ethanol (1:2) with the gold ring-shaped CE, producing sharp silver probes with controllable production of tips with apex size of only 20-60 nm.¹²² Bin Ren *et al.*¹²⁶ showed EC etching of Ag tips using an electric control circuit with very fast cut-off of less than $1 \mu\text{s}$, preventing over-etching and providing tips with radius size smaller than 50 nm.

The **Figure 2.14b** below shows typical chronoamperogram with the current-time curve from the EC etching of Ag microwire in an aqueous solution of 8 M ammonium nitrate NH_4NO_3 . The EC sequence was performed for 10-15 s at a DC voltage of 2.0 V, using 2-electrode system with Pt wire loop as a cathode and Ag microwire as an anode. This method produced probes with radius size below 30 nm.

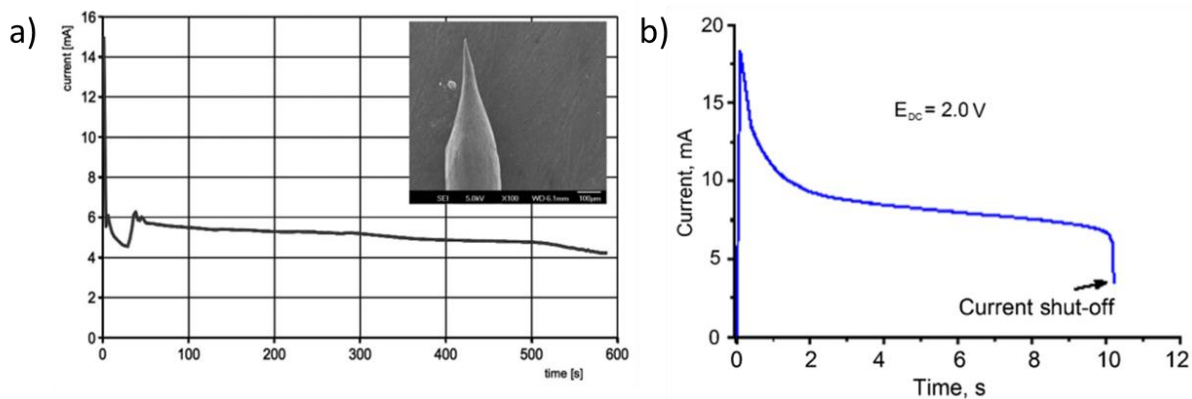


Figure 2.14. a) Typical chronoamperometry graph obtained during etching of a silver wire in concentrated H_2SO_4 (96 %) at 6 V.¹²³; **b)** typical chronoamperogram observed during EC etching of Ag microwires at DC voltage 2.0 V in 8 M NH_4NO_3 aqueous solution.¹⁰⁸

Hence, the majority of EC etching sequences for Ag wires were proposed in a two-step polarization sequence. This approach was first proposed by Iwami *et al.* (1998)¹²⁴ in electrolyte composed of perchloric acid and methanol (1:4) at AC voltage of 19 V (polishing process) in the first step and continuing with a second step at DC voltage of 5 V. Fabricated tips were obtained with ROC size of approximately 100 nm. This two-step approach was proposed also by Bin Ren *et al.*¹²⁶, using fast EC etching with the repetitive etching, providing sharp tips with smooth surface. The technique drawback is the unpredictable cut-off of the etching current, given that the timing for the introduction of the low reference voltage needs to be set precisely.

2.1.4. AFM probes from bulk metal to AFM-TERS probes

AFM-TERS probe can be also manufactured from bulk metal, following a procedure developed to produce AFM probe, which can be used in scanning electrochemical microscopy (AFM-SECM), as initially introduced by Macpherson *et al.*¹²⁷ and further developed by Demaille *et al.*¹²⁸. The TERS activity of such probe had been demonstrated in Zhan's group by Snitka *et al.*¹²⁹ in 2011 (gold probe), Rodriguez *et al.* in 2012¹³⁰ (silver probe) and Kolchuzhin *et al.* in 2016¹³¹ (gold probe). This technical solution has been the one chosen in this work.

General manufacturing procedure - The general procedure of fabricating AFM-TERS probes in 4-steps from metal wire was inspired from Macpherson *et al.*¹²⁷. The procedure consists of pressing a metal microwire (Pt ¹²⁷, Au ¹³²) to produce a reflective and flexible metal beam (cantilever) and its bent extremity at 90°, which remains unflattened. The bent part of the wire is electrochemically etched to produce a tapered tip either before¹²⁷ or after¹³² the

flattening process. Etching protocols, involving saturated sodium nitrite (97 %) electrolyte/ AC polarization at 1.2 V/Pt coil CE or electrolyte mixture of saturated CaCl_2 (10 mL), Milli-Q water (40 mL), ethanol (5 mL)/DC polarization of 7 V /aluminum foil CE¹³², have been proposed. Finally, the cantilever is glued on an AFM silicon chip. To be used as an SECM probe, tip and cantilever are insulated by deposition of cathodic electrophoretic paint. A small metal electrode is exposed, by either heat curing (paint retraction)¹²⁷, seen on **Figure 2.15**, or electrostatic discharge¹³² (paint removal). This procedure yields bulk metal AFM probes with cone shape tip.

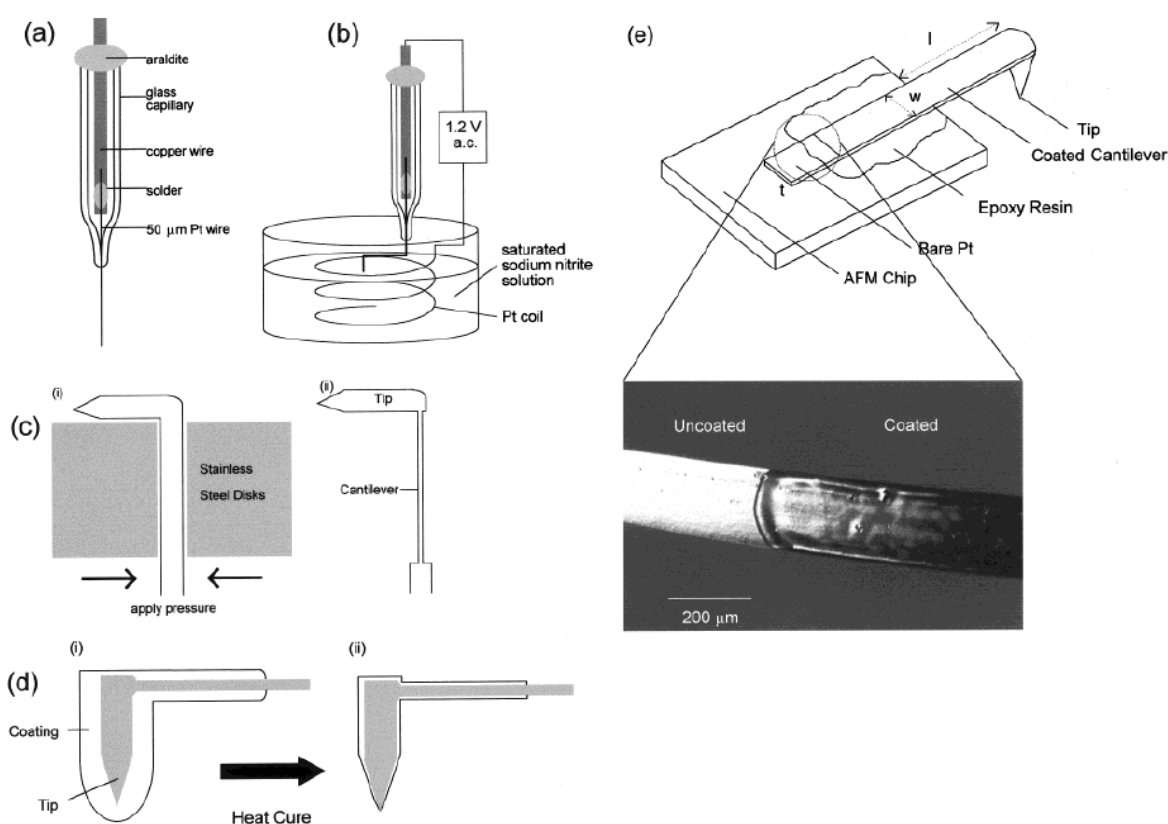


Figure 2.15. Schematic of the steps involved in the fabrication of SECM-AFM tips.¹²⁷

Protocol adaptation to TERS application - The adapted protocol of TERS-AFM probe manufacturing has been introduced by Zhan's group, using the same approach, to produce metallic cantilevers useable in tapping and contact mode AFM.

The procedure consists of flattening (between two flat surfaces, glass or silicon) and etching a 50 μm diameter wire (Au, Ag) to produce the cantilever. The tip tapered profile is shaped by electrochemical etching^{129,130} in a drop of a CaCl_2 solution deposited on an aluminum foil or by mechanical cutting of the bent part of the unflattened wire with a sharp razor blade (**Figure**

2.16) ¹³⁰ The cantilever/tip is immobilized on commercial AFM chip using epoxy glue. This procedure provided probes, compatible with TERS set-up of side-illumination and AFM imaging in both modes¹³³, tapping and contact mode with the EF 2.5×10^7 and 2.7×10^7 , respectively.¹³⁰

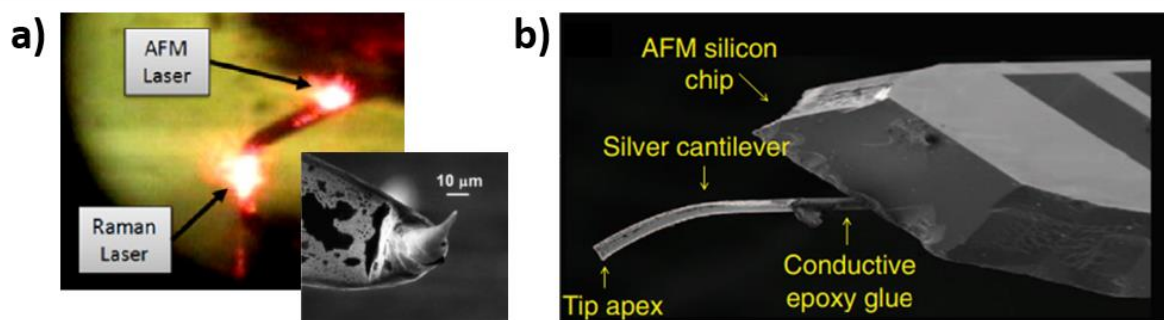


Figure 2.16. TERS active AFM probes made from bulk metal: a) gold wire (adapted from Snitka *et al.*¹²⁹; **b)** silver wire (50 μm diameter)¹³⁰ shaped and glued on a commercial AFM silicon chip.

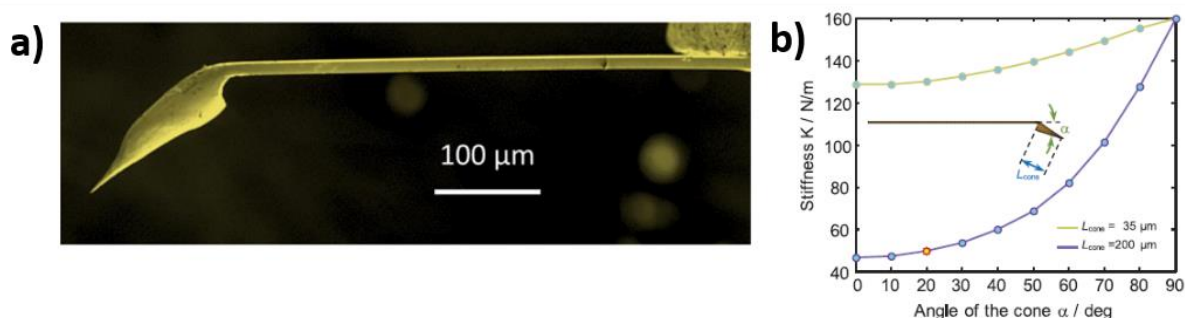


Figure 2.17. TERS active AFM probes made from bulk metal: a) SEM image of produced probe by Kolchuzhin *et al.* after optimization of the mechanical properties; **b)** dependences of spring constant of the gold tip on the angle of cone as calculated by FEM. Adapted from [131].

By using finite element method (FEM), Kolchuzhin *et al.*¹³¹ determined the dynamic and static mechanical properties of cantilevers response (eigen frequencies, mode shapes) and extracted key parameters, as cantilever spring constant and frequency depend on the cantilever characteristics (length 500-2100 μm, width 60-140 μm, thickness 5-50 μm, tip length 130-210 μm, tip angle 0-90°). This work demonstrated that the spring constant could be tuned by changing the angle of tip cone. The manufacturing procedure by Kolchuzhin *et al.*, reproduced the one of Snitka, except that the part of the wire left unflattened is bent at a 20-30° angle (**Figure 2.17a** above).

The TERS, properties of the manufactured probes were tested in the ambient on an inverted microscope (*NTEGRA* - NT-MDT) and two upright microscopes (*OmegaScope* -AIST-NT), coupled to a *XploRA* Raman spectrometer (Horiba) and an *AFM 5420* from Agilent

Technologies, coupled to a *LabRam HR- 800* Raman system (Horiba). No TERS mapping was demonstrated using the manufactured probes in any of these study, only TERS point spectra on high cross section (graphene on glass) or Raman resonant compounds (2 to 30 nm of an organic layer of cobalt phthalocyanine – CoPc - on gold).

2.2. Fabrication/optimization of TERS active AFM probes in this work

The strategy and technical solution developed in this work consists in a combination between manufacturing techniques for bulk metal AFM-probes and electrochemical etching protocols optimized in our group for the production of STM-TERS probe procedure. This chapter will cover the 4-step manufacturing process and detail the different optimization steps developed in this work.

2.2.1. From bulk metal wire to AFM probe

The fabrication process starts with the production of reflective cantilever. A 25 μm diameter Au wire (MaTeck, purity 99.99%) was first placed between two glass slides maintained together by two metal paper clips and bent with a cotton swab at a 90° angle along the edge of the glass slide assembly. In the next step the part of the wire, sandwiched between the glass slides, was pressed and flattened using a hydraulic press (see **Figure 2.18**).

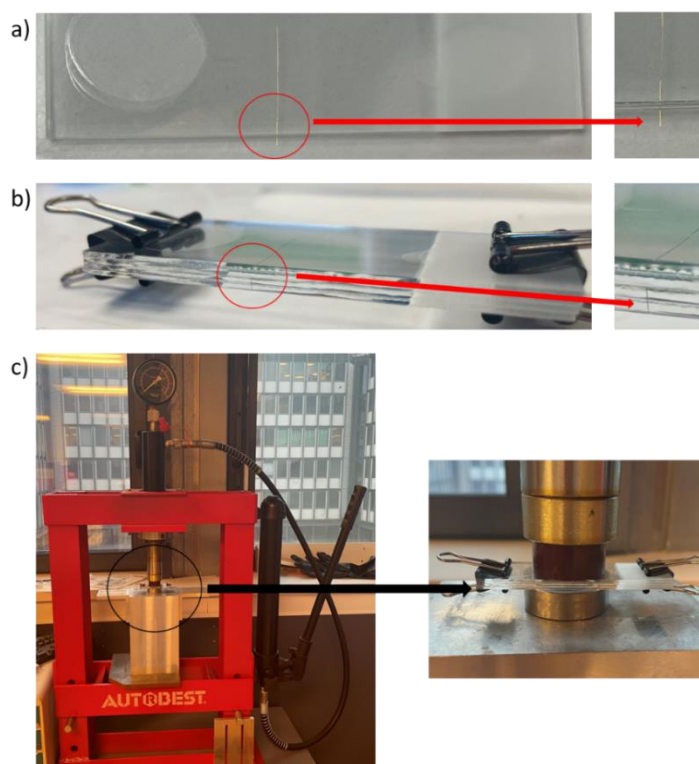


Figure 2.18. Gold wire flattening and bending steps - **a)** gold wire placed between 2x2 glass slides assembly and protruding of a few millimeters; **b)** gold wire bent at a 90° angle; **c)** hydraulic press for wire flattening creating reflective cantilever (zoomed picture on the right).

The initial diameter of the gold wire and the pressure applied to the gold wire/glass assembly determine the final roughness, width and thickness of the flattened wire, and the reflectivity and flexibility of the resulting cantilever (**Figure 2.19** below). Pressure up to 1 ton for a few minutes was necessary to produce reflective cantilever, which could be detected by the automatic cantilever screening of the AIST-NT system (IR AFM registration laser), as will be discussed later.

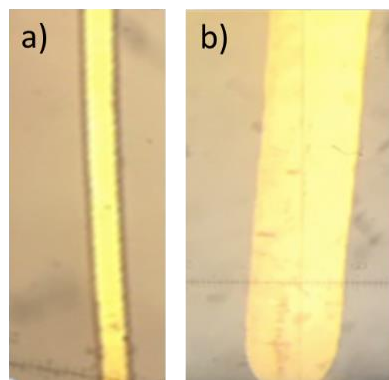


Figure 2.19. From 25 μ m-diameter gold wire to reflective cantilever - **a)** gold wire before and **b)** after flattening as observed under the optical microscope.

2.2.2. Cantilever immobilization on Si chips

In the next step, the flattened and bent wire was taken out from the glass slides sandwich and taped on a support, which can be handled with ease. The wire on its support was then attached to a micro-positioning system and placed on a gluing station (**Figure 2.20a-b**). The exact positioning of cantilever onto the AFM silicon chip was achieved by precise movement of mechanical positioner in all three directions (x , y , z) under video control (Teslong endoscopes). The cantilever was glued on the chip, using a two-component epoxy glue. A small drop of glue was deposited (**Figure 2.20d**) with the tip of a needle on the top surface of the flattened wire and at some distance from the chip edge to avoid the glue to spread on the flexible part of the cantilever. Note that the glue spread by capillarity at the interface of the wire and the silicon chip till the edge of the chip. The glue was left to dry for approximately 10 minutes, before the chip could be manipulated (and the wire detached from its support).

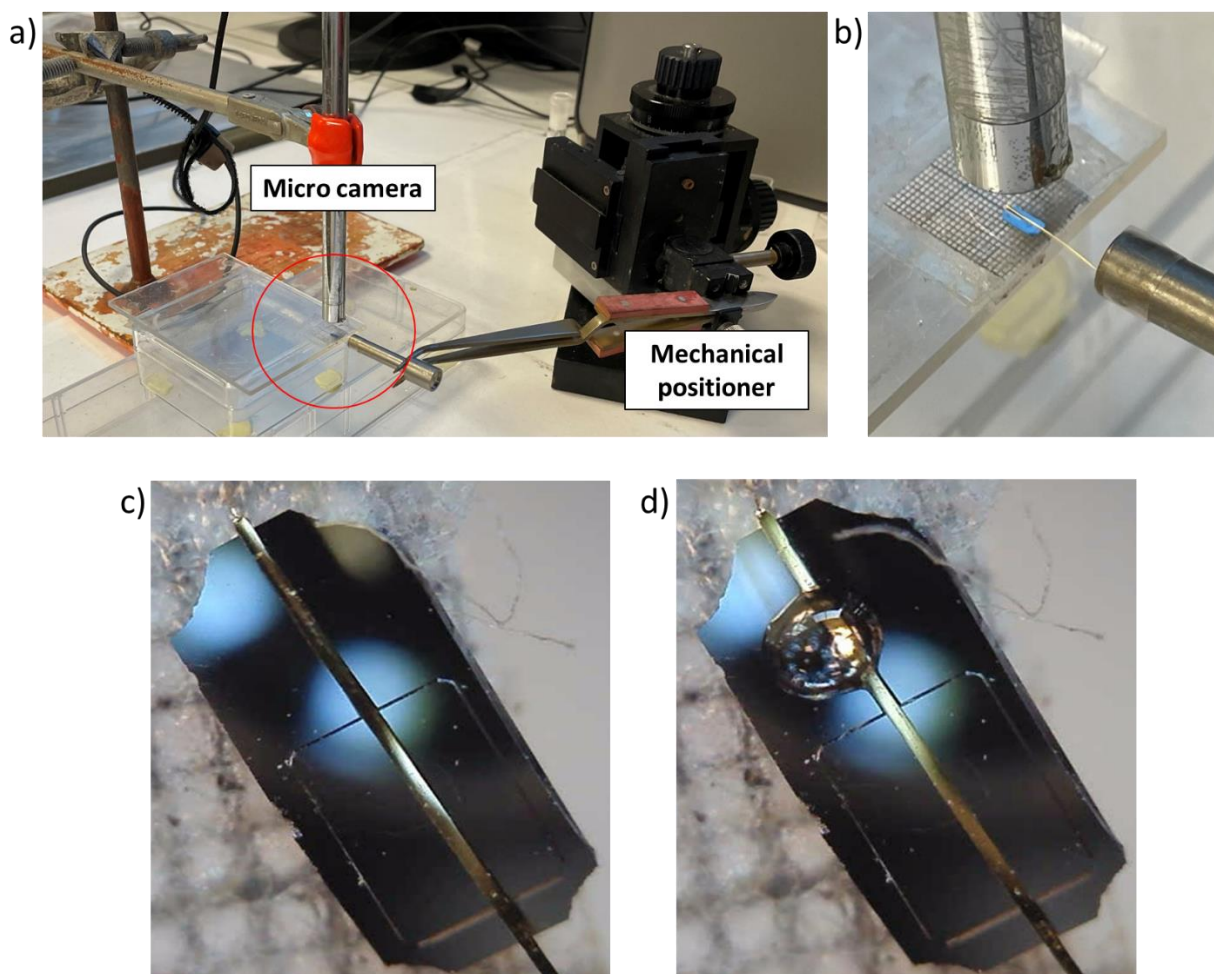


Figure 2.20. Cantilever immobilization on AFM silicon chip - a) “gluing station” equipped with micro camera and mechanical positioner; **b)** approach and positioning of the flattened wire attached to its support on a recycled silicon AFM chip; **c)** flattened gold wire positioned on the chip before gluing (the non-flattened part of the wire bent at 90° is facing up), **d)** drop of two-component epoxy glue deposited at some distance from the chip edge.

2.2.3. “Shaping” of tapered gold tip by electrochemical etching

In the final etching step, the chip was held firmly with a flat tip metallic tweezer (wrapped with copper foil) and placed onto the mechanical positioner on the etching station, equipped with a micro-camera to monitor the etching process. The etching station uses a Pt ring CE, and pseudo-reference electrode (silver wire) and an etching bath, composed of HCl and absolute ethanol with the volume ratio 1:1. The Au wire (WE) is positioned in the middle of the ring-shaped CE, the RE is brought in close proximity to the outer side of the CE (**Figure 2.21a**). The electrical contact of the gold wire, attached to the silicon chip, is ensured through the metal tweezer. The three electrodes are connected to a potentiostat (*PGstat 100N*, Metrohm). A beaker-type electrochemical cell, which was initially used, was later-on replaced by a cell, enabling electro-etching in a drop.

An additional “cut-off” voltage box, connected between the counter-electrode and the potentiostat, has been developed in LISE to automatize and precisely control the termination of the etching process and to avoid over-etching of the gold wire. The cut-off box is configured to physically disconnect the CE when the current flowing in the system falls below a set threshold value and interrupt the polarization. As the CE is disconnected, the etching process is interrupted and the etching sequence on the potentiostat, which is apparently still running, reads zero current. Note that as the cut-off box uses a current/voltage converter, the voltage associated with the desired current threshold, depends strongly on the current range set in the potentiostat. The influence of the “cut-off” current value on the performance of the tip is illustrated hereafter.

Once the electrochemical cell is set, the etching process can take place. As mentioned earlier, when gold etching proceeds, the immediate surroundings of the wire become rich in gold-chlorine complexes and poor in Cl^- . Gold cations starts therefore reacting with oxygen, forming insulating gold oxides that temporarily passivates the gold wire. Dissolution can resume temporally when chlorine complexes diffuse away (relaxation), giving rise to current spikes (oscillations). At higher potential, spikes of dissolution overlay with the oxidation of the solvent (gas evolution). To limit the shift in potential of the gold wire observed in a two-electrode configuration due to the strong oscillation regime, a three-electrode setup has been preferred in our group starting from 2014, when optimizing the manufacturing process of STM-TERS probes. AC potential pulses were also preferred to DC polarization, so that dissolution at higher potential and relaxation at lower potential can alternate in a controlled manner, allowing a fine control of the etching process. The parameters of the electrochemical sequence won't be disclosed here, as two Soleau envelops protecting this know-how have been filed in 2015 and 2019. When the etching was finished (see **Figure 2.21d**), the tip was rinsed in the water and ethanol and eventually stored in a box. Note that the resulting quality of the tip is strongly dependent on parameters as non-fresh solutions, water contamination, CE passivation and “polluted” RE, contact resistance due to corrosion with acid vapors, which influence the correct outgoing of the procedure.

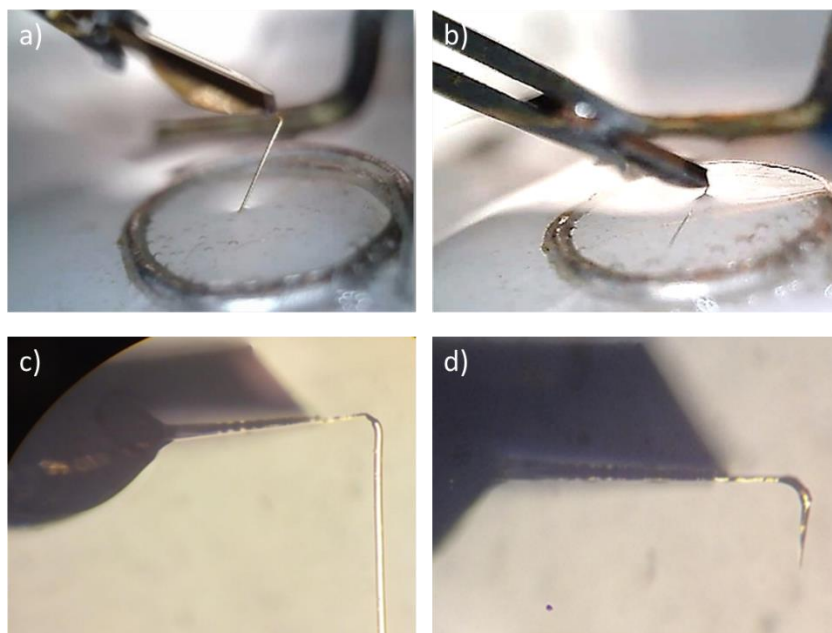


Figure 2.21. Etching process in a drop - a) glued Au wire on the standard AFM chip positioned in the middle of the Pt ring CE (4 mm diameter); **b)** optimization of the immersion depth in the HCl /EtOH solution to limit the final length of the “nose” (tip height) after etching ; **c) & d)** bulk metal probe before and after EC etching respectively.

2.2.4. Optimization of the etching electrochemical cell

The etching process was initially optimized for long gold wire designed for STM-TERS applications. The bulk wire was etched in beaker cell, containing 5 mL etching solution of hydrochloric acid and absolute ethanol in the volume ratio 1:1. The same procedure has been applied for fabrication of AFM probes. The large volume of etching solution, initially used in a beaker cell, was replaced by a single drop, deposited in the Pt ring electrode above a hydrophobic support (PTFE). This allowed to minimize the fluctuation of solution meniscus height during EC etching and therefore a better control of the immersion depth of gold wire to be etched (see **Figure 2.22**). The drop of a freshly prepared etching solution was replaced for each manufactured probe. The AC etching sequence mentioned above, produced tips with an etching time of only few seconds. The optimized etching process yielded probes with a cone shape, smooth probe surface and smaller radius of curvature.

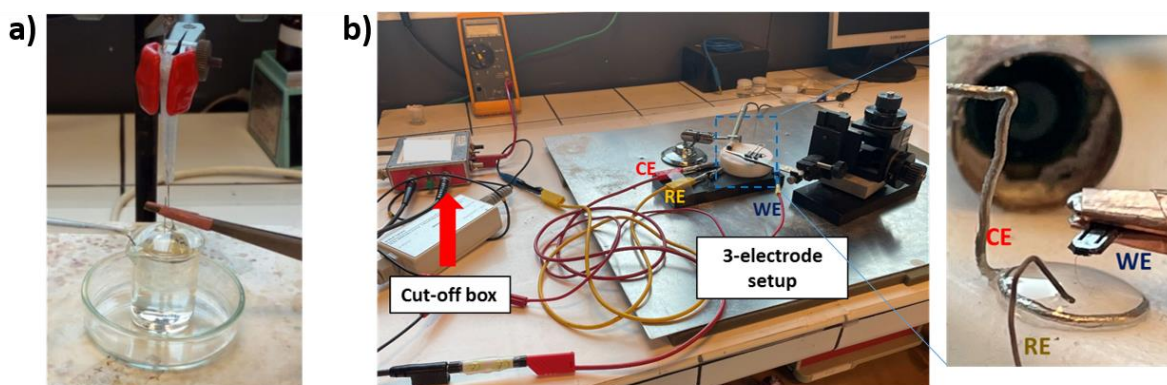


Figure 2.22. Etching set-up for bulk metal AFM-TERS probes: a) beaker-cell initially used; b) optimized setup using only a drop of etching solution (zoomed setup to the right). A cut-off voltage box disconnects the Pt ring counter-electrode and interrupts polarization for precise etching termination. The 3-electrode setup (WE: gold wire/future tip; CE: Pt ring; RE: Ag) is contained in a drop of solution for better control of the immersion depth of the wire to be etched.

Partial conclusion – With all optimization steps of the fabrication process, which have been crucial to produce the set of results presented in Chapter 3 and 4, the handmade approach gained in precision and further considerably decreased time for tip manufacturing, due to the acquired experience, which is non easily transferable to other users. In fine, a set of 10-15 tips could be made in one day, which provided the possibility of fabricating fresh tips before each measurement. These low-cost homemade probes (a few dollars + man power) could be used routinely for TERS experiments, helping the fast development of EC-TERS. This would not have been possible with expensive commercial AFM-TERS probes.

2.3. Characteristics of handmade AFM probes

The choice of AFM probe is critical for the successful and accurate tracking of topography, especially when scanning in different AFM modes (contact, intermittent and non-contact). The quality of AFM imaging strongly relies on tip geometry and further interaction between the tip and sample surface.¹³⁴ Different tip features can cause convolution effect and artifacts on AFM image. The tip mechanical properties affects the imaging process by interacting with the sampled objects, altering their shape/position or have an impact on the tip/object penetration. In this section different characteristics of the manufactured probes will be reviewed, i.e. the tip and cantilever geometry and properties to operate in tapping mode on the AIST-NT/Horiba system.

2.3.1. Tip profile and radius of curvature

In general, smaller tip radius provides higher lateral resolution with better quality AFM image. It is crucial to choose suitable tip regarding to the studied object. More accurate topography is obtained, when the objects on the surface have small height and ratios with smaller sidewalls angles, as compared to the tip. In that matter, the tip radius has only minor influence on the accuracy of the final image. When the objects on the surface are high, tip affects the shape of sub-micrometer features, providing an AFM image with the convolution effect.¹³⁴ Seen on the **Figure 2.23** below, different tip shape provides different profile from the same object. Common radii of commercial AFM probes lay between 10 and 100 nm¹³⁵ in a conical or pyramidal shape. The etching procedure was optimized in this work to better control the tip ROC and opening angle.

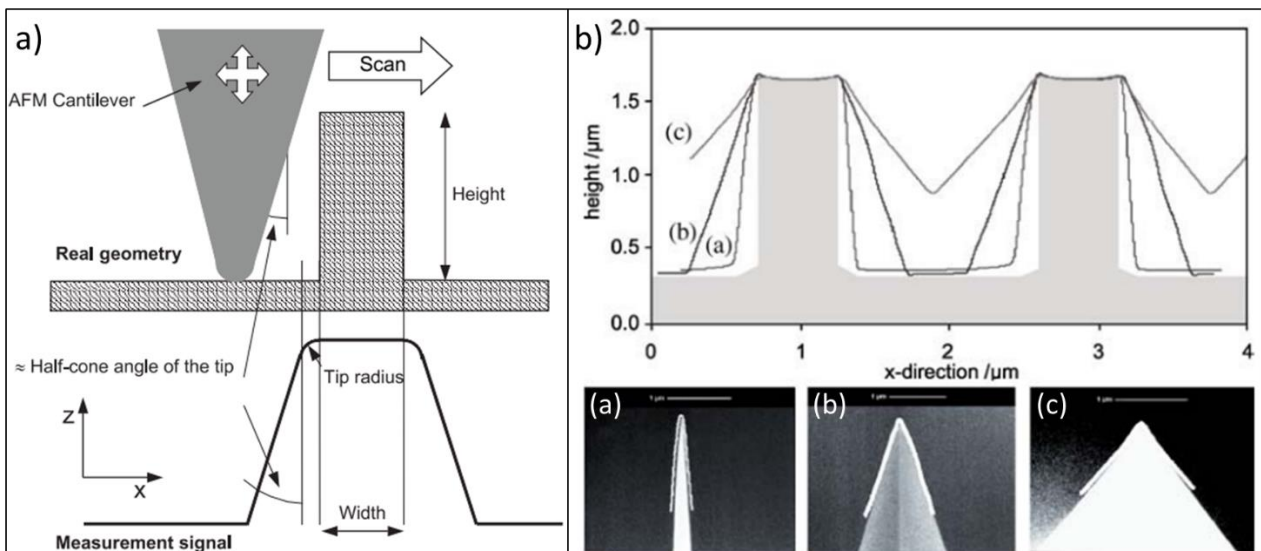


Figure 2.23. Influence of the tip shape on the AFM imaging performance: a) comparison of the real probe geometry with measured signal; b) AFM measurements of the 2D-calibration structures with three different tip shapes (SEM images below; (a) high-aspect-ratio tip (NanoSensors AR5-NCHR); (b) silicon tip (NanoSensors NCH); (c) silicon nitride tip. Adapted from [136].

Optimization of gold tapered profiles - The influence of the current range and cut-off voltage values, used during the electrochemical process on the produced tip, were first evaluated. First, the current range of the potentiostat was set to 100 μA and the cut-off voltage values to 5 and 10 mV. This step resulted in tips with too large radius size and moreover, without consisted radius size among final tips. In the second step, current range was set at 10 μA with cut-offs 5 mV, 10 mV, 20 mV, 80 mV and 100 mV. For each combination of current range and “cut-off” values, the set of etched tips was first analyzed *via* SEM to closely observe their morphology and shape. All final tip apex profiles are shown on the SEM

images on the tables below. SEM images show smoother profile and smaller ROC, when the etching was proceeded in a 10 μ A current range.

Table 2.1. Evolution of Au probe cone shape affected by different value of cut-off at 100 μ A.

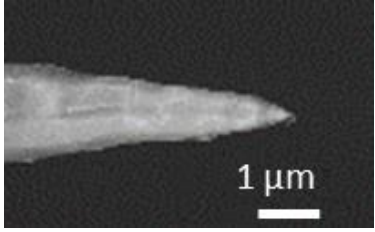
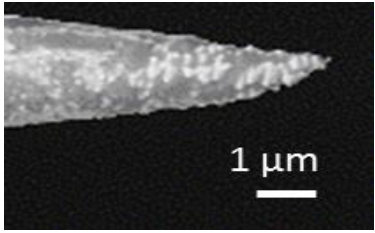
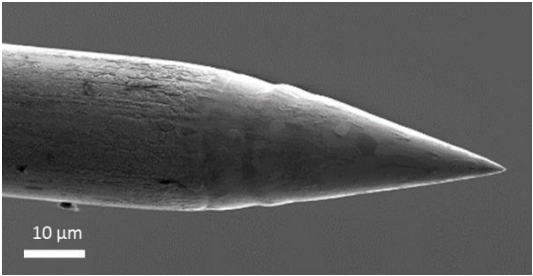
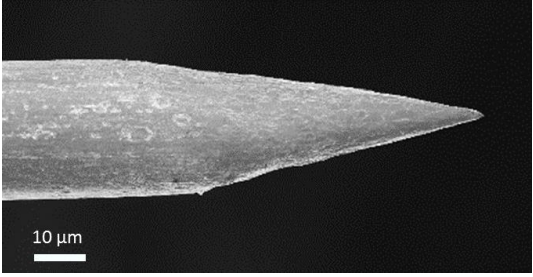
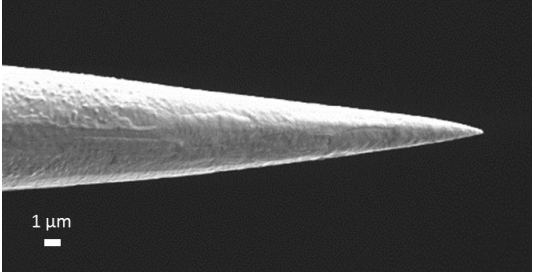
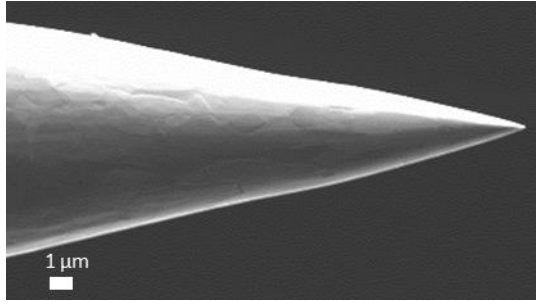
SEM image	Cut-off (mV)	Average radius (nm)
	5	92
	10	195

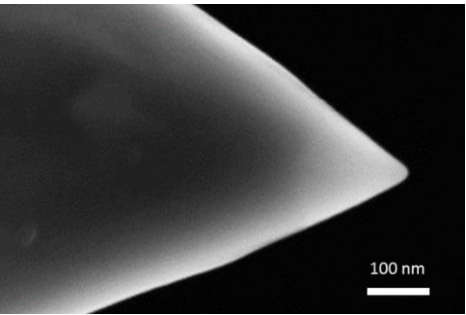
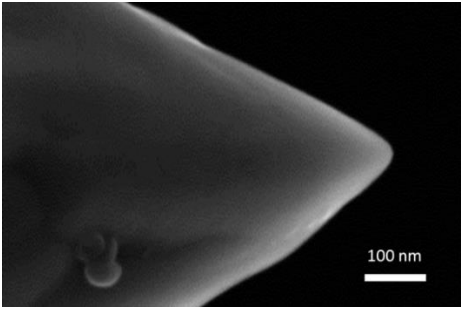
Table 2.2. Evolution of Au probe cone shape affected by different value of cut-off at 10 μ A.

SEM image	Cut-off (mV)	Average radius (nm)
	10	30 – 40
	20	24
	80	20 – 30

	100	35
---	-----	----

The optimized procedure was set at the current range 10 μ A and cut-off 20 mV, producing cone-shape probes with the sharp apex and average radius size of 24 nm (Table 2.2 above). The statistics were retrieved from the fabrication of 20 gold probes with a 90 % (18/20) success rate of yielding TERS active probes. Success rate for etching process was obtained with 83 % (15/18), whereas bulk probes with large radius size ($R > 100$ nm) were acquired in 17 % (3/18).

Table 2.3. Fabricated probes with optimized procedure at current range 10 μ A and cut-off 20 mV.

SEM image	Radius range (nm)	Average ROC (nm)	Percentage of fabricated probes in that ROC range (%)	Tip shape and profile
	$R < 20$	15	45	Cone shape, smooth probe profile
	$R = 20 - 40$	34	25	Cone shape, smooth probe profile

2.3.2. Cantilever features

2.3.2a – Detection by the AFM registration system

As mentioned earlier, the AIST-NT system uses an automatic cantilever screening given that the AFM registration system laser uses an IR source (1064 cm^{-1}), which does not interfere with the Raman signal excitation collection. Both, the probe holder and the photodetector, are mounted on motorized stage (step motors). The automatic positioning/alignment procedure of the cantilever/AFM registration laser/photodetector is realized by displacement of the probe holder below the fixed laser beam and reading of the total reflected intensity on the photodetector and final photodiode position adjustment (centering of the reflected beam on the 4-photodiode detector). Reflective cantilever, obtained by flattening 25- μm diameter gold wires at 1 ton for a few minutes, could be detected by the AIST-NT system (see **Figure 2.24a**). Reflective image of the cantilever can be built by raster scanning of the probe under the laser beam (see **Figure 2.24 c, e, g**). Note that on most manufactured cantilevers, the reflectivity was not homogeneous, as revealed by the intensity image (see **Figure 2.24e**). This can be due to a slight torsion (horizontal) and tilt (vertical) of the cantilever upon gluing.

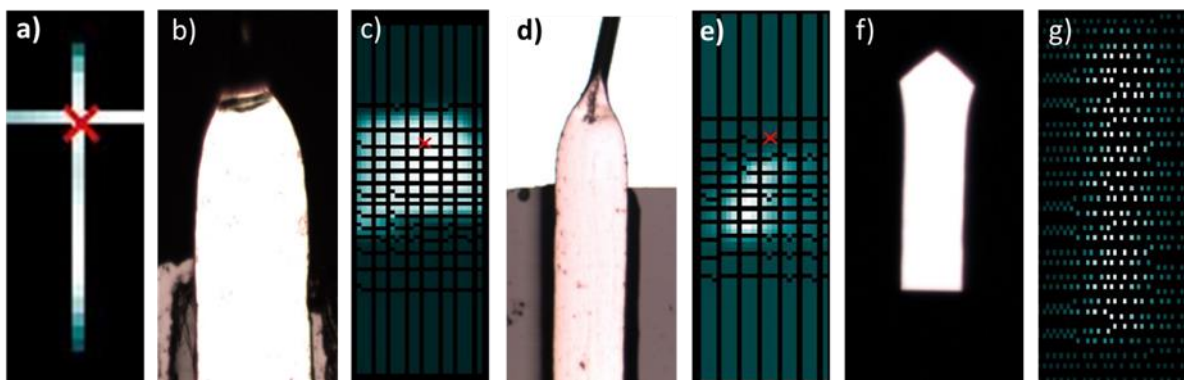


Figure 2.24. Automatic detection of reflective cantilever - a) detection of the contour of the cantilever by the AIST system; top view of cantilever (10x magnification) and reflectivity image obtained by raster scanning of the probe holder below the IR registration laser: **b) & c)** homogeneous reflectivity of homemade cantilever, **d) & e)** inhomogeneous reflectivity of homemade cantilever, **f) & g)** homogeneous reflectivity of commercial cantilever (Mikromash NSC14).

2.3.2b – Operation in tapping mode - Mechanical properties of bulk metal probe

Stiff probes with high resonance frequency (100 kHz) were targeted in this study for fast imaging in tapping mode and in liquid medium. The cantilever weight strongly affects the resonance frequency and the spring constant (described later). Softer and lighter cantilevers

have higher resonance frequency, providing better high speed response in the air and further better imaging at high speed. The resonance frequency can be calculated as:

$$f_0 = \frac{1}{2\pi} \sqrt{\frac{k}{m}} \quad (2.1)$$

with m as cantilever mass (spring mass) and where k is the spring constant, defined as:

$$k = \frac{E \times w}{4} \left(\frac{t}{l}\right)^3 \quad (2.2)$$

with w width, t thickness, l cantilever length. Moreover, the specific calculation for cantilever resonance frequency includes its density ρ and Young's modulus E , which depends on the cantilever material.

$$f_0 = \frac{t}{4\pi l^2} \sqrt{\frac{E}{\rho}} \quad (2.3)$$

Typical values of commercial AFM probes made of silicon, are $E = 168.1$ GPa and $\rho_{\text{Si}} = 2.33 \times 10^3$ kg.m⁻³ (for gold $E = 79$ GPa and density $\rho_{\text{Au}} = 19.3 \times 10^3$ kg.m⁻³). The commercial AFM probes, which were further used for evaluation of AFM imaging quality on nano-objects, were featuring pyramidal silicon tip with approximate cantilever length of 125 μm , width 25 μm and thickness 2.1 μm .

A desirable resonance frequency can be achieved by adjusting the cantilever length, thickness and width in the manufacturing process. Higher resonance frequency can be accessed by decreasing the cantilever length and increasing the thickness. "Nose + tip" of the probe also add to the average probe weight and affect overall imaging quality, and should not exceed the size of 100 μm or the size of cantilever length. Cantilever and nose/tip dimensions are even more critical when operating in liquids, where fluid dragging reduces the quality factor of large cantilevers.

Cantilever geometry - The average parameters of the cantilevers, manufactured in this study, were of length size between 100 – 120 μm , width between 90 – 100 μm and thickness around 5 (4-6 or 5.77) μm . In contrast, hand-fabricated AFM-SECM probes by Zhang *et al.* were reported with the average cantilever thickness around 20 μm and width of 100 μm .¹³³ The average "nose + tip" length in the manufacturing process of homemade probes was obtained

between 90 – 105 μm . With the average cantilever length up to 110 μm , the fabrication process filled the requirement of “nose + tip” size vs cantilever length. Homemade probe with most common cantilever dimensions are seen on **Figure 2.25** below.

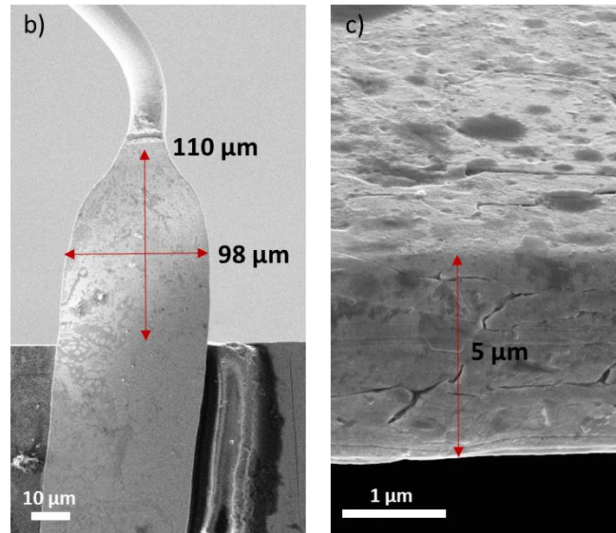


Figure 2.25. SEM images of manufactured probe showing cantilever length, width (b) and thickness (c).

The Table 2.4 below shows average values of hand-made probes features. The statistics were done on 30 different probes, fabricated from the optimized manufacturing process. Note also that the limited displacement range of the AIST detection scheme strongly limited the exploration of cantilevers to short length only. Cantilevers with the length of 800 μm , as reported by Demaille’s group¹³³, could not be detected here.

Table 2.4. Table with average values of hand-made probe features.

	Cantilever length (μm)	Cantilever width (μm)	Cantilever thickness (μm)	Tip length (nose + apex) (μm)
Average	110	98	5	96

Resonance frequency - Resonance frequencies of hand-made probes in this work were obtained in the AIST-NT SPM control software, by varying the frequency excitation or “drive” (35 – 250 kHz) of a piezo element (“shaker”) integrated in the probe holder and measuring the amplitude of the cantilever oscillation on the photodetector. **Figure 2.26a-b** below shows resonance frequency spectrum of one homemade probe in the air and in liquid (water), respectively. The spectrum in liquid shows higher number of peaks with wider profile, which

makes difficult the choice of the resonance frequency. *Cantilever behavior in liquid medium* originates from the additional hydrodynamic forces and forces applied to the tip/cantilever due to fluid squeezing (especially in close proximity with a sample), whereas the first one reduces vibration amplitude and the second one shifts the resonance frequency.¹³⁷ The number of peaks can be explained by the numerous vibration mode of the cantilever/liquid system, related to the mechanical excitation of the cantilever through the probe holder when in contact with the liquid.

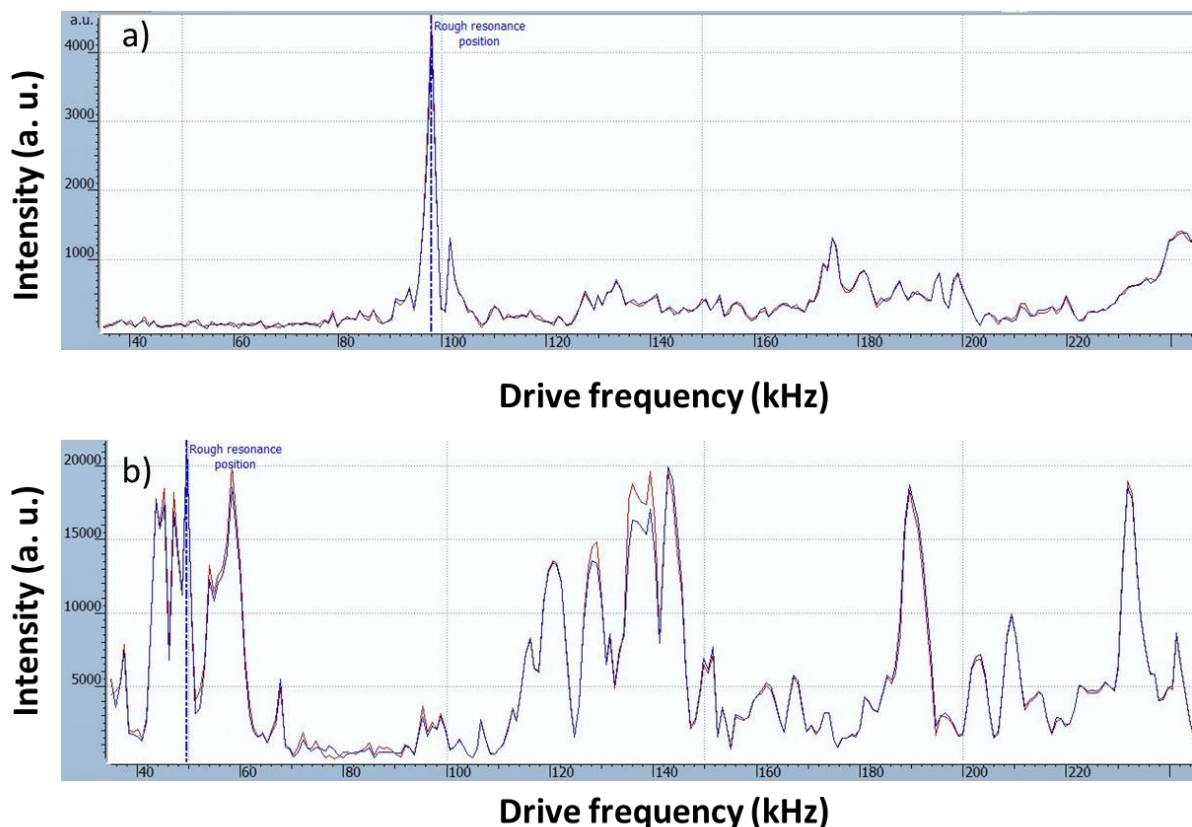


Figure 2.26. The resonance frequency curves of homemade probes in the defined range (35-250 kHz) in the air (a) and in water medium (b) on the AIST-NT/Horiba system.

Quality factor (Q) - Quality factor characterizes damping value of a specific oscillator. The quality factor can be calculated in two ways. First example is shown as the ratio of stored energy per energy lost during each cycle. This can be seen as the sharpness of the resonance frequency curve.

$$Q = \frac{\text{energy stored}}{\text{energy lost per cycle}} \quad (2.4)$$

The general definition includes the ratio between resonance frequency and its full width at its half maximum:

$$Q = \frac{\text{resonance frequency}}{\text{full width at half max.}} = \frac{f_r}{\Delta f} = \frac{\omega_r}{\Delta \omega} \quad (2.5)$$

where f_r is the resonance frequency and Δf the resonance frequency width or full width at half maximum (FWHM).

The image resolution and scan rate can be generally improved by modifying the Q-factor of probe cantilever, when AFM is operating in tapping mode. Larger Q-factor associated with sharper resonance frequency profile provides higher sensitivity.

The quality factor was calculated from the set of 10 probes in the air. The average value of 135 was calculated from the equation (2.5) above.

The **Figure 2.27** below shows a common resonance peak from a homemade probe with the quality factor of 138. Q-factor might be optimized through the probe manufacturing process, by adjusting the mass and controlling the position of the cantilever and the amount of glue deposited.

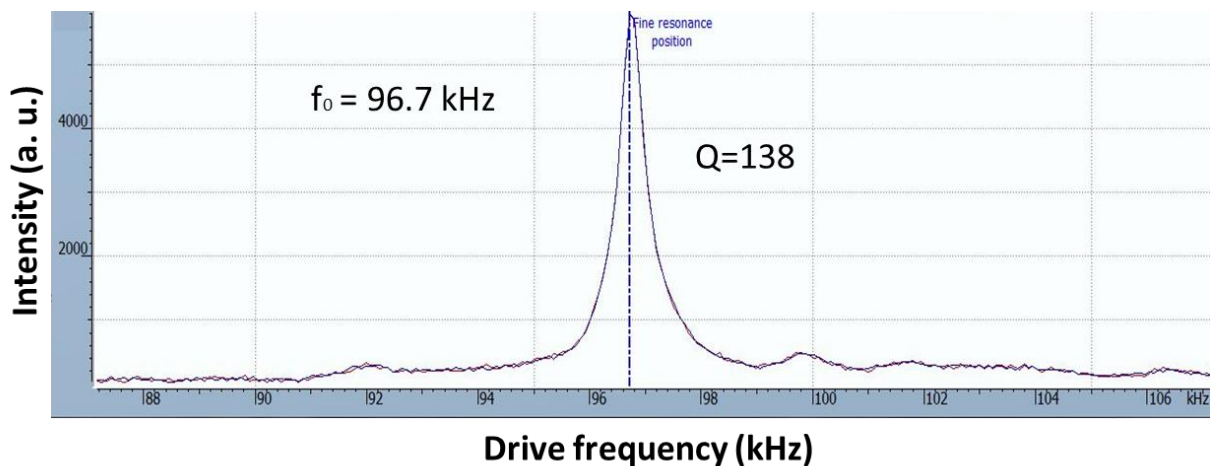


Figure 2.27. Resonance frequency of homemade AFM-TERS probe with calculated quality factor in the air.

When measurements are implemented in liquid, the heavy hydrodynamic interaction of the cantilever with the liquid results in a very low quality factor, roughly two times lower as compared to the air, and is strongly affecting the mechanical behavior of the probe. When quality factor is low, the cantilever oscillation is anharmonic and asymmetric.^{138–140}

The quality factor of our hand-made probes varies between 35 and 60 with the average rate of 45, when implemented in liquid environment (statistic made from 10 different

homemade probes). The **Figure 2.28** below shows resonance frequencies with calculated quality factors of commercial AFM silicon probe (**Figure 2.28a**) and hand-made AFM-TERS probe (**Figure 2.28b**) in liquid environment, where commercial tip exhibits resonance frequency of sharper profile and higher quality factor. For comparison, Zhang *et al.*¹³³ reported quality factor of 32 value, for handmade AFM-SECM probes in liquid environment (see **Figure 2.29**).

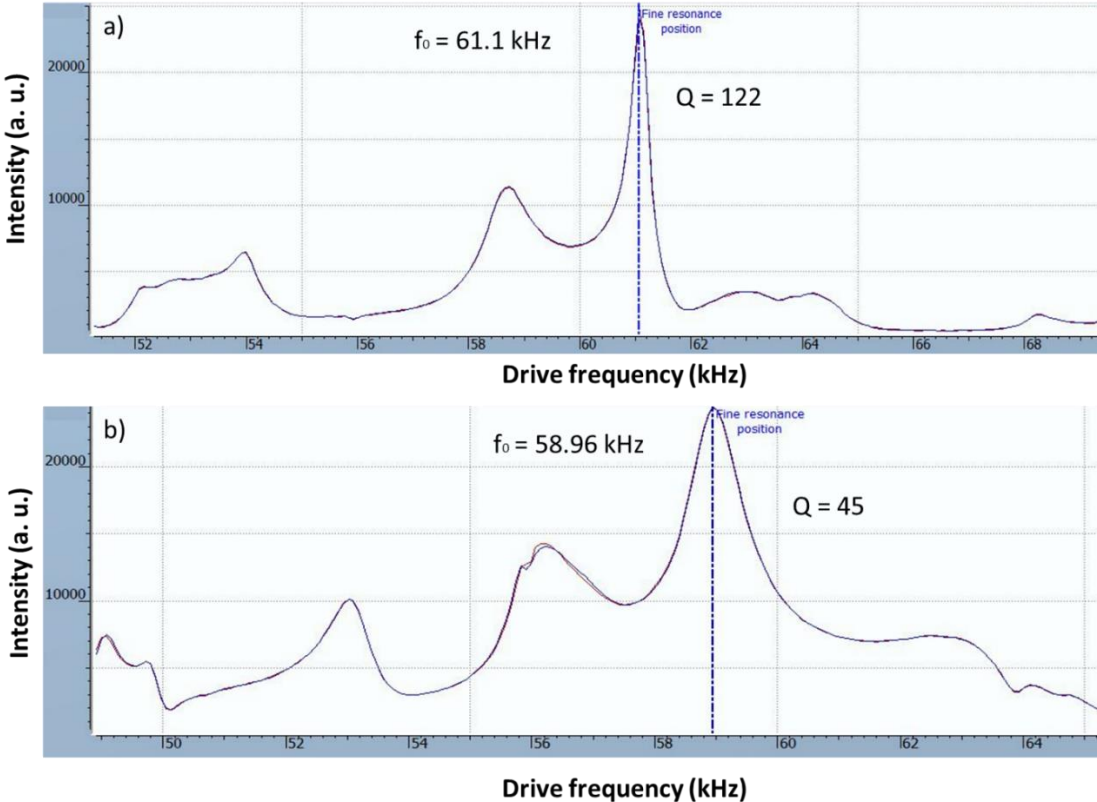


Figure 2.28. Resonance profile in water medium with calculated quality factors: a) of commercial AFM silicon probe; b) of the hand-made AFM-TERS probe.

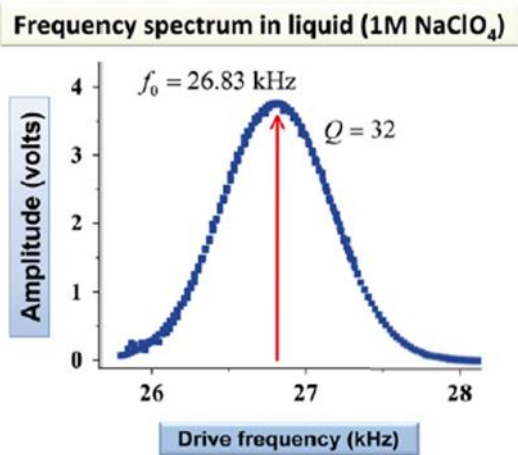


Figure 2.29. Resonance frequency of home-made AFM-SECM probe in liquid solution (aqueous 1 M NaClO₄) from Demaille’s group.¹³³

Cantilever stiffness/ spring constant - In AFM imaging the applied force on the sample should be proportional to the sample hardness. The most straightforward solution for choosing cantilever stiffness is to adjust it to the one of the sample. Therefore, low stiffness should be applied when imaging soft material or particles with low attachment on the sample surface, while stiff cantilevers with higher force constant should be used for imaging harder samples, where the morphology cannot be changed, because of applied strong lateral forces.

A wide range of cantilever spring constants are commercially available. In general, the accessible spring constants of commercial AFM probes are in the range between 0.005 N.m^{-1} and 40 N.m^{-1} . According to the scanning mode, different ranges of cantilever stiffness are used.

Contact mode is typically used for imaging samples with stiff topography, where hard lateral forces are not damaging or modifying the samples morphology. Most suitable Si AFM probes operating in this mode are made of softer cantilevers and low stiffness below 0.5 N.m^{-1} (MikroMasch® AFM silicon probes). Probe stiffness in tapping mode, with the range from $0.3 - 400 \text{ N.m}^{-1}$, depends on the sample stiffness or type of experiment. Zhang *et al.*¹³³ reported that one of the main drawbacks of hand fabricated AFM-SECM probes for tapping operation results in large cantilever size, which determines the quality and stability of AFM imaging. Therefore, high resonance frequency and low force constant are needed for optimal conditions in tapping mode. High frequency reduces the level of noise and allows fast scan rates, while low cantilever force constant enables high force sensitivity and eventually smaller proportion of the tip-sample interaction during AFM imaging.

Cantilever spring constant can be determined *via* thermal tuning (natural vibration of the cantilever in the air) and post-modeling, using known characteristics of the cantilever. This methods did not provide satisfying results of our probe. Alternatively, the spring constant can be calculated from the previously mentioned equation (2.4).¹⁴¹ Typical spring constant values calculated for the handmade probe are in the range from 220 N.m^{-1} to 342 N.m^{-1} (average value 280 N.m^{-1}) (see Table 2.5 below). Average force constant of 268 N.m^{-1} was measured for the probes which could suitably track topography of nanotriangles (NTs) as will be described in Chapter 3. Wide range of spring constant exhibits that homemade probes are fairly stiff. As a comparison, force constant of 140 N.m^{-1} were reported for AFM-SECM probes, produced in Demaille's group¹³³.

Table 2.5. Calculations of spring constant for handmade AFM-TERS probes with Young's modulus of gold wire $E = 79$ GPa and density $\rho_{Au} = 19.3 \times 10^3$ kg/m³ and precise values of probe (cantilever) features, taken for the calculation of spring constant (l = length, w = width, t = thickness).

	Spring constant range ($k_{min} - k_{max}$)	Spring constant average (k_{avg})	Functional probe spring constant
Spring constant (k)	220 – 342 N.m ⁻¹	280 N.m ⁻¹	268 N.m ⁻¹
Probe parameters (μ m)	$l = 100 - 120$ $w = 90 - 100$ $t = 5.77$	$l = 110$ $w = 98$ $t = 5.77$	$l = 111.44$ $w = 97.6$ $t = 5.77$

2.2.3 Fabrication of bulk silver Ag AFM probes

As mentioned earlier, many etching procedures have been proposed for the fabrication of TERS probes by electrochemical etching of silver wires. The varieties of etching baths included ammonia solutions, nitric acid, perchloric acid, etc. As for the gold tips, the possible types of applied voltages were AC, DC, and pulsed. Bin Ren *et al.* proposed etching procedure with pulsed chronoamperometry, by applying two different potentials for a certain time (E_1 for t_1 and E_2 for t_2).⁹⁴

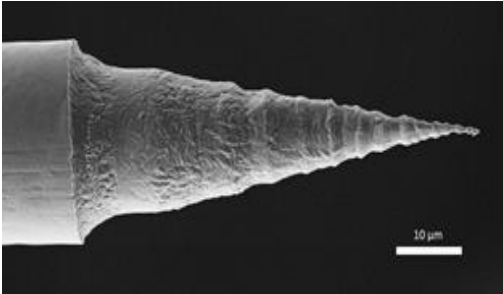
The etching procedure for manufacturing Ag probes in this work was reproduced from the work of T. Touzalin in 2017, from our group.¹⁴² The EC etching was applied with the same setup as for gold tips, using a cut-off switch in the circuit and three-electrode system (CE: Pt ring, RE: Ag wire) with the silver wire as WE.

The etching solution was composed of a perchloric acid (70 %) and absolute ethanol in the volume ratio 1:4. The 25 μ m silver wire was etched applying a DC sequence (constant potential of 4 V) and cut-off value of 20 mV. The etching process (and the associated etching sequence) is more straightforward than for gold, since no electrode passivation occurs in the selected etching bath competition.

This procedure produced etched silver TERS tips in few seconds. Since the etching procedure was not optimized, average ROC size was ranging between 50 and 300 nm. The statistics were made on 10 silver probes and evaluated with SEM imaging. During etching process, it was noticed that the tip apex size, decreased ROC down to 50 nm when using 20

mV cut-off. Therefore, the Table 2.6 below shows SEM image of etched silver probe with the 65 nm apex size, using 20 mV cut-off. This shows the progress in the etching evolution of silver wires, despite it has never been fully optimized.

Table 2.6. Evolution of probe cone shape affected by different values of cut-off at 10 μ A current range. Table shows one of the smallest radius sizes obtained on etched Ag probes (from the statistics of 10 fabricated silver probes).

SEM image	Cut-off (mV)	Radius (nm)
	20	65

After the etching step, all tips were rinsed in absolute ethanol and distilled water, then placed in a glove box filled with argon for tip protection from the oxidation and contamination.

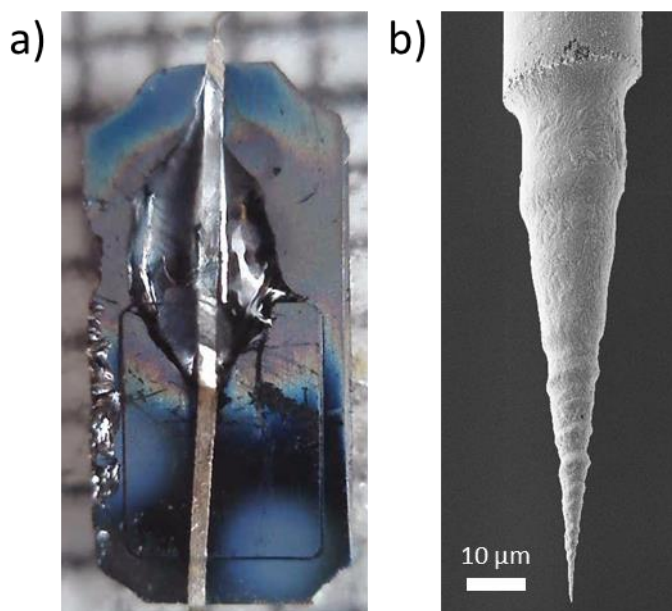


Figure 2.30. Bulk metal AFM-TERS probe made from silver wire: **a)** glued silver wire partially flattened and bent at 90° (wire facing up) on a commercial AFM chip (before etching); **b)** SEM micrograph of the etched silver wire.

Conclusion

This chapter covered the development of TERS-active AFM probes to be used under electrochemical conditions. The number one solution implemented by most research groups consists in coating commercial silicon probes with plasmonic materials, either by physical or electrochemical deposition. Some refinements aiming at fine tuning the plasmonic resonance properties of the TERS probe were proposed in the literature, e.g. FIB milling of tip apex to produce co-axial geometry, grafting of nano-objects at the apex of the tip, but usually at great time and cost expenses. The most straightforward solution consist in deposits of rough metallic layers (corrugated tips) to generate multiple hotspots. If corrugated tips are reported to produce the higher signal enhancements, their mechanical and chemical stability in liquid medium is uncertain. Combination with other metals, dielectric layers or organic molecules, has been proposed to improve the adhesion and stability of the plasmonic layers.

Although LISE is equipped with physical deposition systems, the manufacturing process chosen in this work has been motivated by: **I)** the robustness of bulk metal AFM probes to wear as attested by the commercial success of such solid metal probes for electrical measurement (Pt probes produced by RMN, recently purchased and distributed by Bruker), **II)** the possibility to manufacture such probe “in-house” at minimum cost as evidenced Demaille’s group, **III)** the experience of our group in LISE to electrochemically etch gold wires to produce TERS active tapered tips, useable in STM or shear-force AFM mode.

If the 4-steps micro-manufacturing process including shaping, gluing on silicon chip and etching of gold wire, has been mastered and optimized quite rapidly in this work, the fine tuning of the cantilever geometry (length, width, thickness, angle) to show high reflectivity, to enable automatic detection by the AIST AFM-system (1064 cm^{-1} AFM registration laser), and above all, to display mechanical properties, compatible with intermittent contact mode (tapping mode) implementation turned out to be challenging.

Getting inspiration from commercial silicon probes, designed for tapping mode (fast imaging with reduced noise), probes with $\sim 110\text{ }\mu\text{m}$ long flexible cantilever, showing flexural resonance frequency around 100 kHz with high quality factors, could be designed by playing with the pressure applied to flatten a $25\text{ }\mu\text{m}$ -diameter metal wire (into a $100\text{ }\mu\text{m}$ wide and $5\text{ }\mu\text{m}$ thick metal beam), but however with much higher stiffness ($> 200\text{ N}\cdot\text{m}^{-1}$). The exploration of various cantilever stiffness (playing with flattening and positioning of the cantilever on the

chip) has been limited by instrumental constraints, only relatively short cantilever being identified by the detection scheme (registration laser, tip holder and photodiode mounted on step-motors) in the AFM head of the TERS-ready AIST/Horiba system. Also by aiming at shorter cantilever, fluid dragging impacting operation in liquid is limited.

Finally, the length of the shaft connecting the tip to the cantilever, also called the “nose”, is critical to achieve good performances in tapping mode. Despite our effort, in controlling the etching process by micro-positioning the nose in a small drop of etching solution, tip height remained comparable in size with the cantilever dimensions (around 10 μm for commercial probes). Optimization of the immersion of the bent part of the wire (up to the point where the cantilever arm almost touches the etching solution surface), as proposed by Demaille, could not be achieved without impacting the quality of the etching process (of primary importance for the TERS activity of the probe).

Both, the high stiffness and the relatively high tip height of the manufactured probes, constitutes a bottleneck to the characterization of weakly bound nano-objects especially in liquid, as will be presented in the following chapter, along with the evaluation of their TERS activity.

Chapter 3 - Performances of home-made TERS probes

Introduction

This third chapter will be dedicated to the evaluation of the imaging performances and of the TERS activity of the AFM probes developed in Chapter 2.

The home-made probes, developed from bulk metal (wires), had to meet characteristics intrinsic to the AFM imaging mode chosen in this work, i.e. to be able to operate in semi-contact mode (tapping mode), to approach, stabilize on a sample surface and *in fine* to image weakly bound physisorbed nano-objects, both, in the air and also in liquid. The imaging sensitivity, defined as the ability to detect and image nano-features on a sample, relies on the AFM probe characteristics and on the effectiveness of the tip-sample distance control. This control is also of prime importance in TERS, as the near-field signal amplitude decreases exponentially with the distance and as any contamination of the tip subsequent to harsh contacts with the sample may compromise the analysis. If the cantilever reflectivity (amount of light received by the photodiode), the resonance characteristics (frequency, quality factor), the sharpness of the tip apex and the imaging conditions (scan rate, scan range, feedback parameters) are critical parameters, the SPM microscope performances can also dramatically affect the structural/compositional imaging sensitivity. Two different microscopes developed by AIST, an inverted microscope with an open piezo stage (PI) and an upright microscope using a piezo-stage developed by AIST, were used in this study. The inverted microscope shows a much lower mechanical stability than the upright one due to its open configuration, but still its use was initially favored, because of the ease of the optical coupling between the tip apex and the Raman laser (probe) for TERS implementation in liquid.

In this new chapter, we will first introduce the two microscopes configurations and the specific requirements for TERS implementation in air and liquid. We will then present the imaging performances (sample structure and composition) of the TERS-active AFM probes in the air and on model samples prepared in house (nanotubes, spherical nanoparticles and nanotriangles), using the two configurations. The sample preparation will be extensively detailed when necessary. We will then conclude on the performances of the TERS-AFM probes in liquid, showing AFM mappings and the first implementations of TERS in liquid.

3.1. AFM-TERS configurations

The most frequently used TERS ready setups using AFM feedback for the tip-sample distance control are displayed on **Figure 3.1**, i.e. bottom illumination (on an inverted microscope) and side or top illumination (on an upright microscope). Each of these configurations have benefits, drawbacks and specific requirements in terms of light focusing (type of objective lens) and light polarization (linear, radial), and of sample preparation (opaque vs semi-transparent).

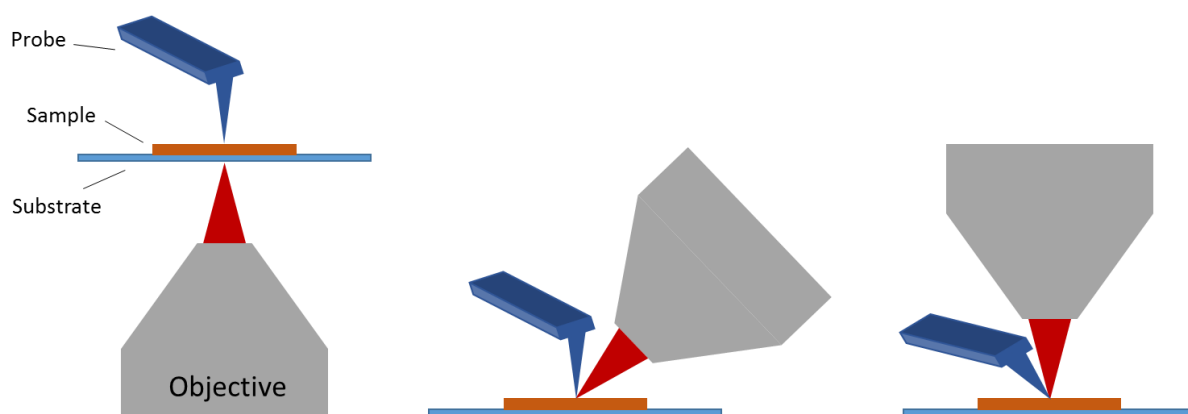


Figure 3.1. Scheme of three commonly used setups for (AFM-)TERS applications; **a)** bottom-illumination; **b)** side-illumination; **c)** top-illumination. An extra configuration using parabolic mirror is not presented here as not often used.

Side illumination/upright configuration - The TERS-ready configuration in reflection is optimized for near-field measurements on any kind of sample (opaque samples) allowing a broad range of application but can also be used for co-localized AFM and confocal Raman imaging. The setup combines the use of long-working distance objectives (with NA up to 0.7) positioned at an angle of 60° respectively to normal plan of the sample. This angle allows the electric field of a linearly polarized laser light to be aligned along the shaft of the tip while minimizing collection of specular light therefore ensures a maximum enhancement of Raman signal and a signal collection efficiency at the tip-sample junction.¹⁴³ However, TERS measurements using this configuration constitute a major challenge when implemented in liquid due the distortion of the optical path at the air-liquid interface.

The implementation in liquid of AFM-TERS also brings additional complications related to the AFM feedback mechanism, as solutions have to be developed to suppress or compensate for the optical distortion at the air-liquid interface for both the AFM feedback laser (aligned on the cantilever) and the Raman probe (focused on the tip apex). The AIST-Horiba system

uses for measurements in liquids an AFM probe holder carrying a lens to compensate for the different liquid/air refractive indexes, enabling proper focusing of the AFM laser on the cantilever. This plano-convex lens (6 mm diameter, 2 mm thick) extends on a distance much larger than the probe cantilever preventing the use of water dipping objective with short working distance as described in Touzalin's work.³⁵ Note that in the TERS-ready system from NT-MDT, the AFM head carrying both the objective lens and the AFM probe enabling the use of a water-dipping objective through which both the AFM and the Raman lasers are focused to the cantilever and the AFM tip apex respectively as described in Chapter 1. This specific design may impact though the overall stability of the AFM measurement.

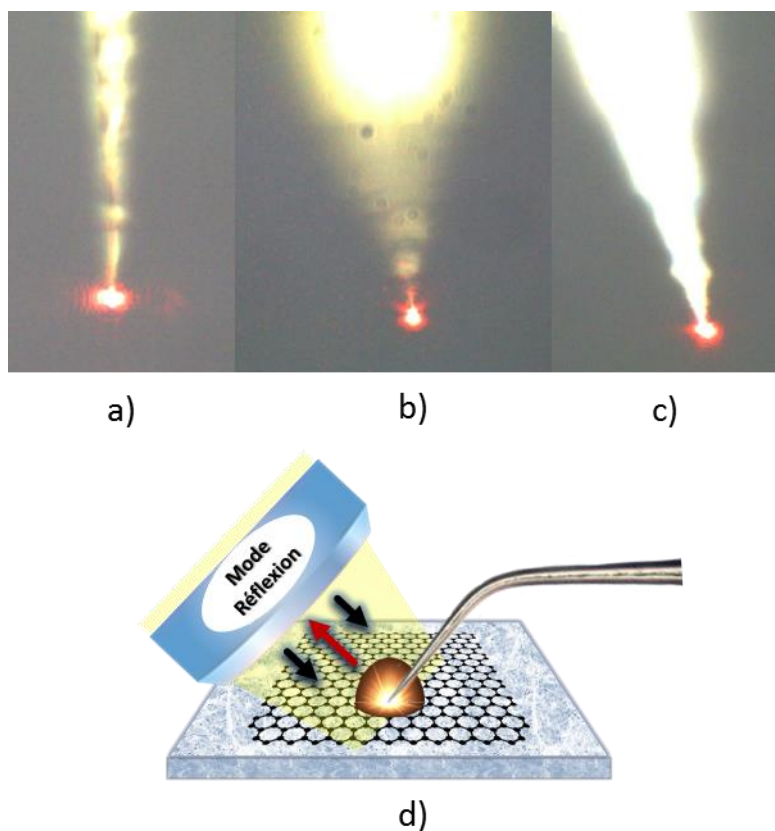


Figure 3.2. Laser alignment in the ambient on the tip apex of homemade probe with different tapered profiles (gold tip with small (a) and larger (b) “opening” angle) and silver tip (c)), using a side illumination through a long distance dry 100x dry objective (Mitutoyo MY100X-806, 100X Plan Achromat WD = 6mm, NA = 0.7) represented on scheme (d) (depiction of the upright microscope configuration with side illumination).

Bottom-illumination - The main advantage of bottom-illumination is the efficient excitation/collection of the Raman signal, associated with the possibility to use short working distance objective with high NA¹⁴⁴, like oil immersion objectives. The free space below the probe also allows a more straightforward implementation of optical coupling in liquid environment. The alignment and focusing of the laser on the tip apex can be achieved even

through homemade semi-transparent gold substrates as demonstrated in **Figure 3.3a**. Such substrate enables the TERS study on the inverted-microscope of molecular monolayers of thiol based derivatives self-assembled on gold (**Figure 3.3b**). The gap-mode created at the tip-sample junction provides maximum enhancement of the TERS signal.

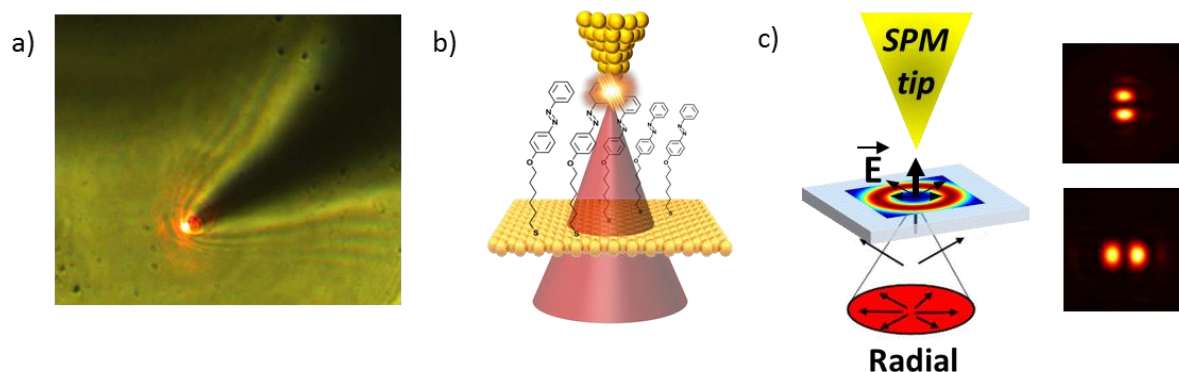


Figure 3.3. Inverted TERS configuration with bottom illumination - **a)** laser alignment and focusing on the homemade gold tip is achieved in the air through a semi-transparent gold sample using a bottom illumination and optical access; **b)** thioazobenzenes derivatives assembled on semi-transparent gold thin films can be studied by TERS in the so-called gap-mode (molecule at the metal/metal junction; **c)** to maximize the contribution of the longitudinal component of the electric field along the shaft of the tip vs its in-plane component, a radial polarization kit combined with a high NA objective lens can be used, giving rise to a typical doughnut shapes which the X and Y contribution of which can be visualized using polarizers.

The illumination of the tip apex through the transparent / semi-transparent substrate may affect the TERS performance as the far-field contribution is more difficult to cancel out when compared to side illumination. This is especially true when using linearly polarized Raman probes since the principal component of the electric field at the output of the objective lens is aligned in the sample plane and not along the shaft of the vertical tip in close proximity. Alternatively, a radial polarization kit, providing a longitudinal component of the electric field aligned with the tip apex (after laser focusing through an objective of high numerical aperture) can be used to maximize the Raman signal enhancement at the tip-sample junction (TERS). Radial polarization converters creates a laser beam with a typical doughnut shape in the sample plane, whose contributions in X and Y sample planes can be visualized using polarizers as seen on the **Figure 3.3c**.

The inverted configuration was used as an easier alternative to the upright configuration with the illuminated tip below the sample for possible further development of (EC-) TERS measurements in liquid.

3.2. AFM imaging performances in the air and in liquid

The imaging performances of the homemade TERS active AFM probes were first evaluated in the air and in the semi-contact mode on various hard nanostructures, i.e. thin gold films (100 nm) deposited directly on flat mica substrates (or glass coverslips) by evaporation, and decorated with nano-objects of different size and shape: multi-walled carbon nanotubes (MWCNTs, 755117-1G, length: 300-2300 nm and diameter: 0.7-1.1 nm, Sigma Aldrich), nanoparticles composed of iron oxides (Fe_2O_3 , 12 nm) or of gold (up to 60 nm) and gold nanostructures, i.e. nanotriangles and hexagons (10 to 25 nm). The nano-objects were deposited from colloidal solutions by either drop-casting or spin-coating. The synthesis protocols of colloids will be briefly recalled.

The properties of the tips (sharpness: radius of curvature and opening angle) were assessed indirectly through the dimensions of the imaged objects (high vs width) extracted from the measurements and their comparison to dimensions deduced from AFM analyses using commercial AFM tips (Mikromash silicon tip, NSC14/AIBS, 160 kHz, 5 N/m, RC: 8nm, full tip cone angle: 40°) or from SEM analyses.

3.2.1. Tip properties and convolution effects

The choice of AFM tip is critical for the successful and accurate tracking of topography, especially when scanning in different AFM modes (contact, intermittent/semi-contact/tapping and non-contact). Probe features as tip radius of curvature, tip opening angle and tip geometry determine the accuracy of the imaging process (common radii of commercial AFM probes lay between 10 and 100 nm in a conical or pyramidal shape). Two most commonly observed artifacts in AFM images are “profile broadening” effect, from the tip-sample convolution, and “height lowering” effect due to the elastic deformation of the imaged objects. Hard nano-objects were preferred in the study to soft ones to minimize the height lowering effect.

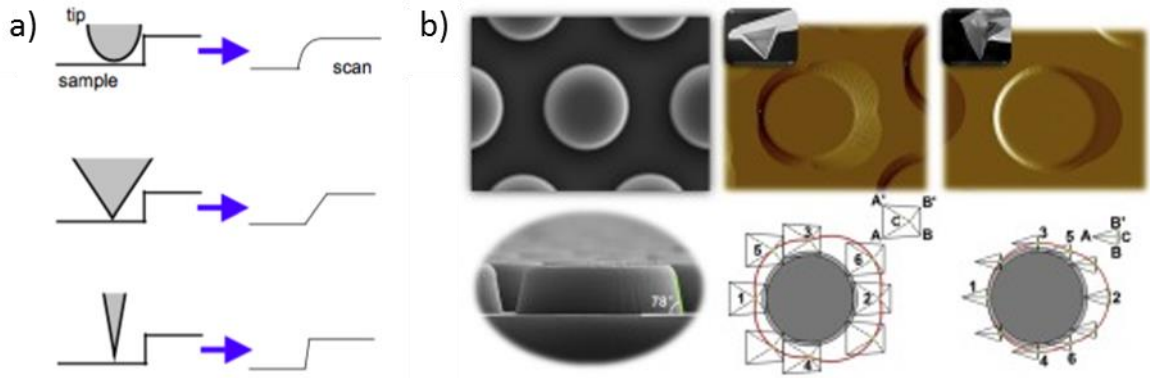


Figure 3.4. Convolution effects – a) influence of the tip properties (geometry, cone angle), **b)** from left to right - Top view SEM image of rigid sapphire cylinder protrusions; plane view AFM image of cylinder obtained by pyramid tip and quadrilateral pyramid tip. Images adapted from [145].The AFM scan was run from right to left.

Profile broadening of the imaged objects are due to tip-sample convolution (see **Figure 3.4a**) and can be generally minimized by using smaller tip radius and lower cone angle providing higher lateral resolution. More accurate topography is obtained when the objects on the surface have small height and ratios with smaller sidewalls angles as compared to the tip. Imaging artifacts will translate differently depending on the tip geometry and scan direction (see **Figure 3.4b**).

Three different situations can be distinguished depending if the tip radius R is much smaller than the feature radius r , if they are of similar dimensions and if the tip radius is much larger.

- When the tip radius is much smaller than the surface feature curvature radius $r - R \ll r$, the object lateral width can be calculated from the equation below, including half cone angle θ :

$$r_c = r(\cos \theta + \sqrt{\cos^2 \theta + (1 + \sin \theta)(-1 + \tan \theta / \cos \theta) + \tan^2 \theta}) \quad (3.1)$$

The imaged object width is broadened by the $2(r_c - r)$, while the height is conserved ($2r$). In this case, the convolution effect is the smallest, which results in AFM image as close to the real topography.

- When the tip radius R is approximately equal to the feature curvature radius $R \approx r$, the displacement of the tip along the surface of the object can be approximated by the radius sphere $R + r$. In that case, imaged object lateral measurements are:

$$r_c = 2\sqrt{Rr} \quad (3.2)$$

with the comparative object height:

$$H = r \left[1 - \sqrt{1 - \frac{r_c^2}{(R+r)^2}} \right] \quad (3.3)$$

- When the tip radius R is much larger than the feature curvature radius $R \gg r$. This part illustrates the most common issue of homemade probe manufacturing process. In this case, AFM images might be highly inaccurate as seen on the **Figure 3.5** below. The size of an artifact can be calculated from the equation (3.4)^{146,147}:

$$W = \sqrt{8hR} \quad (3.4)$$

where W is the objects width, h the object height and R the tip radius. The tip radius (R) can be calculated from the apparent dimension of the object image as:

$$R = w^2/8h \quad (3.5)$$

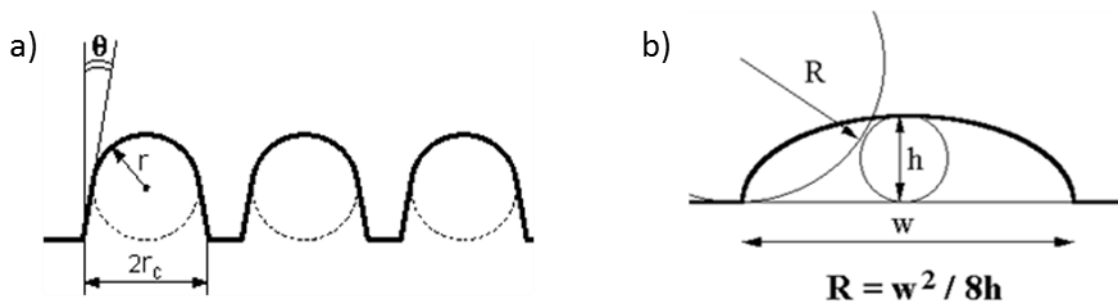


Figure 3.5. Convolution effects – a) Tip radius is much smaller than the surface feature curvature radius $r - R \ll r$ (only the imaged object high is inaccurate); b) Tip radius R is much larger than the feature curvature radius $R \gg r$ (both width and high can be inaccurately measured). Images taken from [148].

3.2.2. Imaging of nano-objects in the air in semi-contact mode

The imaging performances of the bulk gold AFM-tip where first evaluated in semi-contact mode (“tapping mode”) on the “higher performance” SPM microscope available in our lab (AIST *SmartSPM*), then on the inverted microscope (AIST *Combiscope*) more suitable for AFM-Raman coupled measurements in liquid. Nano-objects with various size and shapes were deposited on flat gold surfaces to be imaged.

Gold substrates - Gold substrates were produced either by thermal evaporation of non-transparent 100nm thick gold layers on mica substrates or of semi-transparent thin gold layers (10 nm), on titanium (sputtered: 2 nm) on a glass coverslip (VWR Avantor, pure white Hydrolytic Class 1 glass, 30 mm diameter, 130 μm thick), optimized for the inverted

configuration. **Figure 3.6** below shows the ability of the home-made AFM-tips to track and reveal in tapping mode the topography of both gold surfaces. The thick gold sample show surface inhomogeneity with large surface grains (roughness - Root Mean Square (RMS): 1.3 nm) whereas the thin gold sample (probed on the inverted microscope) look extremely smooth (RMS: 0.7 nm). The roughness of thick gold samples is still compatible with the observation of nanoobjects as will be demonstrated below. Note that despite the very thin layer of gold, semi-transparent substrates show an electrical continuity and a low resistivity (30 – 40 Ω) compatible with the implementation of electrochemical measurements.

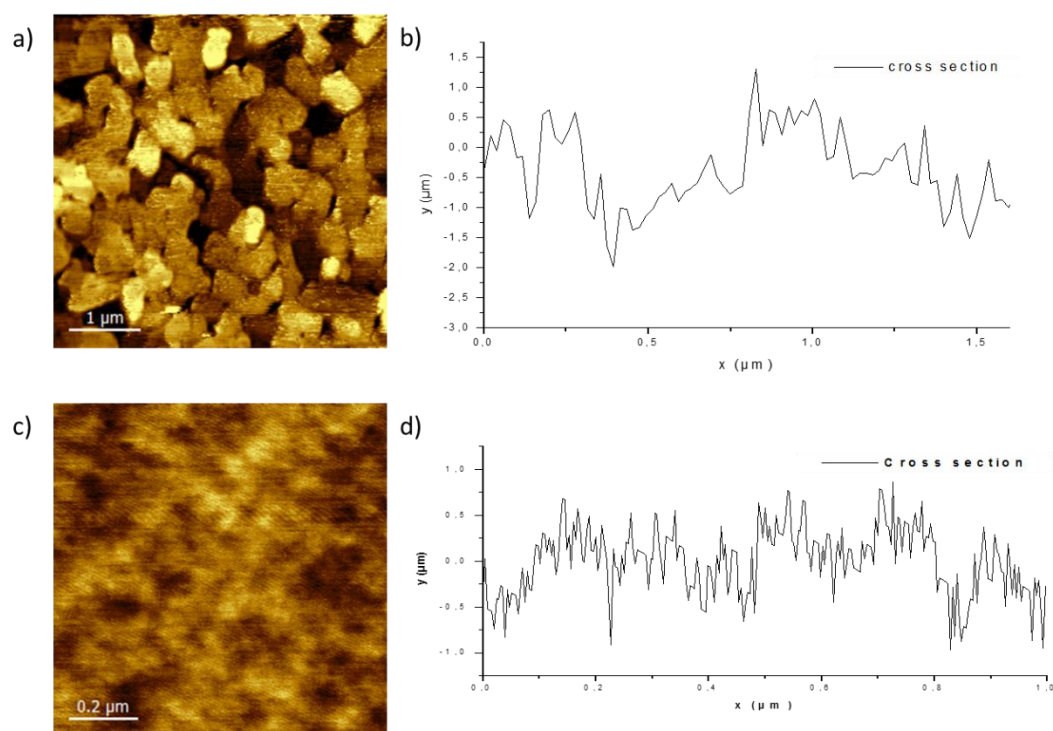


Figure 3.6. Homemade probe performance – a) AFM topography of 100 nm thick gold film on mica and associated cross section **(b)** (RMS: 1.3 nm). AIST *SmartSPM*, scan range $5 \times 5 \mu\text{m}^2$; resolution $256 \times 256 \text{ px}^2$, scan rate 0.8 Hz, resonance frequency 185 kHz. **c)** AFM topography of 10 nm thick gold film on glass (2 nm titanium adhesion layer) and associated cross-section **(d)** (RMS: 0.7 nm). AIST *Combiscope*, scan range $1 \times 1 \mu\text{m}^2$; resolution $256 \times 256 \text{ px}^2$, scan rate 1 Hz, resonance frequency 70.5 kHz.

Large nanoplates – Gold nanotriangles (NTRs) were studied as a possible model sample/ functional nanomaterial for *ex situ* TERS study (see further down) and for nanoscale redox mapping by EC-TERS (see Chapter 4) once functionalized with redox active SAMs. These thin nanotriangles with large contact surface (strong Van der Waals interaction) are less subject to displacement or removal upon possible interaction with the AFM tip during non-suitable imaging conditions (tip oscillation amplitude and frequency, feedback parameters...).

Colloidal samples of Au-NTrs were prepared following the procedure of P. Van Duyne *et al.*¹⁴⁹. Single crystal gold nanoplates (equilateral triangles with possibly some truncated edges and hexagons) have been synthesized from reduction of gold salt (HAuCl_4) by lemongrass. Chopped lemongrass (50 g) was boiled in 250 mL of distilled water for 5 min. After cooling down to room temperature, 5 mL of aliquot was added to 45 mL of 1 mM HAuCl_4 . The solution was left to react for approximately 24 hours at the room temperature with no stirring; the solution changed color from light yellow to dark purple/brown. The solution was purified by successive centrifugation (a 25 mL aliquot, for 10 minutes at 5000 rpm), removal of supernatant and addition of 25 mL of distilled water. The process was repeated twice. A 100 μL aliquot of purified gold nanoplate solution was drop-casted on pre-cleaned substrates (glass coverslips, gold on glass, gold on mica, ITO) and placed in the oven (80 °C) to evaporate the solvent. Samples are then sonicated in ethanol and in distilled water for 10 min to remove possible reactions products and contaminants. Au NTrs surface were then analyzed by SEM to evaluate their dimension and also their surface distribution. The drop-casting conditions (concentration and volume of NTr colloidal solution) were adapted to produce surface with isolated NTrs. SEM images show individual NTrs but also piled structures. The average lateral dimensions of NTr, obtained by SEM, are between 0.5 and 2 μm as shown on **Figure 3.7**.

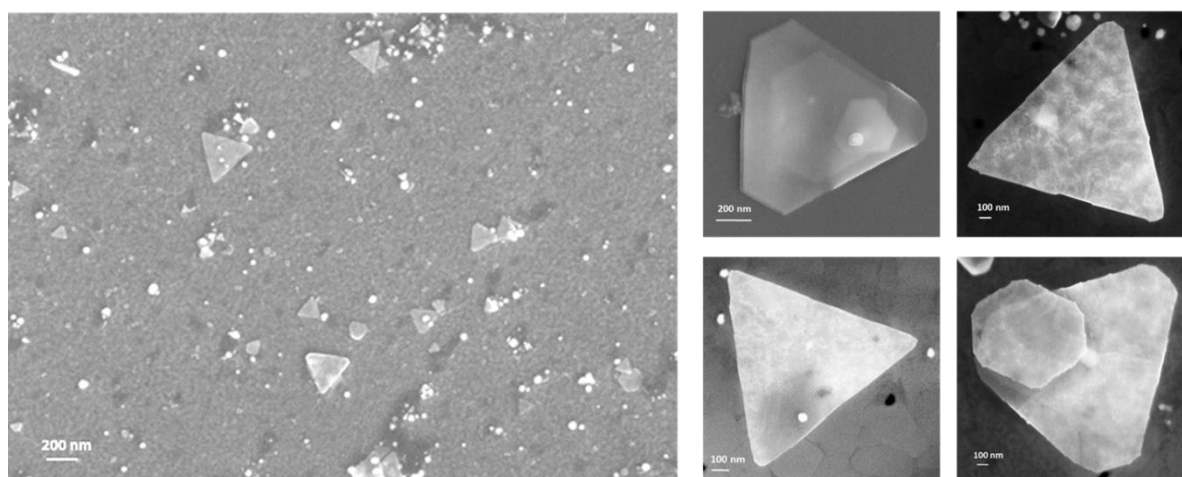


Figure 3.7. SEM Images of gold nanotriangles (equilateral NTrs with truncated edges) deposited on gold with an average size between 0.5 – 2 μm (SEM parameters: acceleration voltage 10.00 kV, *InLens* detector, WD = 4.5 – 5.1 mm, magnification= 50 – 100 K).

AFM imaging of gold NTs decorated substrates were then successfully achieved in tapping mode with the bulk gold AFM probes revealing both triangles and hexagons with average width between 0.2 – 2.1 μm and height from 10 to 25 nm as displayed in **Figure 3.8** and **3.9**.

Such dimension were confirmed using μ Mash commercial probes. Different resonance frequencies were screened and initially tested for imaging in tapping mode, resonance frequency below 100 kHz gives usually the best imaging performances, although higher frequency were sometimes picked when landing process turn out to be tedious (piezo scanner oscillation) as exemplified on **Figure 3.10, 3.12, 3.25**.

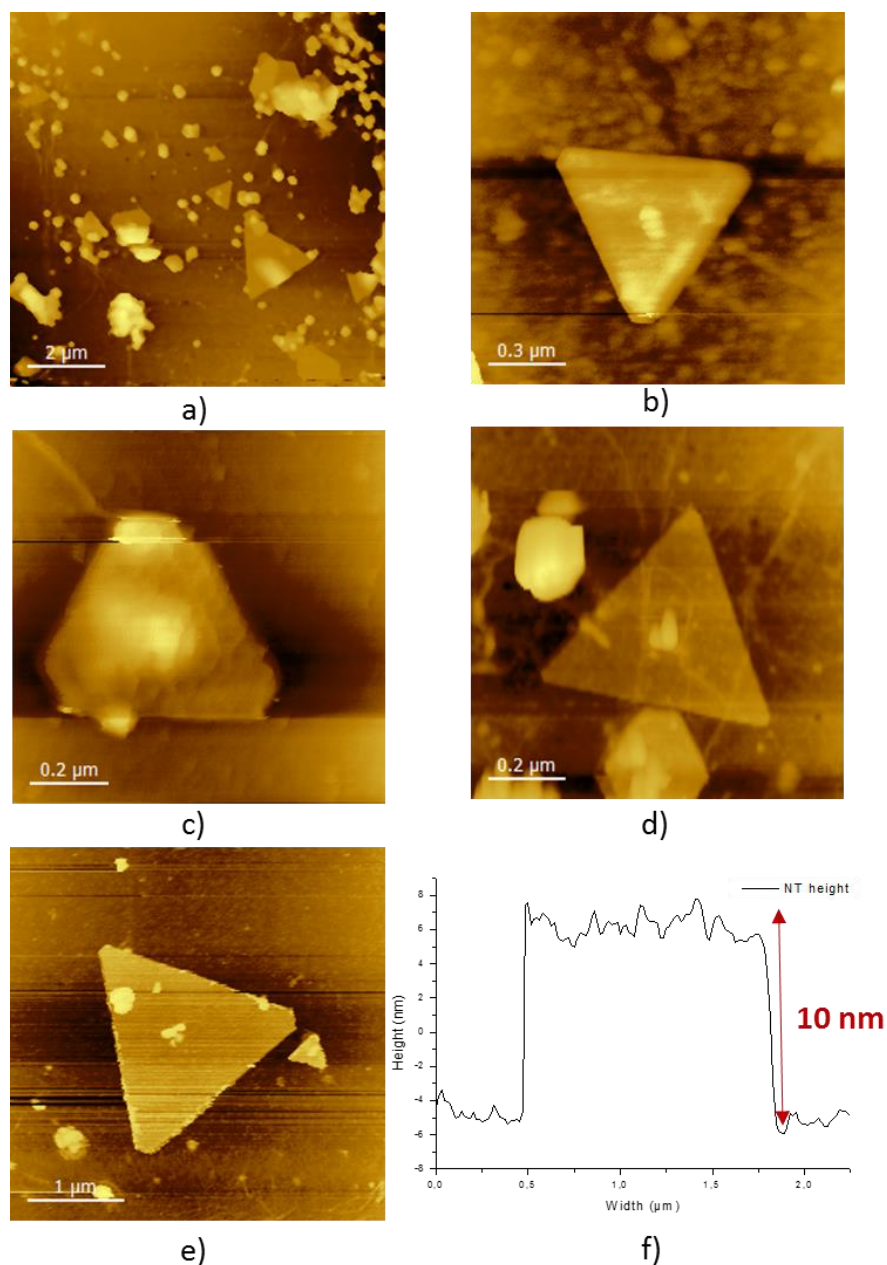


Figure 3.8. Homemade probe performance - AFM topography in tapping mode in the ambient of gold nanotriangles on gold (*SmartSPM* upright microscope, resolution 256 x 256 px², scan rate 1.0 Hz); **a)** resonance frequency 79 kHz, scan range 10 x 10 μ m²; **b)** resonance frequency 75 kHz, scan range 2 x 2 μ m²; **c)** resonance frequency 54 kHz, scan range 1 x 1 μ m²; **d)** resonance frequency 69 kHz, scan size 1 x 1 μ m²; **e)** resonance frequency: 64 kHz, scan range 5 x 5 μ m², and **f)** cross section of 10 nm height and dimension size 2.4 μ m taken from (e).

Gold hexagons were also imaged, revealing height between 10 and 25 nm similar to the one of NTRs, with dimensions around 0.5 μm (see **Figure 3.9a** and **3.9b**). Note that the processing of the image (flattening using n order polynomial fitting) produced with the homemade tip, is not as effective as for the commercial tips, i.e. residual slope and dark background around the nanoobjects, implying that the sample tracking on the fast scanning axis (X) is not perfect at the used scanning rate (1Hz).

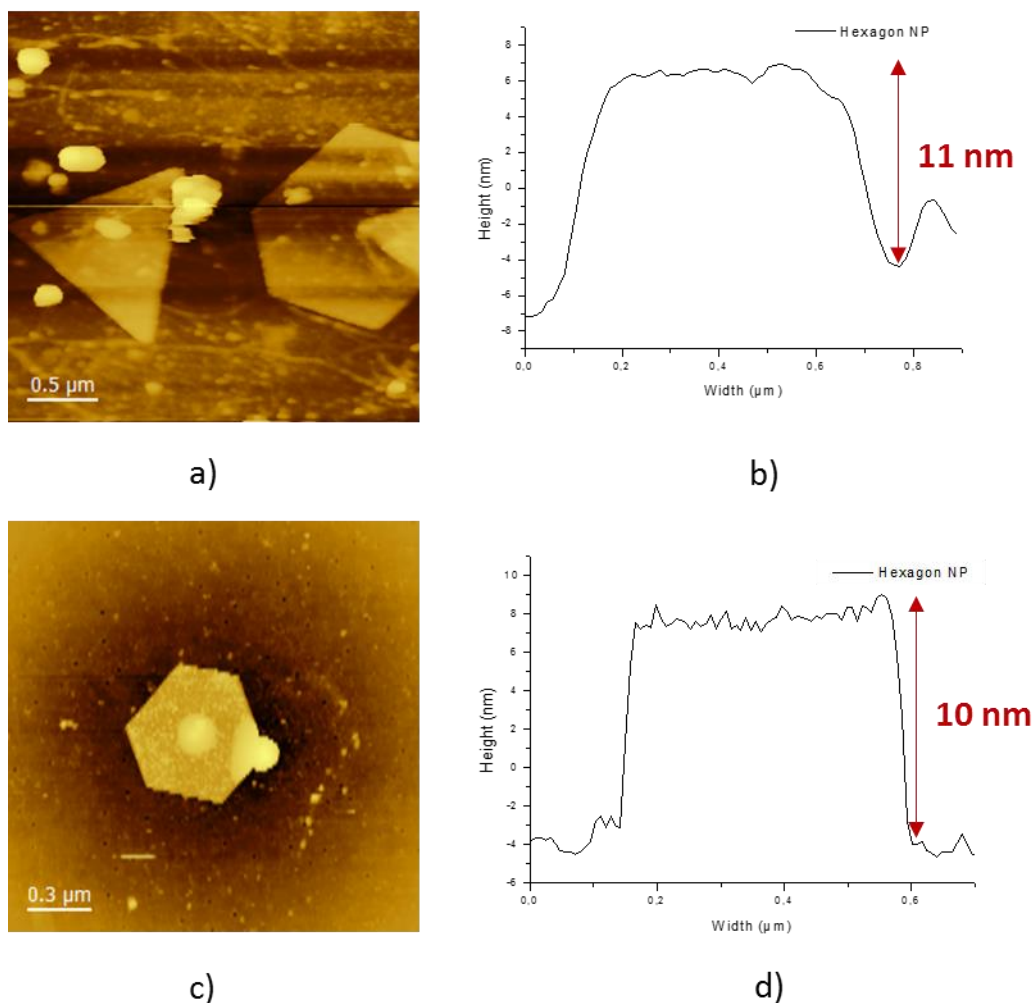


Figure 3.9. Homemade probe performance - **a**) AFM topography of gold hexagons on glass in tapping mode (*SmartSPM*) in the ambient - **a**) homemade tip with associated cross section **(b)** of NTR and hexagon width 1.3 μm and height 11 nm (scan rate 1.0 Hz, scan size 3 x 3 μm^2 , resonance frequency 75 kHz); **c**) topography obtained with commercial tip $\mu\text{Mash NSC14}$ (scan rate 1.0 Hz; scan size 2 x 2 μm^2 ; resonance frequency 183 kHz) with associated hexagon cross section **(d)** showing similar height as acquired with homemade probe (10 nm).

Spherical nanoparticles (NPs) – Spherical nanoparticles of different composition and size (iron oxides and gold nanoparticles) were then imaged to evaluate the ability of the homemade probes to image weakly bound objects. These particles of different sizes ranging from 12 to 60 nm were also used to evaluate the convolution effect associated with the tip

properties. Gold colloidal nanoparticles with increasing sizes (~ 20 & ~ 60 nm) were synthesized following a seeded growth protocol developed in LISE^{150,151}. The AFM images obtained on the AIST *Combiscope* in tapping mode reveal different particle sizes (H: 60 nm, W: 200 nm and H: 25 nm, W: 130 nm) with large ratio W/H and a difficulty to track properly the particle contour on the fast axis (X) of the scan as suggested by the elongated shape of the gold particle on the X axis on **Figure 3.10c**.

Iron oxide NPs with an average size of 12 nm were obtained from Phenix lab in Sorbonne University (E. Dubois). *Magnetic colloidal suspension of maghemite* ($\gamma\text{-Fe}_2\text{O}_3$) nanoparticles, were synthesized by co-precipitation of iron (II) and iron (III) in alkaline medium, forming a mixed valence iron oxide ($\text{Fe}^{\text{II}}\text{Fe}^{\text{III}}_2\text{O}_4$: magnetite) which can be oxidized in a solution of $\text{Fe}^{\text{III}}(\text{NO}_3)_3$ at high temperature into maghemite $\gamma\text{-Fe}^{\text{III}}_2\text{O}_3$.¹⁵² AFM images are reported on **Figure 3.10**. Large W/H ratio 3-7 are also observed for these smaller particles.

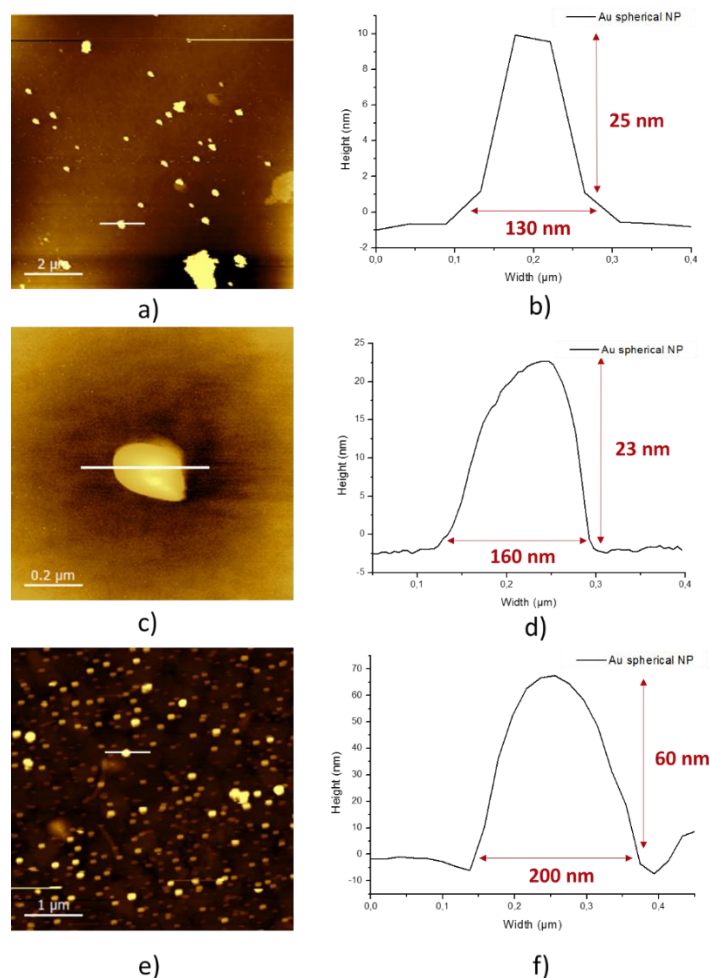


Figure 3.10. Homemade probe performance - AFM topography of gold spherical nanoparticles (NPs) in tapping mode (*Combiscope* inverted microscope) in the ambient with resolution $256 \times 256 \text{ px}^2$ and scan rate 1.0 Hz. **a)** $10 \times 10 \mu\text{m}^2$ AFM image (resonance frequency 91 kHz) and associated cross-section, **(b)** 25 nm height, 130 nm

width, **c**) $1 \times 1 \mu\text{m}^2$ AFM image of a single NP (resonance frequency 164 kHz) and associated cross-section **(d)** 23 nm height and 160 nm width, **e**) $10 \times 10 \mu\text{m}^2$ AFM image (resonance frequency 91 kHz) and associated cross-section **(f)** (60 nm height and 200 nm width).

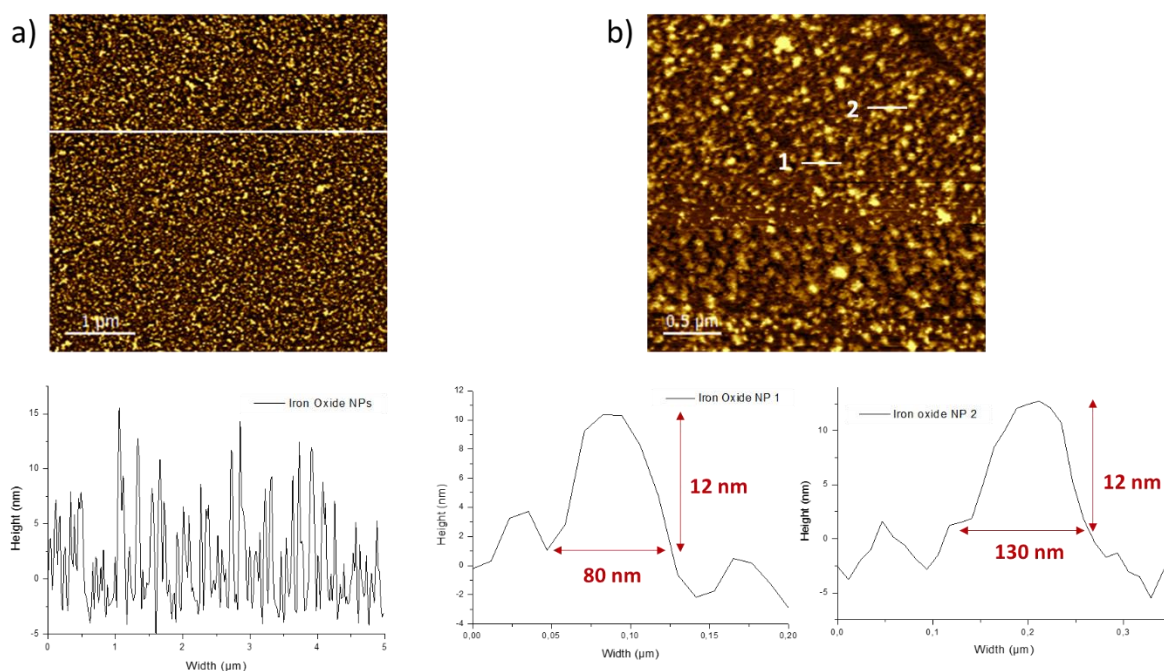


Figure 3.11. Homemade probe performance - AFM imaging in tapping mode (*SmartSPM* upright microscope) in the ambient of iron oxide NPs deposited on gold: **a**) AFM image $5 \times 5 \mu\text{m}^2$ (resolution $256 \times 256 \text{ px}^2$, scan rate 0.8 Hz, resonance frequency 40.3 kHz) and cross section with the height range from 10 – 17 nm; **b**) AFM image $3 \times 3 \mu\text{m}^2$ and cross sections revealing large convolution effects on the extracted width of the two particles (80-130 nm).

Carbon nanotubes (CNTs) on gold – Thin multi-wall carbon nanotubes (Sigma Aldrich, 755117-1G) were used without further purification, dispersed into solution and deposited onto a gold surface by spin coating (approximate speed 1000 rpm), CNTs could be detected using the handmade probes in semi-contact mode as seen in **Figure 3.12**. The AFM images ($5 \times 5 \mu\text{m}^2$ and $1 \times 1 \mu\text{m}^2$) reveals elongated objects between 2 and 2.5 nm high coherent with the CNTs characteristics provided by the manufacturer and with a width around 40 nm.

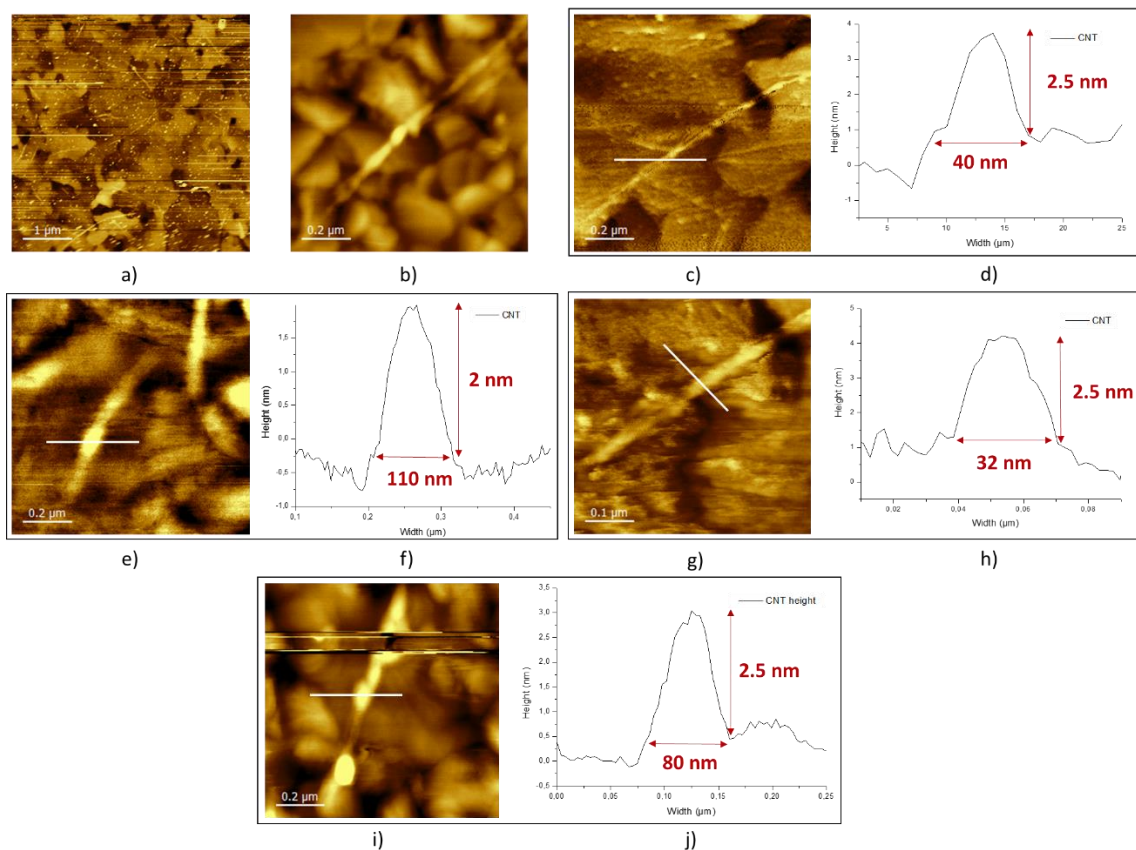


Figure 3.12. Homemade probe performance - AFM topography of CNTs on gold in the air (*SmartSPM* upright microscope); tapping mode, resolution $256 \times 256 \text{ px}^2$, scan rate 1.0 Hz: **a)** scan size $5 \times 5 \mu\text{m}^2$, resonance frequency: 96 kHz, **b)** scan range $1 \times 1 \mu\text{m}^2$, resonance frequency 104 kHz; **c)** scan size $1 \times 1 \mu\text{m}^2$, resonance frequency 96 kHz with associated CNT cross-section (d) (2.5 nm height, 40 nm width), **e)** scan range $1 \times 1 \mu\text{m}^2$, resonance frequency 57 kHz with associated CNT cross-section (f) (2 nm height, 110 nm width), **g)** scan range $0.5 \times 0.5 \mu\text{m}^2$, resonance frequency: 96 kHz with associated CNT cross-section (h) (2.5 nm height, 32 nm width), **i)** scan size $1 \times 1 \mu\text{m}^2$, resonance frequency 118 kHz with associated CNT cross-section (j) (2.5 nm height, 80 nm width).

Convolution effect – As mentioned earlier the ability to accurately resolve the size and shape of nano-objects strongly depends on the tip characteristics and possible convolution effects.

Aspect ratio A between the object height h and width w $A=h/w$ can be calculated to assess the effect of the convolution on the imaging; low and high A correspond respectively to higher and lower convolution error. When considering tip radius much larger than the feature curvature, small objects are more likely to show larger convolution error.^{153,154} Aspect ratio on 10 to 20 imaged surface objects and tip radii were calculated from the apparent dimension of the imaged object (see § 3.2.1) and presented in Table 3.1.

Table 3.1. Average dimensions, height and width, of various nano-object as reported by AFM measurements using homemade tips. The aspect ratio giving an idea of the convolution error is calculated, the tip radius deduced using equation (3.5).

	CNT	Iron oxide nanoparticles	Gold spherical nanoparticles	Gold spherical nanoparticles
Height h (nm)	2.5	12	25	60
Width w (nm) Home-made tip (Commercial tip)	110/80/40 (30)	130/80 (50)	130 (80)	200 (100)
Aspect ratio $A = h / w$	0.02/0.03/0.06	0.09/0.15	0.2	0.3
Tip radius $w^2 / 8h$	600/300/80	176/67	85	83

While the height of the imaged objects corresponds either to their specification (CNT) or to the dimensions extracted with commercial AFM tips (μ Mash NSC14), large convolution error is associated with the homemade probes. Note that the lowest aspect ratio, i.e. extremely large convolution effects are observed for CNT and iron oxide particles samples which were imaged in the early phase of this work using probes elaborated with a non-optimized etching procedure (cut-off value Chapter 2 § 2.3.1). Gold nanoparticles imaged using tips produced through the optimized etching procedure still reveal important convolution effects, the calculated tip radius being 4 to 5 time larger than the one extracted from SEM.

Such discrepancy can be explained by the degradation over time of the tip tapered profile upon imaging, in the situation where the mechanical properties of the homemade probe do not allow a precise and fast feedback control of the tip-sample distance. To assess the possible wear of the tip upon imaging, some tips were examined by SEM after imaging of glass substrate decorated with 20-60 nm spherical gold nanoparticle. SEM reveals a radius of curvature of the tip of 130 nm much higher than the one expected with the optimized etching procedure but in agreement with the one deduced from the aspect ratio ($h = 23$ nm, $w = 160$ nm) of the surface nano-objects (see **Figure 3.13**) confirming the possible degradation of the tip during raster scanning of the glass surface.

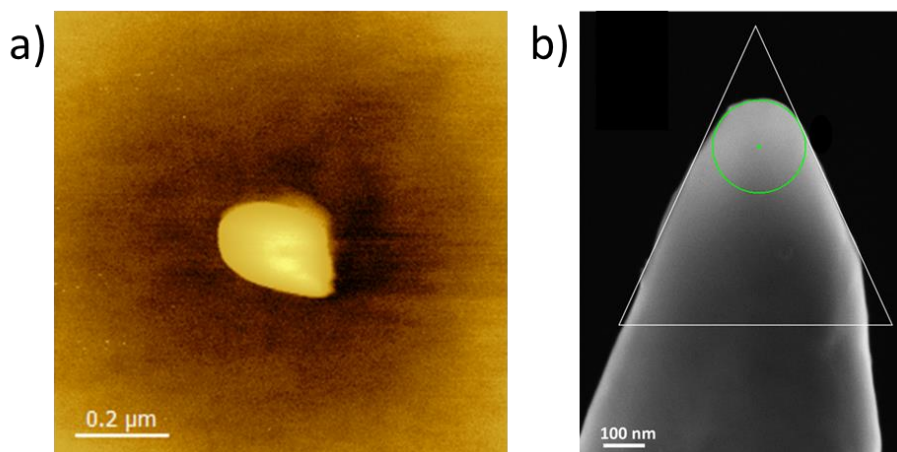


Figure 3.13. a) AFM image of a gold spherical nanoparticle deposited on a glass substrate (width: 160 nm, height: 23 nm); **b)** SEM image of the tip after the AFM measurements: radius of curvature: 130 nm and half-cone angle of 23°.

Partial conclusion – We demonstrated in this part, the ability of the manufactured bulk gold AFM probe to operate under tapping mode, using infrared AFM feedback laser (automatic positioning of the laser on the reflective cantilever). Weakly adsorbed nano-objects, gold nanoplates, spherical nanoparticles and CNTs down to 2.5 nm could be detected and imaged in the air. This is to our knowledge the first demonstration of CNT imaging using such bulk probe made of a ductile material. Pretty large convolution effects were detected though, indicating of either large radii of curvature, non-proper tracking of the surface upon imaging due to unsuitable mechanical properties (mixed deflection/torsion vibration modes of the cantilever at the selected frequency) and wear-out of the tip apex upon imaging, compromising high resolution imaging. However, the primary goal of this study, i.e. to produce bulk metal probe whose the approach to a surface can be controlled and achieved even on non-conductive substrates, is met. This opens up the exploration of their TERS activity presented in the following section.

3.3. TERS activity of bulk metal AFM probes in the air

The TERS activity of fabricated AFM probes in the air was evaluated through spectroscopic characterization of model samples, small object with high cross-section for Raman scattering carbone nanotube (CNT), Raman resonant compounds like Nile Blue dye NB deposited on glass (non-gap mode tip sample configuration) and self-assembled monolayers of non-Raman resonant compounds (thioazobenzene derivative and 4-nitrobenzyl mercaptan: 4-NBM).

The ability of the probe to extract the Raman signature of these compounds was evaluated through the recording of point spectra and hyperspectral composition mapping (one full spectrum per pixel), either using the objective lens scanner enabling the positioning of the Raman probe on the tip apex (“hotspot” screening) or the sample scanner of the AIST microscope (*SmartSPM* upright or *Combiscope* inverted microscope).

The TERS activity of the fabricated bulk metal AFM probe was first evaluated in the ambient on the upright microscope (side illumination) which provides an easy optical coupling with the Raman spectrometer when no air/liquid interface is present. We then moved to the inverted configuration and tested several optical improvements like radial light polarization and various high NA objective lens.

3.3.1. Sample preparation

SAM of thio-azobenzenes derivatives - SAMs of 4-[(phenylazo)phenoxy]hexan-1-thiol (ProChimia, Poland) were achieved following the procedure described by R. Ossikovski *et al.*^{155,156} by immersing gold substrates in a 1 mM ethanolic solution of thioazobenzene for minimum 2 h, followed by soaking/ rinsing for minimum 30 min in pure ethanol to remove any physisorbed molecules. Sample were then dried under an argon flow.

Deposition of SAM 4-NBM - SAMs of 4-nitrobenzyl mercaptan (4-NBM: Sigma Aldrich) were prepared following the procedure described by T. Touzalin *et al.*¹⁴² (developed for 4-nitrothiophenol: 4-NTP) by contacting a gold substrate in a 0.1 mmol.L⁻¹ ethanolic solution of 4-NBM. The gold plates were incubated in the solution for approximately 3 hours and rinsed afterwards in pure ethanol for 30 minutes.

Deposition of NB - The sample was prepared by soaking the substrate (gold and glass) in a 10 μM ethanolic solution of Nile Blue perchlorate (Sigma Aldrich) overnight following the procedure of P. Van Duyne *et al.*¹⁴⁹ The NB excess was removed by immersion in 20 mL of pure ethanol for 20 min.

3.3.2. Point TERS spectra using side illumination

Using a 100x objective lens (Mitutoyo *MY100X-806 - 100X Plan Achromat Objective*, 436 - 656 nm, 0.70 NA, WD: 6 mm), and a beam splitter enabling optical control and laser focusing, the alignment of the laser on the gold tip apex turned out to be rather straightforward on bulk metal tips (see **Figure 3.2** above) as compared to gold-coated silicon tips as the tip shaft is

much longer and brighter. By scanning the 633 nm red Raman probe around the apex of the tip (far from the sample and close to the sample) using the piezo objective (accessible scanning range $30 \times 30 \mu\text{m}^2$), a localized hotspot ($\sim 500 \times 500 \text{ nm}^2$) could be imaged for pretty much all manufactured probes tested (some example will be shown after).

Raman signatures of molecular layers - Using regular tip approach and landing in tapping mode, no Raman signature of the probed sample could be extracted as the tip apex is only a fraction of millisecond in close proximity with the sample considering an amplitude of 10 nm and a resonance frequency around 100 kHz. An option “*To contact*” available on the AIST soft stops the oscillation drive of the probe cantilever and changes the feedback control to “deflection” measurements, enabling immediate switching between tapping mode and contact mode, the normal force (set-point) of which can be adjusted. When switching from tapping mode to contact, strong and neat Raman signal could be recorded for all the above-mentioned samples as illustrated on **Figure 3.14b-d**, even at low laser power (1 % of the nominal laser power, i.e. $160 \mu\text{W}$ down to $1.6 \mu\text{W}$) and short acquisition time (1 s down to 0.1 s). Raman signatures could be extracted on a specific point of a sample while the probe stays engaged, for the thiolated derivatives azobenzene and 4-NBM as well as for NB dye deposited on gold surfaces. Note that this fast transition from tapping mode to contact mode is at the base of the hybrid imaging mode developed by Horiba, i.e. “*Top-mode*”, to perform TERS imaging (see Chapter 4).

This neat transition between “no signal” and “strong signal” upon slight change of the tip-sample distance is the ultimate proof of the effective extraction of a near-field optical signal, i.e. of a TERS signal (when not using bottom illumination). Note that the flat spectral signature visible on the three spectra (b) (c) and (d) when the tip is in close vicinity to the substrates in “*To contact*” mode implied that no far-field signal, i.e. no μRaman signal is collected under the acquisition conditions (low laser power, short acquisition time). Note that possible contamination of the tip (molecular adsorption) is verified after the measurements. By bringing the tip in close contact with a bare gold surface, the signature of the contaminant in the tip-gold junction is enhanced and immediately observed.

As seen on the TERS spectrum (**Figure 3.14b**), the azobenzene derivative displays several characteristic Raman bands: a band with strong intensity at 1143 cm^{-1} (C – N stretching mode), a band with medium intensity at 1184 cm^{-1} (C – C stretching mode), a characteristic triplet of strong intensities, involving a band at 1443 cm^{-1} (N=N stretching mode) and two bands at 1415

and 1465 cm^{-1} (ring deformations), and a broad band with medium intensity at 1590 cm^{-1} (aromatic ring breathing).^{157–160}

For 4-NBM, only three major bands are acquired in the Raman spectra: a band at 1107 cm^{-1} , assigned to CH bending, characteristic signature of symmetric NO_2 stretching at 1340 cm^{-1} and 1590 cm^{-1} band, belonging to ring stretching (**Figure 3.14c**). Nile Blue shows a characteristic Raman band of strong intensity at 591 cm^{-1} (**Figure 3.14d**).

Moreover, the hotspot screening shown on **Figure 3.15** realized by hyperspectral mapping of the tip-sample junction using the objective scanner, reveals a strongly localized signal of the SAM, typical of a TERS signature.

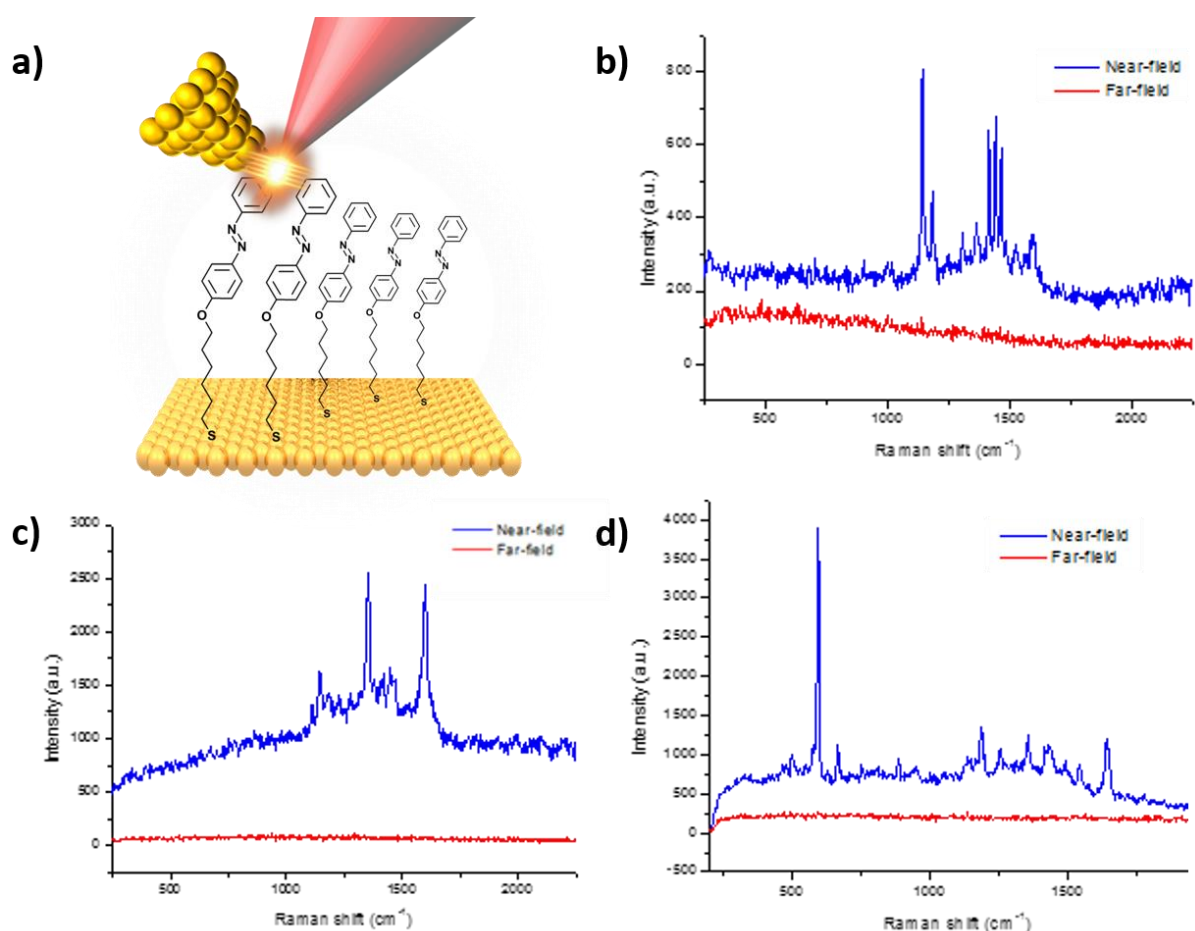


Figure 3.14. TERS activity of homemade probe with side illumination - Spectral signatures in the air of functionalized gold substrates upon approach of a bulk gold homemade probe illuminated with a 632.8 nm laser probe (side illumination, upright microscope, linear polarization); **a**) in the side illumination TERS set-up, the TERS-active probe has to be in close contact (*“To contact”* mode) with the sample (here a thiolated derivative of azo-benzene) to extract a TERS signature. The recording of Raman signatures successively in semi-contact mode (tapping mode: red) and contact mode (blue) enables us to distinguish the far and near-field contributions; Raman signatures of **b**) thioazobenzene derivative on gold (laser power: $\sim 160\text{ }\mu\text{W}$ (1% of the nominal laser power), acquisition time 1 s, 4 accumulations); **c**) 4-NBM on gold (laser power: $\sim 160\text{ }\mu\text{W}$ (1% of the nominal laser power), acquisition time 1 s, 3 accumulations) and **d**) Nile Blue (NB) dye on gold (laser power $16\text{ }\mu\text{W}$, 0.1% of the nominal laser power), acquisition time 1 s, 4 accumulations).

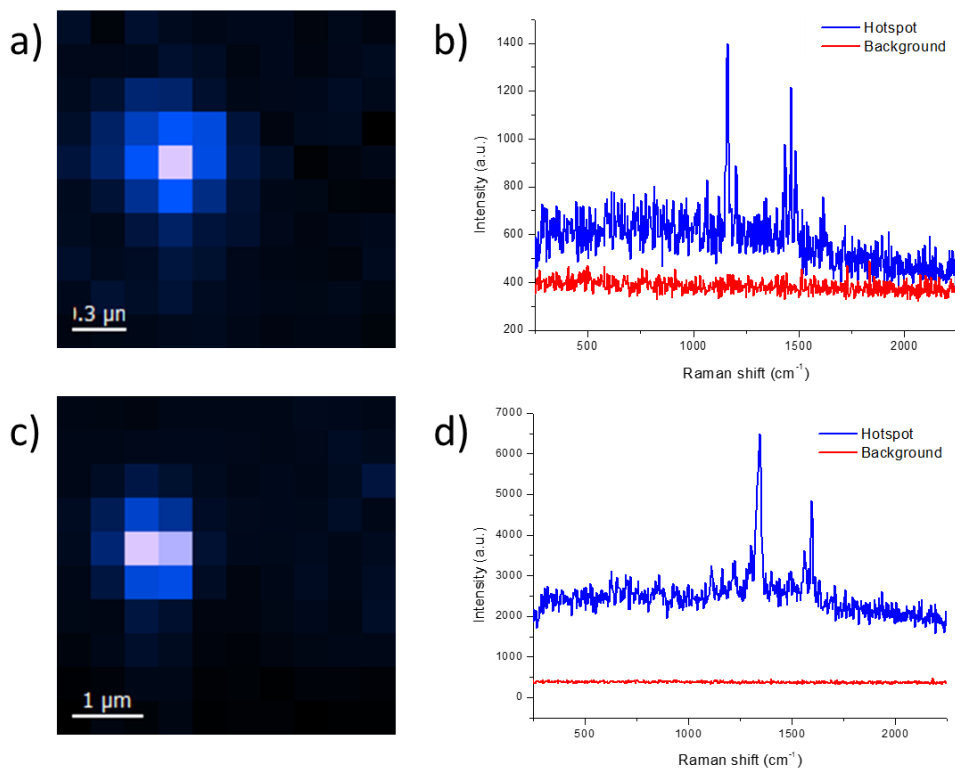


Figure 3.15. Hotspot screening in the ambient with side illumination: a) $2 \times 2 \mu\text{m}^2$ X,Y objective map on azobenzene SAM on gold with associated TER spectra (b) - laser power $160 \mu\text{W}$ (1% of the nominal laser power), acquisition time 0.3 s); **c)** $5 \times 5 \mu\text{m}^2$ X,Y objective map on 4-NBM on gold with associated TER spectra (d) - laser power $\sim 160 \mu\text{W}$ (1% of the nominal laser power), acquisition time 0.3 s.

Raman signatures of carbon nanotubes – A gold sample functionalized with the azobenzene derivative and further decorated with CNTs (2 nm high) was then analyzed. To identify the scattered CNTs on the surface, an AFM mapping in tapping mode was first realized and then point spectra were collected in contact mode. The $1 \times 1 \mu\text{m}^2$ AFM image displayed on **Figure 3.16a** shows two CNTs overlapping in the center of the image. TERS point spectrum collected exactly on the CNT in contact mode shows only characteristic G band (in-plane vibrational mode along the CNT axis) of carbonaceous materials at 1590 cm^{-1} , and not the D band (lattice defect) at 1350 cm^{-1} ,¹⁶¹ as it can be seen on the **Figure 3.16**. When moving the tip slightly away from the CNTs the signature of the azobenzene derivative covering the whole gold surface is observed but the signature of the CNT disappears which illustrate the high lateral resolution of the composition screening by TERS.

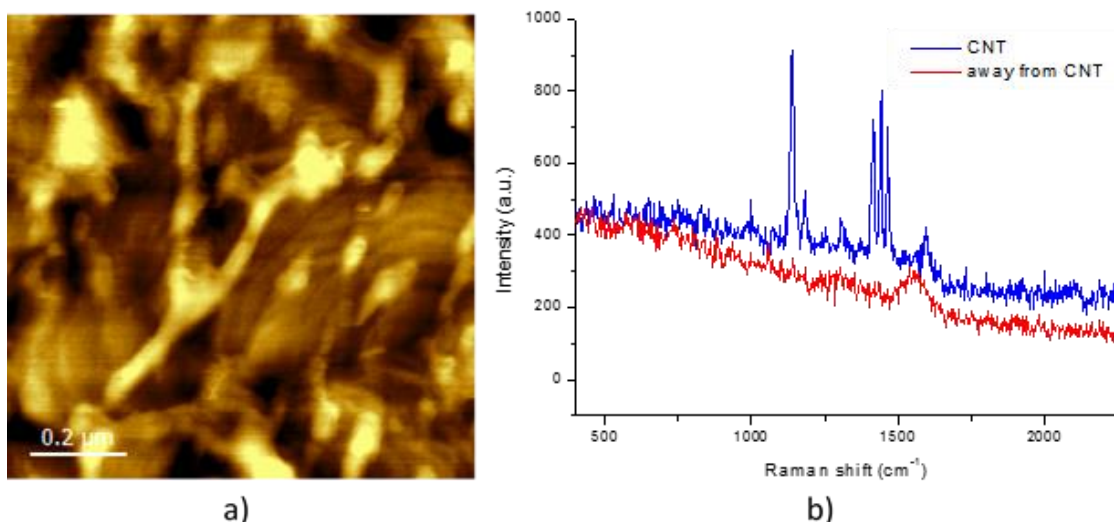


Figure 3.16. TERS activity of homemade probe with side illumination - Gold functionalized with azobenzene and further decorated with CNTs: **a)** AFM topography in the air recorded in tapping mode (scan rate 1.0 Hz, scan range $1 \times 1 \mu\text{m}^2$, resonance frequency 97 kHz); **b)** point TERS spectra on a CNTs (red) and slightly away in lateral position (thioazobenzenes SAM signature in blue) – Raman probe 632.8 nm, laser power $\sim 160 \mu\text{W}$ (1% of the nominal laser power), acquisition time 4s, accumulations 3, “To contact” mode.

3.3.3. Point TERS spectra using bottom illumination

Our initial trials to achieve TERS on the TERS-ready inverted microscope provided by Horiba turned out to be challenging, due to several factors impacting the TERS excitation and the TERS signal collection efficiency:

- the divergence of the optical path (long optical path as compared to the *Omegascope* optical coupling platform) and the intercalation of numerous mirror on the optical path (in a “periscope” used to adapt the beam height while maintaining the suitable polarization),
- the use of objective lens with extremely large entrance pupil 7 mm (Nikon *CFI Plan Fluor 100X*, N.A. 0.90, WD: 0.3 mm dry lens) as compared to the objective lens used on the *Omegascope* ~ 2.8 mm (Mitutoyo *MY100X-806 - 100X Plan Apochromat Objective*, 436 - 656 nm, 0.70 NA, WD: 6 mm),
- the use of glass coverslip transparent substrates which introduces new interfaces on the optical path and the difficulty to produce samples (non-Raman resonant molecular layer) on such substrates which can be used as “standards” for TERS evaluation in the inverted configuration,
- the requirement to transform the polarization of the 633 nm Raman probe from linear to radial for maximal near-field signal enhancement and far-field signal reduction,

- the use of commercial TERS active tips (gold/silver coated silicon AFM tips, Horiba),
- the instability of the microscope and of the sample holder.

To assess the ability to collect a TERS signal in the inverted configuration using the homemade probes, the Raman-resonant Nile Blue was deposited either on a glass coverslip or on semi-transparent gold-coated glass coverslips and non-Raman resonant compounds (4-NBM or thiolated derivative of azobenzene) self-assembled on semi-transparent gold-coated glass coverslips. Glass substrates decorated with CNTs were also tested. The influence of several parameters on the TERS signal quality (intensity, background), i.e. light polarization, laser beam size, objective lens, (non)gap-mode and laser wavelength, was also assessed.

TER signature of molecular compounds in the ambient - Using an air objective (Nikon CFI Plan Fluor 100X, N.A. 0.90, WD: 0.3 mm) and the homemade gold AFM probes, the alignment of the Raman probe (633 nm, linearly polarized) on the tip apex through both the glass coverslip and the gold-coated coverslip turned out to be straightforward as the tip apex can be identified optically as mentioned earlier and as seen on **Figure 3.3**. Signal intensity imaging ($5 \times 5 \mu\text{m}^2$) of the tip apex using the XY objective scanner and the 633 nm Raman probe reveals a very localized “hotspot” ($< 1 \mu\text{m}$) for both NB and 4-NMB derivatized gold substrates as depicted on **Figure 3.17a** and **3.17c**. Very strong Raman signatures (TERS) of both compounds could be extracted from the hyperspectral map at the hotspot location at very short acquisition time (0.3 s) and low laser power ($\sim 160 \mu\text{w}$, 1% of the nominal laser power) as can be seen on **Figure 3.17b** and **3.17d**.

The disappearance of the Raman signature slightly away from the hotspot attests of the very weak far-field contribution (flat baseline) of the sample despite the illumination and signal collection through the derivatized glass substrates. The observation of a neat TERS signature is even more surprising given that the geometry of the tip (vertical cone) and the polarization of the incident laser (linear) do not favor the excitation of the TERS signal neither the reduction of the in-plane far-field signal from the sample. Moreover, the switch between tapping mode and contact mode do not induce much TERS intensity change as observed on the configuration with side illumination. The fact that near-field interaction and the resulting TERS intensity are not impacted by the constant variation of the tip-sample distance with time (10-20 nm in theory using commercial tips) is not yet understood, but also reported by other groups, such as S. Bonhommeau⁴⁸ (GSM, Bordeaux). A possible tip contamination with NB or 4-NBM could be invoked but has been ruled out by subsequent testing of the TERS response

of the tip on a bare gold substrate (*Omegascope* optical coupling platform with upright microscope).

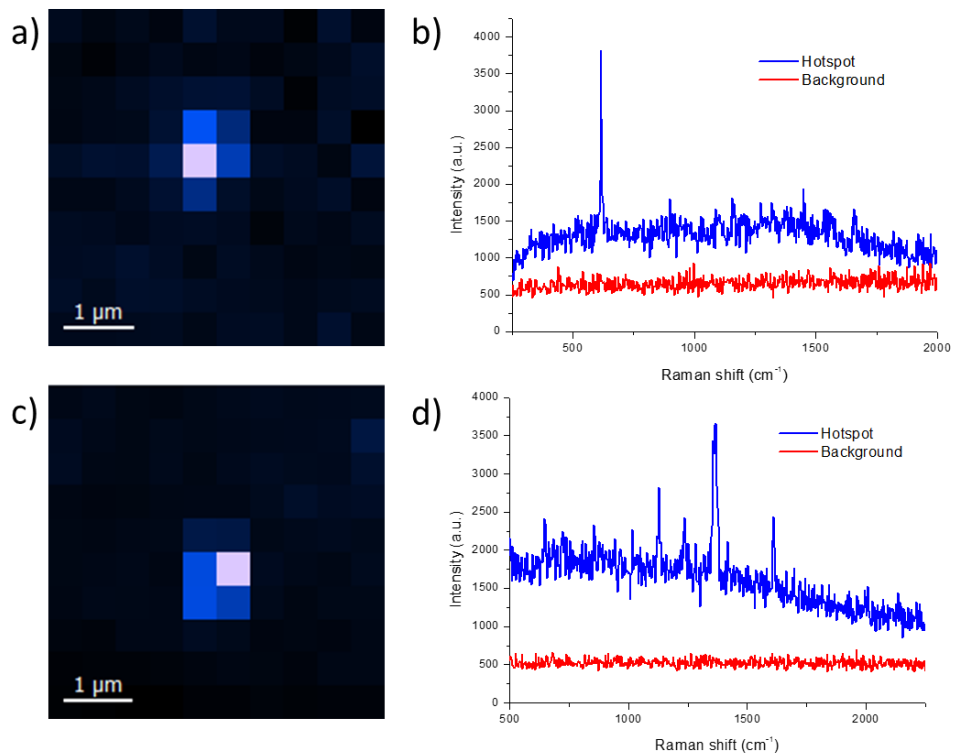


Figure 3.17. TERS activity of homemade probe using bottom illumination on Nile Blue on gold (a and b) and of 4-NBM on gold (c and d) – a) and c) XY objective scanner mapping 5 x 5 μm²; b) and d) spectra extracted from the maps a and c respectively, at the exact hotspot location (blue) and slightly away (red). Dry 100x objective, λ_{exc} 632.8 nm, laser power: ~160 μW (1% of the nominal laser power), acquisition time: 0.3 s.

Note that the TERS signature of NB compound deposited on glass (non-gap mode configuration) could not be proven, as this resonant sample shows a strong far-field signal even at minimum laser excitation as illustrated in **Figure 3.18**.

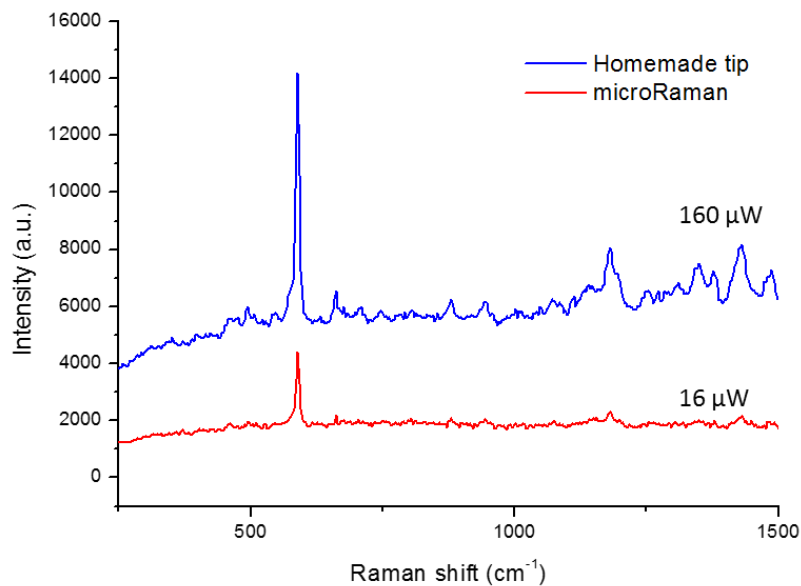


Figure 3.18. NB on glass with side illumination in the ambient – Spectra in blue showing NB signature obtained with homemade gold probe - 632.8 nm, laser power $\sim 160 \mu\text{W}$ (1% of the nominal laser power), acquisition time 1s - and in red showing NB band acquired in the far-field - 632.8 nm, laser power $\sim 16 \mu\text{W}$ (0.1% of the nominal laser power), acquisition time 1s.

TER signature of CNTs in the ambient - Using the same instrument configuration, TERS signal could be also extracted on CNT decorated glass coverslips with surprisingly no far-field contribution as can be seen on the spectra extracted from the hyperspectral objective scanner map presented in **Figure 3.19a**. CNTs chemical signatures can be indeed observed by micro-Raman given the large Raman scattering cross-section of carbonaceous materials providing that high laser power are used, which is not the case here ($\sim 160 \mu\text{W}$; 1% of the nominal laser power).

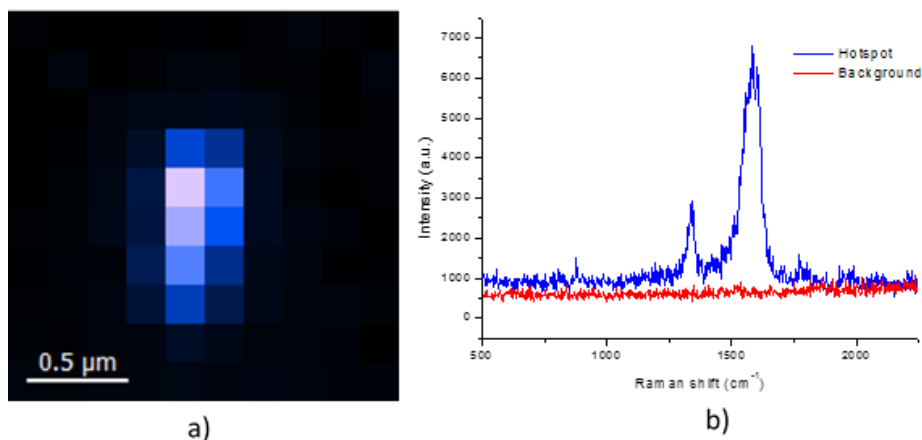


Figure 3.19. TERS activity of homemade probe using bottom illumination and CNT decorated glass substrate: **a)** $2 \times 2 \mu\text{m}^2$ hotspot imaging (XY objective scan), **b)** Raman spectra at the exact hotspot (blue spectrum) and slightly away (red) showing characteristic CNT D-band (1350 cm^{-1}) and G-band (1590 cm^{-1}) (blue spectrum). 100x air objective, λ_{exc} 632.8 nm, laser power $160 \mu\text{W}$, acquisition time 0.3 s.

Polarization and laser beam size - The transfer on our lab Raman set-up of the 633 nm laser from the HR800 Horiba enclosure to an optical bench at the rear of the spectrometer allowed the introduction and the testing of the radial light polarization kit (Arc Optics) described above and of a variable beam expander (Edmund, 2X-8X, VIS, #87-569) to increase the laser beam size (from 3 mm to 7) and match the large dimension of the Nikon objectives pupil. Because of the specific construction of the HR800 Raman microscope (see Chapter 1), the introduction of these optical elements before the rejection filter (reflecting the out coming excitation laser filtering the incoming scattered signal) is important to limits the impact on the signal collection.

No clear beneficial effect on the TERS signal intensity nor on the background signal level could be observed using the radial polarization kit, although it is globally accepted in the community.¹⁶² However, strong TERS signal has been reported in transmission and linearly polarized laser (electric field perpendicular to the main tip axis) when using largely corrugated tips (obtained by rough deposition of plasmonic materials on silicon AFM probes), which can be explained by localized surface plasmon resonances (LSPR) at nano-size surface features of the tip.¹⁶³ This corrugation is difficult to invoke here given the very smooth surface of the tip produced in this study as described in Chapter 2.

The enlargement of the laser beam size did not provide neither better TERS to background signal ratio which can be explained by the divergence of the beam on the long optical path between the Raman microscope and the *Combiscope* inverted microscope. Note also that the reduce size of the rejection filters (5 mm x 5 mm) installed in the Horiba spectrometer limits considerably the possible tuning of the laser beam size.

Oil immersion objective lens - To ensure an optimal excitation and collection efficiency of the TERS signal through thin glass coverslips, an oil immersion objective with very short working distance (NIKON Plan Apo 100X, N.A. 1.45, W.D. 0.13mm, Lambda oil immersion objective) and oil whose the refraction index ~ 1.5 matches the one of glass (1.52) allowing minimization refraction at optical interfaces and offering large angle of collection (N.A. 1.45) was acquired, tested and compared to a dry objective. TERS signal intensity of the azobenzene derivative observed with oil immersion objective shows a five-fold higher signal compared to the spectra signal obtained with the air objective¹⁶⁴ as displayed on **Figure 3.20**, highlighting the importance of the air-glass interface suppression and of high signal collection angle. The increase of the TERS signal intensity using oil immersion objective is however at the expense

of the AFM stability, as a mechanical coupling between the sample and the objective through the thin layer of oil impacts the regulation of the tip-sample distance upon imaging (even during objective scans), causing tip damage upon repeated crashes.

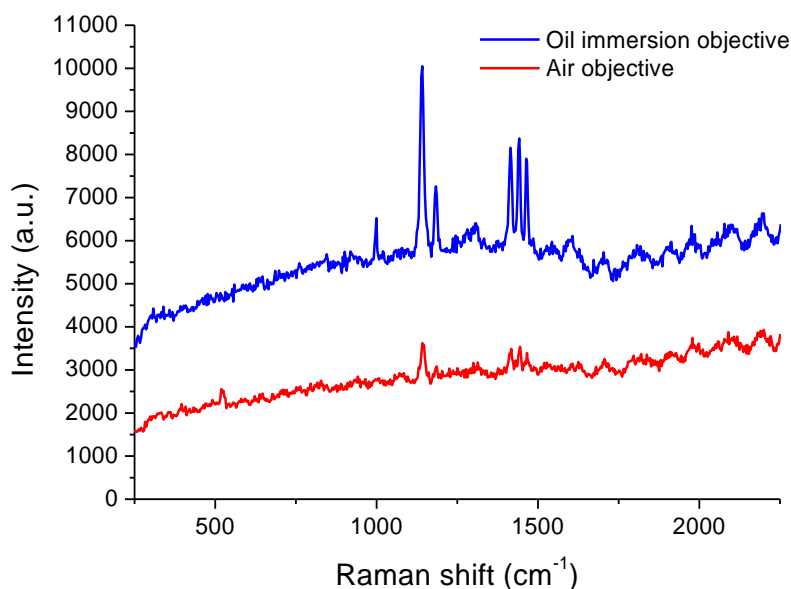


Figure 3.20. TERS activity of homemade probe using bottom illumination – Raw TERS spectra of thioazobenzenes on semi-transparent gold-coated glass coverslips in inverted configuration recorded with two different 100x objectives: oil immersion (NA = 1.45) and dry objective (NA = 0.90). A 5x higher signal intensity is recorded with the oil immersion objective. TERS parameters: λ_{exc} 632.8 nm, laser power $\sim 160 \mu\text{W}$ (1% of the nominal laser power), acquisition time 4 s, 3 accumulations. Spectra were shifted to ease their visualization.

Note that on the EM-CCD detector (Andor *Newton 971*) which uses a back-illuminated sensor (CMOS) to improve low signal intensity detection, Fabry-Perot interference between the reflected radiation within the sensor and/or the incoming radiation at the same wavelength can occur, translating into ripples (fringes) on the spectra especially above 1500 cm^{-1} (see **Figure 3.20**). This effect is especially pronounced with signal recorded from the inverted configuration where the background signal is always higher than in the upright configuration with side illumination.

TERS activity and Raman probe - To better understand the plasmonic properties of our tip, the associated TERS activity was evaluated at different wavelength on the inverted configuration using semi-transparent gold coated glass coverslips functionalized with the azobenzene derivative. Our system is indeed equipped with 5 different laser lines (473, 532, 591, 633, 785 nm with different nominal laser powers 20, 50, 50, 16, 90 mW respectively) which can be interchanged automatically. If no TERS signal could be extracted using gold probes at 532 nm, TERS activity could be observed both at 591 nm and at 785 nm. A neat TERS

signature of thioazobenzene could be observed at 785 nm (near-infrared sensitive CCD detector with no electron multiplication: Horiba *Syncerity*) and with no far-field signal as can be seen on **Figure 3.21**. The extraction of a TERS signature at 785 nm on a non-resonant molecular compounds in gap-mode, reported for the first time to our knowledge, is striking since Raman scattering at 785 nm is almost 5 times less efficient than that at 532 nm. TERS at 785 nm can be interesting for systems showing strong fluorescence signal at classical 532 and 633 nm excitations used in TERS with silver and gold probes.

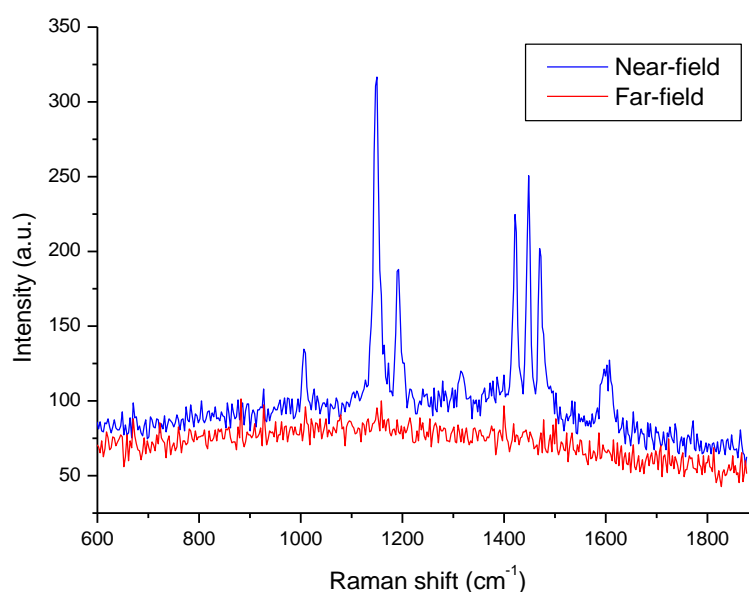


Figure 3.21. TERS activity of homemade gold probe using bottom illumination and near-infrared Raman probe - TERS signal of the thiolated azobenzene derivative signal at 785 nm (blue spectrum at the hot spot, red spectrum slightly away) - λ_{exc} : 785 nm, laser power: $\sim 900 \mu\text{W}$ (1% of the nominal laser power), acquisition time 4 s, 3 accumulations, CCD detector: Horiba “*Syncerity*”.

3.3.4. Comparison of EF between etched silver and gold probe

TERS signal can be achieved with visible excitations with probes made of materials showing plasmon resonance, the most often reported being silver or gold, or the combination of both. It has been reported that silver-coated AFM tip provides much higher enhancement signal compared to the gold-coated tip. Zhang *et al.*⁴⁵ have reported for instance signal enhancement of CNT with the laser wavelength 532 nm to be around 1.5×10^3 with silver-coated tips and only 0.4×10^3 with the gold-coated tips.

A similar comparison of the TERS enhancement properties of homemade gold and silver tips (see manufacturing process in Chapter 2) has been done in this study. The TERS signal intensity of thioazobenzene and 4-NBM monolayers has been evaluated in the upright

configuration (side illumination) using the same 633 nm Raman probe for both probes. Despite the fact that the etching process for silver has not been fully optimized, the tip apex appears quite sharp, as seen on the optical image recorded through the 100x objective (see **Figure 3.22a-b**). As seen on the spectra on the **Figure 3.22c-d**, TERS signal can be collected with both AFM probes, much higher signal enhancement being observed with homemade silver probes as compared to gold probes (3x and 5x higher on the thioazobenzene and the 4-NBM sample, respectively). If difference in TERS intensity could be interpreted by the larger radius of curvature of silver tips (non-optimized etching process leading to blunt tip apex), such enhancement with silver tips is surprising as plasmon resonance is expected with green (532nm) excitation for silver metal.

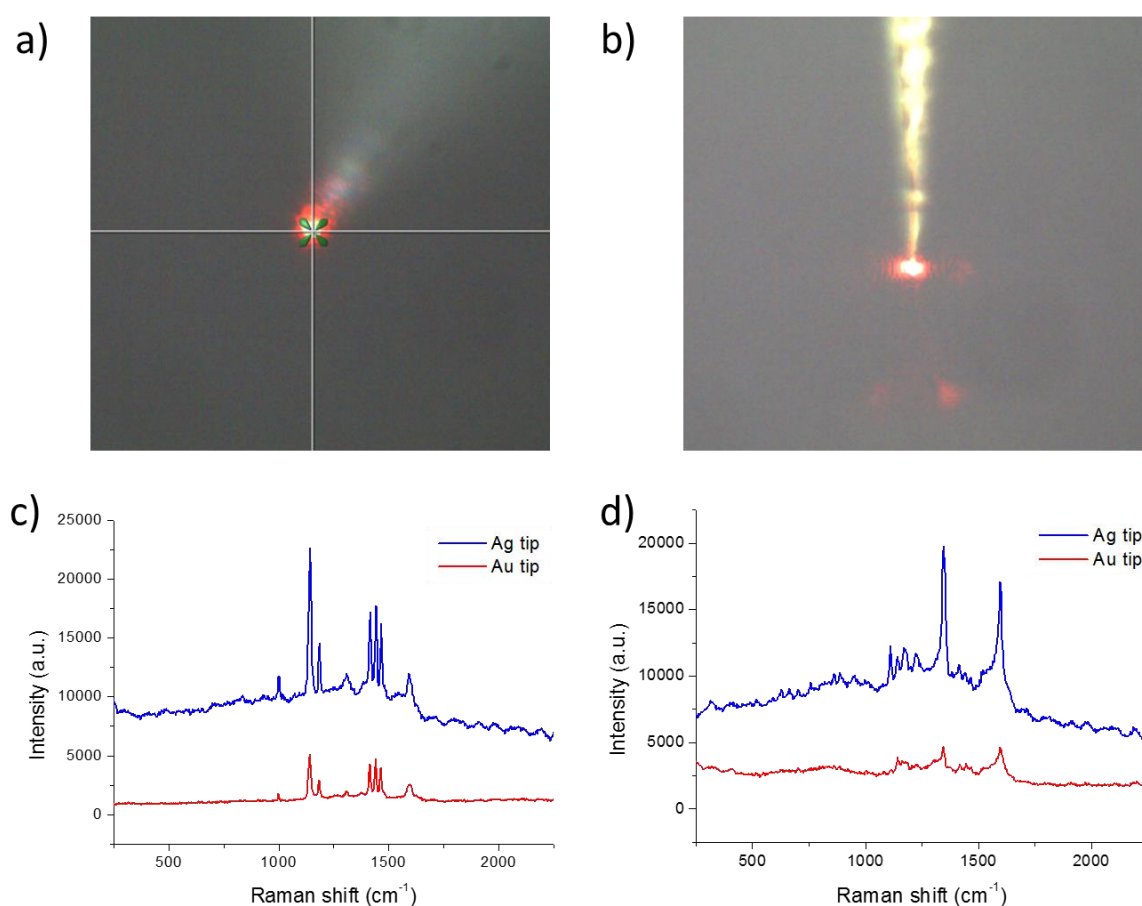


Figure 3.22. Compared TERS activity of homemade silver and gold probes - (a) & (b) laser alignment with side illumination on homemade Ag and Au probe apex respectively. Comparison of TERS signal intensity obtained on SAM-derivatized gold samples with the gold and silver tips with side illumination in the ambient: **c)** thioazobenzene SAM (3x higher signal with silver tip, band at 1141 cm⁻¹), **d)** 4-NBM SAM (5x higher signal with silver tip, band at 1335 cm⁻¹). Point TERS spectra, 632.8 nm, laser power ~160 μW, acquisition time 4 s.

Partial conclusion – We demonstrated in this section 3.3, the TERS efficiency of the manufactured bulk gold (and also silver) AFM probe and their ability to extract in the ambient and on both configurations (upright & inverted) the Raman signatures (point spectra) of molecular layers and carbon nanotubes at plasmonic junctions (gold sample), at low laser power and short acquisition time (< 0.5 s). TERS signature could be obtained with the handmade probes on the inverted configuration using bottom illumination of the tip apex through semi-transparent substrates, linear polarization of the laser beam and in tapping mode (contrary to the upright configuration and side illumination which requires contact mode). A strong TERS activity of the gold probes using other Raman probe than 633 nm has been also observed, including the near-infrared excitation 785 nm which is of interest for systems with strong auto-fluorescence signal. Although oil immersion objectives provide higher excitation and collection efficiency than dry objectives, strong instabilities and subsequent tip damage (and contamination) caused by the mechanical coupling of the objective and the sample have been observed, preventing its use. The successful implementation of TERS measurements on the inverted microscope using bulk metal AFM probes and semi-transparent gold substrates paves the way to AFM-TERS measurements in liquid (and under electrochemical polarization) which will be presented in the last section of this chapter (and in the following chapter).

3.4. TERS mapping performances of bulk metal AFM probes

The ability of the homemade probe to extract and resolve compositions at the nanoscale was evaluated through TERS mapping in the ambient of various substrates in the upright and inverted configuration.

4-NBM derivatized nanostructured gold substrates - AFM-TERS mapping using side illumination was first acquired in tapping mode on a gold substrate decorated with gold spherical NP (dimension range 20 - 60 nm) and functionalized with 4-NBM. Tapping mode had to be used as the imaging mode “*Top-mode*” described earlier alternating tapping and contact mode could not be successfully implemented with the homemade probes.

Simultaneous composition and topography mappings were obtained on a $1 \times 1 \mu\text{m}^2$ area with the resolution of $30 \times 30 \text{ px}^2$ and at the scan rate 1.0 Hz. Measured NP height confirmed the NP size of 20 nm. The Raman signature of 4-NBM is observed all across the gold surface but with a slight decrease in intensity on the particle. The observation of a “TERS” signal in

tapping mode using side illumination is surprising and contradicts the results presented earlier in section 3.3.2. Point TERS spectra of 4-NBM were indeed obtained only in the contact mode. The non-perfect tip sample distance control upon raster scanning of the probe and/or a possible tip contamination can explain the extraction of a Raman signature of 4-NBM using side illumination, even in tapping mode. Possible tip contamination explaining such discrepancy was evaluated on a pristine gold and confirmed by the observed signature 4-NBM signal (spectrum on the **Figure 3.23d** below), indicating that the raster scanning of the tip induces harsh contact of the tip with the sample.

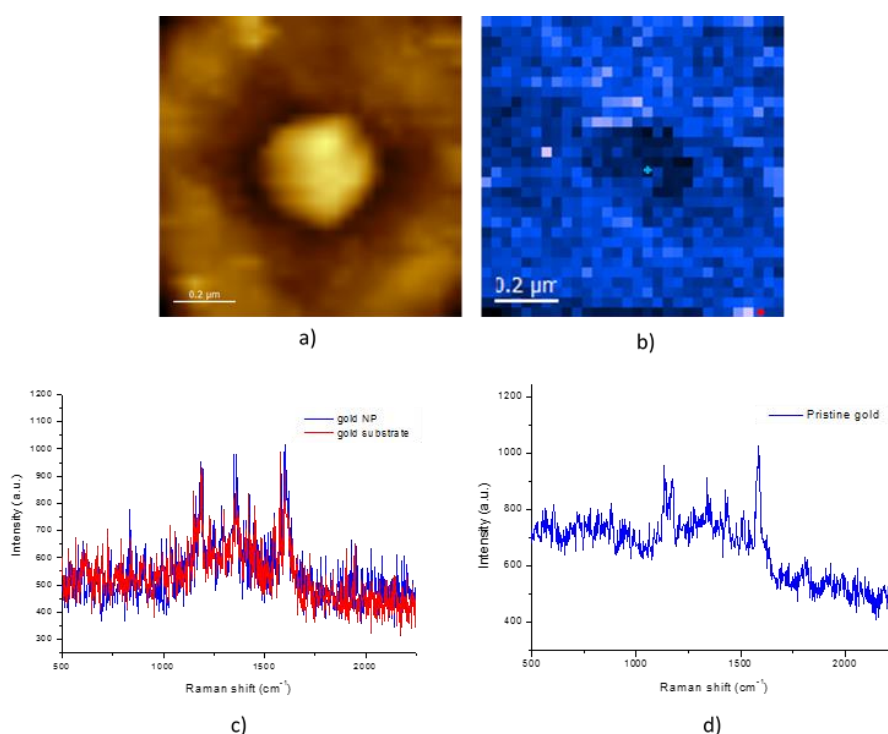


Figure 3.23. AFM-TERS mapping in the ambient of a gold substrate decorated with AuNP and functionalized with 4-NBM (upright microscope / side illumination) - **a)** $1 \times 1 \mu\text{m}^2$ AFM topography of gold spherical NP on gold obtained during TERS mapping ($30 \times 30 \text{ px}^2$, resonance frequency 89 kHz, scan rate 1 Hz); **b)** TERS map obtained by integration of the 1335 cm^{-1} band intensity ($\lambda_{\text{exc}} = 633 \text{ nm}$, $\sim 160 \mu\text{W}$: 1% of the nominal laser power, acquisition time 0.3 s, 1 accumulation, magnification $\times 100$, resolution $30 \times 30 \text{ px}^2$); **c)** point TERS spectra of 4-NBM signal on gold NP and gold substrate with spectra associated with red points on TERS map (b); **d)** TERS spectrum on pristine gold showing tip contamination after TERS mapping of 4-NBM derivatized substrates (acquisition time 4 s).

Further analyses by SEM after TERS mapping show the tip apex contaminated with nanoparticles (seen in **Figure 3.24a-c**), which were picked up during raster scanning of the AFM-TERS probe on the sample surface. Note that heavy damages were also revealed on some tips as shown on **Figure 3.24d** after scanning of the sample.

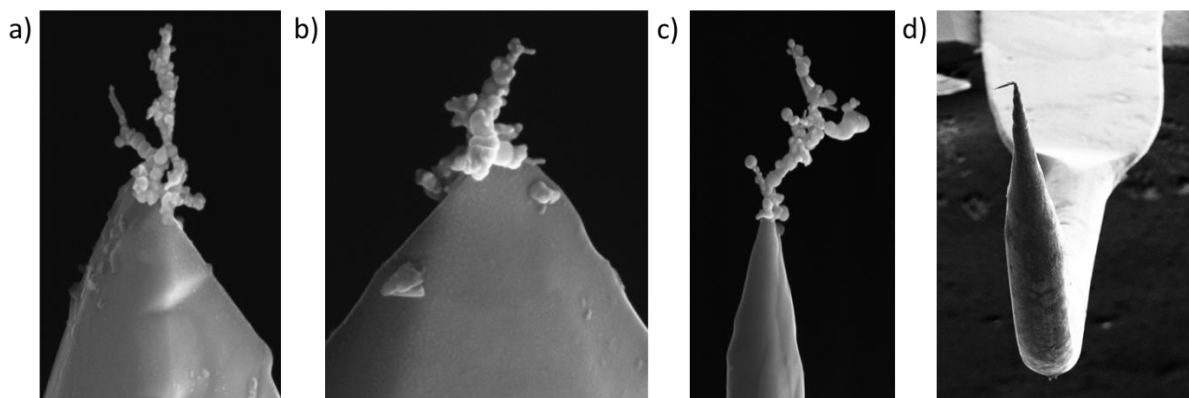


Figure 3.24. SEM images showing tip contamination with nanoparticles (a-c) and tip damage (d) caused from AFM-TERS imaging.

Functionalized gold nanotriangles on glass - To limit the occurrence of contamination by nano-objects (and molecules), large nanotriangles functionalized with 4-NBM were deposited onto glass and imaged by AFM-TERS with both configurations.

Upright configuration / side illumination - A Raman signature of 4-NBM could be extracted in tapping mode upon raster scanning of the tip over the nanotriangles only, as can be seen on **Figure 3.25**. Note that no contamination of the tip was detected subsequently upon measurement on a pristine gold sample as opposed to the previous example with spherical nanoparticles. The inhomogeneity of the surface signal intensity, i.e. higher intensity at the center of the nanotriangles is however surprising. Note that a similar composition pattern was found at twice the scan rate on the fast axis X ($30 \times 30 \text{ pixels}^2$). If some signal can be recovered on the two particles at the left bottom corner of the image, the small triangle at the right side of the large one is not detected by TERS.

The extraction of a TERS signal in tapping mode on the upright configuration can be explained by the fluctuations of the tip-sample distance (down to the near-field range) during the raster scanning of the probe across the nanotriangles, due to flaws in the AFM feedback control despite the slow scan rate (18 s per line: 60 pixels per line, 0.3 s per pixel). The difficult choice of the resonance frequency to operate the homemade probes (very high here: 210 KHz) could be incriminated here also. This set of data was supplemented by another set of results obtained on the inverted configuration and presented in the following.

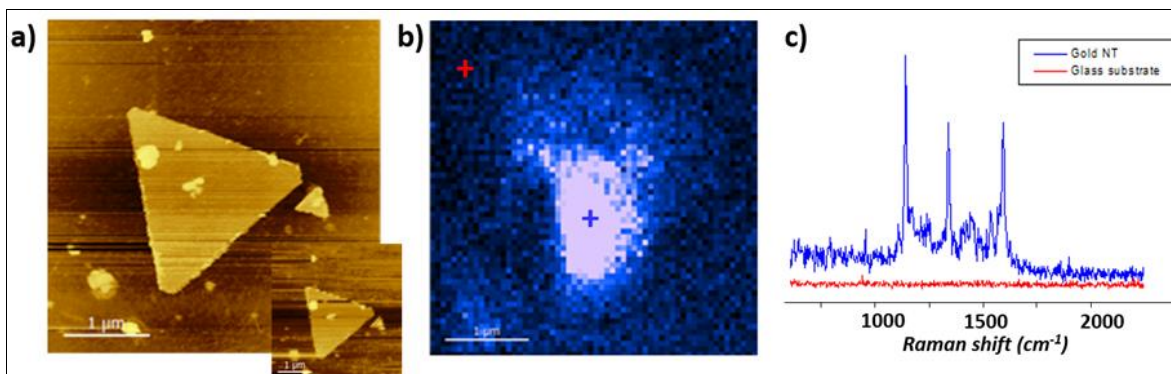


Figure 3.25. AFM-TERS mapping in the ambient of gold nanotriangle (NT) deposited on glass coverslips and functionalized with 4-NBM (upright microscope / side illumination): **a)** $4 \times 4 \mu\text{m}^2$ AFM topography (tapping mode, high resonance frequency 210 kHz, scan rate 1.0 Hz, resolution $256 \times 256 \text{ px}^2$), insert $30 \times 30 \text{ px}^2$ AFM image ; **b)** TERS map ($\lambda_{\text{exc}} = 633 \text{ nm}$, laser power $160 \mu\text{W}$, acquisition time 0.3 s, accumulation 1, resolution $60 \times 60 \text{ px}^2$) by integration of the 1340 cm^{-1} band intensity; **c)** TERS spectra extracted from the TERS map (b) with blue and red spectra corresponding to tip position on NT and on glass substrate respectively.

Inverted configuration / bottom illumination – Similar TERS Pattern as the one measured using side illumination was found using bottom illumination as depicted on **Figure 3.26 I**.

No chemical signature of 4-NBM could be extracted from this sample by μRaman (Raman imaging using the sample scanner or of the objective scanner with the AFM-TERS probe retracted) as can be seen on **Figure 3.27** at two different magnifications $4 \times 4 \mu\text{m}^2$ and $15 \times 15 \mu\text{m}^2$. One can therefore conclude that the AuNT on glass platforms are not SERS active and that the signal extracted is a TERS signal.

The higher intensity at the center of the nanotriangles contrasts with the surface intensity distribution measured by Kurouski *et al.*¹⁶⁵ on similar nanoplates functionalized with 4-nitrobenzenethiol (4-NTP) and deposited on ITO. Edges of nanotriangles are indeed expected to be brighter than their center due to the concentrated charge distribution at corners or edges of nanostructure and the strong tip-nanoplates plasmonic interaction at the edge. Although, one can decipher the contour of the nanotriangles on the TERS images, a stronger TERS intensity at the center of the large triangle is systematically observed (when no contamination occurs).

Note that on a different sample, for which high quality topography images had been recorded (see **Figure 3.26 II**), tip contamination is revealed by TERS mapping showing TERS signature all across the surface, with surprisingly smaller intensity over the nanostructures. This signal damping on nanostructure observed with contaminated tip is consistent, as seen also on **Figure 3.23**.

Improvement in the excitation and feedback associated to the control of the tip-sample distance could be achieved through a proper assessment and control of the tip oscillation amplitude, which with the AIST-NT software is not possible, as the procedure used to calculate the amplitude from the probe characteristics depending on the drive applied to the piezo-shaker (the cantilever length is the only input parameter) is not accessible to users.

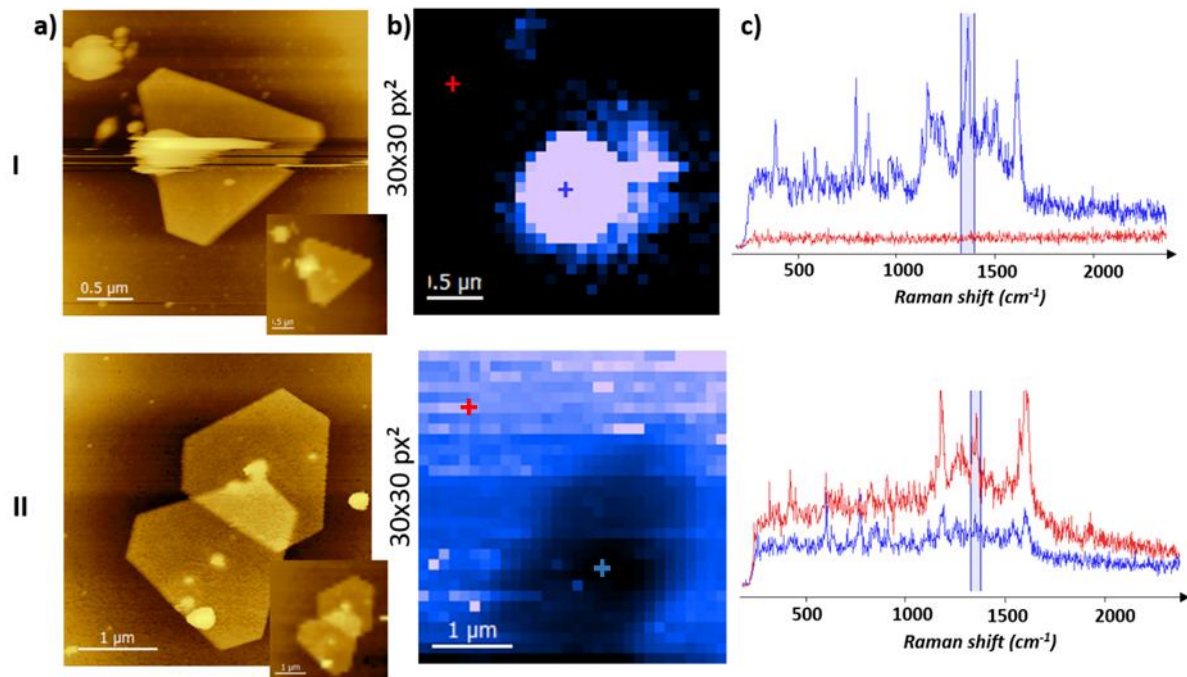


Figure 3.26. AFM-TERS mapping in the ambient of gold nanotriangle (NT) deposited on glass coverslips and functionalized with 4-NBM (inverted microscope / bottom illumination): a) AFM topography, b) corresponding TERS mapping by integration of the band intensity highlighted in blue in (c) ($\lambda_{exc} = 633$ nm, laser power ~ 160 μ W, acquisition time 0.3 s, accumulation 1), c) individual spectra extracted from map (b) at location indicated by colored markers. Serie I): tapping mode, resonance frequency 106 kHz, scan rate 1.0 Hz, resolution 256 x 256 px^2), insert 30 x 30 px^2 ; serie II): tapping mode, resonance frequency 59 kHz, scan rate 1.0 Hz, resolution 256 x 256 px^2), insert 30 x 30 px^2 . Tip contamination is observed on this second sample.

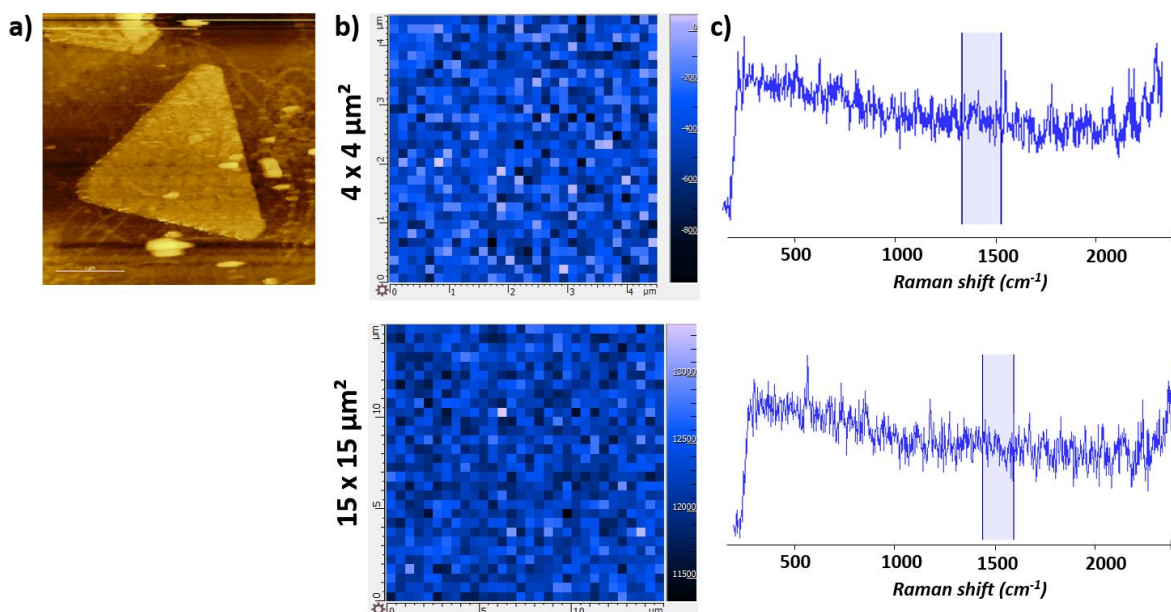


Figure 3.27. μ Raman mapping in the ambient of gold nanotriangle (NTr) deposited on glass coverslips and functionalized with 4-NBM (inverted microscope / bottom illumination). Composition mappings were realized at the exact same location where nanotriangles were found by AFM (resonance frequency 77 kHz), by moving away the AFM tip (retraction of the sample) and refocusing the Raman probe on the sample surface ($\lambda_{\text{exc}} = 633$ nm, laser power ~ 160 μ W, acquisition time 0.3 s, accumulation 1).

3.5. First TERS implementation in liquid (point spectra) using bulk metal AFM- probes

The exploration of TERS implementation in liquid is presented in the following on the inverted configuration using semi-transparent gold substrates which can be functionalized with non-Raman resonant self-assembled monolayers (4-NBM and thioazobenzene derivative). The choice of the inverted configuration is motivated by the ease of the tip-laser optical coupling using a bottom illumination/collection while enabling AFM implementation in liquid with bulky liquid tip holder.

Prototypes of liquid cells – A first prototype of a liquid cell was made of a rubber O-ring, glued directly on the transparent thin glass coverslip with an epoxy glue as displayed in **Figure 3.28b**. Note that to avoid possible contamination related to the manipulation and gluing of the O-ring on the sample, a new cell made of PEEK was designed later as a flat ring-shape hosting 6 small magnets (SuperMagnet) and an O-ring. Thanks to the magnets, this cell can be immobilized on a new sample holder made of a thin ferro-magnetic plate (size 30x20x0.3 mm) designed for the inverted microscope. The pressure on the cell/O-ring/sample/metallic plate applied by the six magnets is sufficient to avoid any possible leakage of liquid, while still

allowing an easy dismantling of the cell after use, leaving the sample intact. The total cell weight was kept minimal to ensure similar performances in liquid compared to those realized in the air, particularly minimization of the sample drift.

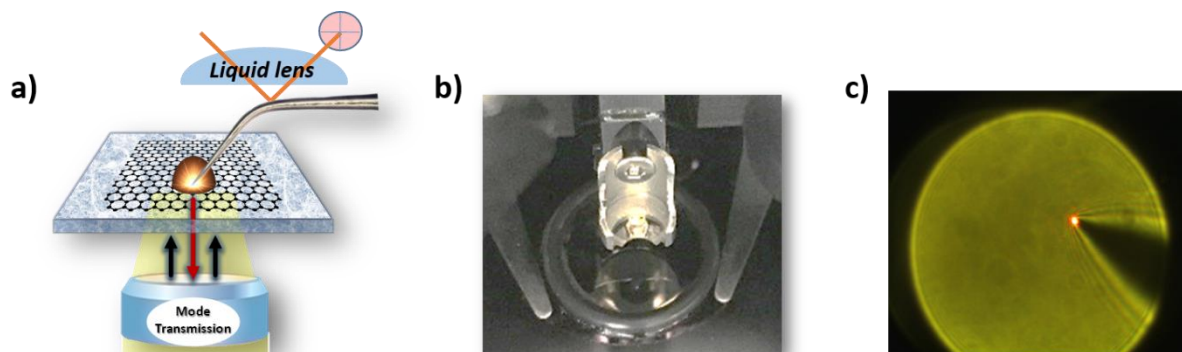


Figure 3.28. TERS implementation in liquid using bottom illumination – a) bottom illumination enables the use of AFM-tip holder carrying a bulky plano-convex lens (6 mm diameter, 2 mm thick) for the proper AFM-laser focusing on the cantilever in liquid (the lens compensates for the deviation of the AFM-laser beam at the air-liquid interface); **b)** liquid cell made of a rubber O-ring glued on the gold-coated glass coverslip; **c)** laser focusing on the homemade tip apex through the gold-coated glass coverslip covered by water.

AFM feedback in liquid - A semi-transparent gold sample was functionalized with the thiolated azobenzene derivative, an O-ring glued on its surface, installed on the sample scanner of the inverted microscope (*Combiscope*), and covered by some deionized water. The bulk gold AFM probe was attached to the AFM tip holder designed for liquids (see **Figure 3.28b**). In water, the automatic AFM laser alignment proceeded successfully as in the ambient with no additional difficulties. A slight drop in the overall intensity reflected on the cantilever to the photodiode was noticed in water, but the signal level is still high enough to ensure a proper regulation of the tip-sample distance. The screening of the resonance frequency of the tip oscillation for tapping mode shows a forest of peak as usually observed in liquids when using piezo driving (“shaker”) of the tip oscillation (see **Figure 2.31** in Chapter 2). The selection of the resonance peak was made according to the following criteria: high oscillation amplitude, narrow full width at half maximum (high quality factors) and frequency below 100 kHz (see **Figure 3.29**). The approach to the sample and stabilization of the tip position on the sample surface proceeded normally as in the ambient attesting that the tapping-AFM feedback mechanism operates correctly in liquid with the homemade probes.

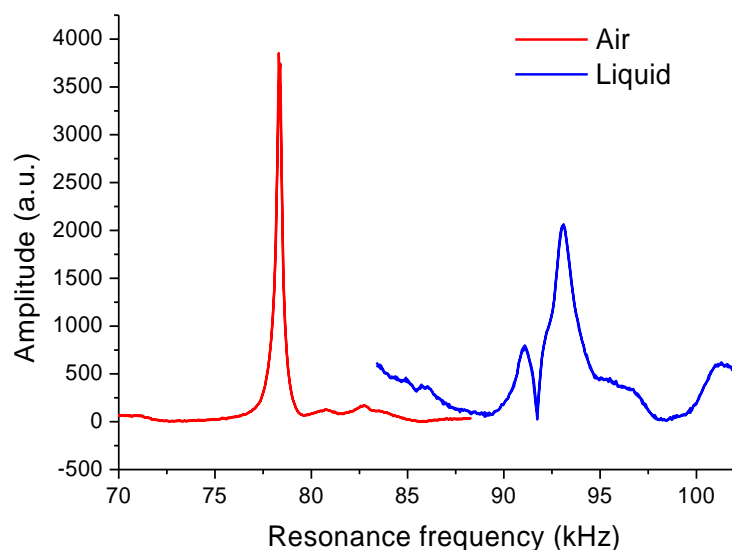


Figure 3.29. Screening of resonance frequency – Comparison between “selected” resonance frequency peaks in the air (red) and in liquid (blue) acquired with homemade TERS-active AFM probes on Combiscope inverted microscope.

TERS enhancement in liquid vs in ambient - The rough optical alignment of the laser on the tip apex though the semi-transparent substrate was as straightforward as in the ambient, as expected with the inverted configuration. The TERS signature of the azobenzene derivative could be successfully extracted in liquid at low laser power (1% of the nominal laser power $\sim 160 \mu\text{W}$) as depicted in **Figure 3.30** (red spectrum). A 2.5-fold decrease of the signal intensity was observed in water as compared to the ambient. N. Kumar *et al.*⁸⁷ also observed a drop of the plasmonic enhancement in aqueous environment as compared to the air, regardless the configuration gap mode or non-gap mode which they interpret through calculation by the decrease of the electric field enhancement due to the change of dielectric environment between air and water. The level of signal extracted with the bulk gold probes are however high enough to carry out TERS analyses in liquid medium.

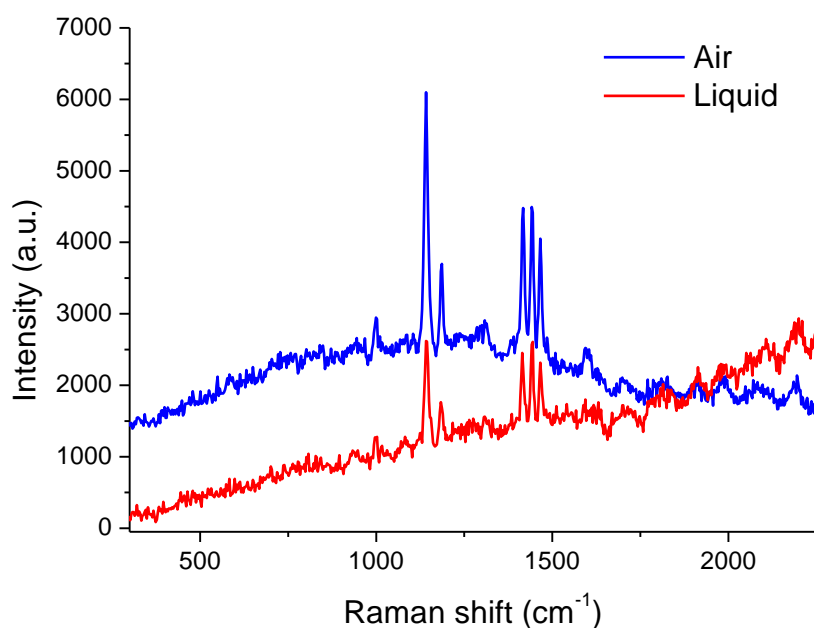


Figure 3.30. Comparison of TERS signal intensity in the air (blue) versus in liquid (red) medium obtained with gold probe on thiolazobenzene-derived substrates using bottom illumination. A 2.5x higher signal (band at 1141 cm^{-1}) is obtained in the air. 633 nm, laser power $\sim 160\text{ }\mu\text{W}$, acquisition time 4 s, 3 accumulations.

Conclusion

In this chapter the imaging performances and TERS activity of bulk metal AFM probes developed in this work have been assessed on various samples and configurations (upright, inverted).

Successful tracking of surface nanofeatures or nanoobjects was achieved in the ambient using bulk gold AFM probes and semi-contact AFM imaging mode. The imaging in tapping mode of physisorbed nanoobjects with sizes ranging from 60 nm down to 2 nm, using bulk metal probes made of gold, more ductile than bulk Pt or Pt/Ir probes commercially available (<https://rmnano.com/>) is to our knowledge unprecedented. A significant decrease of convolution effect upon imaging was observed following the optimization of the etching process procedure of the gold tips leading to smaller radius of curvature (down to do 20 nm according to SEM analyses). However, the imaging performance of the manufactured tips appear to degrade quite fastly upon raster scanning of the tip due to either tip contamination with nanoobjects or tip wear (bending). This traduces flaws in the tip-sample distance control, due to non-reproducible mechanical properties of the tip, difficulty to select the proper resonance frequency resulting possibly in mixed vibration modes (deflection, torsion) and to control precisely the cantilever oscillation amplitude.

The TERS activity of the manufactured probe (gold but also silver) was then evaluated in the ambient on low cross-section compounds like self-assembled monolayers (azobenzene derivative and 4-NBM) and Nile Blue. TERS signature of non-Raman and Raman resonant compounds could be successfully extracted on plasmonic junctions, i.e. on gold substrates (upright configuration) but also through thin gold layers (inverted configuration). On the inverted configuration, with bottom illumination, strong intensity TERS point spectra could be collected at low laser power and short acquisition time using non optimal conditions, i.e. linear polarization of the excitation probe, dry objective and AFM tapping mode. On the upright configuration, with side illumination, contact mode (drive amplitude set to zero, “*To contact*” option) was required to observed a TERS response from molecular layers (point spectrum). 3 to 5-fold higher intensity was observed with silver AFM probes with respect to gold ones when using similar excitations conditions (633 nm, laser power, acquisition time).

No TERS signature on glass substrates derivatized with Nile Blue (non-plasmonic junction), could not be observed due to high background signal level. Either, the manufactured probes with smooth tip apex (as opposed to “corrugated” probes) are not suitable for dielectric samples or the sample preparation - probe metal/Raman probe selection were not suitable. As the main goal of this work is the development of TERS measurements on electroactive substrates, no further effort were engaged on the characterization of non-metallic samples.

The hybrid mode “*Top-mode*” developed by AIST-NT, alternating tapping mode and contact mode for TERS signal collection at each imaging pixel could not be suitably implemented with the manufactured probes, compromising TERS mapping using side illumination. Tip contamination can explain the possible TERS signal observation in tapping mode using side illumination. TERS imaging in tapping mode on the inverted configuration proved successful although the composition contrast suffers from the flaws in the tip-sample distance control.

Finally, the TERS signatures of azobenzene and 4-NBM were successfully acquired in water on the inverted configuration which eases the optical coupling between the Raman probe and the tip apex, with only a 2-3 fold signal intensity damping as compared to the air. The extraction in liquid of the TERS signature of redox-active compound such as 4-NBM self-assembled on metallic substrates, opens the way to the EC-TERS characterization of electrochemical systems presented in Chapter 4.

Chapter 4 - Characterization of electroactive systems by EC-AFM-TERS

Introduction

Characterization of functional material under their condition of operation is the prerequisite to the understanding of their mechanism of operation and degradation. TERS, which combines the advantages of (micro)Raman spectroscopy (rich chemical signature, chemical mapping possible, measurements in liquid due to the weak scattering signal of most solvents), while boosting its sensitivity and spatial resolution, stands as a powerful alternative to ultrahigh vacuum spectroscopy techniques for the *in situ/operando* characterization of nanomaterials.

Still, the difficult optical coupling in liquid, the low signal-enhancing efficiency of TERS-active AFM probes and their sensitivity to wear (especially in liquid) and the difficult implementation of STM-based TERS measurements when not in the ambient, has impaired the fast development of TERS measurements in liquid and under electrochemical conditions (EC).

After the demonstration in 2009 by Zenobi group of AFM-TERS in liquid (point spectra), using an inverted configuration, two successful implementations of EC-AFM-TERS were proposed 10 years later. The first one was by the group of R. Van Duyne in 2019¹⁴⁹ on ITO decorated gold nanotriangles derivatized with Nile Blue compound (Home-made system with bottom illumination, TERS mapping in contact mode) and by the group of B. Ren in 2020 on flat gold sample functionalized with polyaniline¹⁶⁶ (NT-MDT system with top illumination, TERS point spectra in contact mode, electrolyte HCl 0.1 mol.L⁻¹).

After we demonstrated in Chapter 3 the TERS activity in water of the bulk metal probes developed in this work, we propose in this fourth chapter to further push the developments to the implementation under EC conditions. More specifically AFM-TERS measurements will be applied to nitrobenzene derivatives, commonly used in the TERS community (photo-induced coupling of nitro groups), and already studied in the group under electrochemical conditions, first by T. Touzalin in 2017 using “single hot-spot SERS” platforms (TERS active microelectrodes functionalized with para-nitrothiophenol 4-NTP, in acidic medium) and then in a work run in parallel to this one, by A. Fiocco through EC-STM-TERS measurements (gold

electrodes functionalized with para-nitrobenzen mercaptan 4-NBM, in acidic and alkaline medium).

This chapter will first introduce the system of study 4-NBM, its electrochemical properties and then focus on its characterization by EC-TERS using bottom illumination after a few optimizations of the electrochemical conditions for TERS analyses. We will conclude this chapter by introducing our latest developments enabling EC-TERS measurements with side illumination and some associated preliminary results.

4.1. Electrochemical reduction of 4-NBM

4.1.1. Description of 4-NBM

The studied system was selected based on its electroactivity (nitro entity) and ability of being immobilized on a metallic surface (electrode), along with exhibiting clear Raman signatures using enhancement techniques like SERS or TERS (weak far-field contribution). Such organic molecules, terminated with thiol group, can self-assemble onto gold surfaces by chemisorption, creating a bond between sulfur groups and the surface gold atoms (Au-S bond, **Figure 4.1** below).^{167,168} Note that the formation of this bond is still subject to debates.

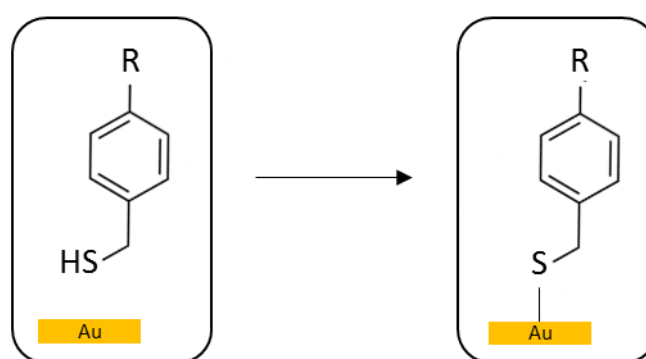
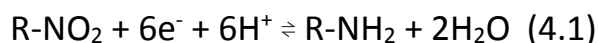


Figure 4.1. Chemical absorptions of thiol group onto the gold surface with the formation of an Au-S bond. The radical R can be any functional group. Electron transport can occur through the molecule backbone and be therefore transfer between the gold electrode and an electroactive radical like NO₂[•], explaining the electrochemical activity of such compounds.

4-NBM vs 4-NTP - The studied system in this work, 4-nitrobenzyl mercaptan (4-NBM) is an aromatic thiol derivative with a redox active nitro group in the 1 position. This model system was preferred to the analogue 4-nitrothiophenol (4-NTP, also referred in the literature as 4-NBT for 4-nitrobenzenethiol), well described in the literature and previously studied in our group by EC-Tip-SERS (Touzalin *et al.*, 2017).¹⁴² Cross-contaminations between successive experiments were indeed observed by Touzalin with 4-NTP. Moreover, strong signal surge leading to the saturation of CCD detector, was observed upon polarization to reductive potential, compromising the dynamic study of its electrochemical reduction. This observation has not been explained. In 4-NBM, the additional carbon between the benzene ring and sulfur as compared to 4-NTP, is expected to provide better stability of the SAM due to the diluted attractive inductive/mesomeric effect of the nitro group on the gold/sulfur bond strength. Strongly attached covalent bond S-Au provides narrowed flexibility of 4-NTP, while additional methylene group of 4-NBM provides supplemental flexibility of the molecular structure and

expands the accessible space of nitro group to react more easily. This was confirmed by the study of A. Fiocco, ran in parallel to this work by STM-TERS.

Similarly to 4-NTP, the nitro group (-NO₂) in 4-NBM may undergo a total six-electron and six-proton reduction into aniline (-NH₂, 4-aminobenzyl mercaptan (4-ABM)):



Electrochemical reduction mechanism - Although the electrochemical transformation of 4-NTP has been intensively studied by electrochemistry alone or combined with Raman spectroscopy (SERS)^{169–173}, the reaction mechanism of 4-NTP is not yet fully understood. The 4-NTP transformation is believed to follow the general reduction process from nitro group (-NO₂) to aniline (-NH₂), through the formation of two intermediates (**Figure 4.2**). The reduction path proceeds with the reduction of the nitro group into nitroso R-NO, then to hydroxylamine R-NHOH, which can be reversibly oxidized back to nitroso or reduced to aniline, depending on the polarization conditions (**Figure 4.2**). This electroreduction process has been under investigation since 1906, described in one of the early work of Haber *et al.*¹⁷⁴.

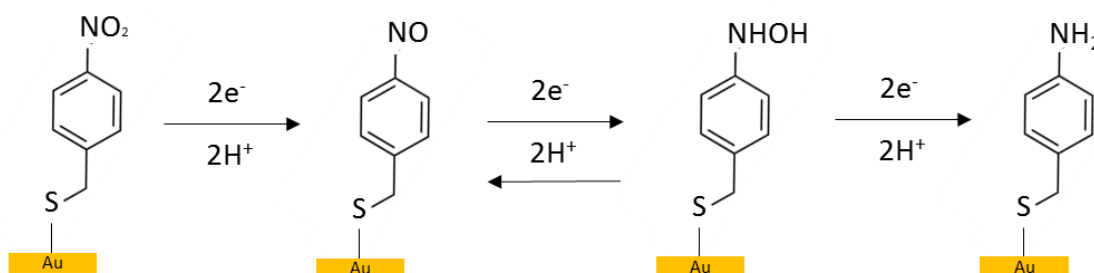


Figure 4.2. Multistep reduction process of 4-NBM molecule adsorbed on gold.

Our group has shown in the previous study of the work of Thomas *et al.*¹⁷⁵ that upon the reduction of 4-NTP in acidic medium, a fast conversion of 4-hydroxylamino-thiophenol (4-HATP) into 4-aminothiophenol (4-ATP) takes place. The highest conversion ratio was obtained in the second cycle and decreased during next cycles, showing full conversion of 4-HATP or remaining 4-NTP into 4-ATP. However, the vibrational modes of possible products/intermediates, 4-nitrosothiophenol (4-NSTP) and 4-HATP, with a signature band of N = O stretching mode, could not be detected during the experiments. The main result about 4-NTP reduction process was the disappearance of the main band at 1335 cm⁻¹, attributed to the NO₂ symmetric stretching, which defined the formation of 4-ATP.

In this new study we aim at characterizing the reduction process in both acidic and alkaline media, to assess possible kinetics limitation inherent to the pH-dependency of the reaction mechanism and to possibly capture reaction intermediates.

Note that an alternative (electrochemical) “bimolecular” path, introduced by Gao *et al.*¹⁷⁶ and recently supported by Fiocco *et al.*, involves a condensation between nitroso and hydroxylamine in the alkaline medium, leading to the formation of 4,4'-dimercaptazoxybenzene (DMAOB), which can be reduced irreversibly into 4,4'-dimercaptazoazobenzene (DMAB). According to Gao, that latter form can further convert reversibly into 4,4'-dimercaptohydrazobenzene (DMHAB) and be finally reduced and formed into two molecules of amino monomers (**Figure 4.3**), although not observed by Fiocco. This bimolecular mechanism, was reported to mainly appear in alkaline medium. Here, the nitrosyl group of 4-NSBM becomes highly electrophilic¹⁷⁷, which accelerates its reaction with 4-HABM and their formation into DMAOB.

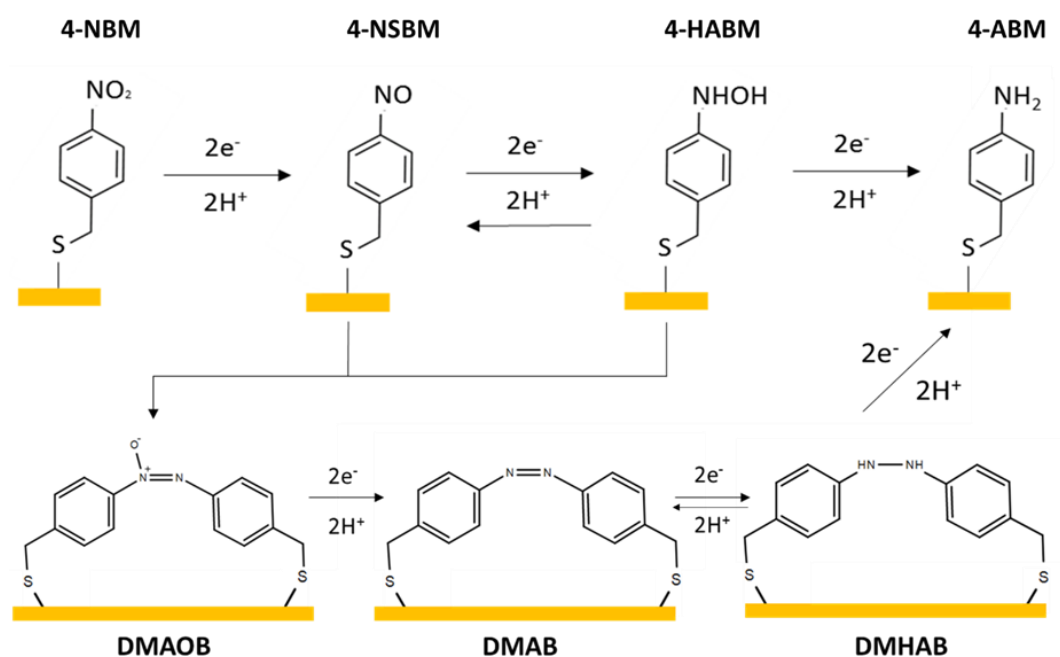


Figure 4.3. Possible electrochemical reaction paths for the reduction of 4-NBM into 4-ABM.

Photo-induced dimerization - Another way of forming azo bonds has been observed via photo-induced dimerization with plasmonic tip-induced reactions (TERS study), which has been first reported by Deckert and Weckhuysen group.¹⁷⁸ Tip-catalyzed process formed dimer *p,p'*-dimercaptazoazobenzene (DMAB) from 4-NTP and 4-,4'-dimercaptomethanazobenzene (DMMA) from 4-NBM by dimerization process with the new N=N bond (azo bond) along with

disappearance of the NO₂ nitro group.¹⁷⁹ This effect, observed on silver AFM tip silver SERS substrate illuminated with a green laser (532 nm), is explained by the charge transfer between the metal and the molecules, combined to the local photo-induced temperature-rise¹⁸⁰. This effect is expected to be minimized in liquid and under illumination at 633 nm, but may still occur. In the STM-TERS work of A. Fiocco *et al.*¹⁸¹ though, 4-NBM layers in contact with alkaline buffer, were subjected to increasing illuminating power, from 250 μW to 4 mW. Dimer formation was not detected upon irradiation, only an increase in the background signal as shown on **Figure 4.4**.

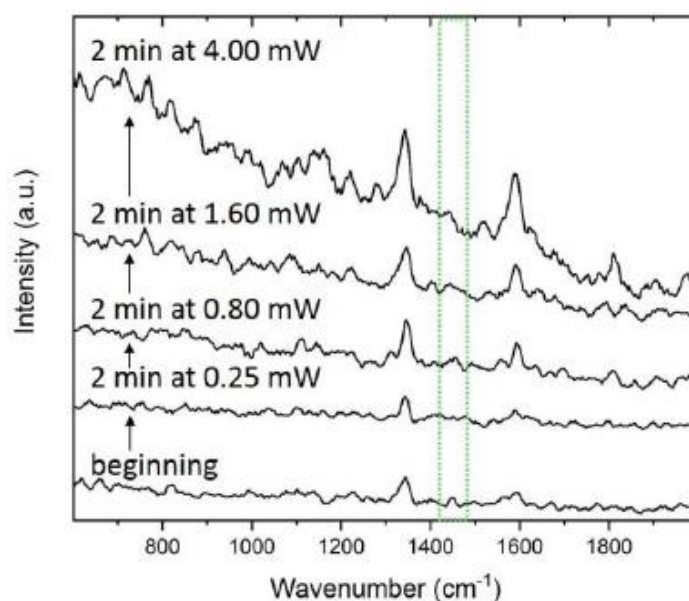


Figure 4.4. Influence of the irradiance of the Raman probe. STM-TER spectra acquired in the alkaline buffer after a 2-min irradiation of the sample using a red laser (632.8 nm) at increasing illuminating power (original source power increasing from 250 μW to 4 mW (1.56% to 25% of the nominal laser power), BV = 0.1 V, IT = 1 nA). Each spectrum was acquired for 1 s and the tip was let scanning during the whole experiment. The spectra have been lightly smoothed, while the background was not removed. The green dotted lines identify the range where the “dimer” bands should be observed.¹⁸¹

4.1.2. Electrochemical signature of 4-NMB on model electrodes

SAM formation protocol - Self-Assembled Monolayers (SAM) of 4-NBM were prepared on various gold substrates and electrodes (3 mm diameter gold disk electrode, Orignalys) by contact, for approximately 3 hours¹⁶⁸ in the 4-NBM solution (ethanolic solution with a concentration of 10⁻⁴ mol.L⁻¹ from the initial stock powder, Sigma Aldrich), then rinsing thoroughly for 30 minutes in absolute ethanol under gentle steering to remove physisorbed 4-NBM moieties. Finally, functionalized surface were dried under an argon gas flow. Note that the 3 mm disk electrode was previously polished with alumina and polarized (cyclic

voltammetry) in a 5 mmol.L⁻¹ sulfuric acid (H₂SO₄) for surface reconstruction, prior each functionalization and electrochemical experiment.

Electrochemical characterization - All electrochemical measurements were performed on a 3-electrode system (saturated calomel electrode (SCE), platinum (Pt) or silver (Ag) electrode as the reference electrode and platinum (Pt) ring as counter electrode), an Autolab potentiostat (model *PGSTAT100N*, Metrohm) and an electrochemical argon-purged cell to prevent reaction/interference with dissolved oxygen. The cell was filled with either 50 mmol.L⁻¹ (pH = 1.1) or 5 mmol.L⁻¹ (pH = 2.3) sulfuric acid, when working in acidic medium. The chosen alkaline medium was bicarbonate buffer, prepared by mixing 100 mL of 0.05 mol.L⁻¹ NaHCO₃ (NORMAPUR®) and 40.4 mL of 0.1 mol.L⁻¹ NaOH (Carlo Erba) with the final pH 10.7. The pH of the buffer is low enough to ensure the protection of the optics and optomechanical parts on the TERS set-up, while the concentration of ionic species is still high enough to minimize electrolyte resistance and associated ohmic drop.

The EC analyses presented in the following, were obtained on gold disk electrode (as WE) during electrochemical sequence of approximate scan range between 450 mV to -350 mV in acidic medium and between 0 V and -900 mV in alkaline, with scan rate 50 mV.s⁻¹.

Acidic vs alkaline medium - The electrochemical signature (cyclic voltammetry, 50 mV.s⁻¹) of 4-NMB functionalized gold electrode in a 5 mmol.L⁻¹ H₂SO₄ solution was first evaluated and presented on **Figure 4.5**. During the first cycle (highlighted in blue), an irreversible peak appears at -290 mV on the first forward potential scan, together with a reversible oxidation peak at +230 mV vs Ag, on the backward scan. The reversible reduction peak is seen in the beginning of the second cycle and following cycles.

The reversible oxidation/reduction peak is the outcome of the 4 electron and 4 proton reduction from the initial 4-NBM (4-nitrobenzyl mercaptan) to 4-HABM (4-hydroxylamine benzyl mercaptan), possibly followed by the 2 electron and 2 proton exchange reaction between 4-HABM and 4-NSBM (4-nitroso benzyl mercaptan). Note that the anodic peak intensity decreases after the first cycle, indicating that a fraction of the 4-HABM, formed during the first cycle, has been irreversibly reduced during the second one and is no longer electrochemically active (on the screened potential range).

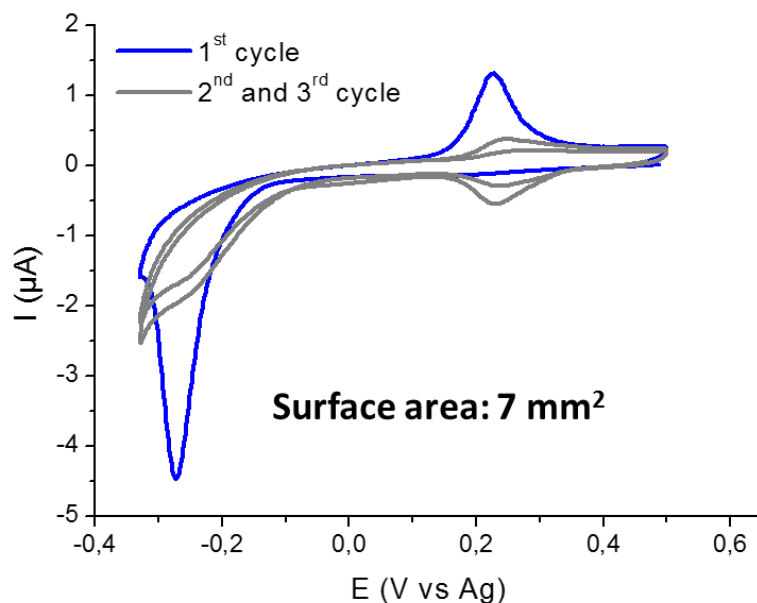


Figure 4.5. Electrochemical reduction of a 4-NBM in acidic medium - Electrochemical response (cyclic voltammetry) of a 4-NBM functionalized gold disk electrode (diameter 3 mm, electrode surface 7 mm²) in a 5 mmol.L⁻¹ H₂SO₄ solution (scan rate: 50 mV.s⁻¹, silver wire pseudo-reference electrode). Nitro group of 4-NBM may partially reduce to hydroxylamine below -100 mV and reversibly oxidized into nitroso at +230 mV.

The results are consistent with the ones of 4-NTP described in the literature, as well as in the work of T. Touzalin (reduction of 4-NTP observed during EC-tip-SERS experiments on a functionalized TERS-active gold tip in acidic medium).¹⁷⁵

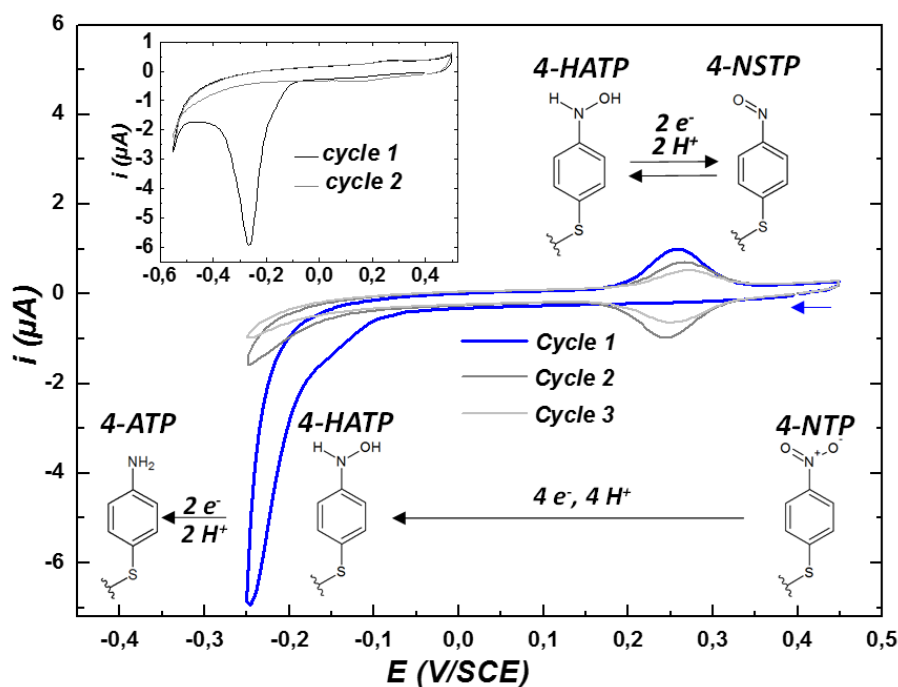


Figure 4.6. Electrochemical reduction of a 4-NTP in acidic medium. A 4-NTP functionalized gold sphere electrode was subjected to cyclic voltammetry (CV) in a 50 mM H₂SO₄ solution (scan rate: 100 mV.s⁻¹) with a -250 mV vs SCE vertex potential. 4-NTP is partially reduced to 4-hydroxylamine thiophenol (4-HATP) below -100 mV vs SCE. 4-HATP is reversibly oxidized into 4-nitrosothiophenol (4-NSTP) at +241 mV vs SCE. Reproduced from [142].

Note that the molecular surface coverage can be evaluated from the integration of reductive and oxidative currents on the voltammograms^{181,182}. For 4-NBM, it has been calculated as $7.06 \times 10^{-10} \text{ mol.cm}^{-2}$, which is consistent with values reported earlier for 4-NTP, implying (together with the symmetrical bell shape of the current peaks) that 4-NBM is well anchored on the gold surface in an ordered monolayer.

Reduction of 4-NBM was then investigated in alkaline medium to extend the probability to observe possible reaction intermediates by TERS (not reported in acidic medium in the previous study of T. Thomas *et al.*, as mentioned earlier), as the nitrobenzene reduction mechanism, and possible life time of reaction intermediate, is pH-dependent. Similar to the results in the acidic medium, the CV in alkaline medium shows a main reduction peak and the reversible oxidation/reduction peak (**Figure 4.7**). Note that the current, associated to the reversible peak, does not drop in alkaline medium as fast as in acidic medium, implying that the irreversible conversion/electrochemical reduction of possible intermediates to the amino compounds is less favored.

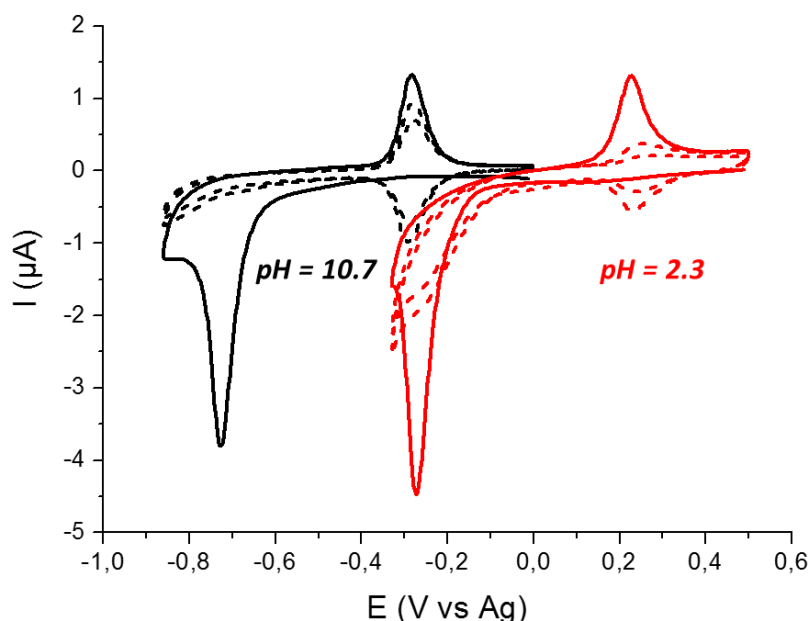


Figure 4.7. Influence of the pH on the electrochemical response of 4-NBM. Cyclic voltammetry acquired on 4-NBM absorbed on gold electrode, showing response of a 4-NBM in alkaline medium of bicarbonate buffer solution (black curve, 0/-900 mV) and in a $5 \text{ mmol.L}^{-1} \text{ H}_2\text{SO}_4$ solution (red curve, scan range +500/-300 mV). The solid and dotted lines represent the first and the second cycles, respectively. The scanning rate was 50 mV.s^{-1} .

4.2. Experimental design for EC-TERS on transparent samples

This section covers different developments and optimizations, associated with EC-TERS implementation in AFM mode, and also few control and optimization steps, regarding the electrochemical performance of the TERS cell, based on the electrochemical response of 4-NBM.

4.2.1. Electrochemical cell for EC-TERS using bottom illumination

Significant efforts have been engaged in this work to improve the TERS compatible electrochemical cell, initially developed in Touzalin's work in LISE for Tip-SERS and STM-TERS measurement (see **Figure 4.8**), and to adapt it to the inverted microscope constrains. Ease in mounting/dismounting of the cell/sample assembly and of the electrodes, leakage-proof of the cell, and especially reproducibility, have driven the design optimization.

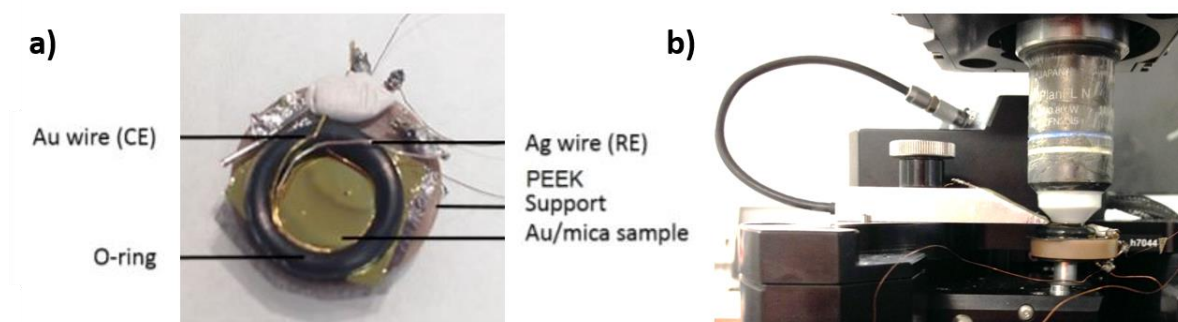


Figure 4.8. First TERS-compatible electrochemical cell developed in the group (2018): **a)** 3-electrode cell prototype and **b)** set-up showing the cluttered arrangement of the EC-Cell including a STM tip-holder (conductive unit behind) and a water-dipping objective lens. Adapted from [175].

A newly designed AFM EC-cell, composed of a flat PEEK ring (Polyether Ether Ketone, 30mm internal diameter), is maintained on the ferromagnetic substrate/sample holder by a series of magnetic disks. Dimensions of the cell were chosen to accommodate the bulky AFM probe-holder, specifically designed for measurements in liquid media. The air objective with the magnification of 100x and NA 0.7 was used as described in Chapter 3. An O-ring (30 mm internal diameter), sandwiched between the cell and the substrate, prevents any leakage of electrolyte, while defining the active area of the electrode. The cell is filled with 0.5 mL electrolyte. A platinum wire (CE) with a ring shape is positioned inside the cell, together with a pseudo-reference electrode (silver or platinum). The reference and counter electrodes are maintained firmly in place over the cell magnets through the use of small insulated

ferromagnetic plates. The electrical contact on the working electrode is achieved by direct contact on the gold surface outside of the cell. Approximately 10 cm long electrical wire of small section (flexible to minimize mechanical coupling with the AFM piezo-stage) are connected to the WE, pseudo RE and CE electrode and extended with shielded wires connected to a potentiostat (model *Autolab PGSTAT100N*, Metrohm), to minimize electrochemical noise initially observed on CVs (**Figure 4.9** below).

As mentioned in Chapter 3, semi-transparent gold sample, developed in LISE lab as platform for SAM functionalization, proved suitable for their subsequent characterization by AFM-TERS in the inverted configuration. These surfaces made of only 10 nm thick gold layer and 2 nm thick titanium adhesive sublayer deposited on glass coverslips, show an electrical continuity and a conductivity ($R \leq 40 \Omega$; 30-40 Ω) suitable for electrochemical measurement and then for EC-AFM-TERS. 4-NBM-derived gold surfaces were prepared in a similar way as gold disk electrodes (see paragraph **4.1.2**).

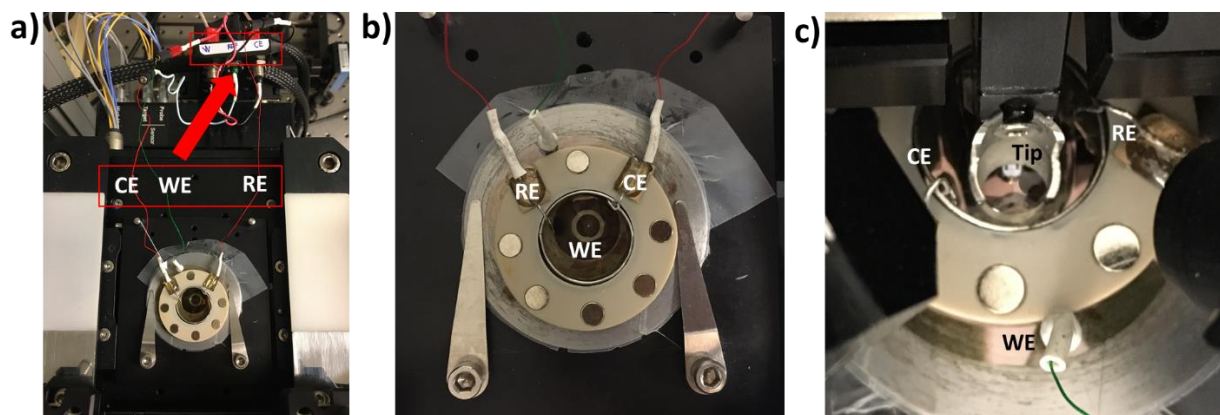


Figure 4.9. Electrochemical TERS-ready set-up. Homemade EC-AFM cell mounted on the inverted microscope (*Combiscope*, AIST). The pseudo-reference (Pt or Ag wire) and counter electrodes (Pt ring) are immobilized on the cell wall through magnets, the electrical contact on the working electrode is achieved by direct contact on the gold surface outside of the cell. The 100x dry objective, enabling bottom illumination, can be seen through the semi-transparent but conductive gold sample (middle picture). The cell dimensions were chosen to host the bulky AFM tip holder design for liquid experiments (right picture).

4.2.2. Optimization of electrochemical conditions for TERS analyses

The aim of the following optimization is to assess the performance of the EC-cell, since this latter is open to the ambient (no environment control) and possibly uses large working electrode area.

4.2.2a – Electrochemical behavior in the ambient

The presence of highly soluble oxygen in aqueous electrolytes is likely to alter the electrochemical response of analytes during electrochemical experiment. To avoid any interference with dissolved oxygen during EC reaction, electrolytes can be purged with inert gas (nitrogen, argon) prior to the measurements. A constant flow of inert gas is usually maintained above the cell during the measurements to minimize further oxygen contaminations.

4-NBM derivatized gold electrodes (gold disk electrode 3 mm diameter) were subjected to CVs in contact with carbonate buffer electrolytes purged or not with argon. A saturated calomel reference electrode (SCE) and a pseudo-reference electrode (a silver or platinum wire) were tested successively. The voltammograms are presented on **Figure 4.10**. When the electrolyte is not purged with argon, one can notice the onset of the oxygen reduction around -0.3 V (vs SCE), which superimposes to the reduction current associated with 4-NBM around -0.8 V (**Figure 4.10b**). An additional reduction process seems to take place around -1 V, without however altering much the reversible peak observed around -0.3 V. Electrolyte was then systematically purged with argon prior to the TERS experiments. To minimize reintroduction of oxygen in the electrolyte with time, an argon flow was initially maintained above the EC cell, however without proven efficiency as the atmosphere above the inverted microscope cannot be easily controlled without a strong argon flow, which induces in turn mechanical noise.

When working with the pseudo RE, an important shift of potential (c.a. 150 mV) in the electrochemical response appears (see the voltammogram on **Figure 4.10a**), which originates from a change of the silver wire potential due to a modification of its surface composition in contact with oxygen in alkaline conditions. As the potential of the silver wire may change with exposure to oxygen during experiment, a platinum wire (less prone to oxidation) was preferred in alkaline electrolyte. If the presence of oxygen affects the reactivity of the SAM functionalize electrode, as can be seen on **Figure 4.11**, shift in the current-potential response are minimized.

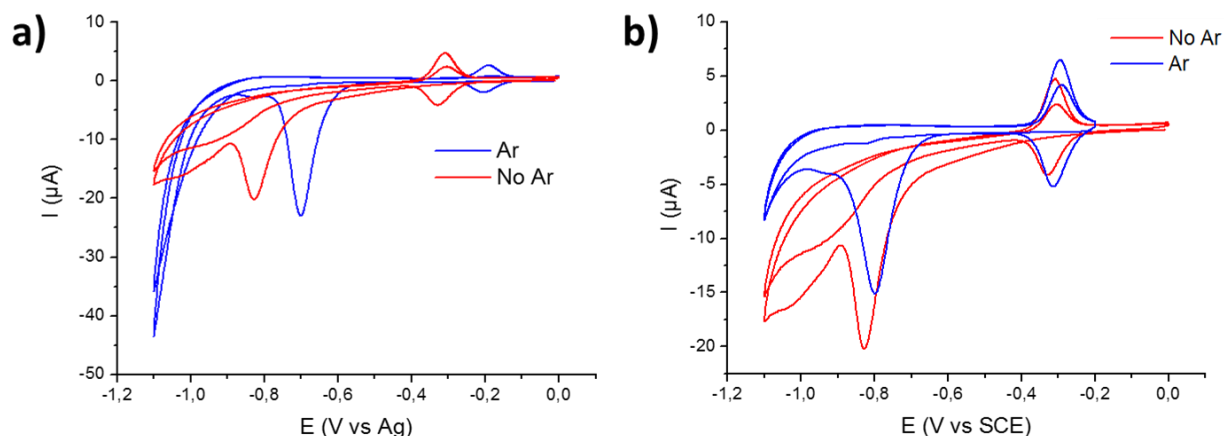


Figure 4.10. Influence of oxygen - Electrochemical response (CV, scan rate $50 \text{ mV}\cdot\text{s}^{-1}$) of a 4-NBM functionalized gold disk electrode in alkaline electrolyte (carbonate buffer) in the absence (blue) or in the presence of oxygen (red): **a)** using a silver wire pseudo reference electrode, **b)** using a reference electrode (SCE).

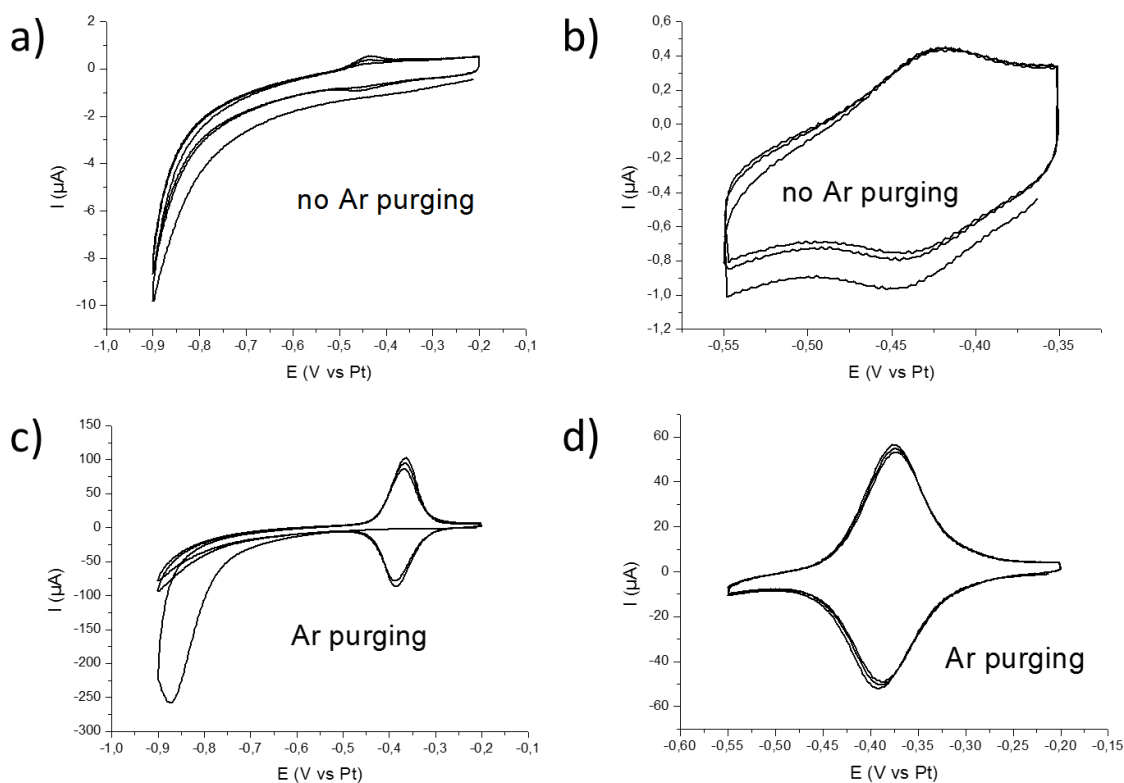


Figure 4.11. Influence of oxygen on the performance of the TERS compatible EC-cell. Electrochemical response (CV, scan rate $50 \text{ mV}\cdot\text{s}^{-1}$) of a 4-NBM functionalized gold disk electrode (electrode surface, 7 mm^2) in alkaline electrolyte (carbonate buffer) in the absence (**c, d**) or in the presence (**a, b**) of oxygen using a pseudo platinum reference electrode.

4.2.2b – Electrode dimensions

The electrochemical response of the gold transparent working electrodes in the homemade EC-AFM cell was assessed prior to *in situ* measurements. The EC-cell, designed to

accommodate the liquid AFM probe holder, uses large sample (working electrodes), a 0.5 mL volume of electrolyte and a positioning of the reference electrode at some distance of the probe area (1 cm). The uncompensated resistance (electrolyte resistance mostly) and capacitive current, associated with such large electrode upon polarization, may impact respectively the surface homogeneity of the reaction and the potential sweeping rate accessible respectively.

The electroactive surface of the sample can be minimized by patterning the active gold surface using masks during the Ti/Au deposition process. The small active area (approximately in the middle of the sample) can be either contacted electrically in the cell, using a contact immersed in the electrolyte (solution chosen for the cell designed for side illumination, see section 4.4), or outside on a strip of metal deposited on the glass substrate and connected to the electrode area. These two configurations may result in high contact resistance (example (a) on **Figure 4.12** below) or additional electrochemical reaction on the contact, risk of delamination/damage of the metal strip in contact with the cell O-ring (and/or with the electrolyte), or non-uniform reactivity at the electrode due to the non-symmetrical current path (**Figure 4.12b**). An alternative consists in partially coating the metal exposed to the electrolyte with insulating layers, inorganic (silica, alumina) or polymeric (**Figure 4.12c**).

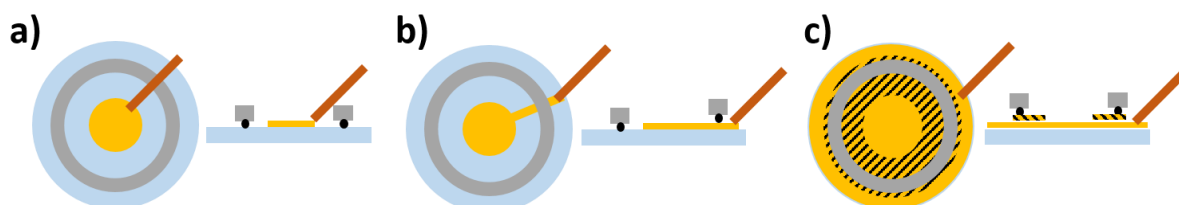


Figure 4.12. Different strategies to minimize the active surface of the electrode (top and side view): a) electrical contact within the cell through the electrolyte, **b) & c)** contact outside or the cell (glass substrate in blue, gold electrode in yellow, electrical contact in red, insulating coating: hatched area).

This latter option was tested in this work. *Zapon* varnish (Laverdure, Paris), which our group uses to partially insulate STM-TERS tips for applications in liquid, was applied on the surface of the gold-coated glass substrates. The size of the working electrode was thereby decreased to a size comparable to the commercial standard gold disk electrode with the diameter of 3 mm (surface of approximately 7 mm²). *Zapon* varnish was precisely applied onto the sample surface and hardened in the furnace at 80°C for approximately 10 minutes.

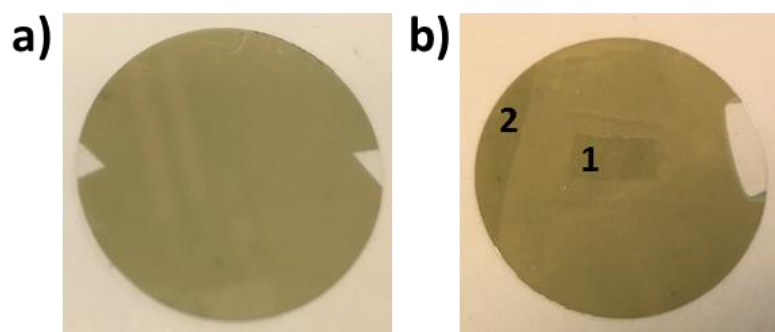


Figure 4.13. Partial insulation of the gold surface - Picture showing before (a) and after (b) substrate surface decrease (Au on glass coverslip) by using *Zapon* varnish. The area noted 1 and 2 are left uncoated, 1 defining the active area of the electrode, which will be in contact with the electrolyte and 2 the area where the electrical contact is established.

The electrochemical responses (CVs at $50 \text{ mV}\cdot\text{s}^{-1}$) of immobilized 4-NBM on coated and non-coated surface, were probed and compared in the TERS EC-cell filled with a carbonate buffer solution (see **Figure 4.9**). The large capacitive current, observed on the voltammograms of non-coated surface, is drastically reduced on coated electrodes (**Figure 4.14a**). Moreover, the resistive behavior observed on large electrodes, which can be evaluated from the splitting of the redox pics around the voltammogram, tends to be reduced on smaller electrode (18 mV and 27 mV, respectively). By partial coating of the electrode surface with *Zapon*, the effect of the uncompensated resistance can be reduced even at scan rates as high as $100 \text{ mV}\cdot\text{s}^{-1}$, as can be seen on **Figure 4.15**.

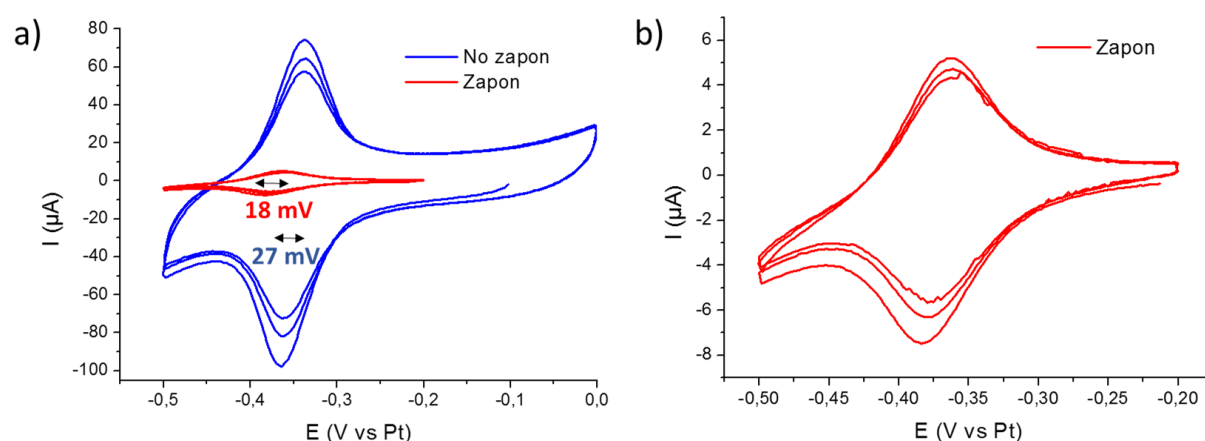


Figure 4.14. Influence of the electrode surface in the EC-TERS cell: a) CV responses (scan rate $50 \text{ mV}\cdot\text{s}^{-1}$) of 4-NBM in homemade AFM liquid cell in alkaline medium (bicarbonate buffer $\text{NaOH}/\text{NaHCO}_3$, Pt pseudo-reference electrode) before and after decrease of the electrode surface with *Zapon* varnish, b) the peak separation which traduces the uncompensated ohmic drop is around 18 mV after partial insulation of the electrode.

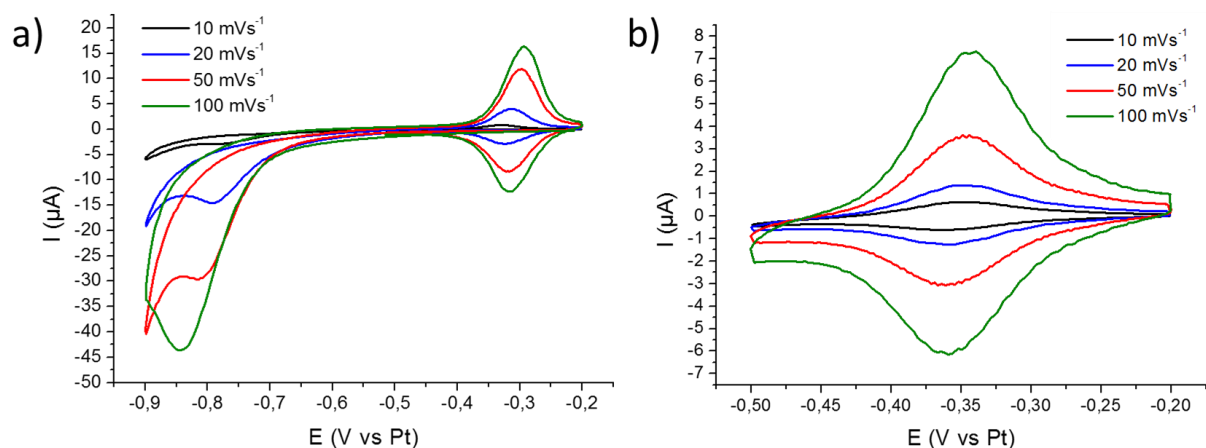


Figure 4.15. Influence of scan rates on partially coated electrodes in TERS compatible EC-cell: **a)** full scan range (-200/-900 mV); **b)** reversible peak (scan range -200/-500 mV). Alkaline medium (bicarbonate buffer), Pt pseudo-reference electrode.

4.3. Study of 4-NMB electrochemical reduction by EC-TERS

4.3.1. *Ex situ* TERS characterization

4-NBM functionalized gold samples (gold on mica) were first analyzed by *ex situ* TERS; before and after their electrochemical reduction in acidic medium. A potential ramp from +200 mV down to -700 mV with a $2 \text{ mV}\cdot\text{s}^{-1}$ scan rate was applied to the sample. The latter was mounted in the home-made 3-electrode cell, which was filled with a $5 \text{ mmol}\cdot\text{L}^{-1} \text{ H}_2\text{SO}_4$. A 100 nm gold layer, deposited on mica, was used as WE, a platinum ring as CE and a silver wire as pseudo-reference electrode.

TERS measurements were acquired in the ambient, using the home-made gold probes in the upright configuration with side illumination (100x dry objective, $\text{NA} = 0.7$, acquisition time 1 s, 3 accumulations, excitation wavelength 632.8 nm, laser power 1% of the nominal laser power $\sim 160 \text{ }\mu\text{W}$). The TERS spectra in **Figure 4.16** shows 4-NBM signature bands, obtained before and after the potential ramp.

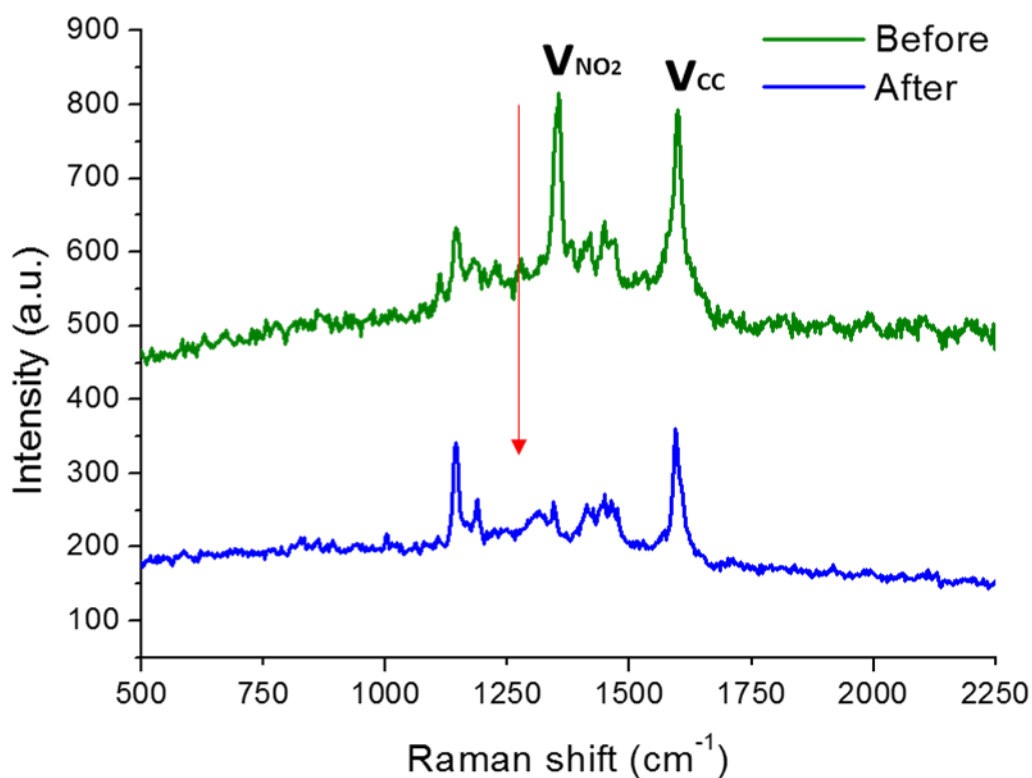


Figure 4.16. *Ex situ* TERS on gold coated mica substrates functionalized with 4-NBM – TERS spectrum before (green) and after (blue) reduction in acidic medium; $\lambda_{\text{exc}} = 632.8$ nm, laser power ~ 160 μW , 1 s acquisition.

The spectral feature can be compared to the one of 4-NTP (and 4-ATP), already studied by T. Touzalin (see Table 4.1). Before reduction, the characteristic 4-NBM bands were observed at 1340 cm^{-1} (NO_2 stretching band) and at 1590 cm^{-1} (C=C ring stretching band). The main observation after applied potential ramp, was the drastic decrease in intensity of the NO_2 band as the C-C stretching band stays almost unchanged (only slightly shifted) (**Figure 4.16**). This indicates the almost complete nitro reduction at reductive potential down to -700 mV .

Table 4.1. Main spectral features of 4-NTP and its fully reduced analogue 4-ATP – vs: very strong, s: strong, m: medium, w: weak intensities.^{142,175}

Molecule	Vibration	Raman shift (experimental)
4-NTP	Ring breathing	1079 m (1080, m)
	C-H bending	1100 s (1110, s)
	C-H bending	1181 m (1180, w)
	NO_2 symmetric stretching	1335 vs (1335, vs)
	C=C stretching	1577 s (1570, s)
4-ATP	C-S stretching	1089 vs (1080, s)
	C-H bending	1173 m (1180, m)
	C=C stretching	1593 s (1588, s)

The slight dissimilar structure of 4-NTP and 4-NBM (extra methyl group) explains the small red shift in energy of the main Raman bands. A recent SERS study of W. Koopman *et al.*¹⁷⁹ showed comparison of band positions between 4-NTP and 4-NBM, assembled on gold nanotriangles. The experimental results of their work showed C-H symmetric band assigned at 1078 cm^{-1} and 1107 cm^{-1} , NO_2 symmetric stretching at 1332 cm^{-1} /1334 cm^{-1} and C=C stretching at 1575 cm^{-1} /1594 cm^{-1} for 4-NTP/4-NBM, respectively.

During the reduction process of 4-NBM, additional bands originating from the intermediate 4-HABM ($4e^- 4 \text{H}^+$ partial reduction of 4-NBM) are expected, if the reduction is not complete. CH bending and CN stretching are expected to be seen in the 1110-1200 cm^{-1} range and NO stretching in the 1300-1400 cm^{-1} range. However, T. Touzalin suggested that with 4-NTP the very fast conversion (72.5 %) of 4-HATP to 4-ATP in acidic medium prevented its observation by enhanced-Raman.

Upon laser illumination of 4-NTP, 4-NBM self-assembled on SERS substrate, photodimerization, leading to an azobenzene derivative can be expected¹⁷⁹, especially in the air when using a 532 nm Raman probe. The azobenzene Raman bands have been reported to appear in the region between 1075 and 1200 cm^{-1} and from 1400 to 1540 cm^{-1} . Experimentally, the bands were found at 1137, 1383 and 1434 cm^{-1} , assigned to C-H scissoring, C-N symmetric stretching and N=N stretching vibrations, respectively.

The reference spectra of possible reaction products, extracted from [181], are given in **Figure 4.17**. Note that these chemical signatures were collected on powders of the different compounds and may differ significantly from the one of the corresponding SAM of thiolated derivatives, especially in contact with electrolyte (see part **4.3.2b**).

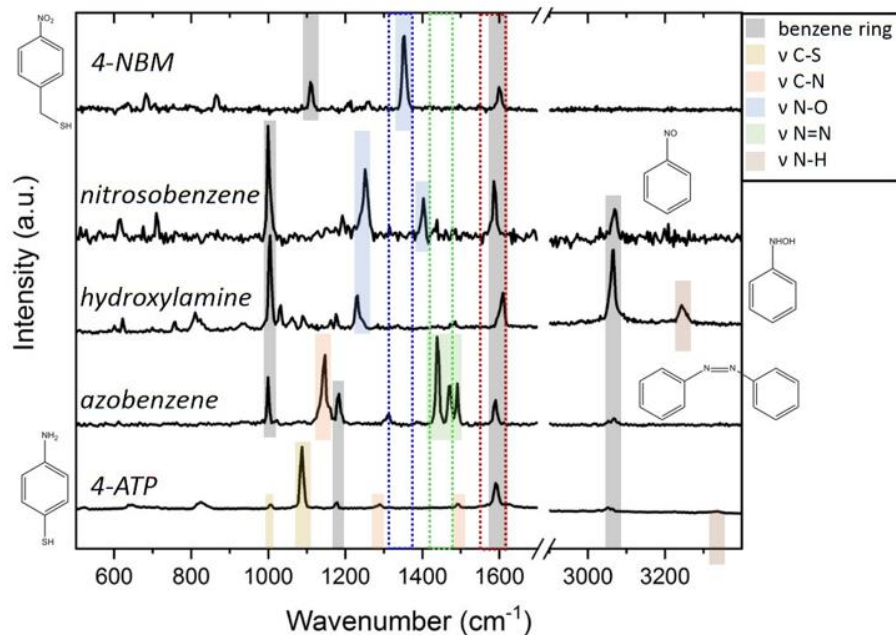


Figure 4.17. MicroRaman signature of 4-NBM powder and of benzene derivative analogue powder. Adapted from [181].

The Table 4.2, reprinted from A. Fiocco's work¹⁸¹, gathers the main spectral features of the nitro benzene derivative, of the reduced monomeric forms (hydroxyamino-, nitroso-, and amino) and of the so-called dimeric form (azobenzene derivatives DMMA and DMAB).

Table 4.2. Characteristic Raman bands for 4-NBM and its main predicted products of the reduction (4-ABM, 4-NSBM, 4-HABM, azobenzene) with band assignment from the literature of the 4-NTP reduction. The values in the parentheses correspond to the EC-TERS experiment in the alkaline medium on the transparent gold substrate, observed with the TERS-active gold tip. Intensities: vs, very strong; s, strong; m, medium; w, weak. The references in bold have been taken from the literature, experimentally observed and assigned to 4-NBM.¹⁷⁹

Attribution	Raman shift (cm ⁻¹) TERS on adsorbates	Raman shift (cm ⁻¹) μRaman on powder	References
Nitrobenzene			
δ (C-H)	1107 w (1098 w) 1078 & 1107	1100 m (1108 m)	176,177,179
CH ₂ wagging + ring stretching	1220 w (1222 s)	1220 w (1222 s)	183
ν (N-O) _{sym}	1346 vs (1339 vs) 1332 (4-NTP) / 1334 (4-NBM)	1352 vs (1346 vs)	176,177,179
Ring stretching	1594 s (1586 s) 1575 (4-NTP) / 1594 (4-NBM)	1600 s (1586 s)	176,177,179
Monomers			
δ (C-H)	1165 m, 1504 w (1170 w, 1494 w amino) 1110-1200	1001 vs (1002 vs nitroso) 1005 s (996 m hydroxylamine) 1177 w (1178 w amino)	175,176,179,183

v (C-S) + ring modes	/	1006 w, 1087 vs (1002 w, 1076 vs amino)	183
v (C-N) + ring modes	1309 w	1288 w, 1493 vs (1284 w, 1484 w amino)	176,183
v (N-O)	1343 m (1332 m nitroso) 1300-1400	1252 m + 1403 m (1265 s + 1407 m nitroso) 1230 m (1230 hydroxylamine)	175,176,179,184
Ring stretching	1592 s (1589 s nitroso, 1585 s hydroxylamine, 1595 s amino)	1587 s (1593 s nitroso) 1606 m (1585 m hydroxylamine) 1591 s (1588 s amino)	176,183
v (C-H)	/	3067 w (nitroso) 3020 s (hydroxylamine) 3054 w (3055 s)	185
v (N-H)	/	3244 w (hydroxylamine) 3336 w (3355 m amine)	185
Dimers			
δ (C-H)	1075-1200 (1137 experimentally) (azobenzene: DMMA/DMAB)	1000 m, 1183 m (1002 s, 1182 m azobenzene)	176,179,186
v (C-N) + ring modes	1138 s (1144 s azoxybenzene, 1146 s azobenzene)	1146 s (1147 s azobenzene)	176,186
v (C-N)_{sym}	1383 (azobenzene DMMA/DMAB)	/	179
v (N=N) + ring modes	1408 m, 1452 s (1388 m, 1424 s, 1463 w azobenzene) (1434 experimentally; azobenzene DMMA/DMAB)	1439 vs, 1471 m, 1491 m (1440 vs, 1472 m, 1492 m azobenzene)	176,179,186
Ring stretching	1578 m (1590 m azoxybenzene, 1592 m azobenzene)	1589 m (1590 m azobenzene)	176,186

4.3.2. Real-time tracking of composition changes by *in situ* TERS

4.3.2a - 4-NBM reduction in acidic medium

EC-TERS characterization of 4-NBM functionalized gold electrodes was first performed in acidic medium (5 mmol.L⁻¹ H₂SO₄, previously purged with Ar gas) on the inverted microscope.

TERS spectra were initially collected at the OCP to optimize the tip-laser alignment. Objective mapping was first performed in the electrolyte at the OCP (laser power 160 μW, acquisition time 0.3 s, number of pixel 15 x 15 px²), it shows a localized hot spot as seen on **Figure 4.18**, with no contribution of the far-field signal. No signal originating from sulfate ions

in the electrolyte (symmetric stretching mode of the SO_4^{2-}) has been observed during hot spot screening by contrast with the EC STM-TERS results, reported by T. Touzalin *et al.* using top illumination (see Chapter 1, **Figure 1.15a**). This can be explained by the 10-fold higher concentration of electrolyte used by Touzalin (Na_2SO_4 50 mM) and the long working distance of the water dipping objective (WD : 3 mm).

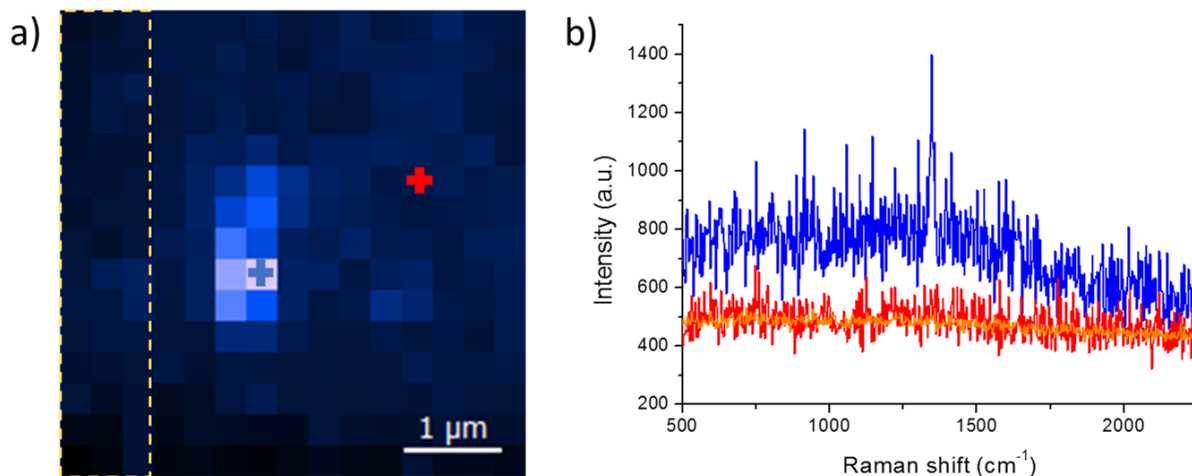


Figure 4.18. Hotspot screening in acidic medium: a) $5 \times 5 \mu\text{m}^2$ XY objective mapping before EC-TERS 4-NBM reduction (at the OCP) in acidic medium ($5 \text{ mmol.L}^{-1} \text{H}_2\text{SO}_4$) obtained by integration of localized hot-spot position obtained by integration of the Raman band at 1340 cm^{-1} of 4-NBM b) associated acquired TER spectra at the exact hotspot (blue), slightly away (red: FF/background) and averaged spectrum for the dashed rectangle area on the objective map (orange); $\lambda_{\text{exc}} = 632.8 \text{ nm}$, laser power $\sim 160 \mu\text{W}$ (1% of the nominal laser power), 0.3 s acquisition.

The TERS signal intensity extracted at low laser power ($\sim 160 \mu\text{W}$) and short acquisition time (0.3s) in the electrolyte during hotspot mapping (acidic here but also alkaline hereafter), enabled the collection of clear high intensity point TERS spectra of 4-NBM SAM at acquisition time as low as 1s (see experiment in alkaline medium).

The potential-dependent TERS response of 4-NBM was then evaluated between 200 mV and -700 mV vs an Ag pseudo-reference electrode (potential ramp, scan rate 2 mV.s^{-1} , acquisition time 10s, each spectrum covering 20 mV).

The obtained voltammogram on **Figure 4.19a** displays a unique cathodic peak at -570 mV vs Ag. The shift of the reduction peak towards more negative potentials ($\sim -100 \text{ mV}$), as compared to the one presented on **Figure 4.5** (gold disk electrode, H_2SO_4 5 mmol.L^{-1}), may origin from the uncompensated resistance (low concentration electrolyte, small surface counter-electrode). Note that the strong H_2 evolution at $E < 600 \text{ mV}$ may explain the observed discontinuity in the current profile, but did not affect the TERS collection signal.

The TERS signature evolution with the potential is presented in **Figure 4.19b**. The progressive disappearance of the NO_2 band attests of the effectiveness of reduction process of the 4-NBM SAM. The spectrum obtained at -700 mV shows no NO_2 band, indicating that the molecular layer is fully reduced and not desorbed under negative polarization as attested by the ring stretching bands of high intensity around 1600 cm^{-1} .

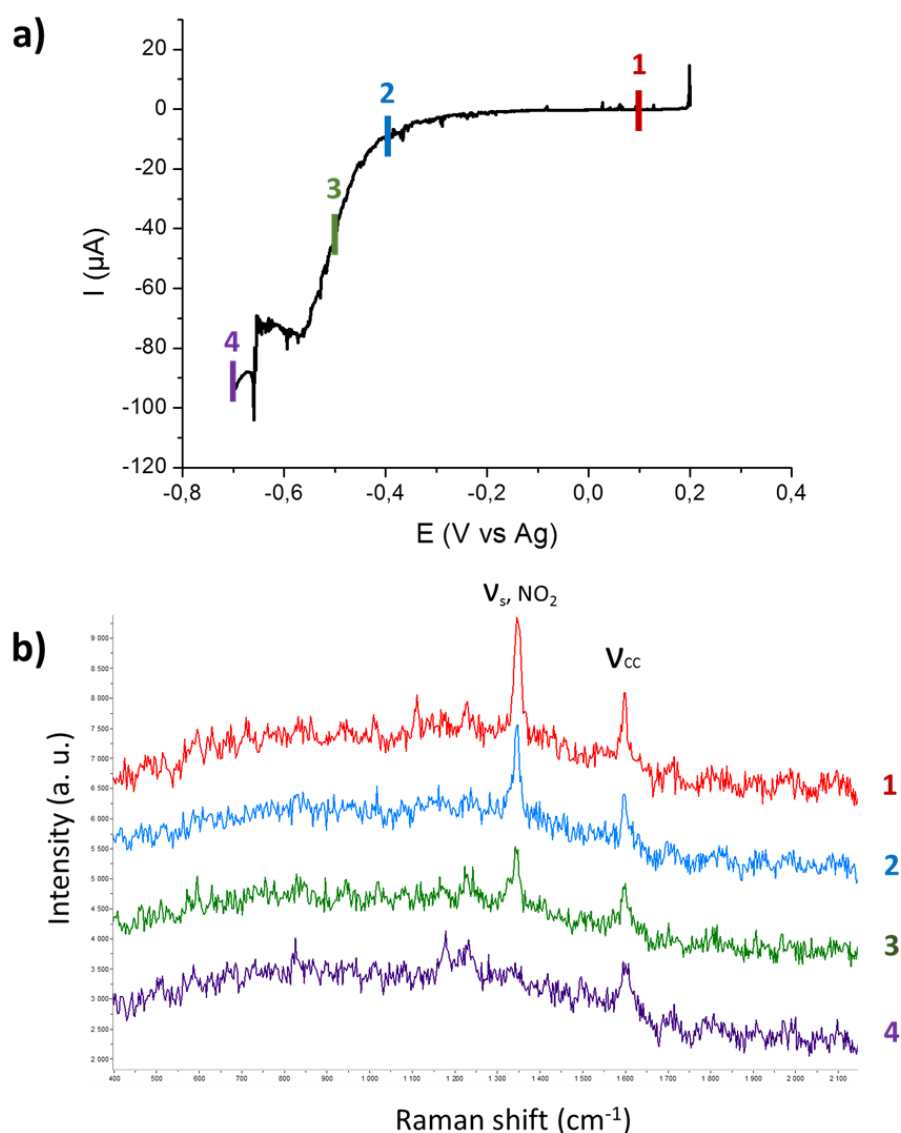


Figure 4.19. EC-TERS tracking of the 4-NBM reduction in acidic medium: a) voltammetry (potential ramp, scan rate $2\text{ mV}\cdot\text{s}^{-1}$) in $5\text{ mmol}\cdot\text{L}^{-1}\text{ H}_2\text{SO}_4$ showing a main reduction peak at -570 mV vs Ag ; **b)** TERS spectra showing the total disappearance of NO_2 band upon reduction: 100 mV (1), -400 mV (2), -500 mV (3), -700 mV (4). $\lambda_{\text{exc}} = 632.8\text{ nm}$, laser power $\sim 160\text{ }\mu\text{W}$ (1% of the nominal laser power), 10 s acquisition, bulk gold AFM probe. WE: gold-coated glass substrate functionalized with 4-NBM, CE: Pt ring, pseudo-reference electrode: silver wire.

Note that the real-time tracking of the TERS signal of this nitro benzene derivative during the potential exploration represents a noteworthy breakthrough, since our previous study by tip-SERS¹⁴² failed in doing so under similar conditions, as mentioned at the beginning of this

chapter (sudden surge of signal intensity observed during the potential ramp indeed led to the detector saturation). However, similarly to study of Touzalin of 4-NTP by EC-tip-SERS, the chemical signatures of possible reaction intermediates of 4-NBM could not be detected here by EC-TERS in acidic medium.

4.3.2b - 4-NBM reduction in alkaline medium

All further *in situ* experiments were carried out in alkaline medium in the inverted configuration. The possibility to detect possible reaction intermediates was assessed at faster potential scan rates than the one presented in acidic medium (50 vs 2 $\text{mV}\cdot\text{s}^{-1}$). Highly concentrated electrolyte (buffer $\text{NaOH}/\text{NaHCO}_3$), to minimize the occurrence of uncompensated resistance and a platinum pseudo-reference electrode, was preferred in such medium to Ag to avoid unexpected potential shift of the reference due to composition evolution.

The signal hotspot (position, intensity) was first evaluated at the OCP, the $2 \times 2 \mu\text{m}^2$ XY objective map displayed on the **Figure 4.20**, show a localized hot-spot (obtained by integration of the Raman band at 1340 cm^{-1} of 4-NBM) and no far-field contribution slightly away from the hot-spot position. The spectra confirm pristine tip by the absence of 4-NBM band in the far-field. Note that the hot-spot position was found at the exact same position after the measurement, indicating of the robustness of the optical coupling.

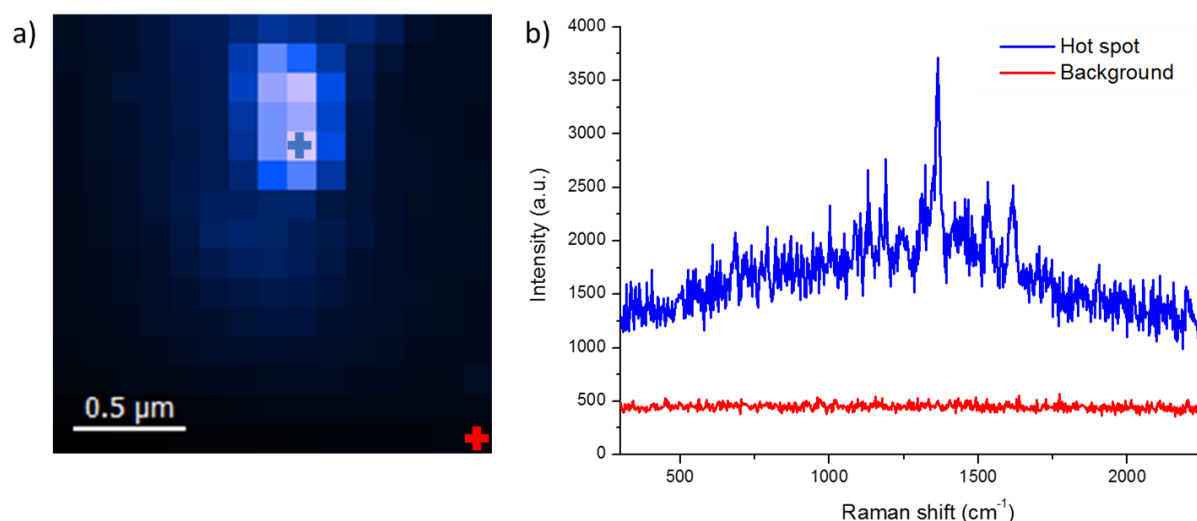


Figure 4.20. Hotspot screening – $2 \times 2 \mu\text{m}^2$ XY objective mapping at the OCP in alkaline medium (buffer $\text{NaOH}/\text{NaHCO}_3$) before EC-TERS 4-NBM reduction: **a)** localized hot-spot position obtained by integration of the Raman band at 1340 cm^{-1} of 4-NBM; **b)** TERS signal obtained at the exact hotspot position (blue) and far-field/background slightly away (red). $\lambda_{\text{exc}} = 632.8 \text{ nm}$, laser power $\sim 400 \mu\text{W}$ (2.5% of the nominal laser power), 0.3 s acquisition.

The 4-NBM SAM reduction was then recorded over scan range from 0 V to -900 mV vs Pt at a scan rate of 50 mV.s⁻¹. A first CV was recorded over one full cycle in order to initiate the reduction process, the followings CVs were restricted to the [0; -500 mV] range to focus the analysis on the reversible oxidation/reduction process. TERS spectra were continuously acquired every second, each spectrum therefore covering a 50 mV potential range. The spectra collected during the first CV cycle are presented as a 2D temporal map, seen on **Figure 4.21a**.

The characteristic 4-NBM signature acquired at the OCP, exhibits characteristic symmetric NO₂ stretching band at 1340 cm⁻¹, CH bending at 1105 cm⁻¹ and ring stretching at 1590 cm⁻¹. During potential exploration, the signature stays unchanged until around -600 mV, where the NO₂ band intensity diminishes to completely disappear at -750 mV (**Figure 4.21c**). While the nitro band intensity dropped, the intensity of ring stretching band kept being strong as observed in acidic medium. The two purple marks on the **Figure 4.21b** show the first and last acquired TERS spectra, following the nitro reduction (**Figure 4.21c**). The full disappearance of the band, associated with the nitro vibration at a scan rate as high as 50 mV.s⁻¹ is surprising, given the limited effective time the electrode is polarized at highly reductive potential.

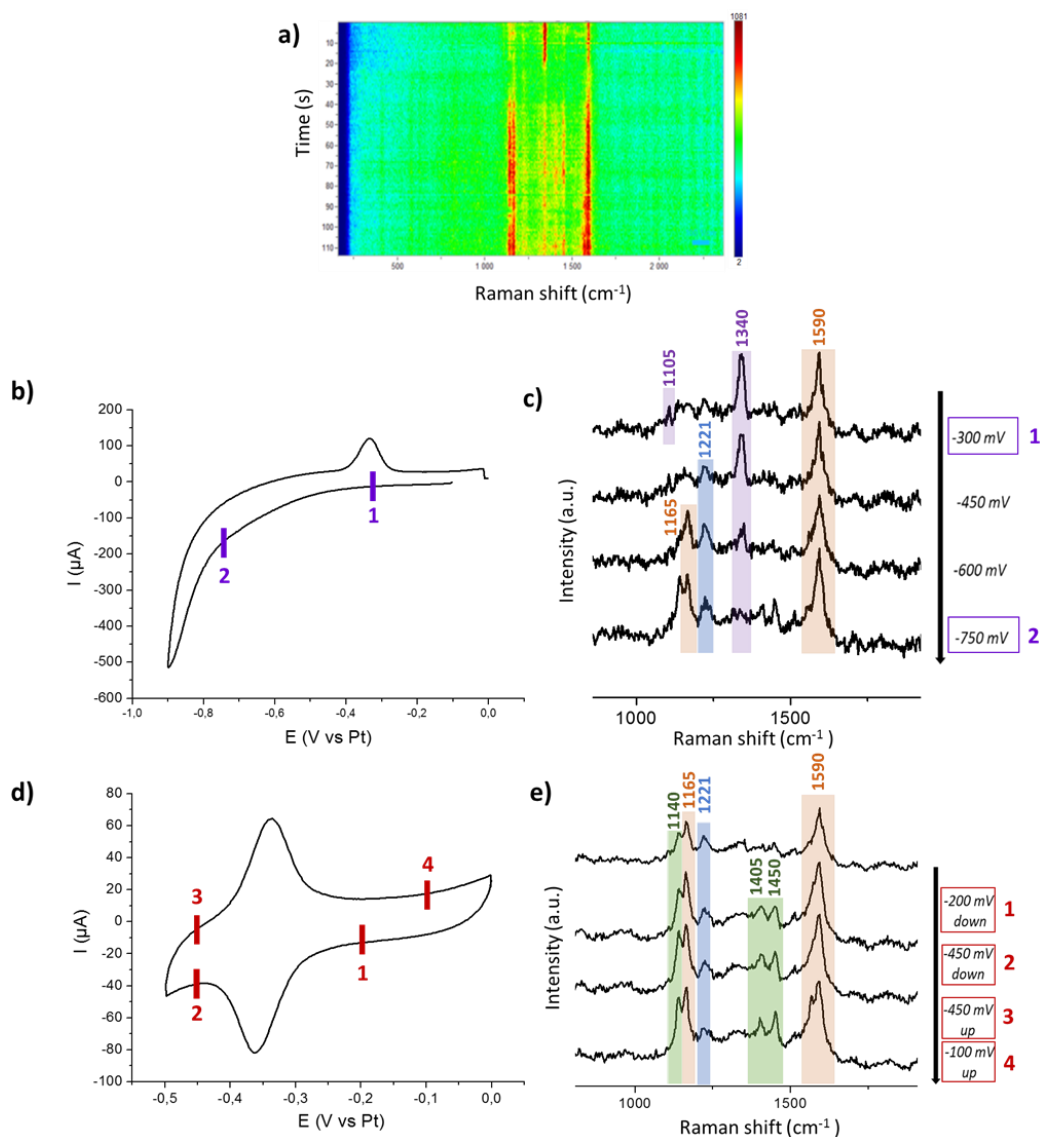


Figure 4.21. *In situ* 4-NBM reduction in alkaline medium (buffer NaOH/NaHCO₃, pH=10.7): **a)** TERS time mapping ($\lambda_{\text{exc}} = 632.8$ nm, laser power 160 μW , 1 s acquisition); **b)** CV of one cycle with scan range 0 V to -0.9 V vs Pt pseudo RE, scan rate 50 $\text{mV}\cdot\text{s}^{-1}$; **c)** TERS spectra at selected potential values of the CVs (b) ; **d)** CV on limited scan range from 0 to -500 mV vs Pt pseudo RE focused on the reversible current peak, scan rate 50 $\text{mV}\cdot\text{s}^{-1}$; **e)** TERS at potentials -200 mV, -450 mV and -100 mV; “down” and “up” indicate respectively the scan directions; “forward” towards lower potential range and “backward” towards higher potentials. TERS acquisition parameters: $\lambda_{\text{exc}} = 632.8$ nm, laser power ~ 160 μW (1% of the nominal laser power), 1 s acquisition.

Beside, new intense features appear at 1138, 1408, 1452 cm^{-1} (+ shoulder at 1583 cm^{-1}) and could match with the a_g -type bands of azobenzene (attributed to the C-N stretching and to the N=N stretching modes). The occurrence of these bands will be further discussed hereafter.

Furthermore, the second set of TERS spectra was recorded in the reduced potential range mentioned above. The TERS spectra at the potentials -200 mV, -450 mV and -100 mV, marked in red on the associated CV cycle, are presented in **Figure 4.21** (d, e). The latter shows clear

anodic and cathodic current peaks, associated with the reversible conversion of 4-HABM into 4-NSBM. The features already observed at -900 mV, appear more pronounced during this second cycle on a limited potential range no pattern of band appearance/disappearance is clearly observed following the potential scan around the reversible current peak, which may indicate that the intermediate hydroxyamino and nitroso are either not detected or show chemical signatures identical to the one of the amino derivative (monomeric specie) or of the azo compound (dimer).

4.3.2c - Discussion on the reduction mechanism

Dimer formation through photochemical effect – Zhao *et al.*¹⁷⁷ studied the 4-NTP reduction on gold and silver by SERS and the SEIRA (surface-enhanced infrared adsorption). They concluded that while the electro-reduction of 4-NTP proceeds fully towards 4-ATP under IR irradiation, visible light may promote the formation of dimeric products. They reported that dimerization can occur on silver either by direct photo-reduction of adjacent 4-NTP molecules or photooxidation 4-ATP, since the illumination of the surface promotes the metal-to-molecule (or molecule-to-metal) charge transfer. However, gold surfaces have been reported to promote these reactions less efficiently^{187,188}. To minimize the occurrence of such photothermal coupling, similar *in situ* TERS experiments were performed (STM-TERS work of A. Fiocco and AFM-TERS in this work), while the TERS probe kept scanning the sample surface and while the laser power was kept at minimum (~160 μ W; 1% of the nominal laser power). Still the same TERS signatures initially assigned to N=N stretching vibrations, were observed at 1405 and 1450 cm^{-1} .

SERS chemical effect – For many years the above-mentioned bands have been unanimously attributed to the dimeric intermediates, Kim *et al.*¹⁸⁹, however, have proposed an alternative explanation after they carried out SERS study on 4-ATP and DMAB adsorbed on gold, using a 633 nm excitation source and various pH media. They showed that the two compounds, have similar spectral features in alkaline media (not in acidic), although originating from different vibrational modes. In DMAB, they arise from total-symmetric a_g -type modes, assigned to the C-N and to the N=N stretching vibrations of dimers, where as in 4-ATP, they consists in b_2 -type symmetry bands, arising from the $\pi \rightarrow \pi^*$ transition (${}^1A_1 \rightarrow {}^1B_1$). As this transition does not match standard Raman selection rules, the b_2 -mode cannot be detected by classical μ Raman analyses on powder or liquid samples. However, once 4-NTP/4-NBM is adsorbed on SERS-

active substrates, symmetry-forbidden transitions can be observed as a result of the new electron density distribution. The sample polarization, the excitation wavelength and especially the pH of the medium influence the possible detection of the b_2 -type mode bands. For instance, following the protonation of the amino functionality at $\text{pH} \leq 4$, the bands disappear as the gap between the highest and the lowest occupied molecular orbitals (HOMO and LUMO) is too large for the transitions to be excited in the visible range.

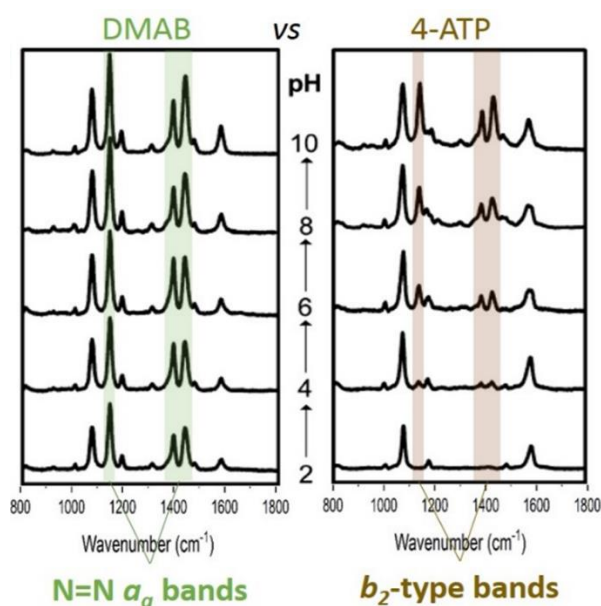


Figure 4.22. SER spectra acquired on gold surface functionalized with DMAB thiol (left) and 4-ATP (right) at different pH values using a 632.8 nm excitation source. Adapted from Kim *et al.*¹⁸⁹.

Electrochemical formation of dimer (Gao's "bimolecular path") – Static and dynamic analyses were performed on both, 4-NBM and 4-ATP SAMs, under different experimental conditions by A. Fiocco in our group (polarization, pH change). It was shown that after reduction of the 4-NBM compounds in alkaline medium, and subsequent transfer into acidic medium, the bands at $1405/1450 \text{ cm}^{-1}$ did not disappear, implying that dimeric species DMAB are formed electrochemically by condensation of 4-HABM with residual nitroso derivative 4-NSBM (or even 4-HABM self-condensation) following Gao's mechanism (**Figure 4.3**). Note that the dimer formation through photo-reduction, if cannot be totally excluded, is minimized under the chosen operating conditions (minimal laser power, 633 nm illumination-gold sample/tip, liquid environment). It has been shown by Fiocco that it does not originate from 4-ABM photo-oxidation. It seems however, that under the mild conditions used here and in Fiocco's work (pH 11 or pH 3, reductive polarization limited to -1 V vs Pt), the electrochemical

reaction does not get to completion, as DMAB azo bond cannot be “open” to form DMHAB and eventually split into two 4-ABM monomers.

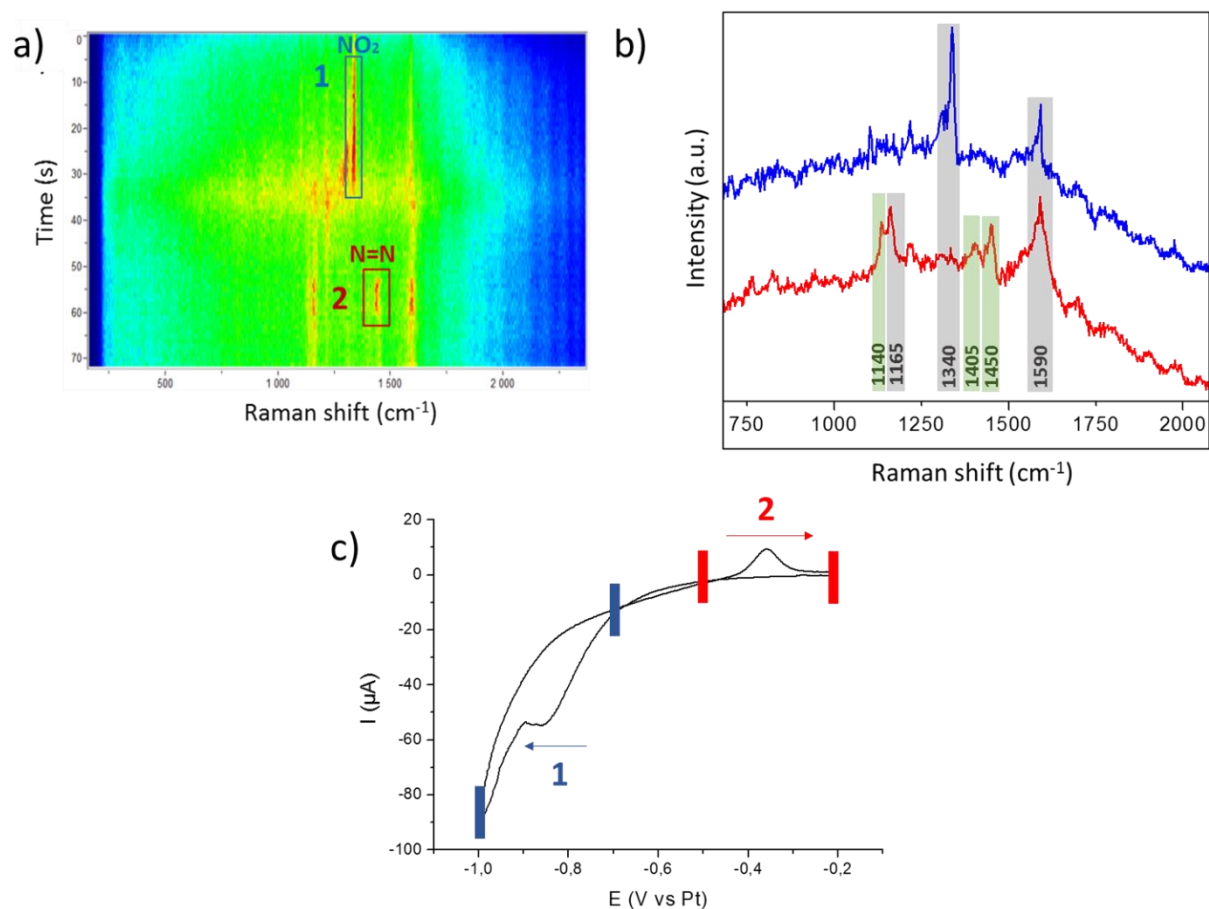


Figure 4.23. *In situ* 4-NBM reduction in alkaline medium (buffer NaOH/NaHCO₃, pH=10.7): **a)** TERS time mapping ($\lambda_{exc} = 632.8$ nm, laser power ~ 160 μ W, 1 s acquisition); **b)** individual spectra extracted from (a) (region 1 and 2), showing the disappearance of nitro group and the appearance of new spectral features; **c)** CV of one cycle with scan range 0 V to -0.9 V vs Pt pseudo RE, scan rate 50 mV.s⁻¹.

Partial conclusions - In this section, we illustrated the performance of the EC-TERS setup using bottom illumination. The *in situ* tracking of the electrochemical transformation of 4-NBM SAM by AFM-TERS was achieved with the use of long working distance dry objective with high numerical aperture through transparent gold substrate and additional electrochemical optimization of homemade AFM liquid cell. This configuration provided larger working space and easier optical coupling during experiment as compared to upright configuration. Overall optimization process included some preliminary electrochemical and technical adjustments, such as replacement of silver wire with platinum as pseudo RE, minimizing the working electrode size and limiting the oxygen presence in the electrolyte. The electrochemical 4-NBM reduction was studied by conventional CV experiment and EC-TERS.

The main observations in acid media showed disappearance of NO₂ band at 1340 cm⁻¹, while the alkaline medium revealed a few new bands, possibly attributed to hydroxylamine and dimers (azobenzene DMAB) following Gao's reduction mechanism, although not complete under the mild conditions used in our studies.

4.4. EC-TERS implementation on opaque samples

The following section will focus on the *in situ* TERS implementation using side illumination, which enables the characterization of non-transparent samples to broaden the range of systems to be studied. Toward this aim, a liquid cell prototype designed by Horiba to perform TERS in liquid, using side illumination, was tested in the framework of a collaboration and later modified to add electrochemical features. Associated preliminary results are presented.

4.4.1. Liquid cell design for side illumination

The TERS liquid cell prototype designed by Horiba is equipped with a side glass window (cover slip), tilted at 30° to enable side illumination of the AFM tip apex and signal collection using long distance air objective (Mitutoyo Plan Apo SL Infinity Corrected Objective, magnification: 50x, NA: 0.42, working distance: 20.5 mm). The optical path was corrected by an additional lens, placed in front of the objective, as seen in **Figure 4.24a**.

The liquid cell equipped with two stainless steel sample clips has been modified by integrating a half-ring platinum counter electrode (CE) following the cell wall contours (sides and rear part) and a platinum wire as pseudo-reference electrode (RE) attached to the side. A gold thin film deposited on mica acting as a working electrode (WE), was connected through a Pt wire attached to one of the sample clip, previously insulated with heat shrink plastic tubing (**Figure 4.24b**). All the electrical wires were insulated, attached on a side of the microscope system (**Figure 4.24c**) and connected to a potentiostat (Autolab, model PGSTAT100N, Metrohm; **Figure 4.24d**). The cell was mounted on the AFM piezo-stage of the *SmartSPM* platform and filled with approximately 1 mL of electrolyte.

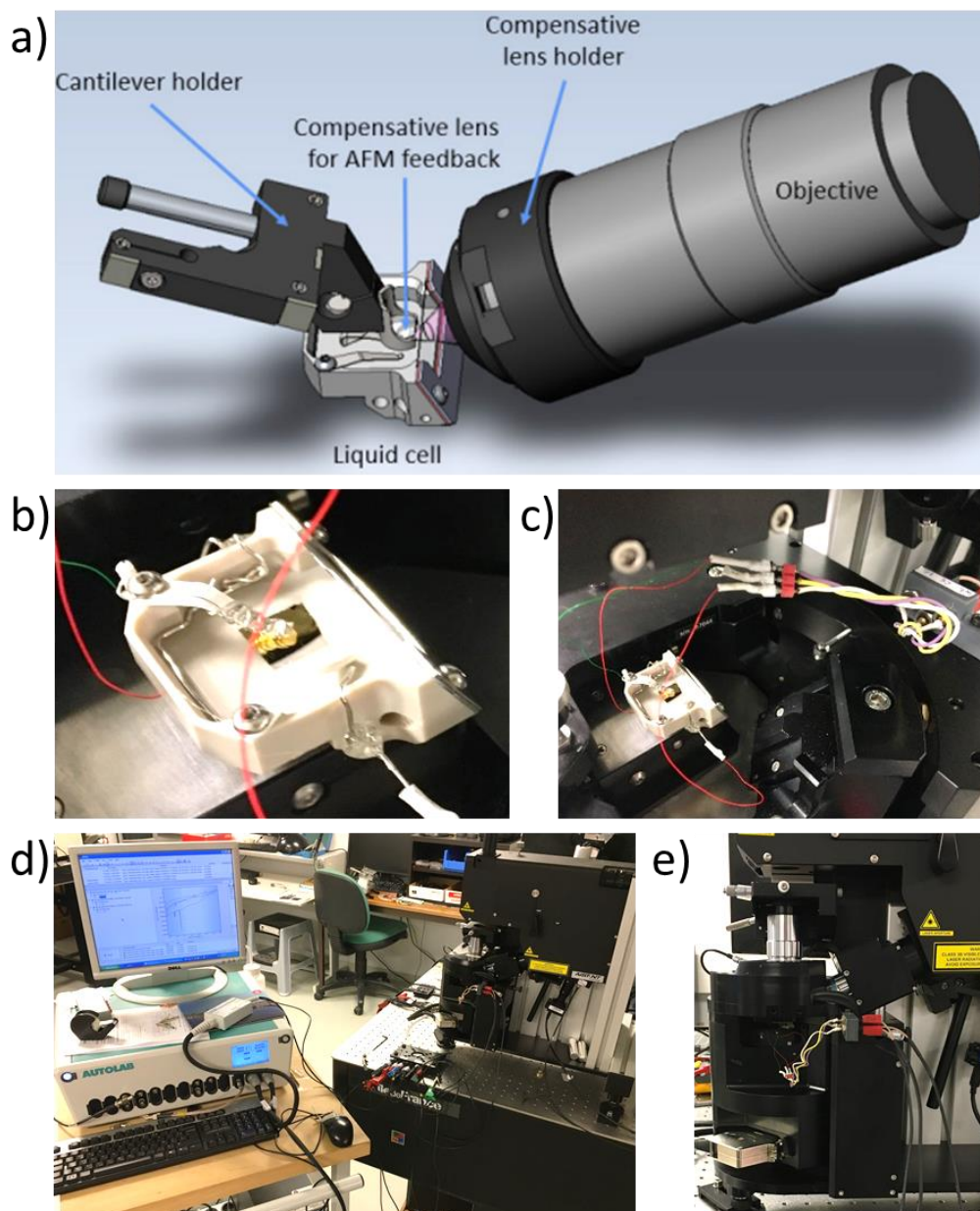


Figure 4.24. EC-AFM-TERS set-up for non-transparent substrates (upright configuration, side illumination)- **a)** scheme of the optical coupling using a liquid AFM probe holder, liquid cell with a side window and a side air objective equipped with a correcting lens (Horiba design); **b)** top view of the liquid cell modified to implement EC-TERS equipped with a gold coated mica substrate as *WE*, a platinum ring as *CE* and a platinum wire as pseudo-reference electrode; **c)** cell mounted on the microscope base and connected electrically; **d)** the *SmartSPM* microscope is placed on the *Omegascope* optical coupling system, and the 3-electrode EC-TERS cell is connected through shielded electrical wires to an external potentiostat (model *Autolab PGSTAT100N*, Metrohm); **e)** adjustment of the position of the *SmartSPM* microscope on the *Omegascope* base using X,Y,Z micrometer screws allows the initial rough optical alignment of the Raman probe on the AFM tip apex *via* optical control using the two objectives (top 10x and side 50x) mounted on the *Omegascope* base. The screening of the hotspot position is then realized by X,Y and X,Z displacement of the 50x side objective mounted on a piezo scanner.

The electrochemical response of the cell was tested on a gold thin film electrode on mica functionalized with 4-NBM and immersed in alkaline medium (bicarbonate buffer NaOH/NaHCO₃). The silver pseudo-reference electrode was replaced by a Pt wire in the

carbonate buffer to avoid “uncontrolled” potential shift. The surface of the working electrode is chosen minimal (possible coating with *Zapon* varnish) to reduce the influence of the uncompensated resistance, while allowing the positioning of the AFM probe liquid holder and of the clip ensuring the electrical contact.

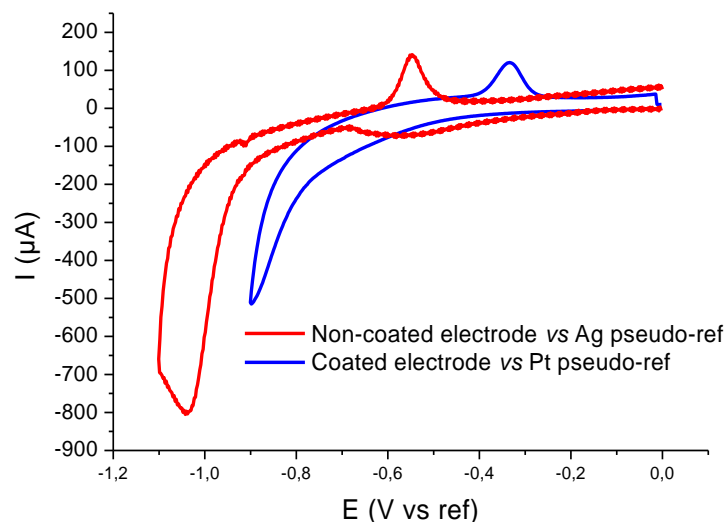


Figure 4.25. TERS cell electrochemical response – CV response (scan rate $50 \text{ mV}\cdot\text{s}^{-1}$) in the bicarbonate buffer of a gold thin film on mica electrode functionalized with 4-NBM and mounted in the EC-TERS cell designed for non-transparent samples. In blue: WE electrode partially coated with *Zapon* varnish combined with a Pt pseudo RE; in red: larger working electrode associated with an Ag pseudo RE).

4.4.2. Laser focusing and hot-spot mapping in liquid

The rough adjustment of the laser position on the apex of the AFM probe in the upright configuration is achieved by manual micro-positioning of the *SmartSPM* head in front of the objective in all three directions *XYZ*, *via* the optical control using two cameras (side and top). **Figure 4.26a** and **4.26b** show the TERS-AFM probe (10x top objective lens) and the rough laser positioning on the tip apex within the electrolyte (50x side objective lens), respectively.

Note that upon vertical approach of the sample/cell to the probe, the relative position of the glass window between the tip apex and the side objective (therefore the thickness of electrolyte) is changed, drastically altering the optical alignment. To minimize this problem, an approach sequence at an angle of 25° (Z and X step motors carrying the sample/cell moving simultaneously) has been developed by Horiba to maintained the tip apex-laser alignment upon approaching. This specific approach also allows ones to bring the probe holder as close as possible to the window of the EC-spectro cell, to minimize the thickness of electrolyte between the window and the tip apex, and therefore maximize the TERS excitation/collection efficiency and the ratio near-field/far-field signal.

Accurate focusing of the laser beam on the probe tip apex is then achieved by XY and XZ objective scanning, after the TERS-AFM probe is in close proximity with the sample (“landed”). **Figure 4.26c** shows the acquired hotspot after laser adjustment, which appears more diffuse than the one usually collected in the inverted configuration using a 100x objective lens.

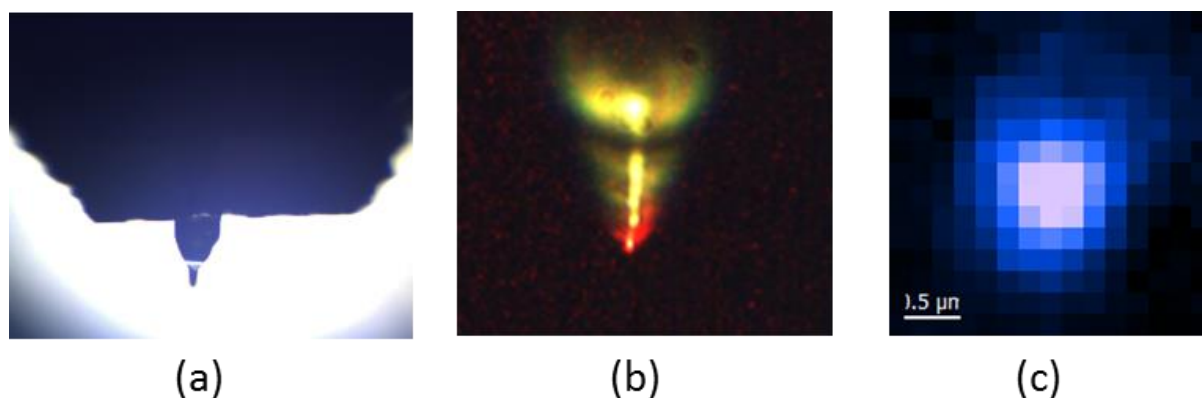


Figure 4.26. Optical alignment in liquid (EC-TERS cell, upright configuration, side illumination): **a)** top view (through the lens of the liquid AFM-tip holder) of the chip, cantilever and the tip immersed in liquid using a top 10x objective; **b)** image the tip apex through the EC-TERS cell filled with liquid using a side 50x objective equipped with a correcting lens ; **c)** $3 \times 3 \mu\text{m}^2$ XY objective map showing the hot spot; $\lambda_{\text{exc}} = 632.8 \text{ nm}$, laser power $\sim 160 \mu\text{W}$ (1% of the nominal laser power), 0.3 s acquisition.

4.4.3. EC-TERS study using side illumination – Preliminary results

4.4.3a – TERS point spectra in liquid

Home-made probes - The optical coupling efficiency in liquid was first confirmed by the TERS signatures obtained in aqueous medium on gold samples, functionalized with azobenzene and 4-NBM SAMs (see **Figure 4.27** below). Note that the TERS point spectra were obtained in contact mode, as no Raman response is obtained in tapping mode (see discussion in Chapter 3).

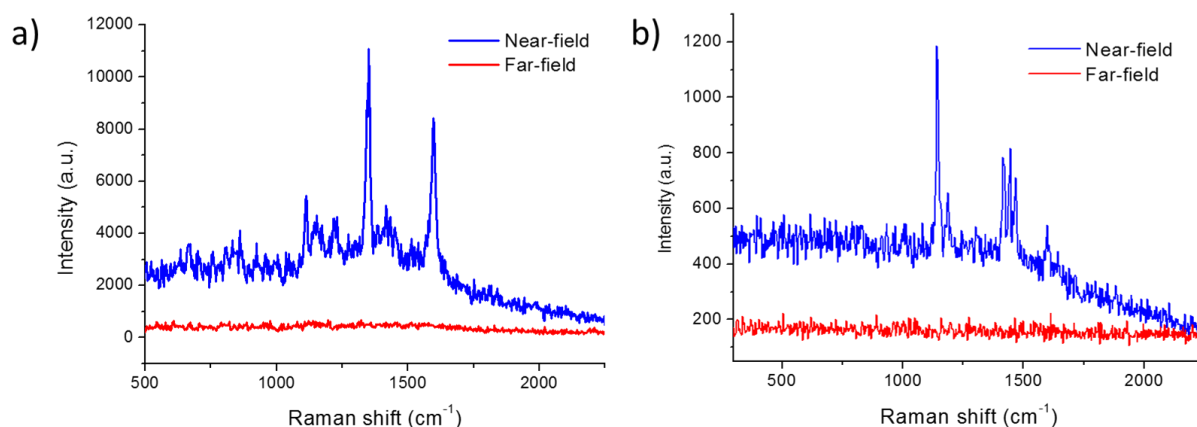


Figure 4.27. AFM-TERS on non-transparent sample in liquid (side illumination/upright configuration/homemade gold AFM probe): **a)** thioazobenzene SAM on gold on mica; **b)** 4-NBM SAM on gold on mica. Both spectra were obtained with homemade gold probe in contact mode (blue) and tapping mode (red) using $\lambda_{\text{exc}} = 632.8 \text{ nm}$, laser power $\sim 160 \mu\text{W}$ (1% of the nominal laser power) and 1 s acquisition.

Hybrid mode implementation using commercial probes – In the framework of a collaboration with Horiba, TERS-active probes prepared by thin coating of plasmonic materials (gold and silver, characteristics not disclosed) were tested to benefit from the use of the hybrid imaging mode (“*Top-mode*” alternating tapping and contact imaging mode), enabling TERS mapping using side illumination. The probe manufactured by “*AppNano*” have the following characteristics: “*OMNI TERS-SNC-Au-5*” - Soft Non-contact TERS Probes (Gold) Cantilever- *L*: 150 μm , *W*: 50 μm , *T*: 2 μm - *f*: 150 kHz, Tip *H*: 12-16 μm).

4.4.3b – Electrochemical reduction of 4-NBM using commercial probes

The electrochemical reduction of 4-NBM reduction was first followed by TERS using commercial probes over four CV cycles in alkaline medium (bicarbonate buffer; pH 10.7) at a scan rate of 50 $\text{mV}\cdot\text{s}^{-1}$ on a 4-NBM functionalized gold substrate WE (Pt counter and reference electrodes). The characteristic 4-NBM TERS signature with strong NO_2 band and ring stretching bands was observed at the OCP in conditions similar to the one used with the home-made probes ($\lambda_{\text{exc}} = 632.8 \text{ nm}$, laser power $\sim 160 \mu\text{W}$ and 1 s acquisition).

As depicted in **Figure 4.28**, the signature of NO_2 started decreasing around -700 mV and disappeared completely when reached -1000 mV vs Pt. New spectral features at 1140, 1405 and 1450 cm^{-1} assigned to DMAB dimer (and possibly monomers) were observed in agreement with what was observed on transparent samples (inverted configuration) with homemade probes.

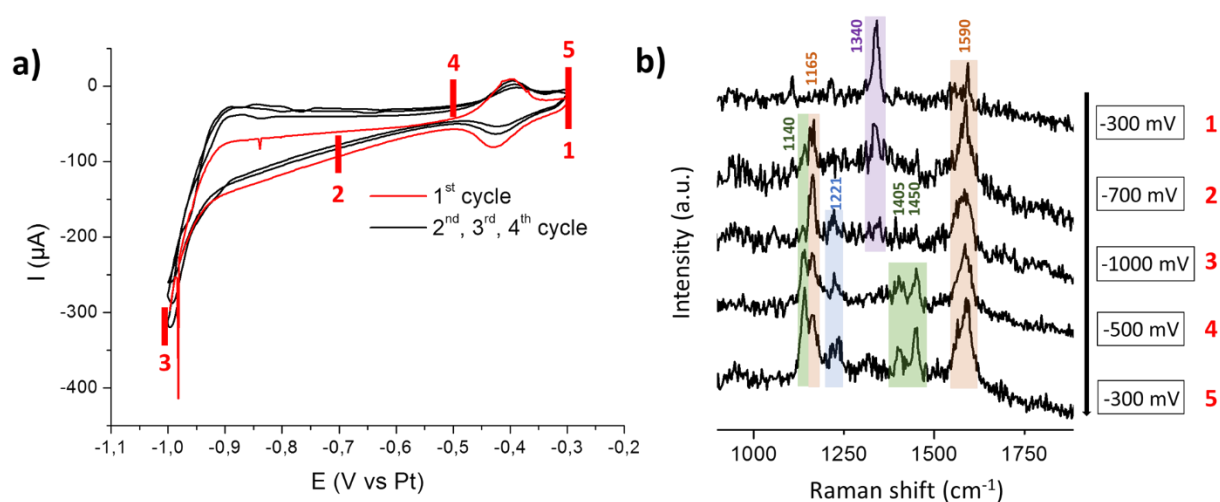


Figure 4.28. EC-TERS tracking of 4-NBM reduction in alkaline medium using commercial probes (side illumination, upright configuration): **a)** CV scans associated with the EC-TERS analysis (4 cycles in the scan range from -300 to -1000 mV) - 3-electrode EC-TERS-cell, Pt pseudo RE and CE, bicarbonate buffer pH 10.7, scan rate 50 mV.s⁻¹ ; **b)** TER spectra associated with potential value highlighted in red in (a) showing NO₂ band disappearance and in the first half cycle between -300 mV and -1000 mV and appearance of new bands obtained at anodic peak at potentials -500 and -300 mV. $\lambda_{exc} = 632.8$ nm, laser power ~ 160 μ W (1% of the nominal laser power), 1 s acquisition.

This set of data confirms the resistance of the commercial probes to chemical and mechanical wear, under the mild condition used in this study. The performance of the two probes, i.e. homemade TERS probe on transparent sample in tapping mode and commercial TERS probes in contact mode on non-transparent samples (bottom illumination), are similar as can be seen on **Figure 4.29**, representing the *in situ* average spectra of 4-NBM after electrochemical reduction in alkaline buffer. TERS signal intensity are similar with higher intensity background for the homemade probe using bottom illumination through the gold-coated glass substrate.

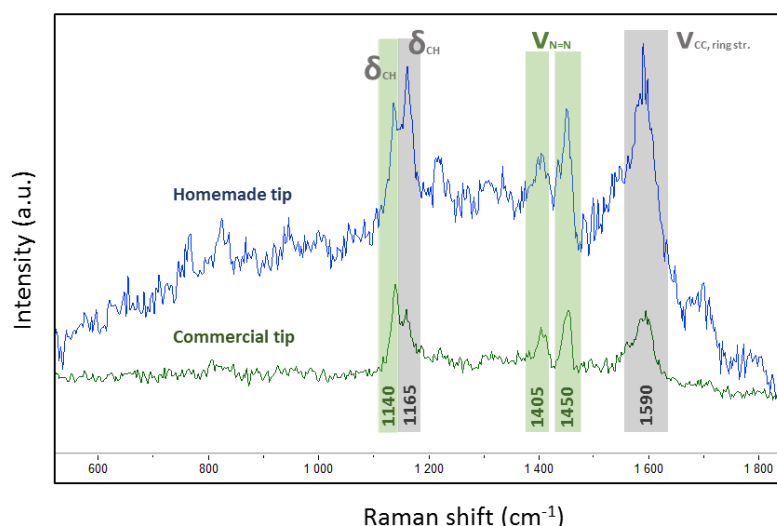


Figure 4.29. Relative performance of commercial and homemade TERS active AFM probes - Average EC-TERS spectra, obtained after electro-reduction of a 4-NBM functionalized gold electrode: homemade probe on a transparent gold electrode using bottom illumination and tapping mode (blue) and commercial probe on a non-transparent substrate using side illumination and contact mode (green). $\lambda_{exc} = 632.8$ nm, laser power ~ 160 μ W (1% of the nominal laser power), 1 s acquisition.

4.4.3.c – Failed redox nano-mapping attempt

To relate topography to composition information, a second series of EC-TERS experiments was run on a gold and ITO electrodes, decorated with nanotriangles and hexagons (see preparation in Chapter 3), and functionalized with 4-NBM. The study by EC-AFM-TERS aimed

spatially resolved local heterogeneities and redox behavior at the nanoscale on an electrode surface similarly to the study of Van Duyne *et al.*¹⁴⁹ in 2019.

A first sample topographical image was performed in the electrolyte at the OCP in tapping AFM mode to locate the nanoparticles. Truncated nanotriangles could be identified relatively easily, despite the high roughness of the underlying gold film, as can be seen on **Figure 4.30**. However, the use of the hybrid “*top-mode*” in liquid turned out to be a lot more tedious. Strong interaction of the commercial probes with the surface nano-objects indeed led to their detachment from the substrate. This is highly surprising as the group of Van Duyne successfully imaged similar systems in classical contact mode¹⁴⁹. To try to circumvent this problem, the largest nanoobjects (with stronger Van der Waals interaction with the surface) were selected for topography and composition imaging.

A 2 x 2 μm^2 AFM-TERS composition mapping, 30 x 30 px², 0.3s per pixel (**Figure 4.31** a and d) was performed before and after electrochemical reduction. The TERS mapping, realized by integration of the band at 1340 cm^{-1} , shows an uniform chemical signature across the surface during the first scan at the OCP (**Figure 4.31c**), while the topography revealed that the large nanotriangle had been removed from the surface, during the second scan after polarization of the electrode at reducing potential (**Figure 4.31d**). Despite nano-object removal, the second TERS mapping reveals typical bands of reduced 4-NBM molecule as reported in the already reported EC-TERS experiments above. However, averaged spectra revealed band at 1340 cm^{-1} , belonging to the nitro group. This could show either not homogeneous (or complete) *in situ* reduction of NO_2 on the electrode surface or tip contamination.

The latter was further observed *ex situ* (after the EC-TERS measurement) on a pristine gold substrate, confirming the lack of control of the tip-sample interaction in “*Top-mode*” in liquid and explaining the lack of contrast on the TERS mapping. Applications engineers at Horiba are currently trying to understand the origin of the flaws in *Top-mode* implementation in liquid. Poor mechanical properties of the “*AppNano*” probe in liquid and/or non-suitable selection of the resonance frequency of the probe (59 kHz in liquid vs 150 kHz in the ambient) could be incriminated to explain the poor imaging performance of the supposedly gentle “*Top-mode*” mode.

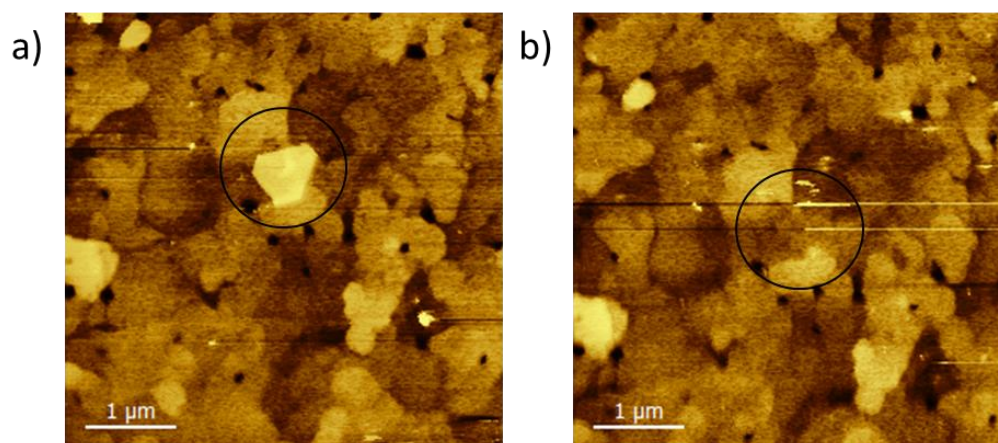


Figure 4.30. AFM topography in liquid using hybrid mode: a) nanotriangles (height 12 nm, length 0.6 μm) deposited on gold surface (resolution 256 x 256 px², scan rate 1.0 Hz, scan range 5 x 5 μm^2 , selected resonance frequency in liquid: 59 kHz) before (a) and after (b) polarization of the electrode at reducing potentials. The black circle shows the position of nanotriangle (a) and its absence (b), with the addition of small drift, acquired between both topographies.

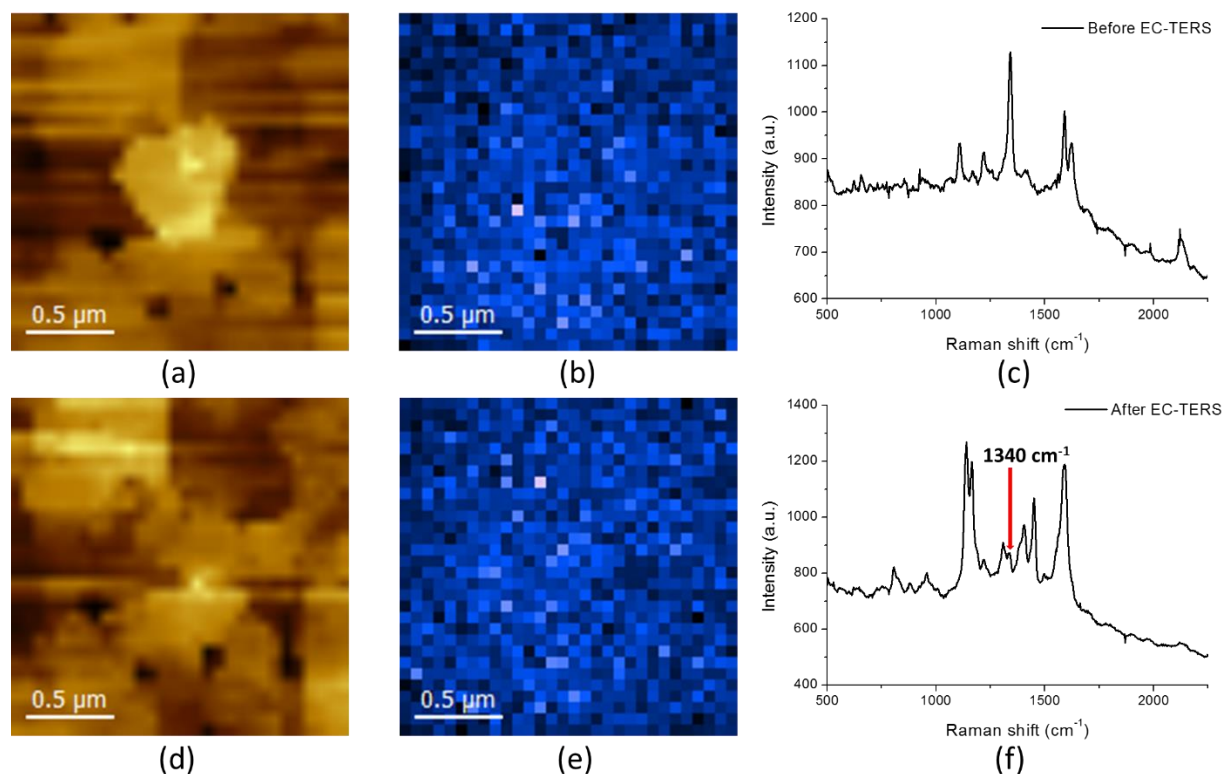


Figure 4.31. EC-AFM-TERS imaging in hybrid mode of a gold electrode decorated with nanotriangles and functionalized with 4-NBM at the OCP (top; a-c) and after polarization at reducing potentials (bottom; d-f). 2 x 2 μm^2 , 30 x 30 px², $\lambda_{\text{exc}} = 632.8 \text{ nm}$, laser power $\sim 160 \mu\text{W}$ (1% of the nominal laser power), 0.3 s acquisition. The spectra (c) and (f) were averaged over the 90 spectra on each images (b) and (d).

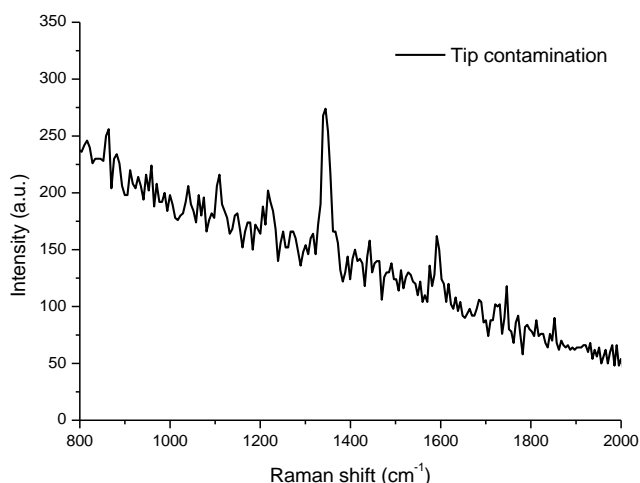


Figure 4.32. Tip contamination on pristine gold sample after the *in situ* TERS measurements; $\lambda_{\text{exc}} = 632.8 \text{ nm}$, laser power $\sim 400 \mu\text{W}$ (2.5% of the nominal laser power), 2 s acquisition.

Conclusions

In this chapter, we introduced two different set-ups enabling AFM-TERS implementation in liquid and under polarization, respectively on transparent and non-transparent electrodes. We could demonstrate the robustness of the two configurations, i.e. 3-electrode spectroelectrochemical cells designed for bottom or side illumination, by tracking the potential-dependent chemical signature of a non-Raman resonant molecular compound.

To this aim, we developed semi-transparent gold electrodes, protocols to minimize ohmic drop contributions in large electrochemical cells, and explored the influence of pseudo-reference electrodes depending on the electrolyte composition (acidity, concentration of dissolved oxygen).

The strong TERS activity of the bulk AFM probes developed in this study, enabled the collection of strong intensity spectra *in situ* at short acquisition time (1s), allowing the real-time tracking of composition signatures during potential scans (cyclic voltammetry) performed at scan rates up to $50 \text{ mV}\cdot\text{s}^{-1}$, while exploring highly reducing potentials down to -1 V. If no reactions intermediates (4-HABM and 4-NSBM) could be formally detected/identified during the electrochemical transformation of 4-nitrobenzene mercaptan, the dynamics of band disappearance and appearance could be followed. Together with the progressive disappearance of the nitro group (1340 cm^{-1}), we could detect new bands at 1140, 1405, 1450 cm^{-1}), similarly to another study (A. Fiocco) performed in our group using EC-STM-TERS. These bands can be assigned to the C-N and N=N stretching vibrations of the azobenzene DMAB (photo-induced) or possibly to the b_2 -type bands of the amino compounds 4-ABM

susceptible to appear in alkaline medium and in contact with metal structures (charge transfer). The set of results obtained in this work, together with the one of Fiocco, supports the formation of DMAB by condensation of 4-HABM with 4-NSBM, following an electrochemical path firstly described by Gao.

Following the pioneering work of B. Ren who introduced in 2020 EC-AFM-TERS measurements, using top illumination (*NT-MDT* system, electrochemical transformation of polyaniline, point spectra/no imaging), and paved the way to the characterization of non-transparent sample, then of a broad range of functional materials, we have demonstrated for the first time EC-AFM-TERS analysis using side illumination in the framework of a collaboration with Horiba (*AIST-NT* system). The liquid cell designed by Horiba and modified in our lab to integrate electrochemical features will be a valuable asset to the forthcoming development of EC-TERS.

General conclusion

To address the pressurizing need for *in situ/operando* analytical techniques with sensitivity and resolution suitable to the characterization of functional materials, we proposed in this work to develop tip-enhanced Raman spectroscopy under electrochemical condition. Introduced in the early 2000, this hyphenated technique coupling scanning probe microscopies, Raman spectroscopy and signal enhancement techniques, using plasmon resonators, met a few decisive successful developments this last decade, which laid the foundation of this project.

Starting from a TERS ready instruments providing a robust optical coupling, we focus our development efforts on two main axes: i) the difficult elaboration of robust TERS-actives AFM probes usable in a broad range of conditions (air, liquid, EC conditions) and of material ((non)-conductive, soft materials, rough surface, weakly adsorbed nano-objects), ii) the conception of spectro-electrochemical cells offering an optimal optical coupling between the Raman probe and the TERS probe, while enabling topography and composition mapping with minimum loss of signal.

Inspired by solid metal robust AFM probes produced by RMN (Utah, USA) for electrical measurement, by Demaille's group for AFM-SECM measurements and by Zhang's group for AFM-TERS measurements in the air, we explored further the potential of such probe for AFM-TERS applications in liquid conditions and under polarization. Following a 4-steps micro-manufacturing process, starting from 25- μm diameter gold (and silver) wire (including "etching in a drop"), AFM-probe with mechanical properties compatible with semi-contact (intermittent/tapping), imaging mode implementation could be produced (high resonance frequency, high quality factors).

Nano-imaging - Successful tracking and imaging of surface nano-features or physisorbed nano-objects (unprecedented to our knowledge), was achieved in the ambient, using bulk gold AFM probes in tapping mode. Large convolution effects affecting the lateral resolution upon imaging could be decreased by optimization of the etching procedure of the gold tips (smaller radius of curvature). Flaws in the tip-sample distance control, due to non-suitable mechanical properties of the tip, led to relatively fast wear or contamination of the tip apex. Both, the stiffness of the produced probe (force constant around 200 N.m^{-1} , 20 times higher than force constant of silicon probes) and the length of the tip nose (comparable to the cantilever

dimensions 90 μm) can be incriminated. The exploration of various cantilever properties was limited by several instrumental constraints: i) relatively short cantilevers being suitable to the cantilever detection scheme of the AIST/Horiba system, ii) only probes with short cantilevers “stabilizing” on sample surface using classical excitations and gain feedback control parameters (the oscillation amplitude could not be evaluated for instance), iii) and shorter nose could not be obtained without impacting the quality of the etching process (uncontrolled immersion of the cantilever). The high stiffness and the relatively high tip height of the manufactured probes constitute major bottlenecks to the characterization of weakly bound nano-objects especially in liquid, as no imaging of nano-objects could be successfully achieved in tapping mode. To circumvent this problem and boost the progress of the project, we initiated discussions with RMN and SATT Lutec in early 2019, after filing of a “Soleau” envelop to explore possible merging of our competence, to produce high quality bulk gold probes with tunable properties. If RMN showed strong interest for the product and its marketing potential, the multiple confinement periods and the on-going licensing of RMN products by Bruker postponed possible collaborative projects.

TERS activity - Using either bottom or side illumination, the manufactured probes (gold and silver) successfully produced TERS point spectra on gold sample functionalized with non-Raman resonant compounds (“gap” mode where the tip-molecule-substrate forms a plasmonic junction), at low laser power, short acquisition time, both in the ambient and in liquid. No TERS activity was however measured on dielectric sample with the smooth surface tips, produced through the developed etching process. As the main goal of this work was the development of TERS measurements on electroactive substrates, no further effort were engaged on the characterization of non-metallic samples. Variants of the manufacturing protocol, inducing roughening or corrugation of tip to produce multiple hot-spots, may be explored in the future.

TERS hyperspectral mapping - TERS signature could be collected in tapping mode using bottom illumination (with linearly polarized Raman probe), despite the “large” tip-sample distance fluctuations in time. Strong intensity TERS signatures could be extracted using low numerical aperture dry objectives, avoiding mechanical coupling with the sample upon imaging, as observed with oil immersion objective. Hyperspectral TERS mapping (0.3 s / pixel) of 4-NBM-derivatized gold nanostructures, physisorbed on glass, proved successful on the inverted configuration, in the ambient only, although the composition contrast suffers from

the flaws in the tip-sample distance control. Using side illumination, a stricter control of the tip-distance (contact mode) was necessary to recover TERS signature. The hybrid mode “Top-mode” developed by AIST-NT, alternating tapping mode and contact mode for TERS signal collection, could not be suitably implemented with the manufactured probes (and neither with commercial TERS probe in liquid), compromising TERS mapping on opaque sample. Applications engineers at Horiba are currently trying to understand the origin of the flaws in Top-mode implementation in liquid.

Real-time EC-TERS analysis - The strong TERS activity of the bulk AFM probes developed in this study, enabled the collection of strong intensity spectra (point spectra) *in situ* at short acquisition time (1s), allowing the real-time tracking of composition signatures associated with the electrochemical reduction of 4-NBM SAMs on gold during potential scans (cyclic voltammetry), performed at scan rates up to $50 \text{ mV}\cdot\text{s}^{-1}$, while exploring highly reducing potentials down to -1 V. The set of results obtained in this work supports the formation of dimers (DMAB) by condensation of reaction intermediates (4-HABM with 4-NSBM), following an electrochemical path instead of the often reported photo-coupling path. Note that synchronization of data acquisition with the electrochemical sequence (triggering of the CCD camera by the potentiostat) has been developed in the group, and could be put to profit using TERS efficient probes to real-time TERS monitoring of electrochemical process at higher scan rate than the one used in this work.

EC-TERS on opaque samples - EC-TERS analyses have been possible through the development and optimization of 3-electrode spectro-electrochemical cells, compatible with bottom or side illumination. Following the pioneering work of B. Ren, who introduced in 2020 EC-AFM-TERS measurements using top illumination and paved the way to the characterization of non-transparent sample, we demonstrated for the first time EC-AFM-TERS analysis using side illumination. The liquid cell designed by Horiba, and modified in our lab to integrate electrochemical features, will be a valuable asset to the forthcoming development of EC-TERS. The combination of EC-TERS, using side illumination and environment chambers for the control of the atmosphere, will enable the study of a broad range of functional materials, for catalysis for instance, object of an on-going project in the group developed with Horiba.

SECM-ERS - The coupling of micro/nanoelectrodes with Raman measurements is an interesting development route already pursued by several research groups, e.g. M. Etienne (SECM-Raman) to study corrosion, J.F. Masson (SERS active nano- pipettes) to monitor living

cell activity, our group (single hot-spot SERS active microelectrode: Tip-SERS) and S. Bonhommeau & D. Zigah (SECM-SERS using nano-tip array) for *in situ* SERS studies of electrochemically induced processes. One of the initial goal of this work was to reach a level of development enabling SECM-TERS measurements for simultaneous electrochemical “interrogation” and composition characterization at the nanoscale. The strategy envisaged was to design AFM-SECM probes, similar to the one developed by Demaille and Zhang’s groups, but using non-Raman active insulating coating instead of electrophoretic paints. Thin SiO₂ layers deposited on gold tips by sol-gel techniques, as already demonstrated by Zenobi’s group⁸⁸, or to produce Au@SiO₂ core-shell particles used in SHINERS (also developed in our group). To selectively uncover the tip apex and generate a microelectrode, a prototype of high-voltage electrical pulse generator, similar to the one proposed by Demaille, has been developed in LISE. The high electric field generated at the tip during the electrostatic discharge can be used to blow away thin coatings; alternatively sparks can be produced to reshape the exposed tip by bringing metallic objects in close proximity to the tip.

Abbreviations and symbols

Abbreviations

AC	Alternating current
AFM	Atomic Force Microscope
CCD	Charge-Coupled Device
CE	Counter Electrode (auxiliary electrode)
CV	Cyclic Voltammetry
DDA	Dipole/Dipole Approximation
DC	Direct Current
DFT	Density Functional Theory
EC	Electrochemical
EM	Electromagnetic
EF	Enhancement Factor
ET	Electron Transfer
FB	Feedback mode
FDTD	Finite-Difference Time-Domain
FIB	Focused Ion Beam
FF	Far-Field
FWHM	Full Width at Half Maximum (Resonance frequency width)
HOMO	Highest Occupied Molecular Orbital
IBL	Ion Beam Lithography
IR	Infrared
ITO	Indium Tin Oxide
LSP	Localized Surface Plasmon
LSPR	Localized Surface Plasmon resonance
LUMO	Lowest Unoccupied Molecular Orbital
MWCNT	Multi-Walled Carbon Nanotube
NA	Numerical Aperture
NF	Near-Field

NF	Normal Force (TF)
NIR	Near Infrared
NMR	Nuclear Magnetic Resonance
NP	Nanoparticle
NTr	Nanotriangle
OCP	Open Circuit Potential
PI	Piezo stage
PR	Plasmon Resonance
QCL	Quantum cascade laser
QCM	Quartz Crystal Microbalance
QRE	Quasi-Reference Electrode
RE	Reference Electrode
ROC	Radius of Curvature
RR	Resonance Raman
RRS	Resonance Raman Spectroscopy
SAM	Self-Assembled Monolayer
SCE	Saturated Calomel Electrode
SECM	Scanning Electrochemical Microscopy
SEI	Solid-Electrolyte Interphase
SEM	Scanning Electron Microscope
SERS	Surface-Enhanced Raman Spectroscopy
SF	Shear Force
SFG	Sum Frequency Generation
SFM	Shear-Force Microscopy
SHE	Standard Hydrogen Electrode
SHINERS	Shell-Isolated Nanoparticles Enhanced Raman Microscopy
SNOM	Scanning Near-Field Optical Microscopy
SPM	Scanning Probe Microscopy
SP	Surface Plasmon

SPP	Surface Plasmon Polariton
SPR	Surface Plasmon Resonance
STM	Scanning Tunneling Microscope
TERS	Tip-Enhanced Raman Spectroscopy
TF	Tuning Fork
UHV	Ultra High Vacuum
UME	Ultra-Microelectrode
UV	Ultraviolet
VDW	Van der Waals forces
Vis	Visible
WE	Working Electrode
XPS	X-Ray Photoelectron Spectroscopy

Abbreviations and acronyms of chemical compounds

4-ABM	4-aminobenzyl mercaptan
4-ATP	4-aminothiophenol
4-HABM	4-hydroxylaminobenzyl mercaptan
4-HATP	4-hydroxylaminothiophenol
4-NBM	4-nitrobenzyl mercaptan
4-NBT	4-nitrobenzenthio
4-NSBM	4-nitrosobenzyl mercaptan
4-NSTP	4-nitrosothiophenol
CNT	Carbon Nanotube
DMAB	<i>p-p'</i> -dimercaptoazobenzene
DMAOB	<i>p-p'</i> -dimercaptoazoxybenzene
DMHAB	<i>p-p'</i> -dimercaptohydrazobenzene
DMMA	4-,4'-dimercaptomethanazobenzene
MPS	3-mercaptopropyltriethoxysilane
MWCNT	Multiwall Carbon Nanotube

NB	Nile Blue
PEEK	Poly Ether-Ether Ketone
PhS	Thiophenolate

Symbols (and units)

BV	Bias Voltage	V or mV
λ	Wavelength	nm
ω	Angular frequency of an EM field	rad s ⁻¹
ω	Raman shift	cm ⁻¹
ρ	Density	kg m ⁻³
ρ_{Si}	Density (of Silicon)	2.33 x 10 ³ kg m ⁻³
π	Pi	3.14159265359
R	Nanoparticle radius	m
C	Concentration	mol m ⁻³
D	Diffusion coefficient	m ² s ⁻¹
E	Electrode potential	V
E ⁰	Standard redox potential	V
E	Young's modulus	GPa
f ₀ /f _r	Resonance frequency	Hz
Δf	Resonance frequency width	Hz
f _{tap}	Tapping frequency	Hz
f _M	Oscillating mirror	Hz
F	Faraday constant	96 485.3 A mol ⁻¹
i _f	Faraday current	A
i _p	Peak current in CV	A
i _{pa}	Anodic peak current in CV	A
i _{pc}	Cathodic peak current in CV	A
k	Spring constant	N m ⁻¹
l	Cantilever length	μ m

m	Cantilever mass	kg
n	Refractive index	-
Δp	Uncertainty of the momentum	kg m s ⁻¹
Q	Quality factor (TF)	-
R _{tip}	TERS tip radius (radius of curvature)	nm
t	Time	s
t	Cantilever thickness	μm
T	Temperature	K
v	Potential sweep rate in CV	V s ⁻¹
WD	Working Distance	mm
z	Vertical distance	nm
Δx	Lateral Resolution	μm or nm
Δx	Uncertainty of the position	nm
Δz	Depth Resolution	μm or nm
ϵ_m	Dielectric constant (of the metal)	-
ϵ_e	Dielectric constant (of the environment)	-

References

- (1) Chen, C.; Hayazawa, N.; Kawata, S. A 1.7 Nm Resolution Chemical Analysis of Carbon Nanotubes by Tip-Enhanced Raman Imaging in the Ambient. *Nat. Commun.* **2014**, *5* (1), 3312. <https://doi.org/10.1038/ncomms4312>.
- (2) Hersbach, T. J. P.; Ye, C.; Garcia, A. C.; Koper, M. T. M. Tailoring the Electrocatalytic Activity and Selectivity of Pt(111) through Cathodic Corrosion. *ACS Catal.* **2020**, *10* (24), 15104–15113. <https://doi.org/10.1021/acscatal.0c04016>.
- (3) Ahmed Zewail – Nobel Lecture. *NobelPrize.Org. Nobel Prize Outreach AB 2021. Thu. 16 Dec 2021*. <<https://www.nobelprize.org/prizes/chemistry/1999/zewail/lecture/>>.
- (4) Sedigh Rahimabadi, P.; Khodaei, M.; Koswattage, K. R. Review on Applications of Synchrotron-based X-ray Techniques in Materials Characterization. *X-Ray Spectrom.* **2020**, *49* (3), 348–373. <https://doi.org/10.1002/xrs.3141>.
- (5) Saveleva, V. A.; Savinova, E. R. Insights into Electrocatalysis from Ambient Pressure Photoelectron Spectroscopy. *Curr. Opin. Electrochem.* **2019**, *17*, 79–89. <https://doi.org/10.1016/j.coelec.2019.03.016>.
- (6) Anne Myers Kelley. *Molecular Vibrations and Infrared Spectroscopy*; 2012.
- (7) Fiebig, M.; Pavlov, V. V.; Pisarev, R. V. Second-Harmonic Generation as a Tool for Studying Electronic and Magnetic Structures of Crystals: Review. *J. Opt. Soc. Am. B* **2005**, *22* (1), 96. <https://doi.org/10.1364/JOSAB.22.000096>.
- (8) Eric Le Ru, Pablo Etchegoin. *Principles of Surface-Enhanced Raman Spectroscopy*; 2008.
- (9) Bekal, A.; Hebbale, A. M.; Srinath, M. S. Review on Material Processing Through Microwave Energy. *IOP Conf. Ser. Mater. Sci. Eng.* **2018**, *376*, 012079. <https://doi.org/10.1088/1757-899X/376/1/012079>.
- (10) Wollman, A. J. M.; Nudd, R.; Hedlund, E. G.; Leake, M. C. From *Animaculum* to Single Molecules: 300 Years of the Light Microscope. *Open Biol.* **2015**, *5* (4), 150019. <https://doi.org/10.1098/rsob.150019>.
- (11) Lu, C.; Zhang, P.; Chen, S.; Zhu, J.; Xu, X.; Huang, H. Fluorescence Spectrum Photo-Bleaching Analysis for Distinguishing Microorganisms (Bacteria and Fungi) from Other Particles in Air. *Opt. Express* **2018**, *26* (22), 28902. <https://doi.org/10.1364/OE.26.028902>.
- (12) *MLA Style: Press Release. NobelPrize.Org. Nobel Prize Outreach AB 2021. Thu. 16 Dec 2021*. <<https://www.nobelprize.org/prizes/chemistry/2014/press-release/>>.
- (13) Courtland, R. Pushing the Limits: Technological Advances Are Triggering; a Revolution in Electron Microscopy. *Nature*. 2018, pp 462–464.
- (14) Sutter, E.; Jungjohann, K.; Bliznakov, S.; Courty, A.; Maisonhaute, E.; Tenney, S.; Sutter, P. In Situ Liquid-Cell Electron Microscopy of Silver–Palladium Galvanic Replacement Reactions on Silver Nanoparticles. *Nat. Commun.* **2014**, *5* (1), 4946. <https://doi.org/10.1038/ncomms5946>.
- (15) *The Nobel Prize in Physics 1986. NobelPrize.Org. Nobel Prize Outreach AB 2021. Thu. 16 Dec 2021*. <<https://www.nobelprize.org/prizes/physics/1986/summary/>>.
- (16) C. Julian Chen. *Introduction to Scanning Tunneling Microscopy: Second Edition*; 2007.
- (17) Winkel, A. K.; Barner, J.; Henze, T.; Neumann, T.; Körnig, A.; Kumpfe, F.; Haschke, H. The Wide-Open Door: Atomic Force Microscopy 30 Years On. *Microsc. Today* **2016**, *24* (6), 12–17. <https://doi.org/10.1017/S1551929516000900>.
- (18) Rana, M. S.; Pota, H. R.; Petersen, I. R. Improvement in the Imaging Performance of Atomic Force Microscopy: A Survey. *IEEE Trans. Autom. Sci. Eng.* **2017**, *14* (2), 1265–1285. <https://doi.org/10.1109/TASE.2016.2538319>.
- (19) Lucas, I. T.; McLeod, A. S.; Syzdek, J. S.; Middlemiss, D. S.; Grey, C. P.; Basov, D. N.; Kosteckii, R. IR Near-Field Spectroscopy and Imaging of Single Li_xFePO_4 Microcrystals. *Nano Lett.* **2015**, *15* (1), 1–7. <https://doi.org/10.1021/nl5010898>.

- (20) Dazzi, A.; Prazeres, R.; Glotin, F.; Ortega, J. M. Local Infrared Microspectroscopy with Subwavelength Spatial Resolution with an Atomic Force Microscope Tip Used as a Photothermal Sensor. *Opt. Lett.* **2005**, *30* (18), 2388. <https://doi.org/10.1364/OL.30.002388>.
- (21) Dazzi, A.; Prazeres, R.; Glotin, F.; Ortega, J. M.; Al-Sawaftah, M.; de Frutos, M. Chemical Mapping of the Distribution of Viruses into Infected Bacteria with a Photothermal Method. *Ultramicroscopy* **2008**, *108* (7), 635–641. <https://doi.org/10.1016/j.ultramic.2007.10.008>.
- (22) Dazzi, A.; Prater, C. B. AFM-IR: Technology and Applications in Nanoscale Infrared Spectroscopy and Chemical Imaging. *Chem. Rev.* **2017**, *117* (7), 5146–5173. <https://doi.org/10.1021/acs.chemrev.6b00448>.
- (23) B. Schrader. *Infrared and Raman Spectroscopy: Methods and Applications*, John Wiley&Sons, 2008.
- (24) Willets, K. A.; Van Duyne, R. P. Localized Surface Plasmon Resonance Spectroscopy and Sensing. *Annu. Rev. Phys. Chem.* **2007**, *58* (1), 267–297. <https://doi.org/10.1146/annurev.physchem.58.032806.104607>.
- (25) Aubertin, P. Propriétés optiques, spectroscopiques et électrochimiques d’auto-organisation tridimensionnelles de nanoparticules. **184**, **2017**.
- (26) Haidar, I.; Lévi, G.; Mouton, L.; Aubard, J.; Grand, J.; Lau-Truong, S.; Neuville, D. R.; Félidj, N.; Boubekeur-Lecaque, L. Highly Stable Silica-Coated Gold Nanorods Dimers for Solution-Based SERS. *Phys. Chem. Chem. Phys.* **2016**, *18* (47), 32272–32280. <https://doi.org/10.1039/C6CP06218K>.
- (27) Fleischmann, M.; Hendra, P. J.; McQUILLAN, A. J. RAMAN SPECTRA OF PYRIDINE ADSORBED AT A SILVER ELECTRODE. *Chem. Phys. Lett.* **26** (2), 4.
- (28) Jeanmaire, D. L.; Duyne, R. P. V. SURFACE RAMAN SPECTROELECTROCHEMISTRY. **20**.
- (29) Albrecht, M. G.; Creighton, J. A. Anomalously Intense Raman Spectra of Pyridine at a Silver Electrode. *J. Am. Chem. Soc.* **1977**, *99* (15), 5215–5217. <https://doi.org/10.1021/ja00457a071>.
- (30) Nie, S.; Emory, S. R. Probing Single Molecules and Single Nanoparticles by Surface-Enhanced Raman Scattering. *Science* **1997**, *275* (5303), 1102–1106. <https://doi.org/10.1126/science.275.5303.1102>.
- (31) Kneipp, K.; Wang, Y.; Kneipp, H.; Perelman, L. T.; Itzkan, I.; Dasari, R. R.; Feld, M. S. Single Molecule Detection Using Surface-Enhanced Raman Scattering (SERS). *Phys. Rev. Lett.* **1997**, *78* (9), 1667–1670. <https://doi.org/10.1103/PhysRevLett.78.1667>.
- (32) Chapus, L.; Aubertin, P.; Joiret, S.; Lucas, I. T.; Maisonhaute, E.; Courty, A. Tunable SERS Platforms from Small Nanoparticle 3D Superlattices: A Comparison between Gold, Silver, and Copper. *ChemPhysChem* **2017**, *18* (21), 3066–3075. <https://doi.org/10.1002/cphc.201700601>.
- (33) Ringe, E.; Sharma, B.; Henry, A.-I.; Marks, L. D.; Van Duyne, R. P. Single Nanoparticle Plasmonics. *Phys. Chem. Chem. Phys.* **2013**, *15* (12), 4110. <https://doi.org/10.1039/c3cp44574g>.
- (34) Lucas, I. T.; Bazin, D.; Daudon, M. Raman Opportunities in the Field of Pathological Calcifications. *Comptes Rendus Chim.* **2021**, *24* (S2), 1–21. <https://doi.org/10.5802/crchim.110>.
- (35) Touzalin, P. T. Tip-Enhanced Raman Spectroscopy on Electrochemical Systems, Sorbonne Université, **2018**.
- (36) Iftime, G.; Labarthe, F. L.; Natansohn, A.; Rochon, P. Control of Chirality of an Azobenzene Liquid Crystalline Polymer with Circularly Polarized Light. *J. Am. Chem. Soc.* **2000**, *122* (51), 12646–12650. <https://doi.org/10.1021/ja001244m>.
- (37) El-Khoury, P. Z.; Schultz, Z. D. From SERS to TERS and Beyond: Molecules as Probes of Nanoscopic Optical Fields. *J. Phys. Chem. C* **2020**, *124* (50), 27267–27275. <https://doi.org/10.1021/acs.jpcc.0c08337>.

- (38) Handschuh-Wang, S.; Wang, T.; Zhou, X. Recent Advances in Hybrid Measurement Methods Based on Atomic Force Microscopy and Surface Sensitive Measurement Techniques. *RSC Adv* **2017**, *7* (75), 47464–47499. <https://doi.org/10.1039/C7RA08515J>.
- (39) Zhang, Z.; Sheng, S.; Wang, R.; Sun, M. Tip-Enhanced Raman Spectroscopy. *Anal. Chem.* **2016**, *88* (19), 9328–9346. <https://doi.org/10.1021/acs.analchem.6b02093>.
- (40) Kurouski, D.; Dazzi, A.; Zenobi, R.; Centrone, A. Infrared and Raman Chemical Imaging and Spectroscopy at the Nanoscale. *Chem. Soc. Rev.* **2020**, *49* (11), 3315–3347. <https://doi.org/10.1039/C8CS00916C>.
- (41) Halas, N. J.; Lal, S.; Chang, W.-S.; Link, S.; Nordlander, P. Plasmons in Strongly Coupled Metallic Nanostructures. *Chem. Rev.* **2011**, *111* (6), 3913–3961. <https://doi.org/10.1021/cr200061k>.
- (42) Pfisterer, J. H. K.; Baghernejad, M.; Giuzio, G.; Domke, K. F. Reactivity Mapping of Nanoscale Defect Chemistry under Electrochemical Reaction Conditions. *Nat. Commun.* **2019**, *10* (1), 5702. <https://doi.org/10.1038/s41467-019-13692-3>.
- (43) Becker, S. F.; Esmann, M.; Yoo, K.; Gross, P.; Vogelgesang, R.; Park, N.; Lienau, C. Gap-Plasmon-Enhanced Nanofocusing Near-Field Microscopy. *ACS Photonics* **2016**, *3* (2), 223–232. <https://doi.org/10.1021/acsphotonics.5b00438>.
- (44) Benz, F.; Schmidt, M. K.; Dreismann, A.; Chikkaraddy, R.; Zhang, Y.; Demetriadou, A.; Carnegie, C.; Ohadi, H.; de Nijs, B.; Esteban, R.; Aizpurua, J.; Baumberg, J. J. Single-Molecule Optomechanics in “Picocavities.” *Science* **2016**, *354* (6313), 726–729. <https://doi.org/10.1126/science.aah5243>.
- (45) Zhang, M.; Wang, R.; Zhu, Z.; Wang, J.; Tian, Q. Experimental Research on the Spectral Response of Tips for Tip-Enhanced Raman Spectroscopy. *J. Opt.* **2013**, *15* (5), 055006. <https://doi.org/10.1088/2040-8978/15/5/055006>.
- (46) Lee, J.; Crampton, K. T.; Tallarida, N.; Apkarian, V. A. Visualizing Vibrational Normal Modes of a Single Molecule with Atomically Confined Light. *Nature* **2019**, *568* (7750), 78–82. <https://doi.org/10.1038/s41586-019-1059-9>.
- (47) Najjar, S.; Talaga, D.; Schué, L.; Coffinier, Y.; Szunerits, S.; Boukherroub, R.; Servant, L.; Rodriguez, V.; Bonhommeau, S. Tip-Enhanced Raman Spectroscopy of Combed Double-Stranded DNA Bundles. *J. Phys. Chem. C* **2014**, *118* (2), 1174–1181. <https://doi.org/10.1021/jp410963z>.
- (48) Bonhommeau, S.; Lecomte, S. Tip-Enhanced Raman Spectroscopy: A Tool for Nanoscale Chemical and Structural Characterization of Biomolecules. *ChemPhysChem* **2018**, *19* (1), 8–18. <https://doi.org/10.1002/cphc.201701067>.
- (49) Schmid, T.; Yeo, B.-S.; Leong, G.; Stadler, J.; Zenobi, R. Performing Tip-Enhanced Raman Spectroscopy in Liquids. *J. Raman Spectrosc.* **2009**, *40* (10), 1392–1399. <https://doi.org/10.1002/jrs.2387>.
- (50) Kurouski, D.; Mattei, M.; Van Duyne, R. P. Probing Redox Reactions at the Nanoscale with Electrochemical Tip-Enhanced Raman Spectroscopy. *Nano Lett.* **2015**, *15* (12), 7956–7962. <https://doi.org/10.1021/acs.nanolett.5b04177>.
- (51) Zeng, Z.-C.; Huang, S.-C.; Wu, D.-Y.; Meng, L.-Y.; Li, M.-H.; Huang, T.-X.; Zhong, J.-H.; Wang, X.; Yang, Z.-L.; Ren, B. Electrochemical Tip-Enhanced Raman Spectroscopy. *J. Am. Chem. Soc.* **2015**, *137* (37), 11928–11931. <https://doi.org/10.1021/jacs.5b08143>.
- (52) Kang, G.; Yang, M.; Mattei, M. S.; Schatz, G. C.; Van Duyne, R. P. *In Situ* Nanoscale Redox Mapping Using Tip-Enhanced Raman Spectroscopy. *Nano Lett.* **2019**, *19* (3), 2106–2113. <https://doi.org/10.1021/acs.nanolett.9b00313>.
- (53) Bao, Y.-F.; Cao, M.-F.; Wu, S.-S.; Huang, T.-X.; Zeng, Z.-C.; Li, M.-H.; Wang, X.; Ren, B. Atomic Force Microscopy Based Top-Illumination Electrochemical Tip-Enhanced Raman Spectroscopy. *Anal. Chem.* **2020**, *92* (18), 12548–12555. <https://doi.org/10.1021/acs.analchem.0c02466>.

- (54) Touzalin, T.; Joiret, S.; Maisonhaute, E.; Lucas, I. T. Capturing Electrochemical Transformations by Tip-Enhanced Raman Spectroscopy. *Curr. Opin. Electrochem.* **2017**, *6* (1), 46–52. <https://doi.org/10.1016/j.coelec.2017.10.016>.
- (55) Touzalin, T.; Joiret, S.; Lucas, I. T.; Maisonhaute, E. Electrochemical Tip-Enhanced Raman Spectroscopy Imaging with 8 Nm Lateral Resolution. *Electrochem. Commun.* **2019**, *108*, 106557. <https://doi.org/10.1016/j.elecom.2019.106557>.
- (56) Verma, P. Tip-Enhanced Raman Spectroscopy: Technique and Recent Advances. *Chem. Rev.* **2017**, *117* (9), 6447–6466. <https://doi.org/10.1021/acs.chemrev.6b00821>.
- (57) Pettinger, B.; Picardi, G.; Schuster, R.; Ertl, G. Surface-Enhanced and STM-Tip-Enhanced Raman Spectroscopy at Metal Surfaces. *Single Mol.* **2002**, *3* (5–6), 285–294. [https://doi.org/10.1002/1438-5171\(200211\)3:5/6<285::AID-SIMO285>3.0.CO;2-X](https://doi.org/10.1002/1438-5171(200211)3:5/6<285::AID-SIMO285>3.0.CO;2-X).
- (58) Zhu, L.; Georgi, C.; Hecker, M.; Rinderknecht, J.; Mai, A.; Ritz, Y.; Zschech, E. Nano-Raman Spectroscopy with Metallized Atomic Force Microscopy Tips on Strained Silicon Structures. *J. Appl. Phys.* **2007**, *101* (10), 104305. <https://doi.org/10.1063/1.2732435>.
- (59) Oguchi, M.; Mochizuki, M.; Yano, T.; Hara, M.; Hayashi, T. Light-Transmittable Ultrasoother Gold Film for Gap-Mode Tip-Enhanced Raman Scattering Spectroscopy. *Chem. Lett.* **2014**, *43* (6), 808–810. <https://doi.org/10.1246/cl.140093>.
- (60) Sackrow, M.; Stanciu, C.; Lieb, M. A.; Meixner, A. J. Imaging Nanometre-Sized Hot Spots on Smooth Au Films with High-Resolution Tip-Enhanced Luminescence and Raman Near-Field Optical Microscopy. *ChemPhysChem* **2008**, *9* (2), 316–320. <https://doi.org/10.1002/cphc.200700723>.
- (61) Ossikovski, R.; Nguyen, Q.; Picardi, G. Simple Model for the Polarization Effects in Tip-Enhanced Raman Spectroscopy. *Phys. Rev. B* **2007**, *75* (4), 045412. <https://doi.org/10.1103/PhysRevB.75.045412>.
- (62) Ramos, R.; Gordon, M. J. Near-Field Artifacts in Tip-Enhanced Raman Spectroscopy. *Appl. Phys. Lett.* **2012**, *100* (21), 213111. <https://doi.org/10.1063/1.4722805>.
- (63) Tanirah, O.; Kern, D. P.; Fleischer, M. Fabrication of a Plasmonic Nanocone on Top of an AFM Cantilever. *Microelectron. Eng.* **2015**, *141*, 215–218. <https://doi.org/10.1016/j.mee.2015.03.014>.
- (64) Lkhamsuren, G.; Mochizuki, M.; Suthiwanich, K.; Hayashi, T. Fabrication of Mechanically Stable Au-Coatings on Probes of Atomic Force Microscopes for Nano-Mechanical and -Optical Measurements. *Thin Solid Films* **2017**, *636*, 478–484. <https://doi.org/10.1016/j.tsf.2017.06.046>.
- (65) Downes, A.; Salter, D.; Elfick, A. Simulations of Atomic Resolution Tip-Enhanced Optical Microscopy. *Opt. Express* **2006**, *14* (23), 11324. <https://doi.org/10.1364/OE.14.011324>.
- (66) Deckert, V.; Deckert-Gaudig, T.; Diegel, M.; Götz, I.; Langelüddecke, L.; Schneidewind, H.; Sharma, G.; Singh, P.; Singh, P.; Trautmann, S.; Zeisberger, M.; Zhang, Z. Spatial Resolution in Raman Spectroscopy. *Faraday Discuss.* **2015**, *177*, 9–20. <https://doi.org/10.1039/C5FD90014J>.
- (67) Wang, H.; Tian, T.; Zhang, Y.; Pan, Z.; Wang, Y.; Xiao, Z. Sequential Electrochemical Oxidation and Site-Selective Growth of Nanoparticles onto AFM Probes. *Langmuir* **2008**, *24* (16), 8918–8922. <https://doi.org/10.1021/la800380p>.
- (68) Umakoshi, T.; Saito, Y.; Verma, P. Highly Efficient Plasmonic Tip Design for Plasmon Nanofocusing in Near-Field Optical Microscopy. *Nanoscale* **2016**, *8* (10), 5634–5640. <https://doi.org/10.1039/C5NR08548A>.
- (69) Wang, X.; Liu, Z.; Zhuang, M.-D.; Zhang, H.-M.; Wang, X.; Xie, Z.-X.; Wu, D.-Y.; Ren, B.; Tian, Z.-Q. Tip-Enhanced Raman Spectroscopy for Investigating Adsorbed Species on a Single-Crystal Surface Using Electrochemically Prepared Au Tips. *Appl. Phys. Lett.* **2007**, *91* (10), 101105. <https://doi.org/10.1063/1.2776860>.
- (70) Baptista, A.; Silva, F.; Porteiro, J.; Míguez, J.; Pinto, G. Sputtering Physical Vapour Deposition (PVD) Coatings: A Critical Review on Process Improvement and Market Trend Demands. *Coatings* **2018**, *8* (11), 402. <https://doi.org/10.3390/coatings8110402>.

- (71) Taguchi, A.; Yu, J.; Verma, P.; Kawata, S. Optical Antennas with Multiple Plasmonic Nanoparticles for Tip-Enhanced Raman Microscopy. *Nanoscale* **2015**, *7* (41), 17424–17433. <https://doi.org/10.1039/C5NR05022G>.
- (72) Hung, P. Y.; O’Loughlin, T. E.; Lewis, A.; Dechter, R.; Samayoa, M.; Banerjee, S.; Wood, E. L.; Hight Walker, A. R. Potential Application of Tip-Enhanced Raman Spectroscopy (TERS) in Semiconductor Manufacturing; Cain, J. P., Sanchez, M. I., Eds.; San Jose, California, United States, 2015; p 94241S. <https://doi.org/10.1117/12.2175623>.
- (73) Gao, L.; Lemarchand, F.; Lequime, M. Refractive Index Determination of SiO₂ Layer in the UV/Vis/NIR Range: Spectrophotometric Reverse Engineering on Single and Bi-Layer Designs. *J. Eur. Opt. Soc. Rapid Publ.* **2013**, *8*, 13010. <https://doi.org/10.2971/jeos.2013.13010>.
- (74) Yeo, B.-S.; Stadler, J.; Schmid, T.; Zenobi, R.; Zhang, W. Tip-Enhanced Raman Spectroscopy – Its Status, Challenges and Future Directions. *Chem. Phys. Lett.* **2009**, *472* (1–3), 1–13. <https://doi.org/10.1016/j.cplett.2009.02.023>.
- (75) Saito, Y.; Verma, P. Polarization-Controlled Raman Microscopy and Nanoscopy. *J. Phys. Chem. Lett.* **2012**, *3* (10), 1295–1300. <https://doi.org/10.1021/jz300213t>.
- (76) Sharma, G.; Deckert-Gaudig, T.; Deckert, V. Tip-Enhanced Raman Scattering—Targeting Structure-Specific Surface Characterization for Biomedical Samples. *Adv. Drug Deliv. Rev.* **2015**, *89*, 42–56. <https://doi.org/10.1016/j.addr.2015.06.007>.
- (77) Smolyaninov, I. I.; Davis, C. C.; Elliott, J.; Zayats, A. V. Resolution Enhancement of a Surface Immersion Microscope near the Plasmon Resonance. *Opt. Lett.* **2005**, *30* (4), 382. <https://doi.org/10.1364/OL.30.000382>.
- (78) Deckert-Gaudig, T.; Taguchi, A.; Kawata, S.; Deckert, V. Tip-Enhanced Raman Spectroscopy – from Early Developments to Recent Advances. *Chem. Soc. Rev.* **2017**, *46* (13), 4077–4110. <https://doi.org/10.1039/C7CS00209B>.
- (79) Fleischer, M.; Weber-Bargioni, A.; Altoe, M. V. P.; Schwartzberg, A. M.; Schuck, P. J.; Cabrini, S.; Kern, D. P. Gold Nanocone Near-Field Scanning Optical Microscopy Probes. *ACS Nano* **2011**, *5* (4), 2570–2579. <https://doi.org/10.1021/nn102199u>.
- (80) Weber-Bargioni, A.; Schwartzberg, A.; Cornaglia, M.; Ismach, A.; Urban, J. J.; Pang, Y.; Gordon, R.; Bokor, J.; Salmeron, M. B.; Ogletree, D. F.; Ashby, P.; Cabrini, S.; Schuck, P. J. Hyperspectral Nanoscale Imaging on Dielectric Substrates with Coaxial Optical Antenna Scan Probes. *Nano Lett.* **2011**, *11* (3), 1201–1207. <https://doi.org/10.1021/nl104163m>.
- (81) Farahani, J. N.; Pohl, D. W.; Eisler, H.-J.; Hecht, B. Single Quantum Dot Coupled to a Scanning Optical Antenna: A Tunable Superemitter. *Phys. Rev. Lett.* **2005**, *95* (1), 017402. <https://doi.org/10.1103/PhysRevLett.95.017402>.
- (82) Bao, W.; Melli, M.; Caselli, N.; Riboli, F.; Wiersma, D. S.; Staffaroni, M.; Choo, H.; Ogletree, D. F.; Aloni, S.; Bokor, J.; Cabrini, S.; Intonti, F.; Salmeron, M. B.; Yablonovitch, E.; Schuck, P. J.; Weber-Bargioni, A. Mapping Local Charge Recombination Heterogeneity by Multidimensional Nanospectroscopic Imaging. *Science* **2012**, *338* (6112), 1317–1321. <https://doi.org/10.1126/science.1227977>.
- (83) De Angelis, F.; Das, G.; Candeloro, P.; Patrini, M.; Galli, M.; Bek, A.; Lazzarino, M.; Maksymov, I.; Liberale, C.; Andreani, L. C.; Di Fabrizio, E. Nanoscale Chemical Mapping Using Three-Dimensional Adiabatic Compression of Surface Plasmon Polaritons. *Nat. Nanotechnol.* **2010**, *5* (1), 67–72. <https://doi.org/10.1038/nnano.2009.348>.
- (84) Bek, A.; De Angelis, F.; Das, G.; Di Fabrizio, E.; Lazzarino, M. Tip Enhanced Raman Scattering with Adiabatic Plasmon Focusing Tips. *Micron* **2011**, *42* (4), 313–317. <https://doi.org/10.1016/j.micron.2010.05.017>.
- (85) Yeo, B.-S.; Schmid, T.; Zhang, W.; Zenobi, R. Towards Rapid Nanoscale Chemical Analysis Using Tip-Enhanced Raman Spectroscopy with Ag-Coated Dielectric Tips. *Anal. Bioanal. Chem.* **2007**, *387* (8), 2655–2662. <https://doi.org/10.1007/s00216-007-1165-7>.
- (86) Taguchi, A.; Hayazawa, N.; Saito, Y.; Ishitobi, H.; Tarun, A.; Kawata, S. Controlling the Plasmon Resonance Wavelength in Metal-Coated Probe Using Refractive Index Modification. *Opt. Express* **2009**, *17* (8), 6509. <https://doi.org/10.1364/OE.17.006509>.

- (87) Kumar, N.; Su, W.; Veselý, M.; Weckhuysen, B. M.; Pollard, A. J.; Wain, A. J. Nanoscale Chemical Imaging of Solid–Liquid Interfaces Using Tip-Enhanced Raman Spectroscopy. *Nanoscale* **2018**, *10* (4), 1815–1824. <https://doi.org/10.1039/C7NR08257F>.
- (88) Opilik, L.; Dogan, Ü.; Li, C.-Y.; Stephanidis, B.; Li, J.-F.; Zenobi, R. Chemical Production of Thin Protective Coatings on Optical Nanotips for Tip-Enhanced Raman Spectroscopy. *J. Phys. Chem. C* **2016**, *120* (37), 20828–20832. <https://doi.org/10.1021/acs.jpcc.6b02147>.
- (89) Liu, Z.; Wang, X.; Dai, K.; Jin, S.; Zeng, Z.-C.; Zhuang, M.-D.; Yang, Z.-L.; Wu, D.-Y.; Ren, B.; Tian, Z.-Q. Tip-Enhanced Raman Spectroscopy for Investigating Adsorbed Nonresonant Molecules on Single-Crystal Surfaces: Tip Regeneration, Probe Molecule, and Enhancement Effect. *J. Raman Spectrosc.* **2009**, *40* (10), 1400–1406. <https://doi.org/10.1002/jrs.2431>.
- (90) Blum, C.; Opilik, L.; Atkin, J. M.; Braun, K.; Kämmer, S. B.; Kravtsov, V.; Kumar, N.; Lemeshko, S.; Li, J.-F.; Luszcz, K.; Maleki, T.; Meixner, A. J.; Minne, S.; Raschke, M. B.; Ren, B.; Rogalski, J.; Roy, D.; Stephanidis, B.; Wang, X.; Zhang, D.; Zhong, J.-H.; Zenobi, R. Tip-Enhanced Raman Spectroscopy - an Interlaboratory Reproducibility and Comparison Study: TERS Interlaboratory Comparison. *J. Raman Spectrosc.* **2014**, *45* (1), 22–31. <https://doi.org/10.1002/jrs.4423>.
- (91) Walke, P.; Fujita, Y.; Peeters, W.; Toyouchi, S.; Frederickx, W.; Feyter, S. D.; Uji-i, H. Silver Nanowires for Highly Reproducible Cantilever Based AFM-TERS Microscopy: Towards a Universal TERS Probe. *Nanoscale* **2018**, *10* (16), 7556–7565. <https://doi.org/10.1039/C8NR02225A>.
- (92) Shi, X.; Coca-López, N.; Janik, J.; Hartschuh, A. Advances in Tip-Enhanced Near-Field Raman Microscopy Using Nanoantennas. *Chem. Rev.* **2017**, *117* (7), 4945–4960. <https://doi.org/10.1021/acs.chemrev.6b00640>.
- (93) Agapov, R. L.; Sokolov, A. P.; Foster, M. D. Protecting TERS Probes from Degradation: Extending Mechanical and Chemical Stability: Protecting TERS Probes from Degradation. *J. Raman Spectrosc.* **2013**, *44* (5), 710–716. <https://doi.org/10.1002/jrs.4268>.
- (94) Yang, L.-K.; Huang, T.-X.; Zeng, Z.-C.; Li, M.-H.; Wang, X.; Yang, F.-Z.; Ren, B. Rational Fabrication of a Gold-Coated AFM TERS Tip by Pulsed Electrodeposition. *Nanoscale* **2015**, *7* (43), 18225–18231. <https://doi.org/10.1039/C5NR04263A>.
- (95) Huang, T.-X.; Huang, S.-C.; Li, M.-H.; Zeng, Z.-C.; Wang, X.; Ren, B. Tip-Enhanced Raman Spectroscopy: Tip-Related Issues. *Anal. Bioanal. Chem.* **2015**, *407* (27), 8177–8195. <https://doi.org/10.1007/s00216-015-8968-8>.
- (96) Li, Z. L.; Wu, T. H.; Niu, Z. J.; Huang, W.; Nie, H. D. In Situ Raman Spectroscopic Studies on the Current Oscillations during Gold Electrodeposition in HCl Solution. *Electrochem. Commun.* **2004**, *6* (1), 44–48. <https://doi.org/10.1016/j.elecom.2003.10.012>.
- (97) Barsegova, I.; Lewis, A.; Khatchaturians, A.; Manevitch, A.; Ignatov, A.; Axelrod, N.; Sukenik, C. Controlled Fabrication of Silver or Gold Nanoparticle Near-Field Optical Atomic Force Probes: Enhancement of Second-Harmonic Generation. *Appl. Phys. Lett.* **2002**, *81* (18), 3461–3463. <https://doi.org/10.1063/1.1507618>.
- (98) Coluccio, M. L.; Francardi, M.; Gentile, F.; Candeloro, P.; Ferrara, L.; Perozziello, G.; Di Fabrizio, E. Plasmonic 3D-Structures Based on Silver Decorated Nanotips for Biological Sensing. *Opt. Lasers Eng.* **2016**, *76*, 45–51. <https://doi.org/10.1016/j.optlaseng.2015.04.020>.
- (99) Anger, P.; Bharadwaj, P.; Novotny, L. Enhancement and Quenching of Single-Molecule Fluorescence. *Phys. Rev. Lett.* **2006**, *96* (11), 113002. <https://doi.org/10.1103/PhysRevLett.96.113002>.
- (100) Umakoshi, T.; Yano, T.; Saito, Y.; Verma, P. Fabrication of Near-Field Plasmonic Tip by Photoreduction for Strong Enhancement in Tip-Enhanced Raman Spectroscopy. *Appl. Phys. Express* **2012**, *5* (5), 052001. <https://doi.org/10.1143/APEX.5.052001>.
- (101) Vakarelski, I. U.; Higashitani, K. Single-Nanoparticle-Terminated Tips for Scanning Probe Microscopy. *Langmuir* **2006**, *22* (7), 2931–2934. <https://doi.org/10.1021/la0528145>.
- (102) Walke, P.; Fujita, Y.; Peeters, W.; Toyouchi, S.; Frederickx, W.; De Feyter, S.; Uji-i, H. Silver Nanowires for Highly Reproducible Cantilever Based AFM-TERS Microscopy: Towards a

- Universal TERS Probe. *Nanoscale* **2018**, *10* (16), 7556–7565.
<https://doi.org/10.1039/C8NR02225A>.
- (103) Lehmann, V. *Electrochemistry of Silicon: Instrumentation, Science, Materials and Applications*, 1st ed.; Wiley, 2002. <https://doi.org/10.1002/3527600272>.
- (104) Djokic SS, Magagnin L (2014). *Electrodeposition and Surface Finishing. Fundamentals and Applications*. Springer, New York.
- (105) Zhang, Q.; Wu, M.; Zhao, W. Electroless Nickel Plating on Hollow Glass Microspheres. *Surf. Coat. Technol.* **2005**, *192* (2–3), 213–219. <https://doi.org/10.1016/j.surfcoat.2004.06.013>.
- (106) Gao, L.; Zhao, H.; Li, Y.; Li, T.; Chen, D.; Liu, B. Controllable Fabrication of Au-Coated AFM Probes via a Wet-Chemistry Procedure. *Nanoscale Res. Lett.* **2018**, *13* (1), 366. <https://doi.org/10.1186/s11671-018-2789-6>.
- (107) Dutheil, P.; Thomann, A. L.; Lecas, T.; Brault, P.; Vayer, M. Sputtered Ag Thin Films with Modified Morphologies: Influence on Wetting Property. *Appl. Surf. Sci.* **2015**, *347*, 101–108. <https://doi.org/10.1016/j.apsusc.2015.04.052>.
- (108) Ramanauskaitė, L.; Xu, H.; Griskonis, E.; Batiuskaite, D.; Snitka, V. Comparison and Evaluation of Silver Probe Preparation Techniques for Tip-Enhanced Raman Spectroscopy. *Plasmonics* **2018**, *13* (6), 1907–1919. <https://doi.org/10.1007/s11468-018-0705-7>.
- (109) Lopes, M.; Toury, T.; de La Chapelle, M. L.; Bonaccorso, F.; Giuseppe Gucciardi, P. Fast and Reliable Fabrication of Gold Tips with Sub-50 Nm Radius of Curvature for Tip-Enhanced Raman Spectroscopy. *Rev. Sci. Instrum.* **2013**, *84* (7), 073702. <https://doi.org/10.1063/1.4812365>.
- (110) Kim, D. H.; Lee, C.; Jeong, B. G.; Kim, S. H.; Jeong, M. S. Fabrication of Highly Uniform Nanoprobe via the Automated Process for Tip-Enhanced Raman Spectroscopy. *Nanophotonics* **2020**, *9* (9), 2989–2996. <https://doi.org/10.1515/nanoph-2020-0210>.
- (111) Ren, B.; Picardi, G.; Pettinger, B. Preparation of Gold Tips Suitable for Tip-Enhanced Raman Spectroscopy and Light Emission by Electrochemical Etching. *Rev. Sci. Instrum.* **2004**, *75* (4), 837–841. <https://doi.org/10.1063/1.1688442>.
- (112) Billot, L.; Berguiga, L.; de la Chapelle, M. L.; Gilbert, Y.; Bachelot, R. Production of Gold Tips for Tip-Enhanced near-Field Optical Microscopy and Spectroscopy: Analysis of the Etching Parameters. *Eur. Phys. J. Appl. Phys.* **2005**, *31* (2), 139–145. <https://doi.org/10.1051/epjap:2005049>.
- (113) Neacsu, C. C.; Berweger, S.; Raschke, M. B. Tip-Enhanced Raman Imaging and Nanospectroscopy: Sensitivity, Symmetry, and Selection Rules. *NanoBiotechnology* **2007**, *3* (3–4), 172–196. <https://doi.org/10.1007/s12030-008-9015-z>.
- (114) Kharintsev, S. S.; Noskov, A. I.; Hoffmann, G. G.; Loos, J. Near-Field Optical Taper Antennas Fabricated with a Highly Replicable Ac Electrochemical Etching Method. *Nanotechnology* **2011**, *22* (2), 025202. <https://doi.org/10.1088/0957-4484/22/2/025202>.
- (115) Melmed, A. J. The Art and Science and Other Aspects of Making Sharp Tips. *J. Vac. Sci. Technol. B Microelectron. Nanometer Struct.* **1991**, *9* (2), 601. <https://doi.org/10.1116/1.585467>.
- (116) Ito, T.; Bühlmann, P.; Umezawa, Y. Scanning Tunneling Microscopy Using Chemically Modified Tips. *Anal. Chem.* **1998**, *70* (2), 255–259. <https://doi.org/10.1021/ac970498w>.
- (117) Yang, B.; Kazuma, E.; Yokota, Y.; Kim, Y. Fabrication of Sharp Gold Tips by Three-Electrode Electrochemical Etching with High Controllability and Reproducibility. *J. Phys. Chem. C* **2018**, *122* (29), 16950–16955. <https://doi.org/10.1021/acs.jpcc.8b04078>.
- (118) Dickmann, K.; Demming, F.; Jersch, J. New Etching Procedure for Silver Scanning Tunneling Microscopy Tips. *Rev. Sci. Instrum.* **1996**, *67* (3), 845–846. <https://doi.org/10.1063/1.1146655>.
- (119) Kharintsev, S. S.; Hoffmann, G. G.; Fishman, A. I.; Salakhov, M. K. Plasmonic Optical Antenna Design for Performing Tip-Enhanced Raman Spectroscopy and Microscopy. *J. Phys. Appl. Phys.* **2013**, *46* (14), 145501. <https://doi.org/10.1088/0022-3727/46/14/145501>.
- (120) Dauphin, A.; Lucas, I.; Maisonhaute, E. MISE AU POINT DE SONDES T. 16.

- (121) Gorbunov, A. A.; Wolf, B.; Edelmann, J. The Use of Silver Tips in Scanning Tunneling Microscopy. *Rev. Sci. Instrum.* **1993**, *64* (8), 2393–2394. <https://doi.org/10.1063/1.1143892>.
- (122) Lloyd, J. S.; Williams, A.; Rickman, R. H.; McCowen, A.; Dunstan, P. R. Reproducible Electrochemical Etching of Silver Probes with a Radius of Curvature of 20 Nm for Tip-Enhanced Raman Applications. *Appl. Phys. Lett.* **2011**, *99* (14), 143108. <https://doi.org/10.1063/1.3646106>.
- (123) Hodgson, P. A.; Wang, Y.; Mohammad, A. A.; Kruse, P. Note: Electrochemical Etching of Silver Tips in Concentrated Sulfuric Acid. *Rev. Sci. Instrum.* **2013**, *84* (2), 026109. <https://doi.org/10.1063/1.4793243>.
- (124) Iwami, M.; Uehara, Y.; Ushioda, S. Preparation of Silver Tips for Scanning Tunneling Microscopy Imaging. *Rev. Sci. Instrum.* **1998**, *69* (11), 4010–4011. <https://doi.org/10.1063/1.1149215>.
- (125) Zhang, C.; Gao, B.; Chen, L. G.; Meng, Q. S.; Yang, H.; Zhang, R.; Tao, X.; Gao, H. Y.; Liao, Y.; Dong, Z. C. Fabrication of Silver Tips for Scanning Tunneling Microscope Induced Luminescence. *Rev. Sci. Instrum.* **2011**, *82* (8), 083101. <https://doi.org/10.1063/1.3617456>.
- (126) Li, M.; Lv, R.; Huang, S.; Dai, Y.; Zeng, Z.; Wang, L.; Ren, B. Electrochemical Fabrication of Silver Tips for Tip-Enhanced Raman Spectroscopy Assisted by a Machine Vision System: Electrochemical Fabrication of Silver Tips for TERS. *J. Raman Spectrosc.* **2016**, *47* (7), 808–812. <https://doi.org/10.1002/jrs.4898>.
- (127) Macpherson, J. V.; Unwin, P. R. Combined Scanning Electrochemical–Atomic Force Microscopy. *Anal. Chem.* **2000**, *72* (2), 276–285. <https://doi.org/10.1021/ac990921w>.
- (128) Abbou, J.; Demaille, C.; Druet, M.; Moiroux, J. Fabrication of Submicrometer-Sized Gold Electrodes of Controlled Geometry for Scanning Electrochemical-Atomic Force Microscopy. *Anal. Chem.* **2002**, *74* (24), 6355–6363. <https://doi.org/10.1021/ac020385z>.
- (129) Snitka, V.; Rodriguez, R. D.; Lendraitis, V. Novel Gold Cantilever for Nano-Raman Spectroscopy of Graphene. *Microelectron. Eng.* **2011**, *88* (8), 2759–2762. <https://doi.org/10.1016/j.mee.2011.02.046>.
- (130) Rodriguez, R. D.; Sheremet, E.; Müller, S.; Gordan, O. D.; Villabona, A.; Schulze, S.; Hietschold, M.; Zahn, D. R. T. Compact Metal Probes: A Solution for Atomic Force Microscopy Based Tip-Enhanced Raman Spectroscopy. *Rev. Sci. Instrum.* **2012**, *83* (12), 123708. <https://doi.org/10.1063/1.4770140>.
- (131) Kolchuzhin, V. A.; Sheremet, E.; Bhattacharya, K.; Rodriguez, R. D.; Paul, S. D.; Mehner, J.; Hietschold, M.; Zahn, D. R. T. Mechanical Properties and Applications of Custom-Built Gold AFM Cantilevers. *Mechatronics* **2016**, *40*, 281–286. <https://doi.org/10.1016/j.mechatronics.2016.05.015>.
- (132) Abbou, J.; Demaille, C.; Druet, M.; Moiroux, J. Fabrication of Submicrometer-Sized Gold Electrodes of Controlled Geometry for Scanning Electrochemical-Atomic Force Microscopy. *Anal. Chem.* **2002**, *74* (24), 6355–6363. <https://doi.org/10.1021/ac020385z>.
- (133) Rodriguez, R. D.; Anne, A.; Cambril, E.; Demaille, C. Optimized Hand Fabricated AFM Probes for Simultaneous Topographical and Electrochemical Tapping Mode Imaging. *Ultramicroscopy* **2011**, *111* (8), 973–981. <https://doi.org/10.1016/j.ultramic.2011.02.001>.
- (134) Mazeran, P.-E.; Odoni, L.; Loubet, J.-L. Curvature Radius Analysis for Scanning Probe Microscopy. *Surf. Sci.* **2005**, *585* (1–2), 25–37. <https://doi.org/10.1016/j.susc.2005.04.005>.
- (135) Vekinis, A. A.; Constantoudis, V. Quantifying Geometric Tip-Sample Effects in AFM Measurements Using Certainty Graphs. *Micro Nano Eng.* **2020**, *8*, 100067. <https://doi.org/10.1016/j.mne.2020.100067>.
- (136) Hübner, U.; Morgenroth, W.; Meyer, H. G.; Sulzbach, T.; Brendel, B.; Mirandé, W. Downwards to Metrology in Nanoscale: Determination of the AFM Tip Shape with Well-Known Sharp-Edged Calibration Structures. *Appl. Phys. Mater. Sci. Process.* **2003**, *76* (6), 913–917. <https://doi.org/10.1007/s00339-002-1975-6>.

- (137) Horng, T.-L. Analyses of Vibration Responses on Nanoscale Processing in a Liquid Using Tapping-Mode Atomic Force Microscopy. *Appl. Surf. Sci.* **2009**, *256* (1), 311–317. <https://doi.org/10.1016/j.apsusc.2009.08.021>.
- (138) Chen, J.; Workman, R. K.; Sarid, D.; Hoper, R. Numerical Simulations of a Scanning Force Microscope with a Large-Amplitude Vibrating Cantilever. *Nanotechnology* **1994**, *5* (4), 199–204. <https://doi.org/10.1088/0957-4484/5/4/003>.
- (139) Cleveland, J. P.; Anczykowski, B.; Schmid, A. E.; Elings, V. B. Energy Dissipation in Tapping-Mode Atomic Force Microscopy. *Appl. Phys. Lett.* **1998**, *72* (20), 2613–2615. <https://doi.org/10.1063/1.121434>.
- (140) Tamayo, J.; García, R. Deformation, Contact Time, and Phase Contrast in Tapping Mode Scanning Force Microscopy. *Langmuir* **1996**, *12* (18), 4430–4435. <https://doi.org/10.1021/la960189l>.
- (141) Poggi, M. A.; McFarland, A. W.; Colton, J. S.; Bottomley, L. A. A Method for Calculating the Spring Constant of Atomic Force Microscopy Cantilevers with a Nonrectangular Cross Section. *Anal. Chem.* **2005**, *77* (4), 1192–1195. <https://doi.org/10.1021/ac048828h>.
- (142) Touzalin, T.; Joiret, S.; Maisonhaute, E.; Lucas, I. T. Complex Electron Transfer Pathway at a Microelectrode Captured by *in Situ* Nanospectroscopy. *Anal. Chem.* **2017**, *89* (17), 8974–8980. <https://doi.org/10.1021/acs.analchem.7b01542>.
- (143) Wang, Z.; Zervas, M. N.; Bartlett, P. N.; Wilkinson, J. S. Surface and Waveguide Collection of Raman Emission in Waveguide-Enhanced Raman Spectroscopy. *Opt. Lett.* **2016**, *41* (17), 4146. <https://doi.org/10.1364/OL.41.004146>.
- (144) Gao, L.; Zhao, H.; Li, T.; Huo, P.; Chen, D.; Liu, B. Atomic Force Microscopy Based Tip-Enhanced Raman Spectroscopy in Biology. *Int. J. Mol. Sci.* **2018**, *19* (4). <https://doi.org/10.3390/ijms19041193>.
- (145) Shen, J.; Zhang, D.; Zhang, F.-H.; Gan, Y. AFM Tip-Sample Convolution Effects for Cylinder Protrusions. *Appl. Surf. Sci.* **2017**, *422*, 482–491. <https://doi.org/10.1016/j.apsusc.2017.06.053>.
- (146) Gallyamov M.O., Yaminsky I.V. *Scanning probe microscopy: Basic Principles, distortions analysis. 2001. Eletronic publishing: http://spm.genebee.msu.ru/members/gallyamov/gal_yam/gal_yam1.html. http://spm.genebee.msu.ru/members/gallyamov/gal_yam/gal_yam1.html (accessed 2021-11-29).*
- (147) Igor S. Grigoriev; Evgenii Z. Meilikhov; Alexandre A. Radzig ; *Handbook of Physical Quantities Moscow: Energoatomizdat Publ., 1991. – 1231 Pp. ISBN: 9780849328619.*
- (148) NT-MDT Spectrum Instruments. Effect of the Tip Curvature Radius and Cone Angle; [https://www.ntmdt-si.com/resources/spm-theory/theoretical-background-of-spm/2-scanning-force-microscopy-\(sfm\)/25-ultimate-resolution-in-contact-mode/252-effect-of-the-tip-curvature-radius-and-cone-angle](https://www.ntmdt-si.com/resources/spm-theory/theoretical-background-of-spm/2-scanning-force-microscopy-(sfm)/25-ultimate-resolution-in-contact-mode/252-effect-of-the-tip-curvature-radius-and-cone-angle).
- (149) Kang, G.; Yang, M.; Mattei, M. S.; Schatz, G. C.; Van Duyne, R. P. *In Situ* Nanoscale Redox Mapping Using Tip-Enhanced Raman Spectroscopy. *Nano Lett.* **2019**, *19* (3), 2106–2113. <https://doi.org/10.1021/acs.nanolett.9b00313>.
- (150) Gajan, A.; Lecourt, C.; Torres Bautista, B. E.; Fillaud, L.; Demeaux, J.; Lucas, I. T. Solid Electrolyte Interphase Instability in Operating Lithium-Ion Batteries Unraveled by Enhanced-Raman Spectroscopy. *ACS Energy Lett.* **2021**, *6* (5), 1757–1763. <https://doi.org/10.1021/acsenerylett.1c00436>.
- (151) Li, J. F.; Huang, Y. F.; Ding, Y.; Yang, Z. L.; Li, S. B.; Zhou, X. S.; Fan, F. R.; Zhang, W.; Zhou, Z. Y.; Wu, D. Y.; Ren, B.; Wang, Z. L.; Tian, Z. Q. Shell-Isolated Nanoparticle-Enhanced Raman Spectroscopy. *Nature* **2010**, *464* (7287), 392–395. <https://doi.org/10.1038/nature08907>.
- (152) Lucas, I. T.; Durand-Vidal, S.; Dubois, E.; Chevalet, J.; Turq, P. Surface Charge Density of Maghemite Nanoparticles: Role of Electrostatics in the Proton Exchange. *J. Phys. Chem. C* **2007**, *111* (50), 18568–18576. <https://doi.org/10.1021/jp0743119>.

- (153) Canet-Ferrer, J.; Coronado, E.; Forment-Aliaga, A.; Pinilla-Cienfuegos, E. Correction of the Tip Convolution Effects in the Imaging of Nanostructures Studied through Scanning Force Microscopy. *Nanotechnology* **2014**, *25* (39), 395703. <https://doi.org/10.1088/0957-4484/25/39/395703>.
- (154) Marques-Moros, F.; Forment-Aliaga, A.; Pinilla-Cienfuegos, E.; Canet-Ferrer, J. Mirror Effect in Atomic Force Microscopy Profiles Enables Tip Reconstruction. *Sci. Rep.* **2020**, *10* (1), 18911. <https://doi.org/10.1038/s41598-020-75785-0>.
- (155) Picardi, G.; Chaigneau, M.; Ossikovski, R.; Licitra, C.; Delapierre, G. Tip Enhanced Raman Spectroscopy on Azobenzene Thiol Self-Assembled Monolayers on Au(111): Tip Enhanced Raman Spectroscopy on Azobenzene Thiol Self-Assembled Monolayers on Au. *J. Raman Spectrosc.* **2009**, *40* (10), 1407–1412. <https://doi.org/10.1002/jrs.2362>.
- (156) Wickramasinghe, H. K.; Chaigneau, M.; Yasukuni, R.; Picardi, G.; Ossikovski, R. Billion-Fold Increase in Tip-Enhanced Raman Signal. *ACS Nano* **2014**, *8* (4), 3421–3426. <https://doi.org/10.1021/nn406263m>.
- (157) Armstrong, D. R.; Clarkson, J.; Smith, W. E. Vibrational Analysis of Trans-Azobenzene. *J. Phys. Chem.* **1995**, *99* (51), 17825–17831. <https://doi.org/10.1021/j100051a005>.
- (158) Biswas, N.; Umapathy, S. Density Functional Calculations of Structures, Vibrational Frequencies, and Normal Modes of *Trans* - and *Cis* -Azobenzene. *J. Phys. Chem. A* **1997**, *101* (30), 5555–5566. <https://doi.org/10.1021/jp970312x>.
- (159) Fujino, T.; Tahara, T. Picosecond Time-Resolved Raman Study of *Trans* -Azobenzene. *J. Phys. Chem. A* **2000**, *104* (18), 4203–4210. <https://doi.org/10.1021/jp992757m>.
- (160) Toccafondi, C.; Picardi, G.; Ossikovski, R. Molecular Bending at the Nanoscale Evidenced by Tip-Enhanced Raman Spectroscopy in Tunneling Mode on Thiol Self-Assembled Monolayers. *J. Phys. Chem. C* **2016**, *120* (32), 18209–18219. <https://doi.org/10.1021/acs.jpcc.6b03443>.
- (161) Huang, S.; Ling, X.; Liang, L.; Song, Y.; Fang, W.; Zhang, J.; Kong, J.; Meunier, V.; Dresselhaus, M. S. Molecular Selectivity of Graphene-Enhanced Raman Scattering. *Nano Lett.* **2015**, *15* (5), 2892–2901. <https://doi.org/10.1021/nl5045988>.
- (162) Kazemi-Zanjani, N.; Vedraïne, S.; Laguagné-Labarthe, F. Localized Enhancement of Electric Field in Tip-Enhanced Raman Spectroscopy Using Radially and Linearly Polarized Light. *Opt. Express* **2013**, *21* (21), 25271. <https://doi.org/10.1364/OE.21.025271>.
- (163) Gong, Y.; Joly, A. G.; El-Khoury, P. Z.; Hess, W. P. Polarization-Directed Surface Plasmon Polariton Launching. *J. Phys. Chem. Lett.* **2017**, *8* (1), 49–54. <https://doi.org/10.1021/acs.jpcclett.6b02509>.
- (164) Wan, D.-S.; Rajadhyaksha, M.; Webb, R. H. Analysis of Spherical Aberration of a Water Immersion Objective: Application to Specimens with Refractive Indices 1.33-1.40: SPHERICAL ABERRATION OF A WATER IMMERSION OBJECTIVE. *J. Microsc.* **2000**, *197* (3), 274–284. <https://doi.org/10.1046/j.1365-2818.2000.00635.x>.
- (165) Wang, R.; He, Z.; Sokolov, A. V.; Kurouski, D. Gap-Mode Tip-Enhanced Raman Scattering on Au Nanoplates of Varied Thickness. *J. Phys. Chem. Lett.* **2020**, *11* (10), 3815–3820. <https://doi.org/10.1021/acs.jpcclett.0c01021>.
- (166) Bao, Y.-F.; Cao, M.-F.; Wu, S.-S.; Huang, T.-X.; Zeng, Z.-C.; Li, M.-H.; Wang, X.; Ren, B. Atomic Force Microscopy Based Top-Illumination Electrochemical Tip-Enhanced Raman Spectroscopy. *Anal. Chem.* **2020**, *92* (18), 12548–12555. <https://doi.org/10.1021/acs.analchem.0c02466>.
- (167) Poirier, G. E. Characterization of Organosulfur Molecular Monolayers on Au(111) Using Scanning Tunneling Microscopy. *Chem. Rev.* **1997**, *97* (4), 1117–1128. <https://doi.org/10.1021/cr960074m>.
- (168) Ulman, A. Formation and Structure of Self-Assembled Monolayers. *Chem. Rev.* **1996**, *96* (4), 1533–1554. <https://doi.org/10.1021/cr9502357>.
- (169) Mendes, P. M.; Christman, K. L.; Parthasarathy, P.; Schopf, E.; Ouyang, J.; Yang, Y.; Preece, J. A.; Maynard, H. D.; Chen, Y.; Stoddart, J. F. Electrochemically Controllable Conjugation of

- Proteins on Surfaces. *Bioconjug. Chem.* **2007**, *18* (6), 1919–1923.
<https://doi.org/10.1021/bc7002296>.
- (170) Médard, C.; Morin, M. Chemisorption of Aromatic Thiols onto a Glassy Carbon Surface. *J. Electroanal. Chem.* **2009**, *632* (1–2), 120–126.
<https://doi.org/10.1016/j.jelechem.2009.04.005>.
- (171) Schwamborn, S.; Stoica, L.; Neugebauer, S.; Reda, T.; Schmidt, H.-L.; Schuhmann, W. Local Modulation of the Redox State of *p*-Nitrothiophenol Self-Assembled Monolayers Using the Direct Mode of Scanning Electrochemical Microscopy. *ChemPhysChem* **2009**, *10* (7), 1066–1070. <https://doi.org/10.1002/cphc.200900118>.
- (172) Shindo, H. Raman Spectroscopic Observation of Adsorbates on Ag during Electrochemical Reduction of Nitrobenzene. *J. Chem. Soc. Faraday Trans. 1 Phys. Chem. Condens. Phases* **1986**, *82* (1), 45. <https://doi.org/10.1039/f19868200045>.
- (173) Gao, P.; Gosztola, D.; Leung, L.-W. H.; Weaver, M. J. Surface-Enhanced Raman Scattering at Gold Electrodes: Dependence on Electrochemical Pretreatment Conditions and Comparisons with Silver. *J. Electroanal. Chem. Interfacial Electrochem.* **1987**, *233* (1–2), 211–222.
[https://doi.org/10.1016/0022-0728\(87\)85017-9](https://doi.org/10.1016/0022-0728(87)85017-9).
- (174) Haber, F. Haber. Gradual Electrolytic Reduction of Nitrobenzene with Limited Cathode Potential. *Zeitschrift Für Elektrochemie*, 4:506 513, 1898.
- (175) Touzalin, P. T. Tip-Enhanced Raman Spectroscopy on Electrochemical Systems, Sorbonne Université, **2018**.
- (176) Gao, P.; Gosztola, D.; Weaver, M. J. Surface-Enhanced Raman Spectroscopy as a Probe of Electroorganic Reaction Pathways. 1. Processes Involving Adsorbed Nitrobenzene, Azobenzene, and Related Species. **1988**.
- (177) Zhao, L.-B.; Chen, J.-L.; Zhang, M.; Wu, D.-Y.; Tian, Z.-Q. Theoretical Study on Electroreduction of *p*-Nitrothiophenol on Silver and Gold Electrode Surfaces. *J. Phys. Chem. C* **2015**, *119* (9), 4949–4958. <https://doi.org/10.1021/jp512957c>.
- (178) van Schrojenstein Lantman, E. M.; Deckert-Gaudig, T.; Mank, A. J. G.; Deckert, V.; Weckhuysen, B. M. Catalytic Processes Monitored at the Nanoscale with Tip-Enhanced Raman Spectroscopy. *Nat. Nanotechnol.* **2012**, *7* (9), 583–586.
<https://doi.org/10.1038/nnano.2012.131>.
- (179) Koopman, W.; Titov, E.; Sarhan, R. M.; Gaebel, T.; Schürmann, R.; Mostafa, A.; Kogikoski, S.; Milosavljević, A. R.; Stete, F.; Liebig, F.; Schmitt, C. N. Z.; Koetz, J.; Bald, I.; Saalfrank, P.; Bargheer, M. The Role of Structural Flexibility in Plasmon-Driven Coupling Reactions: Kinetic Limitations in the Dimerization of Nitro-Benzenes. *Adv. Mater. Interfaces* **2021**, *8* (22), 2101344. <https://doi.org/10.1002/admi.202101344>.
- (180) Koopman, W.; Sarhan, R. M.; Stete, F.; Schmitt, C. N. Z.; Bargheer, M. Decoding the Kinetic Limitations of Plasmon Catalysis: The Case of 4-Nitrothiophenol Dimerization. *Nanoscale* **2020**, *12* (48), 24411–24418. <https://doi.org/10.1039/D0NR06039A>.
- (181) Fiocco, P. A. Development of Electrochemical Tip-Enhanced Raman Spectroscopy, 2021. 195.
- (182) Diazonium Grafting Control through a Redox Cross-Reaction: Elucidation of the Mechanism Involved When Using 2,2-Diphenylpicrylhydrazyl as an Inhibitor. **2018**, 7.
- (183) Madzharova, F.; Heiner, Z.; Kneipp, J. Surface-Enhanced Hyper Raman Spectra of Aromatic Thiols on Gold and Silver Nanoparticles. *J. Phys. Chem. C* **2020**, *124* (11), 6233–6241.
<https://doi.org/10.1021/acs.jpcc.0c00294>.
- (184) Lin-Vien, D.; Colthup, N. B.; Fateley, W. G.; Grasselli, J. G. *The Handbook of Infrared and Raman Characteristic Frequencies of Organic Molecules*; Elsevier, 1991.
- (185) Schrader, B. *Raman/Infrared Atlas of Organic Compounds*; Wiley, 1996.
- (186) Gruger, A.; Le Calvé, N.; Dizabo, P.; Fillaux, J. Spectres de Vibration Du Trans-Azobenzène et de Quelques Dérivés Isotopiques. *J. Chim. Phys.* **1972**, *69*, 291–298.
<https://doi.org/10.1051/jcp/1972690291>.
- (187) Xu, J.-F.; Luo, S.-Y.; Liu, G.-K. Different Behaviors in the Transformation of PATP Adsorbed on Ag or Au Nanoparticles Investigated by Surface-Enhanced Raman Spectroscopy – A Study of

- the Effects from Laser Energy and Annealing. *Spectrochim. Acta. A. Mol. Biomol. Spectrosc.* **2015**, *143*, 35–39. <https://doi.org/10.1016/j.saa.2015.02.039>.
- (188) Dong, B.; Fang, Y.; Chen, X.; Xu, H.; Sun, M. Substrate-, Wavelength-, and Time-Dependent Plasmon-Assisted Surface Catalysis Reaction of 4-Nitrobenzenethiol Dimerizing to *p*, *p'*-Dimercaptoazobenzene on Au, Ag, and Cu Films. *Langmuir* **2011**, *27* (17), 10677–10682. <https://doi.org/10.1021/la2018538>.
- (189) Kim, K.; Kim, K. L.; Shin, D.; Choi, J.-Y.; Shin, K. S. Surface-Enhanced Raman Scattering of 4-Aminobenzenethiol on Ag and Au: PH Dependence of b_2 -Type Bands. *J. Phys. Chem. C* **2012**, *116* (7), 4774–4779. <https://doi.org/10.1021/jp211730r>.